



Dottorato  
di Ricerca  
Scienze  
Agrarie  
Alimentari e  
Forestali

**UNIVERSITÀ DEGLI STUDI  
“MEDITERRANEA” DI REGGIO CALABRIA**  
DIPARTIMENTO DI AGRARIA  
**Dottorato di Ricerca in  
Scienze Agrarie, Alimentari e Forestali**  
*Curriculum Scienze Forestali*  
Ciclo XXXV, 2019/2022  
SSD: AGR/10 – Costruzioni Rurali e Territorio Agroforestale

*Giandomenico De Luca*

**Use of SAR and multispectral satellite images and remote  
sensing techniques for monitoring and characterization of  
consequences of fire on Mediterranean forest vegetation**

PH.D. THESIS

Tutor

*Prof. Giuseppe Modica*

Co-Tutor

*Prof. João M. N. Silva*

Ph.D. Coordinator

*Prof. Leonardo Schena*

Reggio Calabria 2022

# Index

Abstract .....	4
Riassunto .....	6
1. General Introduction .....	8
1.1. Wildland fire overview .....	8
1.2. The role of spaceborne remote sensing for wildland fire monitoring .....	12
1.3. Objectives and organization of the thesis .....	17
2. Investigation about the pre-fire condition of vegetation .....	19
2.1. Study area .....	22
2.2. Materials and methods .....	23
2.3. Discussion .....	32
2.4. Conclusion .....	37
3. Unsupervised detection of burned area using SAR data .....	38
3.1. Materials and methods .....	42
3.2. Dataset .....	44
3.3. Processing libraries .....	45
3.4. Image pre-processing and layers creation .....	46
3.5. Data preparation .....	47
3.6. Image classification .....	48
3.7. Accuracy assessment .....	49
3.8. Results .....	50
3.9. Discussion .....	55
3.10. Conclusions and recommendations .....	60
4. Regional-scale detection of burned area using a multicomposite process and GEOBIA .....	62
4.1. The compositing criteria: principles and literature review .....	63
4.2. The opportunity for higher resolution data .....	64
4.3. Integration of SAR information .....	65
4.4. Aim and structure of the study .....	65
4.5. Study area .....	66
4.6. Materials and methods .....	67
4.7. Results .....	73
4.8. Discussion .....	82
4.9. Conclusions and recommendations .....	86
5. Fire severity estimation and mapping: an approach using machine learning and the combined optical and SAR data .....	87

5.1.	Study site .....	89
5.2.	Materials and methods .....	90
5.3.	Results .....	92
5.4.	Discussion .....	95
5.5.	Conclusions.....	96
6.	Fire severity estimation and mapping: an approach using deep learning and the combined optical and SAR data.....	98
6.1.	Study area.....	100
6.2.	Materials and methods .....	100
6.3.	Results .....	102
6.4.	Map accuracy .....	104
6.5.	Discussions .....	106
6.6.	Conclusions.....	106
7.	Spectral mixture analysis of forest crown fire damage.....	108
7.1.	Study site .....	109
7.2.	Data and methods .....	111
7.3.	Result.....	114
7.4.	Discussion .....	116
7.5.	Conclusions.....	119
8.	Temporal vegetation recovery post-fire .....	120
8.1.	Masterials and methods.....	124
8.1.1.	Study area.....	124
8.2.	Results .....	129
8.3.	Discussion .....	142
8.4.	Conclusions.....	150
9.	General conclusions and future perspectives .....	152
10.	Acknowledgements .....	154
11.	References.....	155
12.	Websites.....	184

## Abstract

Although wildfires play a crucial role in ecological processes in the Mediterranean Basin, they often represent one of the primary disturbances for forests and other ecosystems, entailing landscape and habitat degradation and economic damages. They also determine the consumption of natural carbon reserves and the emission of greenhouse gasses (GHG) correlated with climate change. Accurate information relating to the impact of fire on the forest environment and how its effects are distributed over time and space, both from a qualitative and quantitative point of view, are a key factor for the subsequent implementation of medium and long-term territorial planning, in order to predict and manage irreversible processes of degradation of forests and landscape. In this context, remote sensing provides reliable tools and techniques for monitoring and quantifying the impact of burned areas with reference to satellite platforms. In post-fire monitoring, most studies have been based on optical satellite data acquired using passive multispectral sensors, that are closely correlated with the physiological and biochemical state of the vegetation. For these reasons, vegetation has its unique spectral signature (depending on the species and environmental conditions), and its observation enables its characterization and subsequent monitoring. Anomalies at the spectral level, indeed, conceal anomalies at the plant level. Although their effectiveness for this purpose has been widely proven, optical systems present some limitations, mainly due to their sensitivity to some environmental conditions, such as sunlight and cloud cover, which reduces the frequency of observation at the visible/infrared wavelength bands or the spectral confusion of burned areas with unburned low albedo surfaces (i.e., dark soils, water surfaces, shadow areas), or the premature signal saturation due to the high sensibility to increasing values of leaf area index (LAI). Furthermore, this type of sensors cannot capture many quantitative aspects since these wavelengths do not interact directly with the structure of the objects. Therefore, methods based on data acquired by cloud-independent and structure-dependent sensors at high spatial and temporal resolutions are needed. Among them, Synthetic Aperture Radar (SAR) are active sensors that generates their microwave impulses (2.4-100 cm) and transmits them from its antenna to a target. Calculating the amount of the signal fraction reflected back to the sensor (backscatter) characterizes the target's spectral radar signature. The penetration capacity of the impulse in the matter is directly proportional to the wavelength. For this reason, the SAR waves can pass through atmospheric particulate or interact with the vegetation cover structure. Therefore, to characterize and quantify the effects of a disturbance on vegetation, radar technology exploits the variations in backscatter caused by the modification of the vegetation cover and soil's structure and moisture content. However, its processing and interpretation complexity causes this sensor not to be widely used compared to optical ones.

Against that background, in this Ph.D. thesis, a complete and open-access workflow aimed at the investigation and mapping of the fire effects on Mediterranean ecosystems in the short term (pre-fire condition assessment; burned area detection; post-fire severity estimation and mapping) and the monitoring of the response of the environment during the first years after the event (post-fire recovery monitoring), was developed. To achieve this, free-available optical (Sentinel-2) and SAR (Sentinel-1) high spatial and temporal data were integrated, assessing the strengths and limitations of each of them and the advantages that are provided by the combination of both information. The first step concerned the construction of an accurate land use/land cover (LULC) map in a heterogeneous Mediterranean forest (located in Portugal) area to have an overview of the qualitative and quantitative state of vegetation present before the fire event. To this end, we applied an exhaustive grid search analysis to set the optimal hyperparameters of a machine learning model (random forest, RF) and the inclusion of different variables



(i.e., vegetation indices time-series, optical biophysical variables, and interferometric SAR - InSAR - coherence). This integration allowed reaching an overall accuracy (F-score) of 0.903, observing an improvement of 2.53% when SAR data were integrated into optical information.

The second step dealt with the accurate detection of burned areas and delimitation of their perimeters. Two approaches were proposed to fulfil the objective: the first concerned only the use of SAR data (backscatter, dual- and single polarized SAR indices, textures) for an unsupervised detection (using the *k*-mean algorithm, set using a silhouette score analysis) of burned areas in two different study sites (located in Portugal and Italy respectively), with a reached F-score of 0.803 (Portuguese site) and 0.853 (Italian site); the second approach proposed a multitemporal composite process, by combining both Sentinel-2 and Sentinel-1 images, and a subsequent object-based geographic analysis (GEOBIA) to map burned areas on regional/national scales occurred during the entire fire season (2017) in Portugal, achieving F-score values of 0.914 (when only optical data is used) and 0.956 (combining optical and SAR information).

In the third step of the main workflow, the short-term fire effects, in the form of fire severity, and their spatial distribution are estimated. Three approaches were presented, two of which are similar and united by the use of the composite burnt index (CBI) protocol to determine the severity classes in the field and to define the training data of the model, which, in one case (study site located in Portugal), was constituted by the RF algorithm, while in the other case (study site located in Italy) an artificial neural network was built. The RF model reached an F-score of 0.838 when both the datasets were combined (S1 + S2), compared with the values achieved by using SAR (0.513) and optical (0.805). The results obtained using the artificial neural network (F-score > 0.95) gave proof of the great potential in the use of these advanced deep learning models. A third approach involved a spectral mixture analysis (SMA) of optical Sentinel-2 imagery to spectrally characterize and quantify the proportion of the three fraction components indicative of the main physical effects immediately after a forest fire (char, scorched vegetation and green vegetation).

For the first years after a fire event, the investigation of temporal and spatial dynamics of the post-fire recovery of different Mediterranean vegetation types characterized the fourth step. Both SAR Sentinel-1 and optical Sentinel-2 time series were analyzed separately according to the fire severity classes (obtained in the previous step), highlighting the complementary and essentiality of both information. Moreover, a burn recovery ratio (BRR), optimized through machine learning regressors for predicting pre-fire conditions, was proposed to estimate and map the spatial distribution of the degree of vegetation recovery.

The development of these approaches and managing this amount of data required advanced techniques and solutions of geo-informatics, geo-statistics, geomatic, image processing, and advanced artificial intelligence models. Nevertheless, the whole process was developed and performed, fulfilling the principle of employing freely available data and open-source software and libraries (e.g., ESA SNAP, Scikit-Learn, OTB, Google Earth Engine) mostly executed in Python-script language.

**Keywords:** fire severity, Sentinel-1, Sentinel-2, burn detection, post-fire recovery, geo-informatic, machine learning

## Riassunto

Nel bacino del Mediterraneo, sebbene gli incendi svolgano un ruolo cruciale nei processi ecologici, spesso rappresentano uno dei principali disturbi per le foreste e gli altri ecosistemi, comportando degradazione del paesaggio e degli habitat, e danni economici. Gli incendi, inoltre, determinano il consumo di riserve naturali di carbonio e l'emissione di gas serra (GHG) correlati al cambiamento climatico. Informazioni accurate relative all'impatto dell'incendio sull'ambiente forestale, e alla sua distribuzione nel tempo e nello spazio, rappresentano fattori chiave per la successiva attuazione della pianificazione territoriale a medio e lungo termine, finalizzata alla prevenzione e gestione di quei processi irreversibili di degrado degli habitat e del paesaggio. In questo contesto, il telerilevamento satellitare fornisce strumenti e tecniche affidabili per monitorare e quantificare l'impatto delle aree bruciate. Nel monitoraggio post-incendio, la maggior parte degli studi si è basata su dati satellitari ottici acquisiti utilizzando sensori multispettrali passivi, strettamente correlati allo stato fisiologico e biochimico della vegetazione. La vegetazione presenta infatti una firma spettrale univoca (con piccole variazioni a seconda della specie e delle condizioni ambientali), e la sua analisi ne consente la caratterizzazione e il successivo monitoraggio: le anomalie spettrali, infatti, si traducono in anomalie a livello della pianta. Sebbene l'efficacia dei sensori ottici per lo scopo appena descritto sia stata ampiamente dimostrata, essi presentano alcune limitazioni. Queste sono principalmente causate dalla sensibilità ad alcune condizioni ambientali: come luce solare e nuvolosità, che ne riducono la frequenza di osservazione; o dalla confusione di aree bruciate con superfici a bassa albedo (es. suoli scuri, superfici idriche, zone d'ombra); o la sensibilità ai valori crescenti dell'indice di area fogliare (LAI) che comporta una prematura saturazione del segnale. Inoltre, questi tipi di sensori non interagiscono direttamente con la struttura degli oggetti non permettendogli la cattura di molti aspetti qualitativi della copertura vegetale. Pertanto, sono necessari dati acquisiti da sensori che presentino sia indipendenza dalla copertura nuvolosa, sia la capacità di interagire con la struttura. Tra questi, i radar ad apertura sintetica (SAR) sono sensori attivi che generano i loro impulsi a microonde (2,4-100 cm) e li trasmettono dalla loro antenna ad un bersaglio posto sulla superficie terrestre. Il calcolo della quantità della frazione di segnale riflessa verso sensore (*backscatter*) caratterizza la firma del radar spettrale del bersaglio. La capacità di penetrazione dell'impulso nella materia è direttamente proporzionale alla lunghezza d'onda. Per questo motivo, le onde SAR possono attraversare il particolato atmosferico o interagire con la struttura della copertura vegetale. Pertanto, per caratterizzare e quantificare gli effetti di un disturbo sulla vegetazione, la tecnologia radar sfrutta le variazioni di *backscatter* causate dalla modifica della copertura vegetale, della struttura del suolo, e del contenuto di umidità degli oggetti osservati. Tuttavia, la sua complessità di elaborazione e interpretazione fa sì che questi sensori non siano ampiamente utilizzati quanto quelli ottici.

In tale contesto, la presente tesi di Dottorato propone un *workflow* completo ed open-source finalizzato all'indagine e mappatura degli effetti del fuoco a breve termine sugli ecosistemi mediterranei (valutazione delle condizioni pre-incendio; rilevamento delle aree bruciate; stima e mappatura della severità post-incendio) e al monitoraggio temporale della risposta della vegetazione durante i primi anni dopo l'evento di incendio (monitoraggio del recupero post-incendio). Per assecondare questi obiettivi, sono stati integrati dati ottici (Sentinel-2) e SAR (Sentinel-1) gratuiti e ad alta risoluzione spaziale e temporale, valutando i punti di forza e i limiti di ciascuno di essi, e i vantaggi forniti dalla combinazione di entrambe le informazioni. Il primo step ha riguardato la realizzazione di un'accurata mappa della copertura e uso del suolo (LULC) in un'area Mediterranea eterogenea (situata in Portogallo) al fine di avere una panoramica dello stato qualitativo e quantitativo della vegetazione presente prima dell'evento di incendio. A tal fine, diverse variabili sono state calcolate ed utilizzate come dati di

input (ad esempio, serie temporali degli indici di vegetazione, variabili biofisiche ottiche e SAR interferometrico - InSAR - coerenza). Inoltre, è stata applicata un'analisi *exhaustive grid search* per impostare gli iperparametri ottimali di un modello di machine learning (foresta casuale, RF). Questa integrazione ha permesso di raggiungere un'accuratezza complessiva (F-score) di 0.903, osservando un miglioramento del 2,53% quando i dati SAR sono stati accoppiate alle informazioni ottiche.

Il secondo step ha riguardato il rilevamento accurato delle aree bruciate e la delimitazione dei loro perimetri. Sono stati proposti due approcci per raggiungere questo obiettivo: il primo riguardava solo l'uso di dati SAR (*backscatter*, indici SAR a doppia e singola polarizzazione, texture) per un rilevamento non supervisionato (utilizzando l'algoritmo k-mean, impostato utilizzando un'analisi *silhouette*) delle aree bruciate in due diversi siti di studio (situati rispettivamente in Portogallo e in Italia), raggiungendo valori di F-score pari a 0.803 (sito portoghese) e 0.853 (sito italiano); il secondo approccio proponeva un processo di *image composite* multitemporale, combinando sia le immagini Sentinel-2 che quelle Sentinel-1, e una successiva classificazione ad oggetti (GEOBIA) per mappare le aree bruciate su scala regionale/nazionale da incendi avvenuti durante un'intera stagione degli incendi (2017) in Portogallo, ottenendo valori F-score di 0,914 (quando vengono utilizzati solo dati ottici) e 0,956 (combinando informazioni ottiche e SAR).

Nel terzo step, vengono stimati gli effetti dell'incendio a breve termine, sotto forma di severità dell'incendio, e la loro distribuzione spaziale. Sono stati presentati tre approcci di cui due simili e accomunati dall'uso del protocollo *Composite Burnt Index* (CBI) per determinare le classi di severità sul campo e per definire i dati di addestramento del modello. In un approccio (sito di studio situato in Portogallo), si è utilizzato l'algoritmo RF come modello; mentre in un secondo approccio (sito di studio situato in Italia) è stata implementata una rete neurale artificiale. Il modello RF ha raggiunto un valore di F-score di 0,838 quando entrambi i set di dati sono stati combinati (S1 + S2), rispetto ai valori ottenuti utilizzando solo SAR (0,513) e solo ottico (0,805). I risultati ottenuti utilizzando la rete neurale artificiale (F-score > 0,95) hanno dato prova del grande potenziale nell'uso di questi modelli avanzati di deep learning. Un terzo approccio prevedeva l'applicazione di una *spectral mixture analysis* (SMA) delle immagini ottiche Sentinel-2 per caratterizzare spettralmente e quantificare la proporzione delle tre componenti frazionali indicativi dei principali effetti fisici riscontrabili immediatamente dopo un incendio boschivo (carbone, vegetazione bruciata e vegetazione verde).

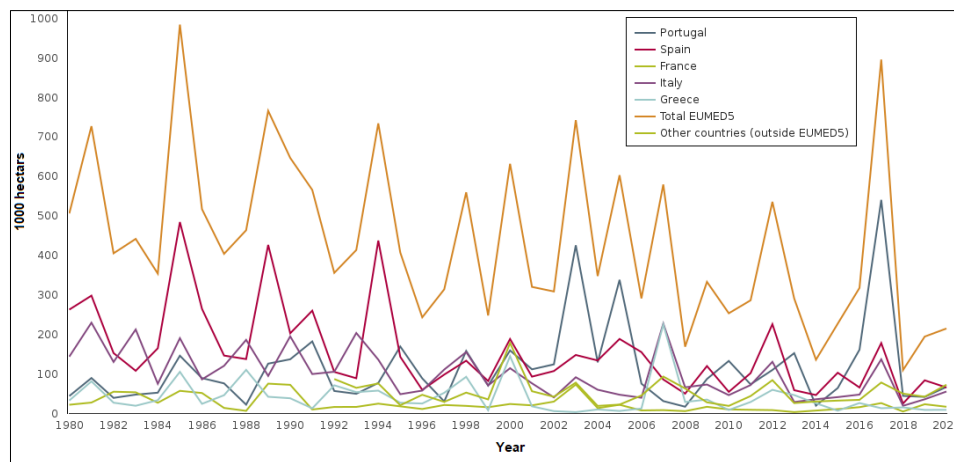
Per i primi anni dopo un evento di incendio, l'indagine sulle dinamiche temporali e spaziali del recupero post-incendio di diverse tipologie di vegetazione mediterranea ha caratterizzato il quarto step. Sia le serie temporali SAR Sentinel-1 che quelle ottiche Sentinel-2 sono state analizzate separatamente in base alle classi di gravità dell'incendio (ottenute nello step precedente), evidenziando la complementarità e l'essenzialità di entrambe le informazioni. Inoltre, è stato proposto un indice *burn recovery ratio* (BRR) per la stima e la mappatura della distribuzione spaziale del grado di recupero della vegetazione. L'indice è stato ottimizzato nella fase di predizione delle condizioni pre-incendio tramite algoritmo di regressione di machine learning.

Lo sviluppo di questi approcci e la gestione di questa quantità di dati hanno richiesto tecniche e soluzioni avanzate di geo-informatica, geostatistica, geomatica, *image processing* e modelli avanzati di intelligenza artificiale. Tuttavia, l'intero processo è stato sviluppato ed eseguito rispettando il principio dell'utilizzo di dati gratuitamente disponibili e software e librerie open-source (ad es. ESA SNAP, Scikit-Learn, OTB, Google Earth Engine) eseguiti principalmente tramite linguaggio Python.

# 1. General Introduction

## 1.1. Wildland fire overview

Wildland fires are a primary natural component that influences the ecological dynamics of many ecosystems at different spatial and temporal scales. On the one hand, fire stimulates bio-physical activities and natural regeneration, and promotes seed germination and production, positively and indirectly affecting the biodiversity of the affected environments (Emilio Chuvieco, 2009; Emilio Chuvieco et al., 2014; Moreira et al., 2020; Valkó & Deák, 2021). Moreover, it can improve soil properties when the frequency is low and/or the temperatures reached are not high enough to cause the volatilization of organic matter and nutrients (Alcañiz et al., 2018; Pereira et al., 2018; Romeo et al., 2020). On the other hand, fire can represent a long-term threat, contributing to environmental degradation, namely, soil erosion, habitat simplification, biomass consumption, and greenhouse gas (GHGs) emissions affecting air quality and global climate (Cascio, 2018; Hardy, 2005; Häusler et al., 2018; Reid et al., 2016; Rosa et al., 2011). Moreover, the direct influence of human activity on its frequency or, indirectly, the negative consequence that such activities have raised on global climate and the modification of landscape and habitat patterns has led to a worsening fire susceptibility of some environments during the last decades (Mitchell et al., 2009; Moreira et al., 2020). Such events negatively impact ecosystem services, such as food production, fresh water stocks, wood products, microclimate, recreation, and tourism (Emilio Chuvieco et al., 2014). Moreover, these events have direct socio-economic damages given by the loss of human life and infrastructure. According to European fire statistics (Figure 1.1) (EFFIS annual fire reports, 2022; European Environment Agency, 2022), although the long-term trend of burned area extension has decreased in Europe, some countries have experienced more extreme events (in terms of the burned surface) during the last decades (e.g., Portugal).



**Figure 1.1.** Annual burned surface in European countries between 1980 and 2020, with more focus on the Mediterranean European countries (EUMED5: Portugal, Spain, France (southern), Italy and Greece). European member countries not included in EUMED5 are designed as “Other countries”. The reference is [https://www.eea.europa.eu/data-and-maps/daviz/burnt-forest-area-in-five-4#tab-chart\\_5](https://www.eea.europa.eu/data-and-maps/daviz/burnt-forest-area-in-five-4#tab-chart_5). The Data are, in turn, supplied by “San-Miguel-Ayaz, J., et al., Forest Fires in Europe, Middle East and North Africa 2020, EUR 30862 EN, Publications Office of the European Union, Luxembourg, 2021, doi:10.2760/216466, JRC1267665”.

Notably, in the Mediterranean basin, although wildland fires are an integral element of natural ecosystems and historically used as a tool for land-use management, their impacts have increased in the last decades, causing

significant economic damages and landscape disasters (Chuvieco, 2009; San- Miguel-Ayanza et al. 2018; San- Miguel-Ayanza et al. 2019; Silva et al. 2019; Otón et al., 2019).

Mediterranean ecosystems constitute a critical biome at the European level due to their high biodiversity and intense interaction with human activities (Aragones et al., 2019; Emilio Chuvieco, 2009; Moreira et al., 2020). The typical Mediterranean climatic regime, characterized by long periods of summer drought, exacerbated by the current global warming, entails an increasing wildfire risk in terms of frequency, extension, and severity (Moreira et al., 2020). Fire severity is defined as the degree of direct environmental chemical-physical alterations, decomposition, and loss of above/below-ground organic and inorganic matter caused by the combustion process (De Santis & Chuvieco, 2007; Key & Benson, 2006; Lentile et al., 2006; Roth et al., 2012). It plays a critical role in the sustainability of Mediterranean habitats, influencing the competitive interactions between species and their post-fire recovery capability (Christopoulou et al., 2019; José Vidal-Macua et al., 2017; Lacouture et al., 2020; Morresi et al., 2019; Tanase et al., 2011; Viana-Soto et al., 2017). Moreover, the widespread accumulation of woody fuel, a consequence of the abandonment of the semi-natural and agricultural areas that has been occurring in Mediterranean landscapes, has been causing suitable conditions for the ignition and the progression of such high intensity fires (Xofis et al., 2022). Fire intensity, defined as the energy released by a fire per length of fire front per unit time (Keeley, 2009; Key & Benson, 2006).

The immediate impact of the fire appears in the form of alteration of the vegetation cover, both structurally (e.g. canopy and biomass consumption) and chemical-physically, with the death or consumption of the organic matter and photosynthesizing tissues, caused by the direct heat transfer generated by the fire or the biomass combustion (Key & Benson, 2006; Lentile et al., 2006). Subsequently, in response to a fire event, Mediterranean habitats activate natural mechanisms for recovery of pre-fire ecological conditions. The effectiveness of these mechanisms depends on the characteristics of the fire itself, in turn, influenced by several environmental factors (combined action of vegetation type, wind, moisture, and topography), on its direct physical impact on the land surface, and on the degree of ecosystems resilience (Filipe X Catry et al., 2012; Fernández-García et al., 2018; Fernandez-Manso et al., 2016; Frazier et al., 2015; Gouveia et al., 2010; Morresi et al., 2019).

Therefore, regarding the short-term effects, it can be argued that they depend on the susceptibility of the ecosystems. First, the energy produced by fire (intensity) is determined by the nature of the fuels available for combustion, and the type of vegetation. In particular, the density and moisture content of fuels. Meteorological conditions play a decisive role (e.g., the rainfall drastically reduce the fire intensity and duration while the winds feed it with comburent), and land topography (e.g., the presence of natural barriers for the advancement of the flames or slopes that, instead, facilitate the contact between them and the surrounding vegetation) (José Vidal-Macua et al., 2017; Key & Benson, 2006; Moreira et al., 2020).

The complexity of fire's effects on the Mediterranean ecosystem reflects the complexity of the ecosystem itself. Each of the thousands of individual components that constitute the ecosystem uniquely responds to the fire event but, if it could be more or less relevant to be individually accounted, depends on the objectives (Key, 2006). In fact, the evaluation of the fire effect remains a judgment that changes according to the study's context and objectives. Although intensity and severity are two highly correlated factors, the same intensity value can produce different degrees of severity burn, depending on the combination of the various environmental and vegetational factors seen above. Moreover, some species are known to have adaptations that make them more resistant to fire than others (Mitchell et al., 2009; Romeo et al., 2020). The fire severity represents the most suitable metric for

describing the post-fire effects on vegetation. It is a coherent numerical scale that measures the magnitude of change on a single factor and as a composite of multiple ecological factors (Key & Benson, 2006).

In this context, the definition of protocols for the qualitative and quantitative description of short and longer effects on Mediterranean ecosystems is crucial for better understanding their dynamics and planning appropriate post-fire management strategies (Chu & Guo, 2013; Emilio Chuvieco et al., 2019; Carmen Quintano et al., 2020). A holistic approach is generally used at large scales and in landscape ecology in order to represent the severity of the burn as an aggregate of effects on a given area.

From a landscape perspective, the widest used and accepted protocol for short-term fire severity effects estimation is the Composite Burn Index (CBI) proposed by Key & Benson (2006) (Key & Benson, 2006) and developed in the framework of the FIREMON Project (2006). This method is used to derive index values that summarize overall burn ecological impacts within an area, that is, the average fire effects on a plot and the main macro-components that compose it: soil, litter and vegetation. To derive the averaged severity value for a sample plot, the metric combines average conditions of many visual-assessed ecological factors (e.g., percent of unaltered green vegetation, torched trees and coal thickness, altered brown foliage) across multiple strata composing an ecosystem (litter, herbs, shrubs, short trees, medium height/sub-dominant trees and high/dominant trees). The short-term fire effects are independently examined by strata so that they can be as relatively associable as possible (Key & Benson, 2006). The CBI is, therefore, a holistic approach that integrates the different fire effects that can be easily observed on the ground converts them to numerical values, and returns an average value, to simplify the severity categorization procedure. It is not surprising, in light of this, that this approach was designed to make the high variability observable in a post-fire context as comparable as possible with the perspective of a multispectral sensor mounted on a satellite platform, whose spatial unit (pixel) is expressed by simple single numbers (Key & Benson, 2006; Sander Veraverbeke & Hook, 2013). Several modifications and optimizations of the CBI protocol have been proposed in the literature (e.g., De Santis & Chuvieco, 2007, 2009; Saulino et al., 2020). However, the relevance of CBI is given by having standardized and made replicable to different ecosystems the approach for fire effects assessing, as well as clarifying their definitions.

Although the effects of burn severity vary within a continuum, for convenience and to be comparable to remote sensing data, burn severity is often summarized into three discrete classes (low, moderate and high), from which it is possible to retrieve intermediate classes (De Luca, Silva, Oom, et al., 2021; De Santis & Chuvieco, 2007, 2009; Lentile et al., 2006). Employing the nomenclature used in several studies that evaluated the pure components observable in an immediate post-fire forest environment (Lentile et al., 2006; Quintano et al., 2013, 2020; A M S Smith et al., 2007; S Veraverbeke et al., 2012; Sander Veraverbeke & Hook, 2013), indicative of the physical fire effects, the definition as mentioned above of severity classes could be replaced to make the assessment as objective as possible (Figure 1.2):

- ❖ Green component (from unburned to low severity): the substrate, the understory vegetation (herbs, shrubs and trees less than 1 meter) and trees canopies could result unaltered by fire or only slightly disturbed by heat. In these conditions, most of the green photosynthetic plant tissues stay alive. Fallen trees should also be considered (due to wind or soil instability) but in which the conditions of the canopy are as described above. From a satellite perspective, and/or according to the variable target under study, this severity class may only refer to the crowns of the dominant trees. Therefore, it could also include sub-areas where the undergrowth has been affected by the fire while the foliage has not.

- ❖ Scorch component (from moderate to moderate-high severity): alteration of pre-fire green healthy vegetation foliage to brown dead plant tissues (scorched), mostly leaves/noodles killed by proximal heat radiated and convected from the surface fire or by fire-induced girdling, with the structural elements (trunk and branches) affected but unconsumed (except for the fine outer branching). The understory is generally heavily altered or consumed. As mentioned above, fallen trees must be counted to describe this effects category. It is expected that delayed mortality will arise in the most affected tree canopies. Fallen trees should also be considered (due to wind or soil instability), but in which the conditions of the canopy are as described above.
- ❖ Charcoal component (from high to very-high severity): Severe alteration or consumption of crown foliage and woody material, implicating conversion to inorganic carbon (charcoal), till, at extreme severities, the complete loss of woody fuel. Since CBI is a visual-based severity assessment approach, blackened woody tree parts from soot or high flames (without effectively affecting the internal tissues) have been generally included in this category of short-term effects. A mantle of coal and ash replaced the total absence of short vegetation.



**Figure 1.2.** The figure illustrates four cases of post-fire effects on tree's canopies, three of which represent the main post-fire components (green, top-left box; scorch, top-right box; charcoal, bottom-right box) and one mixed class (green-scorch, bottom-left box). The photos were taken in Serra de Monchique - Portugal (top-left box; photo on the right of the bottom-left box; photo on the right of the bottom-right box) and in the Aspromonte National Park - Italy (top -right box; photo on the left of the bottom-left box; photo on the left of the bottom-right box).

As mentioned above, the direct impact of fire influences the effectiveness of post-fire recovery strategies that are activated by Mediterranean ecosystems immediately after the event (Filipe X Catry et al., 2012; Fernández-García et al., 2018; Fernandez-Manso et al., 2016; Frazier et al., 2015; Gouveia et al., 2010; Morresi et al., 2019), as well as they can differ based on the combination of same variables that govern the behavior of the fire itself: environment (soil moisture-holding capacity, microclimate), topographic (geomorphology, aspect), vegetation (type and quantity of vegetation present before and after the fire as seed bank able to mature under fire-altered microclimate and soil), human activity (Christopoulou et al., 2019; De Luis et al., 2006; José Vidal-Macua et al., 2017; Key, 2006; Mitchell et al., 2009; Montès et al., 2004)

Once the fire damages have been quantified and categorized, the monitoring of the long-term impacts and the response of environment should be set as a subsequent goal. The post-fire recovery of vegetation cover structure is a natural mechanism that promotes the restoration of numerous ecosystem services, such as the carbon sequestration induced by the regenerating process of forest vegetation, which mitigates the carbon emissions to

the atmosphere due to fire (Frolking et al., 2009; Huang et al., 2020; Morresi et al., 2019; Ryu et al., 2018; Semeraro et al., 2019). In Mediterranean ecosystems, the recovery process is very complex. The first stage of post-fire dynamic auto-succession is usually characterized by prompt and massive colonization of pioneer Mediterranean annual grasses and perennial woody shrubs (*Fabaceae*, *Cistaceae*, *Lamiaceae*, *Pteridofite*) or pioneer trees (Capitania & Carcaillet, 2008; De Luis et al., 2006; Mitchell et al., 2009; Montès et al., 2004). The gaps caused by parts of dead and/or destroyed foliage expose the underlying layers, which are rapidly colonized by flourishing herbaceous pioneer vegetation. Most of the taxa recognizable in a post-fire environment play a fundamental ecological role in the general recovery of degraded or abandoned areas (e.g., former agriculture areas) in Mediterranean territories (Xofis et al., 2022). The second stage (medium and long term) involves the gap filling by the forest seedlings in the areas previously occupied or currently surrounded by forest (Frazier et al., 2015; Montès et al., 2004). This step can be anticipated when the woody species are characterized by a high capacity for asexual (es. *Eucalyptus*, *Quercus*, etc.) or sexual (Mediterranean pines) regeneration (Capitania & Carcaillet, 2008; Filipe X Catry, Moreira, et al., 2013; Montès et al., 2004; Romeo et al., 2020) as adaptations to fire. The following competition phases determine the closure of the foliage of the new individuals. Meanwhile, below the canopies, the seedlings of shade-tolerant trees continue to develop (Capitania & Carcaillet, 2008; Frazier et al., 2015).

## **1.2. The role of spaceborne remote sensing for wildland fire monitoring**

### **1.2.1. The optical domain**

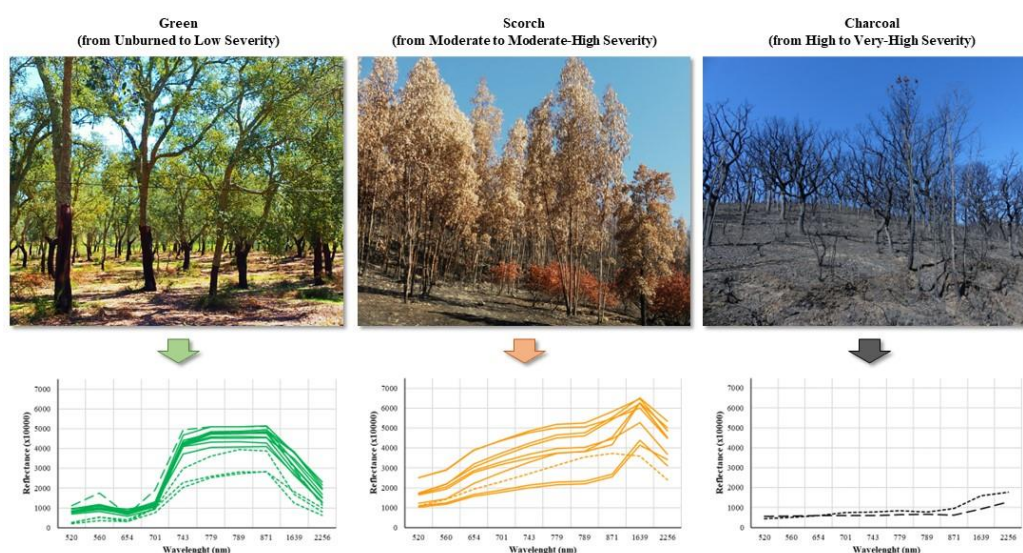
Remote sensing techniques and data have been extensively employed to detect and estimate the effects of fire on ecosystems, promoted by the increasing availability of numerous satellite sensors at rising spatial, spectral, and temporal resolutions, and even more robust analysis algorithms and processing software (Chu & Guo, 2013; Emilio Chuvieco et al., 2019; Corona et al., 2008; I. Gitas et al., 2012a). Most of the methodologies presented in those studies relied on the use of multispectral optical imagery to detect burned areas (Emilio Chuvieco et al., 2016; Filipponi, 2019; Mpakairi et al., 2020; Otón et al., 2019; Pulvirenti et al., 2020; Santos et al., 2020; Silva et al., 2004; Silva et al., 2019; Sousa et al., 2003), estimate the degree and the spatial distribution of burn severity (De Luca, Silva, Oom, et al., 2021; Fernández-García et al., 2018; Morresi et al., 2022; Saulino et al., 2020), and assess other consequences of the fire on environmental biological and structural features, such as biomass consumption (Garcia et al., 2017) and greenhouse gas emissions (Ostroukhov et al., 2022; Rosa et al., 2011).

Multi-spectral optical sensors are passive systems capable of capturing the reflected electromagnetic waves (emanated by the Sun) in the regions of the electromagnetic spectrum including between the visible and the infrared (wavelength around 400 nm to 2300 nm, if thermal-infrared is excluded). The efficiency of these passive sensors is due to the high sensitivity of the visible (VIS), near-infrared (NIR), and short-infrared (SWIR) spectral regions to the surface changes caused by fire (Chuvieco 2009; Chuvieco et al. 2019; Pereira et al. 1999). Using the definitions schematized by Chuvieco et al. (2020): the VIS region (0.4–0.7  $\mu\text{m}$ ) covers the spectral wavelengths our eyes can sense. The VIS is generally decomposed into three primary colors: blue (0.4–0.5  $\mu\text{m}$ ), green (0.5–0.6  $\mu\text{m}$ ), and red (0.6–0.7  $\mu\text{m}$ ). The spectrum's NIR region (0.7–1.2  $\mu\text{m}$ ) lies just beyond the human eye's perception capability and is highly sensitive to plant health (photosynthetic) status and vegetation net primary productivity. Within this region, the Red-Edge (0.7–0.75  $\mu\text{m}$ ) part is distinguished to be particularly sensitive to leaf pigments content. The SWIR region (1.2–2.5  $\mu\text{m}$ ), in which the influence of the Sun's energy is still very



relevant, provides the best estimations of the moisture content of soil and vegetation in the optical domain. A substantial part of these wavelengths strikes objects on Earth's surface and can be partially or wholly absorbed or reflected by them. The magnitude of reflection and/or absorption energy is defined by the physic-chemical characteristics of the material or by physiological processes that can occur within the tissues of the objects. In the case of vegetation, the photosynthesis and the amount of chlorophyll determine a unique interaction with electromagnetic waves if compared to other materials (Figure 1.3, left). For each specific portion of the electromagnetic spectrum, therefore for each wavelength or band, the absorbed/reflected energy balance should be at stable range levels when the vegetation is healthy, obviously with intra-variations as a function of different factors such as vegetation type and environmental conditions (see Figure 1.3). This is because the chlorophyll content is, in turn, related to the degree of stress of the plant and to seasonal-physiological phases. Thus, the quantitative-qualitative analysis of the differences between the spectral signature of healthy vegetation and its signature in a changed condition (for example, due to a fire) is the theoretical basis of remote sensing monitoring (Xie et al., 2008).

In the period immediately after a fire, burned surfaces tend to be relatively dark in the VIS, due the dominant presence of black charcoal and the decrease in other reflective components (such as photosynthetically active pigments of vegetation). Local exceptions may concern the presence of exposed bright soil and/or light ash. At the same time, these conditions cause a significant decrease in NIR reflectance. Wavelengths falling in the SWIR region tend to present higher reflectance due to the decrease in moisture content (Pereira et al., 1999). The specific spectral signature of a portion of the burned vegetation surface, therefore, depends on the grade of occurred severity, namely, on the proportion of the main three post-fire fractional components (green vegetation, scorched brown vegetation, black charcoal) (Figure 1.3) and to the combined effect of diverse factors (changes in the moisture content and temperature, different reflectance from bared soil, etc.) (Pereira et al. 1999; Smith et al. 2005; Inoue et al. 2008).



**Figure 1.3.** Specific spectral signatures of the three main post-fire fractional components, representing the main physical effects induced by the fire on vegetation: unburned/lowly affected green vegetation (left), scorched vegetation (middle), heavily burned/torched vegetation (right). The photos were taken in Coruche - Portugal (left), in the Aspromonte National Park - Italy (middle), in Serra de Monchique (right). At the bottom, there are the respective spectral signatures retrieved from three different sources: spectral

library retrieved by the *Centro de Estudos Florestais (CEF)* of the *Instituto Superior de Agronomia* (Lisbon), ASTER spectral library (Baldrige et al., 2009), and Sentinel-2 image (visual-chosen).

The assessment of fire effects and their severity can be based on a mixture composed of these three typical post-fire fractional cover components, given their strong correlativity with the actual physical effects that occurred on the ground, thus directly comparability to the burn severity parameters traditionally assessed on field monitoring standard protocols (Lentile et al., 2006; 2009; Smith et al., 2007; Sunderman & Weisberg, 2011; Sander Veraverbeke & Hook, 2013), for example, that proposed by Key & Benson (2006), aimed to standardize the measurements of fire effects across space and time, in a context that is otherwise characterized by high variability (Key & Benson, 2006; Sander Veraverbeke & Hook, 2013).

The same principles are applied for the long-term monitoring of post-fire recovery. In the long term, these post-fire components tend to be attenuated with an inverse proportionality to the fire severity that occurred (Pereira et al. 1999; Smith et al. 2005; Inoue et al. 2008). The simultaneous initial re-growth of both herbaceous and woody vegetation, thus the phenological and physiological vegetation trend and the increasing moisture content, causes an increase in reflectance in specific wavelengths (VIS and NIR) and, in any case, a general rise in optical brightness, while the SWIR reflectance tends to return to lower values immediately after the fire (De Luca, Silva, & Modica, 2022; Frazier et al., 2015; Morresi et al., 2019).

However, optical systems present some limitations, mainly for their sensitivity to some environmental conditions, such as sunlight and cloud cover, which reduces the frequency of observation at the visible/infrared wavelength bands, and for the spectral confusion of burned areas with unburned low albedo surfaces (i.e., dark soils, water surfaces, shadow areas) (Lehmann et al., 2015; Minchella et al., 2009; Stroppiana et al., 2015). Furthermore, this type of sensor cannot capture some quantitative aspects, since these wavelengths do not interact directly with the structure of the objects (Santi et al., 2017).

### **1.2.2. SAR sensors**

Concurrently with optical-based data and approaches for burned area detection and fire effects monitoring, the synthetic aperture radar (SAR) sensors are active systems working in the microwave region of the electromagnetic spectrum (2,4-100 cm). The high sensitivity of SAR signal to the structural properties of the vegetation, with a generally linear correlation between backscatter and vegetation biomass (Chen et al., 2019; Quegan et al., 2000; Saatchi et al., 2012; Saatchi, 2019; Yu & Saatchi, 2016), and its capabilities for all-weather and solar radiation independency, make the SAR backscatter complementary information with optical data (Minchella et al., 2009; Polychronaki et al., 2014; Tanase et al., 2011; Tanase, Santoro, Wegmüller, et al., 2010; Zhou et al., 2019).

The response of the radar signal is affected by the ensemble of environmental variables (e.g. land cover, vegetation cover structure, moisture content, dielectric property of objects, size/shape, and orientation of the scatterers in the canopy) and variables related directly to the sensor (e.g., polarization, which describes the orientation of the plane of oscillation of a propagating signal; wavelength, and orbit) or to the local surface properties (e.g., topography, orientation, surface roughness, and local incident angle) (Meritxell Gimeno & San-Miguel-Ayanz, 2004; Hachani et al., 2019; Imperatore et al., 2017; Lapini et al., 2020; Santi et al., 2017; Tanase et al., 2011; Tanase et al., 2020; Mihai A. Tanase, Santoro, Wegmüller, et al., 2010). The behavior of the SAR signal is determined by the wavelength used, as it defines the penetration capacity of microwaves across materials and objects on the Earth's surface: the greater the wavelength, the greater the ability to penetrate the material. For vegetated areas, this implies

that longer SAR bands, such as L-band (15 – 30 cm) and P-band (30 – 100 cm), interact with deeper strata and/or larger elements of vegetation cover than shorter bands, such as the X-band (3.75-7.5 cm) which, on the other hand, are more suitable for examining the superficial layers and small elements of vegetation cover (such as small branches and leaves) (Imperatore et al., 2017; Tanase, Santoro, De La Riva, et al., 2010).

The Earth's microwave backscatter is affected by variations in the structural parts and dielectric permittivity of the surface, triggered by vegetation cover, shape, size, and orientation of the canopy scatterers, soil structure, and moisture content modifications, making it a suitable system for discriminating alterations on the Earth's surface. In detecting burned areas, SAR technology uses these variations in the backscatter caused by the fire-induced modification of vegetation cover and soil structure and moisture content (Donezar et al., 2019; Imperatore et al., 2017; Kurum, 2015; Pepe et al., 2018b; Santi et al., 2017; Tanase et al., 2011; Tanase, Santoro, Wegmüller, et al., 2010). Immediately after a disturbing event and for the first year after, the scattering effect of the damaged vegetation structure is lacking/decreasing. At the same time, the contribution to the back diffusion by the humidity and the roughness of the exposed soil is higher. In Mediterranean ecosystems, this generally results in a lowering of the cross-polarized signal (vertical-horizontal, VH, and horizontal-vertical, HV) due to the consequent reduced volumetric dispersion contribution of forest canopies (volume scattering), and an increase in the co-polarized signal (vertical-vertical, VV or horizontal-horizontal, HH), interacting with small branches, stems and, principally, the soil surface (direct and specular backscatter) which is highly exposed after a fire (Imperatore et al., 2017; Saatchi, 2019a). The backscatter, typically increasing with forest biomass, has been found to be more directly correlated to above-ground biomass at cross-polarization than co-polarizations (Saatchi, 2019a; Saatchi et al., 2012; Yu & Saatchi, 2016). Due to this different interaction with the various aspects of the effects of fire on the environment, both types of polarization can be decisive in detecting burnt forest areas (Chen et al., 2018; Tanase et al., 2014).

### ***1.2.3. ESA Copernicus Sentinel satellites***

Several space missions provide satellite constellations operating SAR and multispectral optical imaging dedicated to environment observation, which is helpful for fire monitoring purposes (Emilio Chuvieco et al., 2019). Copernicus missions, by the European Space Agency (ESA), provides free high spatial and temporal resolution C-band SAR (Sentinel-1) and multispectral (Sentinel-2) data. The Sentinel-1 constellation comprises two polar-orbiting satellites performing C-band (from 3.75 cm to 7.5 cm wavelength) radar imaging. The two Sentinel-1 platforms were launched on 03 April 2014 (A) and the 25 April 2016 (B). The Sentinel-2 constellation is constituted by two polar-orbiting satellites placed in the same sun-synchronous orbit, performing 13 spectral bands: four bands at 10 meters (Blue<sub>492nm</sub>, Green<sub>559nm</sub>, Red<sub>664nm</sub>, NIR<sub>832nm</sub>), six bands at 20 meters (Red-Edge<sub>704nm</sub>, Red-Edge<sub>740nm</sub>, Red-Edge<sub>782nm</sub>, NIR<sub>864nm</sub>, SWIR<sub>1613nm</sub>, SWIR<sub>2202nm</sub>) and three bands at 60 meters (Coastal aerosol<sub>442nm</sub>, Water vapour<sub>945nm</sub>, SWIR-Cirrus<sub>1373nm</sub>) spatial resolution. The first satellite of Sentinel-2 (A) has been in orbit since 23 June 2015, meanwhile the second one (B) was launched on 7 March 2017 (ESA Sentinel Homepage 2022).



**Figure 1.4.** The European Space Agency (ESA) Copernicus multispectral (optical) Sentinel-2 (on the left) and the SAR Sentinel-1 (on the right) platforms. Pictures were retrieved from <https://sentinels.copernicus.eu/web/sentinel/home>.

The high spatial and temporal resolutions, together with the free distribution, make the Sentinel missions particularly suitable for risk monitoring and rapid mapping (Martinis et al., 2017). The spatial resolution has a considerable effect on the detection of burned areas and their subsequent monitoring, lowering the omission errors typical of the coarser resolution data in detecting the smallest areas and improving spectral discrimination (Belenguier-Plomer, Tanase, et al., 2019; Boschetti et al., 2019; Stroppiana et al., 2015; Verhegghen et al., 2016). The advantages become more evident when the acquisition revisit time of these products is a few days, allowing the monitoring of temporal trends at an appropriate temporal scale (Boschetti et al., 2019; I. Gitas et al., 2012a; Mihai A. Tanase et al., 2020; Verhegghen et al., 2016).

Furthermore, ESA itself distributes the Sentinel application platform (SNAP) (ESA SNAP Homepage 2022), a free and open-source software platform containing the toolboxes necessary for pre-processing and processing Sentinel data. The SNAP toolboxes, initially Java-based, can also be accessed from the Python programming language (The Python Language Reference 2022), one of the most popular languages for remote sensing and scientific analysis, widely used in both operational and scientific domains through the ESA SNAP- Python (snappy) interface (ESA SNAP Cookbook 2022).

#### ***1.2.4. Software, libraries, tools, and algorithms for image processing***

Following the acquisition of the raw data from the satellite system, represented by digital images, the remote sensing activity mainly consists of extracting, processing, and analyzing the data and interpreting the information through specific image processing procedures. Since data derived from these systems could be quite diverse, advanced techniques integrate geo-statistics, informatic (geo-informatics), data mining, pattern recognition and machine learning methods in order to organize, analyze, model and map the information extracted (Bot & Borges, 2022; Emilio Chuvieco et al., 2019; Lapini et al., 2020). These include various methods of data analysis in which, through statistical models, advanced algorithms extract and learn information from data, and then they can associate and replicate, recognize and classify this information autonomously into new groups of data (Bot & Borges, 2022; Lary et al., 2016; Ramezan et al., 2019). Remote sensing data processing and analysis, and the implementation of advanced algorithms are operations that require specific information technology (IT) solutions and high computational resources. For this reason, several IT systems and advanced image processing software have been developed in recent years, of which a significant contribution comes from free and open-source distributions. Among these are the libraries and the modules built and implemented in a programming scripting

language (e.g., Python, Java). Decomposition and adaptability are the main features that allow the construction and combination of the most suitable processing solution (L. Wang et al., 2019; Zhong et al., 2018). Implementing the resources provided by different software within the same workflow, increasing its inter-compatibility capabilities, allows for creating increasingly optimized algorithms that optimize the results.

With the remarkable advances in the latest-generation high-resolution Earth observation, the amount of remotely sensed data has been accumulated to an exabyte-scale and has been increasing in petabytes every year. In order to satisfy the huge calculations required, always better specific hardware is necessary, thus facilitating the development and diffusion of cloud computing. Many platforms have also been developed in this area, some of which are available with an open-source license (L. Wang et al., 2019).

### **1.3. Objectives and organization of the thesis.**

In the framework of this Ph.D. thesis, partly carried out abroad in collaboration with the Remote Sensing research laboratory of the Forest Research Centre, School of Agriculture of the University of Lisbon (Portugal), the research activity aims at the development of a complete workflow for the analysis and monitoring of the short and medium terms effects of fires on Mediterranean forest ecosystems, with the primary purpose to supply the state of the art with original contributions. Multisensor procedures have been built by integrating both optical (Sentinel-2) and SAR (Sentinel-1) freely available data and, in some applications, comparing and evaluating the accuracy of the three different possible configurations (optical only, SAR only and optical+SAR) in order to find the most suitable in terms of accuracy achieved.

The workflow constituting this thesis's main structure is composed of four main phases, distributed across six Chapters illustrating six distinct and original scientific contributions carried out by investigating different fire events that occurred in two countries of Mediterranean Europe. Each chapter aimed to optimize the methodologies employed for the respective objective. Summarizing the four phases below:

- A. The workflow starts with the classification of the quantitative and qualitative conditions of the vegetation before the event. The assessment of fire effects is based on the estimation of the fire-induced changes on the pre-fire vegetation status. Information about the pre-fire condition of the sites under study is therefore essential. In Chapter 2 a supervised classification was developed and optimized by integrating optical and SAR information to retrieve a high-accuracy land use and land cover (LULC) map. The single and integrated use of both sensor sources was evaluated, and the results were exploited to improve the accuracy of the final map. The LULC illustrates the scenario of the study site before the fire event.
- B. Timely and accurate detection and quantification of burned areas involve the second operational phase of the workflow and, simultaneously, the first step after the fire occurrence for assessing the damage and addressing the post-event management. It concerns the implementation of two different mapping approaches for burned areas: one using only SAR images for the execution of an unsupervised classification procedure in two distinct Mediterranean sites (Chapter 3); the second approach concerns the integration of multitemporal composite and supervised geographic object-based classification approach (GEOBIA), testing on optical and multisource (optical+SAR) dataset, to map burned areas on a regional scale (Chapter 4).
- C. In the third phase, the analyses are deepened to assess the short-term effects, in the form of fire severity, for assessing and understanding the ecological impacts of the fire and the factors contributing to its behavior and propagation (Chapter 5 and Chapter 6). The integrated use of both optical and SAR data is evaluated in terms

of accuracy in two study cases. A spectral investigation of the short-term damages induced by the fire, at forest crown level, was carried out in Chapter 7, by employing a spectral mixture analysis (SMA).

- D. In the fourth step, the information about the pre-fire vegetation and the severity of the fire that resulted from the previous analyses are essential for assessing the medium-term impacts of fire on ecosystems and their capacity to repriminate the ecosystem services partially lost. Moreover, this knowledge is essential to address initiatives and strategies for post-fire management, particularly in high-risk areas such as Mediterranean countries. For these purposes, optical and SAR spectral time-series were employed for spatially and temporally monitoring the response and recovery of three different vegetation types, differentiating the investigation in function of the recorded fire severity during the three years after the event (Chapter 6).

The remote sensing techniques consists mainly of the phases of data processing and analysis, and interpretation of the information. During the various steps carried out during the research activity, emphasis was placed on developing procedures based on advanced image processing and machine learning algorithms through open-source software, toolboxes and Python-based libraries.

## 2. Investigation about the pre-fire condition of vegetation

Adapted from

De Luca, G., Silva, J.M.N., Di Fazio, S., Modica, G.: *Integrated use of Sentinel-1 and Sentinel-2 data and open-source machine learning algorithms for land cover mapping in a Mediterranean region*. *Eur. J. Remote Sens.* 55, 52–70 (2022). <https://doi.org/10.1080/22797254.2021.2018667>.

EUROPEAN JOURNAL OF REMOTE SENSING  
2022, VOL. 55, NO. 1, 52–70  
<https://doi.org/10.1080/22797254.2021.2018667>



OPEN ACCESS

### Integrated use of Sentinel-1 and Sentinel-2 data and open-source machine learning algorithms for land cover mapping in a Mediterranean region

Giandomenico De Luca<sup>a</sup>, João M. N. Silva<sup>b</sup>, Salvatore Di Fazio<sup>a</sup> and Giuseppe Modica<sup>a</sup>

<sup>a</sup>Dipartimento Di Agraria, Università Degli Studi Mediterranea Di Reggio Calabria, Reggio Calabria, Italy; <sup>b</sup>Forest Research Centre, School of Agriculture, University of Lisbon, Lisboa, Portugal

#### ABSTRACT

This paper aims to develop a supervised classification integrating synthetic aperture radar (SAR) Sentinel-1 (S1) and optical Sentinel-2 (S2) data for land use/land cover (LULC) mapping in a heterogeneous Mediterranean forest area. The time-series of each SAR and optical bands, three optical indices (normalized difference vegetation index, NDVI; normalized burn ratio, NBR; normalized difference red-edge index, NDRE), and two SAR indices (radar vegetation index, RVI; radar forest degradation index, RFDI), constituted the dataset. The coherence information from SAR interferometry (InSAR) analysis and three optical biophysical variables (leaf area index, LAI; fraction of green vegetation cover, fCOVER; fraction of absorbed photo-synthetically active radiation, fAPAR) of the single final month of the time-series were added to exploit their correlation with the canopy structure and improve the classification. The random forests (RF) algorithm was used to train and classify the final dataset, and an exhaustive grid search analysis was applied to set the optimal hyperparameters. The overall accuracy reached an  $F\text{-score}_M$  of 90.33% and the integration of SAR improved it by 2.53% compared to that obtained using only optical data. The whole process was performed using freely available data and open-source software and libraries (SNAP, Google Earth Engine, Scikit-Learn) executed in Python-script language.

#### ARTICLE HISTORY

Received 11 September 2021  
Revised 18 November 2021  
Accepted 11 December 2021

#### KEYWORDS

Synthetic aperture radar (SAR); SAR interferometry (InSAR); interferometric coherence; Google Earth Engine (GEE); SAR and multispectral time-series analysis; biophysical indicators

Mapping the vegetation composition, besides providing information on the quantitative and qualitative status of the area under study, is a necessary early step in the analysis and monitoring protocols of the state of the vegetation and ecosystems' responses affected by various environmental disturbances (Choudhury et al., 2021; Grabska et al., 2020; Monroe et al., 2020; Pollino & Modica, 2013; Rodman et al., 2021; Semeraro et al., 2019), including wildfires (I. Gitas et al., 2012a), storms (Giannetti et al., 2021; Hamdi et al., 2019), deforestation (Nicolau et al., 2021), forest degradation (Giuseppe Modica et al., 2015), desertification (Hill et al., 2008) and climate change effect (Yang et al., 2013). Therefore, mapping the composition of forest vegetation is fundamental for the concrete implementation of sustainable land management policies at any scale, regional to global (e.g., the REDD activities; Gulinck et al., 2018; Nicolau et al., 2021).

In the context of vegetation mapping and monitoring, several remote sensing techniques based on different types of multispectral sensors have been developed and successfully used over the years (De Luca et al., 2019a; Grabska et al., 2019; Giuseppe Modica et al., 2016; Morin et al., 2019; Praticò et al., 2021; Solano et al., 2019). The use of spectral signatures, temporally differentiated following the phenological cycles of the various seasons, allows a better spectral separability of the investigated vegetation types and, therefore, their recognition and characterization (Aragones et al., 2019; Aubard et al., 2019; Grabska et al., 2019, 2020; Morin et al., 2019; Praticò et al., 2021). Grabska et al. (2019) used a Sentinel-2 (S2) time-series to map forest composition showing the effectiveness of seasonal phenology variations in improving spectral discrimination between species, achieving



better accuracy results than using single images. Moreover, the spectral vegetation indices (VIs) enhance the sensibility of single-bands spectral signals to the variability of the bio-physical state of plant tissues, the photosynthetic activity, and leaf productivity (Aragones et al., 2019; Marzioletti et al., 2019; Praticò et al., 2021; Semeraro et al., 2019). Strong correlations were found between specific regions of the electromagnetic spectrum and species-specific physiological characteristics useful in estimating forest cover, especially using VIs based on infrared wavelengths: the normalized difference vegetation index (NDVI) (Marzioletti et al., 2019; Spadoni et al., 2020), the normalized difference red-edge index (NDRE) (Evangelides & Nobajas, 2020), the normalized burn index (NBR) (Praticò et al., 2021; Shaun et al., 2020). The red-edge, near infra-red (NIR) and short wave infra-red (SWIR) regions have, respectively, a long-established correlation to the leaf pigments content, vegetation net primary productivity, and leaf water content, being very effective in vegetation monitoring (Arevalo-Ramirez et al., 2020; Delegido et al., 2011; Eitel et al., 2011; Knipling, 1970).

The free availability of the higher temporal and spatial resolution Copernicus S2 mission multispectral data (ESA Sentinel Homepage, 2022), provided by the European Space Agency (ESA), improved the accuracy of forest cover classification maps and allowed for the launch of several successful monitoring studies at a higher scale of detail (Grabska et al., 2020; Immitzer et al., 2016; Inglada et al., 2017; Praticò et al., 2021; Solano et al., 2019).

In addition to the use of multispectral data, several authors studied the applicability of active synthetic aperture radar (SAR) systems for mapping land cover (Lapini et al., 2020; Nicolau et al., 2021; Perko et al., 2011; Waske & Braun, 2009). Besides the all-day and all-weather operational capability, these sensors provide different and complementary physical information helpful for improving the spectral data when combined with optical imagery (Nicolau et al., 2021; Spracklen & Spracklen, 2021; Stroppiana et al., 2015). The total signal backscattered from forest vegetation results from the combination and interaction of the canopy and ground backscatters (Lapini et al., 2020; Saatchi, 2019a; Yu & Saatchi, 2016). This backscatter response is affected by implicit sensor variables, such as wavelength and polarization, and by some vegetation features as cover shape, structure, and orientation, moisture content, geometric and dielectric property of the surface (De Luca, Silva, & Modica, 2021a; Lapini et al., 2020).

The Copernicus mission provides two polar-orbiting SAR satellite platforms belonging to the Sentinel-1 (S1) constellation (S1-A and S1-B) carrying a C-band sensor (wavelength of 5.6 cm) with both cross-polarized (VH) and co-polarized (VV) polarization (ESA Sentinel Homepage, 2022). At these wavelengths, the backscatter is mainly due to the leaves, needles, and small branches of the upper canopy and presents lower penetration power than longer wavelengths (Lapini et al., 2020). Potentially, the information from the upper canopy could allow the discrimination between forest and non-forest areas. Referring to forest applications, recently, Nicolau et al. (2021) assessed the potential of S1 time-series for land use/ land cover (LULC) purposes in tropical forests, while Numbisi et al. (2019) utilized S1 time series to discriminate agroforests environments in a heterogeneous savannah-forest transition zone. On the other hand, Lapini et al. (2020) assessed the multi-frequency approach for Mediterranean forest classification, discriminating forest from non-forest areas and broadleaved from coniferous forests, using data from different SAR sensors (X-, C- and L-band). These authors concluded that the L-band is better for the first purpose, but C-band and X-band performed better for distinguishing coniferous and broadleaves. The utility of SAR signal in forest vegetation discrimination can be also explicated by its particular sensitivity to the forest stand height (Deutscher et al., 2013; W. Li et al., 2020; Perko et al., 2011; Siqueira, 2019). The simple SAR backscatter is indirectly and empirically related to the forest stand height since its value increases with a high



presence of canopy scattering elements, proportional to forest height (vertical distribution) and canopy density, as a function of wavelength and polarization. Moreover, there is a geometric relationship between the SAR signal and the heights of the objects on the Earth's surface, estimable through SAR interferometry (InSAR) models (Siqueira, 2019). The InSAR technique exploits the phase information of the radar signal to obtain information about the topography and height of the Earth's surfaces (Ferretti et al., 2007; Ghosh et al., 2020). The S1 constellation observes the same scene at two different times, applying the repeat-pass InSAR. The amount of temporal phase decorrelation occurring between two passes is one of the models used to estimate the forest stand height. The temporal decorrelation is assumed to be higher the greater the height of the canopy due to a more significant presence of small scatter elements (Siqueira, 2019). The interferometric coherence can represent the temporal phase decorrelation: the higher is the time phase decorrelation, the lower is the resulting coherence. Several authors (Deutscher et al., 2013; Ghosh et al., 2020; Perko et al., 2011; Siqueira, 2019) applied empirical models to estimate the forest stand height from the interferometric coherence measure, with levels of accuracy that can vary greatly depending on various factors. For this reason, in this study, the coherence relationship with the forest stand height was exploited to discriminate the presence of standing forest concerning the other surrounding LULC classes.

Considering the research experiences mentioned above, the combined use of both optical and SAR data would further improve the identification of forest cover, as confirmed by several authors (Ienco et al., 2019; Morin et al., 2019; Polychronaki et al., 2014; Spracklen & Spracklen, 2021; W. Zhang et al., 2019). Spracklen and Spracklen (2021) used S1 and S2 timeseries to distinguish natural and plantation forests in a tropical monsoon climate zone, concluding that the different sensitivity of these two sensors makes them complementary in analyzing the investigated vegetation surface. In particular, while the SAR backscatter depends on the vegetation's physical properties, the optical signal is correlated to the biochemical state of vegetation. Several studies use combined data S1 and S2 data for vegetation cover purposes. Ienco et al. (2019) proposed a Convolutional Neural Network (CNN) architecture, combining S1 and S2 time-series for LULC mapping in tropical regions, obtaining satisfactory results. Zhang et al. (2019) used the differences in temporal signatures between vegetation cover types, combining three temporal information of S1 and S2, for distinguishing woody canopy from the herbaceous canopy in savanna ecosystems using the Support Vector Machines (SVM) classifier. Morin et al. (2019) combined the use of S1, S2 and ALOS PALSAR data to estimate forest structure parameters and the aboveground biomass in maritime pine plantations. In Mediterranean environment, besides the literature concerning the single use of optical sensors (e.g. Aragones et al., 2019; Aubard et al., 2019; Modica et al., 2016; Praticò et al., 2021), there seems to be a lack of studies exploiting the SAR (Lapini et al., 2020) and its integration with optical imagery for LULC classification. Polychronaki et al. (2014), integrated the *Système Pour l'Observation de la Terre* (SPOT) optical data with the European Remote Sensing (ERS) C-band VV for LULC object-based classification affected by a fire in a Mediterranean landscape. They observed that the use of SAR backscatter improved the accuracy, reducing the commission errors related to forest land cover class and the misclassification between forest and shrub classes in shadowed areas. Chust et al. (2004) assessed the performances of combining ERS and SPOT images for Mediterranean LULC discrimination, resulting in a slight improvement of the obtained accuracy.

Chatziantoniou et al. (2017) evaluated the combined use of Sentinel-1 and Sentinel-2 data for a regional-scale Mediterranean wetlands classification, and they concluded that SAR data did not significantly improve classification accuracy. Some other authors focused on Mediterranean crop detection (Campos-Taberner et al.,

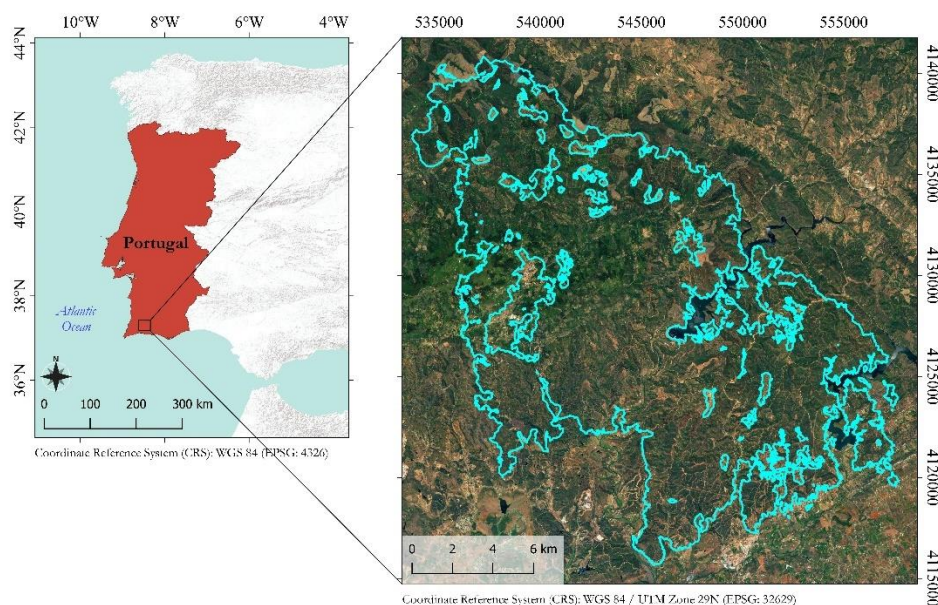
2017; Lobo et al., 1996; Villa et al., 2015). Considering this, more studies should be carried out to explore the potential of integrating multispectral and SAR sensors on mapping heterogeneous Mediterranean ecosystems and to investigate how the single information contributes to the obtained accuracy. This work aimed to develop a supervised classification procedure by integrating S1 and S2 data for forest cover mapping in a Mediterranean area of southern Portugal. The obtained results are essential to fulfilling the main research framework in which this work was conducted, based on applying remote sensing methodologies to analyze and monitor wildfires' effects in Mediterranean forest ecosystems. The first analysis on this study area was carried out to develop an unsupervised classification of the burned areas and based only on SAR S1 data and reported in De Luca et al. (2021a), while the combined use of SAR S1 and optical S2 data allowed to map the spatial distribution of burn severity (De Luca, Silva, Oom, et al., 2021).

The initial goal was to create a binary map to distinguish the forest cover from other LULC classes (pastures/shrubs, urban, agricultural, etc.). Afterward, we decided to implement this workflow further by subdividing the forest ecosystems into three forests LULC classes better representing the territory: Eucalyptus, Pine, and native broadleaf forest (*Quercus suber*, *Q. ilex*, etc.). In the same way, the main surrounding noforest LULC classes were classified individually (pastures/shrubs, bare soil, urban and agricultural). For this purpose, we provided an original and open workflow (i. e., implemented using diverse open-source software and freely available upon a reasonable request to the authors) based on an advanced coupling of SAR (S1) and multispectral (S2) time-series imagery. In particular, the time-series of SAR S1 backscatter (both VH and VV polarizations) and two derived indices, radar vegetation index (RVI) and radar forest degradation index (RFDI), were combined to the time-series of the optical S2 bands and three derived VIs: NDVI, NDRE, and NBR. In order to optimize the classification procedure, the coherence measure coming from InSAR analysis of different pairs of dates in July 2018 was also added as additional information, as well as the optical-based biophysical variables fraction of green vegetation cover (fCOVER), the fraction of absorbed photosynthetically active radiation (fAPAR), and the leaf area index (LAI) calculated for the same month. The well-known Random Forests (RF) machine learning algorithm (Breiman, 2001) was applied for classification through the use of open-source and Python-based libraries (The Python Language Reference, 2022). One of the main problems in applying machine learning classification algorithms is choosing the optimal values of the model's hyperparameters. In this direction, another original contribution of this study was to provide an open workflow in which a thorough grid search approach automatically sets the optimal hyperparameters. The feature importance was performed during the RF classification process to evaluate each input variable's contribution to the final mapping performance.

## 2.1. Study area

The study area (Figure 2.1) extends over the Serra de Monchique Mountain range located in the southern region of Portugal, Algarve (37° 18'N; 08° 30'W). Part of the study area is a Special Area of Conservation (SAC) falling within the European Natura 2000 network (Natura 2000 Site Code: PTCO0037). The territory is characterized by the typical heterogeneous and fragmented Mediterranean mountain landscape. The forest cover was mainly composed of Eucalyptus plantations (*Eucalyptus globulus*, Labill. 1800), mixed Mediterranean indigenous deciduous forests (*Quercus suber* L., *Quercus ilex* L., and other secondary Mediterranean native species), and coniferous plantations, composed by *Pinus pinea* L. or *Pinus pinaster* Aiton. A part of the autochthonous oak forest cover can be associated with the typical semi-natural landscape of the Iberian Peninsula (*dehesa* and

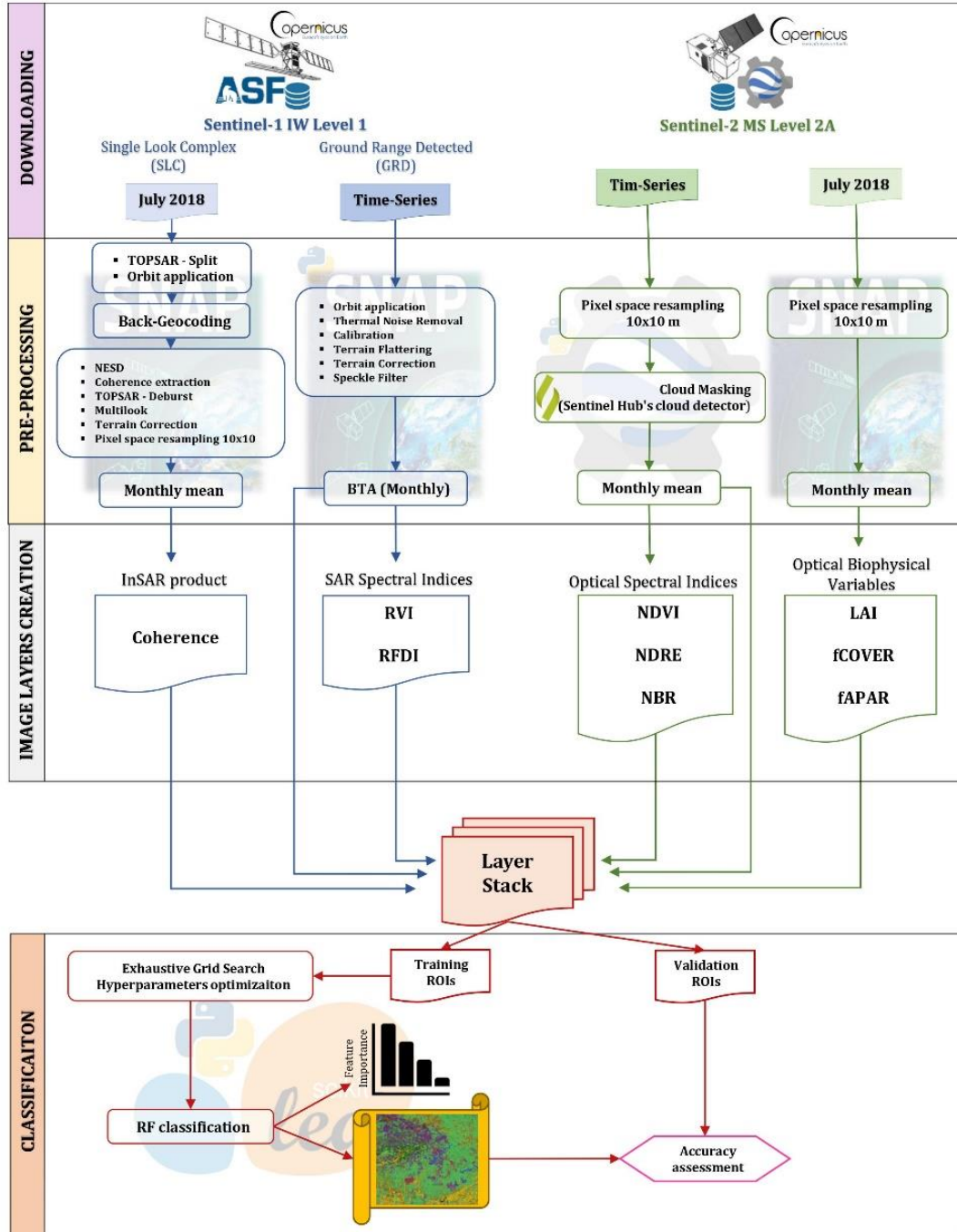
*montado*): woodlands and agro-forestry systems used for cork harvesting and grazing. A large part of the territory was covered by non-forest LULC classes represented by heathlands, sclerophyllous shrublands, pastures, bare soil, general uncultivated lands (e.g., derived from harvested forest plantations, agricultural and urban lands) (Sistema Nacional de Informação Geográfica, SNIG, 2021).



**Figure 2.1.** Location of the study area in Portugal (left). Overview of the study area (right) using the Google Earth image as a basemap; the wildfire's perimeter that occurred in August 2018 is overlaid in light blue.

## 2.2. Materials and methods

The implemented procedure (Figure 2) was carried out using different free and open-source software solutions, starting from download to the classification output and testing and exploiting their interoperability. Most of the Sentinel images were unavailable on the official Copernicus Open Access Hub platform due to the Long-Term Access policy adopted by the ESA (Copernicus Long Term Archive Access, 2021). Therefore, we adopted other alternative ways to speed up the data download phase. The S1 images were downloaded using the Alaska Satellite Facility (ASF) interface (ASF, 2022), while the Google Earth Engine (GEE) Python API (Google Earth Engine Guides, 2022) was employed to pre-process and then download the S2 dataset. The data pre-processing for S1 was carried out using the Sentinel-1 Toolboxes implemented in the SNAP v.8.0.3 open-source software (ESA SNAP Homepage, 2022) provided by ESA. The classification algorithms were processed using the modules integrated into the Scikit-learn Python library (Pedregosa et al., 2011).



**Figure 2.2.** The workflow of the implemented procedure, based on free and open-source software and Sentinel-1 (S1) and Sentinel-2 (S2) time-series imagery.

### 2.2.1. Sentinel-1 dataset and pre-processing

The SAR dataset was composed of a time-series of S1A/B ground range detected (GRD), acquired in interferometric wide (IW) mode, for each of the two available polarizations: co-polarized VV and cross-polarized VH. The time series comprised the period from April 2017 to July 2018, immediately prior to the fire event of August 2018, and it was composed of 82 images deriving from both ascending (42 images) and descending (40 images) flight paths. In order to perform the InSAR analysis for coherence extraction, a total of six Single Look Complex (SLC) format images (three for ascending and three for descending flight path), presenting respective

same orbit-path and covering the month of July 2018, were downloaded. This month was chosen as it was the closest to the fire event, and, presumably, the vegetation conditions were more consistent with those at the time of the event. The images were in IW mode, which contains both amplitude and phase information of the backscattered SAR signal.

#### *2.2.1.1. Sentinel-1 ground range detected (GRD) pre-processing*

Concerning the GRD imagery, the application of the auto-downloaded orbit file and the thermal noise removal started the S1 pre-processing workflow. Subsequently, the images were first radiometric calibrated ( $\beta_0$ ) and then applied the radiometric terrain correction (RTC). The reduction of geometric and topographic errors was carried out by applying the radiometric terrain flattening and the terrain correction processes using the shuttle radar topography mission (SRTM) digital elevation model (DEM), characterized by a spatial sampling of 1 arc-second. The correction of topographical errors, in particular the ground flattening process, is an essential step to map the land cover because it reduces the error due to the difference in the structure and shape of the ground surface and, therefore, in the backscatter values (Mendes et al., 2019; Small, 2011).

The bilinear interpolation resampling method was used for both DEM and output image resampling. All the S1 images were stacked using the product geolocation as the initial offset method. Since the speckle noise is an impactful error for land cover mapping purposes (Lapini et al., 2020), a multitemporal Lee filter (Quegan et al., 2000; Santoso et al., 2015) with a 5x5 pixel window size was applied, followed by a backscatter time (monthly) averaging (BTA). This last step further improves the image signal concerning speckle noise and minimizes the effects of environmental and seasonal variables (De Luca, Silva, & Modica, 2021a; Lapini et al., 2020).

#### *2.2.1.2. Sentinel-1 SLC InSAR pre-processing*

For each of the two S1 platforms (A and B), all the pair combinations of the three SLC images were subjected to TOPS InSAR processing. Before applying the coregistration (Back-Geocoding) and Network Enhanced Spectral Diversity (NESD) optimization for each coregistered S1pair, we split the single images (TOPS-Split) and added the auto-downloaded orbit file. Then, we extracted the coherence information, characterized by a range value from 0 (minimum coherence) to 1 (maximum coherence). A final terrain correction was applied, using the 1 arc-second digital elevation model (DEM) derived from the Shuttle Radar Topography Mission (SRTM) (Farr et al., 2007), where the pixel spacing was resampled to 10 m x10 m. The three coherence maps resulting for each of the two flight paths were averaged to reduce the speckle noise, obtaining one coherence map for ascending and one for descending paths.

#### *2.2.1.3. Sentinel-2 dataset and pre-processing*

The optical S2 Level-2A (Bottom-Of-Atmosphere, BOA) multispectral time-series was composed of 64 images, considering the same time period of the S1 dataset (April 2017 – July 2018). Subsequently, a monthly average for each band were performed, while a pixel size resampling of 10m x10m was performed semi-automatically by the system during the download step, by setting the scale parameter (pixel resampled size = 10) and the projection system (EPSG: 32629), using the default nearest neighbor resampling algorithm. Each single-date image was masked by clouds before this last step, which generated an image for each month and each band from April 2017 to August 2018 (as the final SAR dataset). In this case, we used the S2-Cloud Probability product available in the

GEE data catalog as a mask image up-sampled to 10 m spatial resolution. The cloud probability mask product is created with the Sentinel2-cloud-detector package (s2cloudless) for automated pixel-based cloud detection and it is based on the LightGBM machine learning library (LightGBM documentation, 2022), developed by Sentinel Hub's research team (Sentinel Hub Homepage, 2021). Each pixel contains a value between 0 and 100, representing the probability that the pixel is cloudy. Higher values are more likely to represent dense clouds or highly reflective surfaces but may omit less dense clouds. Lower values, although able to detect all clouds, could increase the risk that medium-high reflective surfaces could be mistaken for clouds (false positives). For our purpose, the value of 10 was considered the pixel's threshold value, greater than which a pixel is considered as a cloud. No-data values replaced the masked pixels of S2, filled by applying a temporal-linear interpolation between consecutive images. Water surfaces were also masked since the study area was characterized by only three static water bodies (*Barragem de Odelouca*, *Barragem do Funcho* and *Barragem do Arade*) and these were not target LCLUs. Effectively, the stable spectral features of the water surfaces, characterized by a significant absorption of most of the NIR wavelength radiation (Donchyts et al., 2016; Gao, 1996; Schwatke et al., 2019), made it simple to detect detected them masking pixels of the S2 B8 band image (Jul2018) using the threshold  $<0.09$ .

### 2.2.2. *Sentinel-1 image layer creation*

From the resulted monthly BTA image layers, two dual-polarimetric SAR indices, adapted for the S1 sensor, were computed (eq. 2.1, 2.2) (Nasirzadehdizaji et al., 2019; Nicolau et al., 2021).

$$RVI_t = 4 \cdot BTA\_VH_t / (BTA\_VV_t + BTA\_VH_t) \quad (2.1)$$

$$RFDI_t = (BTA\_VV_t - BTA\_VH_t) / (BTA\_VV_t + BTA\_VH_t) \quad (2.2)$$

Where  $t$  represents one of the months constituting the time-series (from April 2017 to July 2018). The final SAR dataset used in the classification process was composed of the BTAVV, BTAVH, RVI, RFDI timeseries, and the two coherence maps (ascending and descending) for July 2018. It is expected that the SAR vegetation indices potentially improve the discrimination of land cover because of the combination of VH polarization, related to the scattering elements of the canopy, and the VV polarization, sensitive to the topographic and morphological characteristics of the ground (Nicolau et al., 2021).

### 2.2.3. *Sentinel-2 image layer creation*

The 10 m and original 20 m spatial resolution bands (Drusch et al., 2012; ESA Sentinel Homepage, 2021), constituting the monthly S2 time-series, were used to compute four vegetation indices (eq. 2.3–2.5).

$$NDVI_t = (B8_t - B4_t) / (B8_t + B4_t) \quad (2.3)$$

$$NBR_t = (B8_t - B12_t) / (B8_t + B12_t) \quad (2.4)$$

$$NDRE_t = (B6_t - B5_t) / (B6_t + B5_t) \quad (2.5)$$

Moreover, three additional biophysical variables were automatically computed for July 2018 using the SNAP toolbox biophysical variables processor: LAI, fCOVER, and fAPAR. The criterion of this month's choice for biophysical variables estimation was the same as that already explained for the InSAR analysis. The quantitative-qualitative conditions of the vegetations should be more similar to those at the time of the event (occurred in August 2018). These biophysical variables have been found helpful in integrating the information of the interferometric coherence considering their direct correlation with the structural characteristics of the vegetation

canopy (Ghosh et al., 2020). The final S2 dataset resulted was composed of all the 10 m resampled bands, the relative four vegetation indices for each month, and the three biophysical variables referred to only July 2018. The three biophysical variables calculated for July 2018 were clipped on the same area and stacked to the S1 dataset using the latter dataset as the master extent (S1+ S2).

#### 2.2.4. Image classification

Supervised pixel-based image classification of forest cover was carried out using the RF algorithm (Breiman, 2001; Cutler et al., 2007). This, based on a set of decision trees, is a machine learning model widely used in land cover mapping, forest classification and the estimation of other forest structural parameters (De Luca et al., 2019a; Ghosh et al., 2020; W. Li et al., 2020; Morin et al., 2019; Numbisi et al., 2019; Praticò et al., 2021). The RF algorithm was performed using the RFClassifier function from the Scikit-learn Python library package. In this study, the optimal RF hyperparameters were set using an exhaustive grid search approach implemented in Scikit-learn (GridSearchCV), based on a cross-validation analysis between all the possible combinations of a given set of hyperparameters values (Table 2.1) and for a given training input set.

**Table 2.1.** Set of parameters values tested and combined for exhaustive grid search-based optimization. The name and the definition of each parameter are the original ones reported in the RFClassifier module user guide

Parameter name	Values set	Description
n_estimators	100, 650, 1200, 1750, 2300, 2850, 3400, 3950, 4500, 5050, 5600, 6150, 6700, 7250, 7800, 8350, 8900, 9450, 10000	The number of trees in the RF model
max_depth	10, 20, 30, 40, 50, 60, 70, 80, 90, 100, 110, 300, 500, 800, 1000	The maximum depth of the tree
min_samples_split	2, 5, 10	The minimum number of samples required to split an internal node
min_samples_leaf	1, 2, 4	The minimum number of samples required to be at a leaf node
max_features	“auto”, “None”, “log2”	The number of features to consider when looking for the best split

The image classification has been implemented according to the following seven LULC classes: Eucalyptus, Euc; Pinus, Pin; Autochthonous Forest, AuFor; Soil; Pasture and/or shrubs, Past/Shr; Urban, Urbe; Agriculture, Agri. The training pixels were selected on 950 regions of interest (ROIs) with a square size of  $4 \times 4$  pixels. The ROIs, scattered over the entire study area and with a balanced distribution among the seven LULC classes (Euc, 298; Pin, 78; AuFor, 131; Soil, 95; Past/Shr, 240; Urbe, 52; Agri, 56), were manually drawn by visual interpretation supported by the use of Google Earth very high-resolution satellite images (Google Earth Homepage, 2022).

Numerous scholars (Kattenborn et al., 2019; Nicolau et al., 2021; W. Zhang et al., 2019) stated that training data for land use classification could be based on high-resolution imagery instead of field observations, allowing to achieve comparable results a saving time and costs, and adequate representativeness of the full range of environmental characteristics present in those large portions of territory, which are more challenging to catch by punctual field observation.

#### 2.2.5. Accuracy assessment

The accuracy assessment of the classified map was performed using a validation dataset formed by 658 ROIs of different random sizes (from  $1 \times 1$  to  $20 \times 15$  pixels) drawn with the same criteria used for training ROIs and balancedly distributed among the seven classes. The confusion matrix was implemented and, following the

calculation of the *producer's* and *user's* accuracies (Congalton & Green, 2019), the single-class F-score ( $F\text{-score}_i$ ) (eq. 2.6) and the multi-class F-score ( $F\text{-score}_M$ ) (eq. 2.7) (G. Modica et al., 2021a; Sokolova & Lapalme, 2009) were computed. The  $F\text{-score}_i$  was calculated from the *producer's* and *user's* accuracies, representing the harmonic mean (De Luca, Silva, Oom, et al., 2021; G. Modica et al., 2021a):

$$F\text{-score}_M = 2 \cdot (\text{producer}'_{SM} \cdot \text{user}'_{SM}) / (\text{producer}'_{S_i} + \text{user}'_{S_i}) \quad (2.6)$$

where  $i$  represents the single class.

The  $F\text{-score}_M$  was calculated using the multi-class *producer's* $_{SM}$  (eq. 2.8) and *user's* $_{SM}$  (eq. 2.9) metrics, derived averaging the respective single-class *producer's* and *user's* accuracies for all the classes and expressed as:

$$F\text{-score}_M = 2 \cdot (\text{producer}'_{SM} \cdot \text{user}'_{SM}) / (\text{producer}'_{S_i} + \text{user}'_{S_i}) \quad (2.7)$$

$$\text{producer}'_{SM} = (\sum_{i=1} \text{producer}'_{S_i}) / n \quad (2.8)$$

$$\text{user}'_{SM} = (\sum_{i=1} \text{user}'_{S_i}) / n \quad (2.9)$$

where  $n$  represents the total number of classes.

In addition to the integrated S1 S2 dataset (main target of this study), the entire classification process and subsequent accuracy assessment was applied using each of the two single optical and SAR datasets, in order to compare the results and evaluate how effectively the integration of the two types of information can improve the outcomes. The optimal RF parameter values and the feature importance were also computed for each S1 and S2 datasets.

## 2.2.6. Results

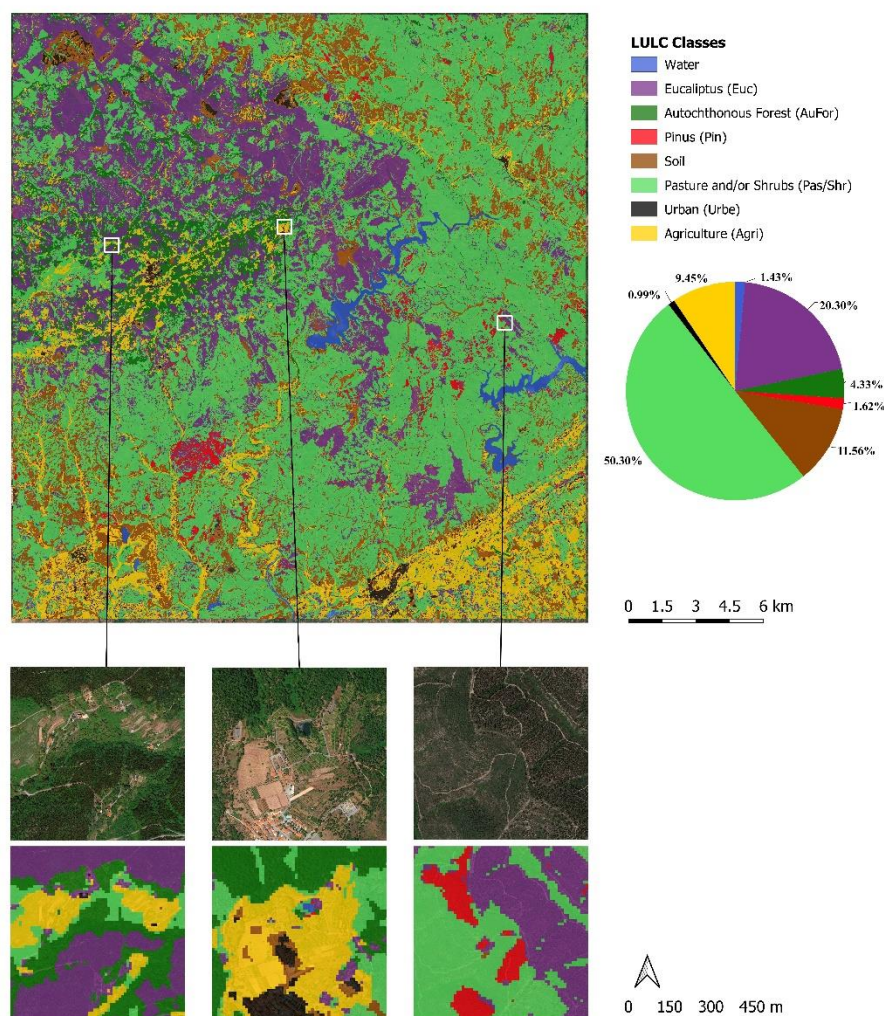
Table 2.2 shows the hyperparameters set for the RF algorithm using the exhaustive grid search optimization approach. The parameter optimization was carried out for each of the three dataset combination: the integrated SAR and optical (S1+S2), the SAR (S1) and the optical (S2). Among the tested ones, the values resulted as optimal were: 1200 (S1+ S2, S2) for the number of trees; 110 (S1+ S2, S2) and 800 (S1) the maximum depth of a tree; the default values 2, 1, and “auto” (S1+ S2, S1, S2) resulted for the *min\_samples\_split*, *min\_samples\_leaf* and the *max\_features*, respectively. The value “auto” implies that the maximum number of features considered equals the square root of the total number of features. The initial out-of-bag (OOB) error, expressing a predicted accuracy performance estimated by the RF model during the training step, resulted in 98.13% (S1+ S2), 88.98% (S1) and 97.40% (S2) using the respective optimized hyperparameters set.

**Table 2.2.** The adopted Random forests (RF) parameters values for each dataset combination tested (integrated SAR and optical, S1+S2; only SAR, S1; only optical, S2), set using the exhaustive grid search approach

Parameter name	Values set		
	S1+S2	S1	S2
n_estimators	1200	1750	1200
max_depth	110	800	110
min_samples_split	2	2	2
min_samples_leaf	1	1	1
max_features	“auto” (square root of the total number of features)	“auto” (square root of the total number of features)	“auto” (square root of the total number of features)



Figure 2.3 (top) shows the land cover map resulted from the RF classification process applied to the S1 S2 dataset and covering the entire study area. They are also magnified (bottom) three sample areas showing the details of the obtained classification. The total surface occupied by forest classes resulting from the classification equals 673.59 km<sup>2</sup> (excluding water surface that accounts for 9.81 km<sup>2</sup>).



**Figure 2.3.** Land cover map resulted from the Random Forests (RF) classification applied to the S1+S2 dataset and referred to the entire study area (top); three exemplary square areas (500 m side) showing the details of the obtained classification (bottom). On the right, the surface distribution (%) of the Land Use Land Cover (LULC) classes resulted from RF classification (pie chart). LULC classes definition: Eucalyptus (Euc), Pinus (Pin), Autochthonous Forest (AuFor), Soil, Pasture and/or Shrubs (Past/Shr), Urban (Urbe), Agriculture (Agri).

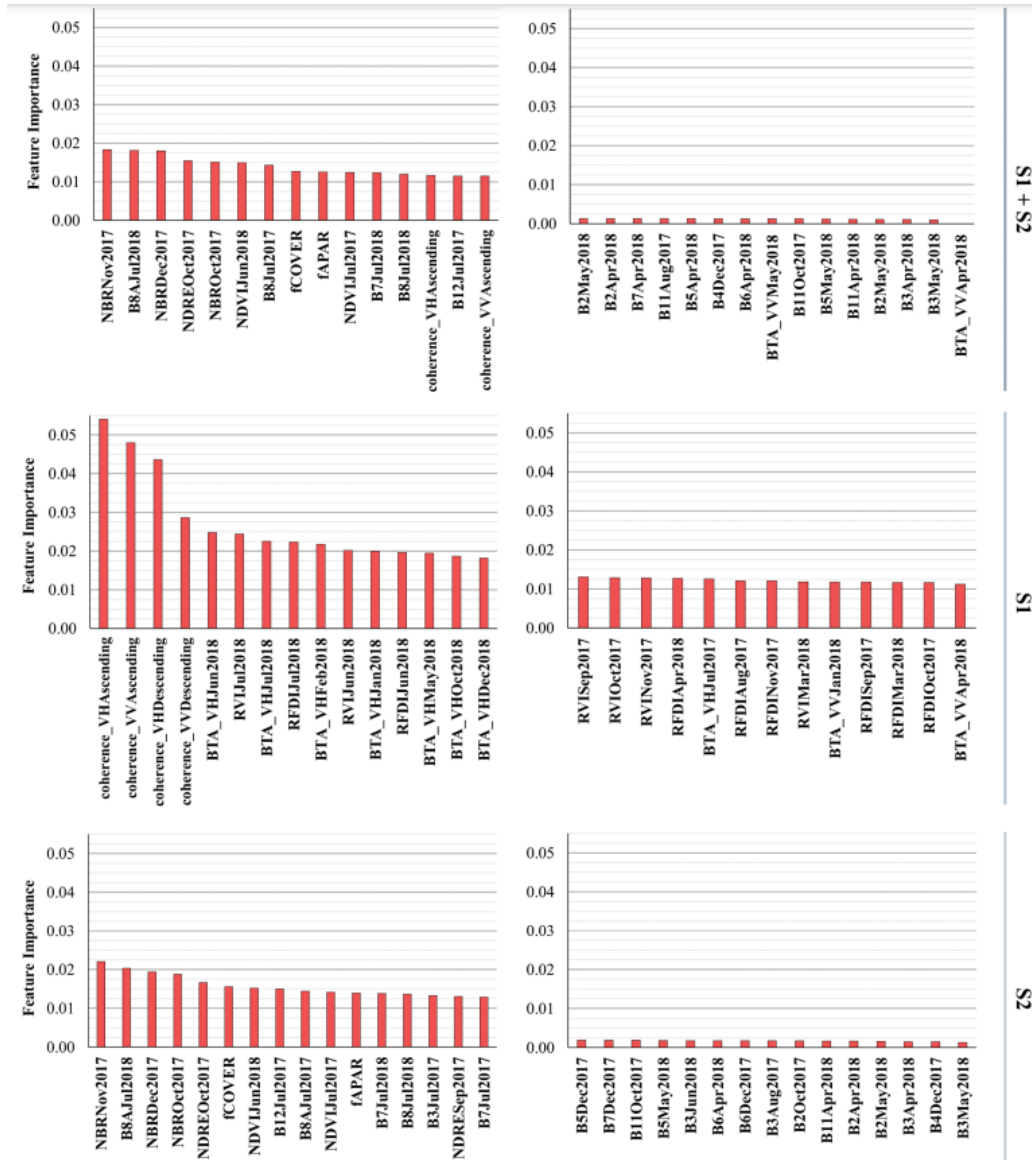
The resulted distribution among the forest classes showed in Figure 3 (pie chart) is 139.13 km<sup>2</sup> for Eucalyptus, 11.13 km<sup>2</sup> for Pinus, 29.71 km<sup>2</sup> for Autochthonous Forest. The classes corresponding to the unforested surfaces present an area equal to 344.77 for Pasture\Shrubs, 79.26 km<sup>2</sup> for Soil, 64.80 for Agriculture km<sup>2</sup>, 6.79 km<sup>2</sup> for Urban.

The Gini feature importance carried out from the RF process for each dataset combination tested (S1+S2, S1 and S2), which expresses the influence of each data layer on the algorithm prediction, is reported in Figure 4. The top

and bottom graphs respectively show the first fifteen layers with the highest importance, and the last fifteen layer bands describing the lowest importance values. The NBR index achieved the highest values of importance 0.0184 (S1+S2) and 0.0220 (S2) (Nov 2017), 0.0180 (S1+S2) and 0.0194 (S2) (Dec 2017), and 0.0151 (S1+S2) and 0.0188 (S2) (Oct 2017), interspersed with the NIR band B8A<sub>Jul2018</sub> (0.0182, S1+S2; 0.0203, S2) and the NDRE<sub>Oct2017</sub> (0.0155, S1+S2; 0.0166, S2). Observing the S1+S2 plot, follow the NDVI<sub>Jun2018</sub> (0.0149), B8<sub>Jul2017</sub> (0.0143), and the two biophysical variables fCOVER (0.0127) and fAPAR (0.0125). The cross- and co-polarized coherence image layers for ascending flight path, deriving from InSAR analysis, are present among the first fifteen layer bands that reached the highest importance, with 0.0117 and 0.0115, respectively. These represent the layers reached the highest importance when the single S1 dataset was used, with 0.0540 and 0.0479 respectively, together to the descending part of cross- (0.0436) and co-polarized (0.0286) coherence. The other optical layers represented were the NDVI<sub>Jul2017</sub> (0.0124, S1+S2; 0.0142, S2), B7<sub>Jul2018</sub> (0.0124, S1+S2; 0.0138, S2), B8<sub>Jul2018</sub> (0.0120, S1+S2; 0.0), B12<sub>Jul2017</sub> (0.0115, S1+S2; 0.0149, S2), NDRE<sub>May2018</sub> (0.0134, S1+S2), B8A<sub>Jul2017</sub> (0.0133, S1+S2; 0.0144, S2), B7<sub>Jul2018</sub> (0.0129, S1+S2; 0.0138, S2), NDRE<sub>Jan2018</sub> (0.0125, S1+S2). Concerning SAR layers, these are represented among the first fifteen only when the single S1 dataset is used: BTA\_VH<sub>Jun2018</sub> (0.02478), RVI<sub>Jul2018</sub> (0.0244), BTA\_VH<sub>Jul2018</sub> (0.0226), RFDI<sub>Jul2018</sub> (0.0223), BTA\_VH<sub>Feb2018</sub> (0.0217), RVI<sub>Jun2018</sub> (0.0202), BTA\_VH<sub>Jan2018</sub> (0.0199), RFDI<sub>Jun2018</sub> (0.0197), BTA\_VH<sub>May2018</sub> (0.0194), BTA\_VH<sub>Oct2018</sub> (0.0187), BTA\_VH<sub>Dec2018</sub> (0.0182). On the other end of the feature importance ranking, the BTA\_VV<sub>Apr2018</sub> expressed the lowest level of importance for both S1+S2 and S1 datasets (0.0 and 0.0112), followed by the B3<sub>May2018</sub> (0.001, S1+S2) that represent the last layer when the single S2 is used. Using both the datasets, the B11<sub>Apr2018</sub>, B2<sub>May2018</sub> and B3<sub>Apr2018</sub> reached a level of importance lower than 0.0012; the B4<sub>Dec2017</sub>, B6<sub>Apr2018</sub>, BTA\_VV<sub>May2018</sub>, B11<sub>Oct2017</sub>, B5<sub>May2018</sub> lower than 0.0013; the B2<sub>May2018</sub>, B2<sub>Apr2018</sub>, B7<sub>Apr2018</sub>, B11<sub>Aug2017</sub> and the B5<sub>Apr2018</sub> equal to 0.0013. The feature importance ranking for S2 resulted to be quite consistent with this order. Observing the S1 plot, RVI<sub>Mar2018</sub>, BTA\_VV<sub>Jan2018</sub>, RFDI<sub>Sep2017</sub>, RFDI<sub>Mar2018</sub>, RFDI<sub>Oct2017</sub>, show importance values less than 0.012; RVI<sub>Oct2017</sub>, RVI<sub>Nov2017</sub>, RFDI<sub>Apr2018</sub>, BTA\_VH<sub>Jul2017</sub>, RFDI<sub>Aug2017</sub>, RFDI<sub>Nov2017</sub>, less than 0.013.

The accuracy level of the land cover map was assessed for each class deriving the *producer's* and *user's* metrics and their harmonic mean (*F-score*) from the confusion matrix showed in Figure 5.

Considering the integrated S1+ S2 dataset, the producer's accuracy reached values of 89.51% (Eucalyptus), 91.65% (Authothonous Forest), 92.22% (Pinus), 76.30% (Soil), 96.72% (Pasture/Shrubs), 94.46% (Agriculture) and 98.98% (Urban). The user's accuracy values were 97.75% (Eucalyptus), 70.32% (Authothonous Forest), 88.68% (Pinus), 93.02% (Soil), 94.64% (Pasture/Shrubs), 89.81% (Agriculture) and 92.70% (Urban). Considering the F-scorei for each class, the values reached are 93.45% (Eucalyptus), 79.58% (Authothonous Forest), 90.41% (Pinus), 95.67% (Pas/Shr).



**Figure 2.4.** The figure shows the feature importance (Gini importance) expressed by the first fifteen image layers with the highest importance (left column) and by the last fifteen image layers with the lowest importance (right column), calculated for each dataset combination tested (integrated SAR and optical, S1+S2; only SAR, S1; only optical, S2).

When one of the single dataset (S1 or S2) was tested, the *producer's* accuracy achieved values of 74.83% and 86.83% (S1 and S2) (Eucalyptus), 56.12% and 89.05% (S1 and S2) (Authoethnous Forest), 62.04% and 91.17% (S1 and S2) (Pinus), 46.10% and 76.60% (S1 and S2) (Soil), 81.68% and 96.59% (S1 and S2) (Pasture/Shrubs), 90.25% and 94.70% (S1 and S2) (Agriculture) and 84.75% and 88.22% (Urban). Th *user's* accuracy values were 90.82% and 97.44 (S1 and S2) (Eucalyptus), 32.25% and 60.36% (S1 and S2) (Authoethonous Forest), 45.41% and 89.32 (S1 and S2) (Pinus), 55.40% and 91.43% (S1 and S2) (Soil), 78.50% and 94.58% (S1 and S2) (Pasture/Shrubs), 72.04% and 87.40% (S1 and S2) (Agriculture) and 86.26% and 85.75% (Urban). The single-class  $F\text{-score}_i$  values were 82.05% and 91.83 (S1 and S2) (Eucalyptus), 40.96% and 71.95% (S1 and S2) (Authoethonous Forest), 52.44% and 91.17% (S1 and S2) (Pinus), 80.06% and 95.57% (S1 and S2) and (Pas/Shr). The overall accuracy of the map, expressed by the  $F\text{-score}_M$  is equal to 90.33% (S1+S2), 68.23% (S1), 87.80% (S2).

	Eu	AuFor	Pin	Soil	Past/Shr	Urbe	Agri	User's	
Eu	8914	108	0	0	93	0	4	97.75%	S1+S2
AuFor	768	2019	29	0	54	0	1	70.32%	
Pin	57	2	830	0	47	0	0	88.68%	
Soil	1	0	0	586	25	17	1	93.02%	
Pas/Shr	212	38	41	76	7735	0	71	94.64%	
Urbe	0	0	0	43	0	546	0	92.70%	
Agri	7	36	0	63	43	0	1313	89.81%	
Producer's	89.51%	91.65%	92.22%	76.30%	96.72%	96.98%	94.46%		
F-score <sub>i</sub>	93.45%	79.58%	90.41%	83.83%	95.67%	94.79%	92.08%		

	Eu	AuFor	Pin	Soil	Past/Shr	Urbe	Agri	User's	
Eu	8282	351	98	0	386	0	2	90.82%	S1
AuFor	1548	926	42	0	321	0	34	32.25%	
Pin	226	1	425	1	282	1	0	45.41%	
Soil	6	4	0	349	263	5	3	55.40%	
Pas/Shr	986	277	120	245	6416	55	74	78.50%	
Urbe	6	1	0	20	27	339	0	86.26%	
Agri	14	90	0	142	160	0	1046	72.04%	
Producer's	74.83%	56.12%	62.04%	46.10%	81.68%	84.75%	90.25%		
F-score <sub>i</sub>	82.05%	40.96%	52.44%	50.32%	80.06%	85.50%	80.12%		

	Eu	AuFor	Pin	Soil	Past/Shr	Urbe	Agri	User's	
Eu	8886	116	2	0	111	0	4	97.44%	S2
AuFor	1062	1733	25	0	51	0	0	60.36%	
Pin	59	6	836	0	35	0	0	89.32%	
Soil	0	0	0	576	27	26	1	91.43%	
Pas/Shr	196	56	53	76	7730	0	62	94.58%	
Urbe	0	0	0	52	0	337	4	85.75%	
Agri	31	35	1	48	49	19	1269	87.40%	
Producer's	86.83%	89.05%	91.17%	76.60%	96.59%	88.22%	94.70%		
F-score <sub>i</sub>	91.83%	71.95%	90.23%	83.36%	95.57%	86.97%	90.90%		

	S1+S2	S1	S2
Producer's <sub>M</sub>	91.12%	70.83%	89.02%
User's <sub>M</sub>	89.56%	65.81%	86.61%
F-score <sub>M</sub>	90.33%	68.23%	87.80%

**Figure 2.5.** The confusion matrix resulted from the accuracy assessment process and relative single-class *User's* and *Producer's* accuracies (upper). The bottom reported the single-class *F-score<sub>i</sub>* and the multi-class *Producer's<sub>M</sub>*, *User's<sub>M</sub>* and *F-score<sub>M</sub>* accuracy metrics. LULC classes definition: Eucalyptus (Eu), Pinus (Pin), Autochthonous Forest (AuFor), Soil, Pasture and/or Shrubs (Past/Shr), Urban (Urbe), Agriculture (Agri)

### 2.3. Discussion

The main objective of this study was to obtain a map of the forest cover of an area around the municipality of Monchique, in southern Portugal, where a high severe fire occurred in August 2018 (De Luca, Silva, & Modica, 2021a; De Luca, Silva, Oom, et al., 2021). The vegetation cover mapping and, especially, the distinction between forest and non-forest vegetation before a disturbance event is a decisive purpose for improving the analysis of its effects on the ecosystem and their monitoring from the short to the long term (Chu & Guo, 2013). The integrated use of S1 and S2 time-series for forest tree species classification was evaluated to deal with this aim. Several SAR vegetation indices (RVI, RFDI) and optical vegetation indices (NDVI, NFRE, NBR) were computed for each month of the time series and included. The coherence information of the last month of the time series (July 2018)

was calculated from the InSAR process and implemented as additional information for image classification. The classification approach was carried out by training the RF machine learning algorithm.

### **2.3.1. Accuracy and uncertainty**

The good overall accuracy achieved by the integrated optical and SAR datasets in this approach, represented by an  $F\text{-score}_M$  equal to 90.33%, is in line with the outcomes obtained from other studies where the combination of optical and SAR data was used (Spracklen & Spracklen, 2021; W. Zhang et al., 2019). This value should have been higher considering that most of the single classes exceeded the 90% threshold of  $F\text{-score}_i$ , with the class relating to the pasture cover (Past/Shr) reaching the value of 95.67%. The lowest  $F\text{-score}_i$  value was obtained by the AuFor (79.58%). It was caused by the wrong classification of pixels belonging to the AuFor class as Eucalyptus cover. These errors of commission of the AuFor class are represented by an user's accuracy equal to 70.32%, in contrast with the producer's accuracy value, equal to 91.65% in the same class. However, it is noticeable how the integration of the two sensors has improved the accuracy of this LULC class, considering that the  $F\text{-score}_i$  value for the optical single dataset was 71.95%. Probably, the origin of these errors relies on the combination of two main factors. First, the AuFor class comprises a mix of different Mediterranean broadleaved species, therefore not constituted by a specific and univocal spectral signature. Second, several isolated nuclei of Eucalyptus are scattered within the mixed Autochthonous forest. At the same time, within some gaps in the areas covered by Eucalyptus, there may be some small nucleus of species belonging to native vegetation, challenging to detect based on satellite imagery with 10 m of spatial resolution. It has to be considered that this spatial resolution of the Sentinel sensors could involve errors and uncertainties in the classification output to identify covers/ crowns smaller than this dimension. Zhang et al. (2019) supposed that this could simultaneously conduct two opposite scenarios for each pixel: overestimation or underestimation/missing of the actual cover of smaller covers/trees. Furthermore, Zhang et al. (2019) pointed out some other elements that could cause uncertainty in its study, based on the classification of wooded areas using S1 and S2 data: the method of selection of training data, which may not be optimally representative of the actual conditions of the study area depending on their number and spatial distribution; a temporal miss-match between the interpreted Google Earth VHR data and Sentinel images; the presence of flooding, residual clouds, and shadows; other disturbances (e.g., fire, deforestation, etc.) that could affect the spectral signatures. Another source of errors could derive from edge pixels between different land classes (Lapini et al., 2020). However, this does not spoil the excellent effectiveness of these data, considering the small extent of these errors on the final accuracy values and, above all, the free availability of the images and software to process them. In fact, the precision obtained in the classification of areas not covered by forest is to be considered optimal, despite the complexity of the cover background that composes it (crops, orchards, towns, pastures, shrubs, grasses, soil, rock, etc.). On the other hand, this result was expected since the use of interferometric coherence is strongly correlated with the structural characteristics of forest arboreal vegetation (Ghosh et al., 2020; Siqueira, 2019). Aspect demonstrated by the relevance resulting from the feature importance analysis of this data.

### **2.3.2. Coherence**

As the tree canopy height is a dendrometric measure describing the vegetation structure and it is a significant indicator of the aboveground biomass of forest areas (Ghosh et al., 2020), in this study, we empirically exploited the geometric relationship between the InSAR coherence and the forest stand height as additional information to discriminate the forest cover. Through the InSAR analysis, it is possible to use the phase information of the SAR

signal to characterize the topography and height of the Earth's surface and the objects present on it. Phase decorrelation, with consequent loss of coherence values, occurs where the surfaces' conditions change during the two moments of acquisition of the pair of interferometric images. The relationship between this decorrelation and the height of the forest surface is based on the empirical assumption that as the height of the trees increases, the volume and quantity of canopy increases, causing greater decorrelation. Therefore, a decrease in coherence could indicate an increase in canopy height (Ghosh et al., 2020; Perko et al., 2011; Siqueira, 2019). In this study, although the time gap was not large between the two acquisition dates of the SAR SLC images the average of the three coherence layers for each of the two flight paths was used to reduce the adverse effects of decorrelation. When observations are made at different times, the targets within a SAR resolution cell (e.g., small branches and leaves) may have moved, causing an error in measuring the trigonometric gaze angle and, therefore, a reduction in the interferometric coherence (Siqueira, 2019). The use of shorter wavelength SARs (X-band, C-band) involves a higher temporal decorrelation due to interaction with smaller objects, even for a time interval of just one day (Ghosh et al., 2020). Concerning the coherence information in this study, the two polarizations resulted equally influent in the dataset classification. About this aspect conflicting testimonies were found in literature: Ghosh et al. (2020) used only the co-polarized (VV) coherence information for forest stand height estimation due the higher noise produced by the volumetric effect of canopy scatter elements on cross-polarized SAR signal; on the other hand, Siqueira (2019) affirms that the cross-polarized coherence signature is in general more appropriate for characterizing forest structure as it is more correlated to the multiple volume scattering of vegetation canopy.

### ***2.3.3. Optical and SAR layer integration; feature importance***

In this study, temporal spectral signatures for each optical band were exploited as a valuable expression of the seasonal phenological and photosynthetic activity variations. In particular, the use of optical vegetation indices is essential in the phenological discrimination and observation of the different types of forest vegetation, such as Mediterranean evergreen conifers and deciduous forests (Aragones et al., 2019). However, the temporal spectral signature may also have limitations. Although their efficiency is proven, in Grabska et al. (2019), it is reported that the species-specific characteristics do not only and uniquely influence the spectral reflectance, but often there are intra-specific variations in reflectance caused by the age of the trees, by states of stress or disease, or by local site conditions such as level of coverage, the effects of the surface texture of the roof and the resulting shadow effects, the type of soil present which in conditions of sparse foliage contributes to the reflected signal. These factors can cause as much significant deviations of the typical spectral signature values as to create overlaps between species and make it difficult for classifiers to discriminate. Vegetation indices improve these aspects, better characterizing the species-specific temporal dynamics of the various forest cover types. Aragones et al. (2019) used the NDVI time-series to characterize the phenological changes of five Mediterranean *Pinus* species for species discrimination. They observed how the index is subject to a significant decrease during the summer drought. Zhang et al. (2019), focusing on a savanna ecosystem, encountered such high differences in NDVI time signatures between woody and nonwoody as to allow their distinction.

However, the feature importance analysis shows that not all the spectral bands/indices contributed equally to the forest cover classification. Whether the integrated dataset or the single dataset is used, the feature importance shows the SWIR-based index (NBR), the red-edge-based (NDRE) and the B8A, B8, B7 and B12 bands as the most significant optical layers for RF prediction. This confirmed the findings of other studies concerning the high efficiency of the SWIR and red-edge bands for vegetation mapping (Grabska et al., 2019; Immitzer et al., 2016).

The red-edge bands are more sensitive to the photosynthetic pigments (chlorophyll a and b) levels and their variations from the biophysical and biochemical points of view. In contrast, the SWIR wavelengths are sensitive to the water content of the surface, since their optical absorbance increases with the increase of water content. Spracklen et al. (2021) observed how the SWIR-based indices were the most important in distinguish plantation from natural forest. This is probably due to the different water content in plant tissues, with a more significant presence in plantations with a high growth rate. Observing the feature importance of respect to the imagery's seasonality, the autumn-winter images seem to have most influenced the algorithm performance, followed by the summer months. In these periods, the phenological difference between species is higher, contributing to the discrimination of broadleaved species (Grabska et al., 2019). The fCOVER and fAPAR S2 biophysical variables also appeared among the most influential image layers. It should be considered that Ghosh et al. (2020), combining the use of S1 coherence and S2 biophysical variables (LAI and fraction of vegetation cover, FVC) and modeling using the RF regressor, found an excellent correlation with the canopy height. They concluded that since coherence information could potentially be affected by any object on the Earth's surface greater than the SAR wavelength, the biophysical variables support this gap by indicating the presence and status of the vegetation cover, as well as by a proven direct correlation with the height of the canopy.

Cloud cover, which is the main obstacle in dealing with time-series of optical data, was effectively addressed in this study by applying the S2-Cloud Probability mask product available in GEE, based on an automated machine learning pixel-based cloud detection, followed by linear interpolation for filling the missing pixel values. Other errors could derive from discontinuities of time series due to cloud covers or other artifacts. In general, the gap-filling methods may impact the quality of the images at various levels. However, the consistency of these errors is relatively not relevant, and, generally, they do not weigh the statistical quality metrics, although they may be visually distinguishable (Inglada et al., 2017). If, on the one hand, the optical data require few and consolidated pre-processing steps, the SAR data are more complicated to manage during the processing and interpretation of the information due to various factors intrinsic to the characteristics of the signal/ sensor and their interaction with the characteristics of the affected surface (De Luca, Silva, & Modica, 2021a; Mihai A. Tanase et al., 2020). In order to reduce speckle noise, both a monthly BTA and a speckle filter were applied. In fact, as Lapini et al. (2020) stated, although the multitemporal averaging inherently introduces a reduction in speckle-noise, a performance improvement was observed when a filter was applied, mainly if the time series consists of a relatively low number of images. Moreover, these authors pointed out how the execution of the backscatter temporal average of the whole SAR time series reduces seasonality effects (soil moistures, presence/ absence of leaves, trees water content, etc.) for forest classification purposes, preserving radiometric discrimination between classes.

Recently several other authors (De Luca, Silva, Oom, et al., 2021; Lasko, 2019; Lehmann et al., 2015; Morin et al., 2019; Spracklen & Spracklen, 2021; Stroppiana et al., 2015; W. Zhang et al., 2019) have demonstrated that the combined use of optical and SAR data optimize both usage potential, filling the gaps of each other's and increasing the accuracy of the returned products. However, excluding the case of InSAR coherence already discussed, no SARderived images are present among the most significant, and a co-polarized BTA image achieved the lowest value of feature importance. This indicates that, in the present case, the information given by the time-series of the SAR data was not actually decisive in classifying the forest cover. This can be confirmed by comparing the accuracy values, where the integration of the two sensors resulted in an improved  $F\text{-score}_M$  of only 2.53%, in line with what was stated by Chust et al. (2004) and Chatziantoniou et al. (2017). However, the accuracy

improvements of more than 7% ( $F\text{-score}_i$ ) found in some classes (e.g., Urbe), probable positive effect of the use of InSAR coherence on surfaces with lower decorrelation, should not be underestimated.

Concerning the SAR information, there are also much more pronounced limitations. Nicolau et al. (2021) demonstrated that classes with similar ground cover and similar backscatter have a lower separability potential than classes with distinct scattering mechanisms. Finally, he concluded that using dual-polarimetric SAR indices, relating the two different types of polarization (VV and VH), improved the spectral separability between classes. In the present study, we calculated the RVI and RFDI for each month, using the respective monthly BTA. The use of both polarizations, combined through dual-polarimetric indices, integrates their respective information (De Luca, Silva, & Modica, 2021a; Nicolau et al., 2021). The cross-polarized backscatter is more sensitive to the distribution of volume scatters of canopy elements (leaves, branches, etc.) than the co-polarized signal. The latter is more associated with the underlayer soil backscatter (Meyer, 2019). Indeed, in the Mediterranean context, Lapini et al. (2020) better individuated the forest land cover when cross-polarization was used, even in a simple visual RGB SAR composite. Nevertheless, other authors such as Nicolau et al. (2021), using S1 time series for land cover classification, observed that the single polarization (VV or VH) did not achieve good results for multiple land cover classes classification. For this reason, besides the simple backscatter values (VV and VH), they used SAR indices such as the VV/VH ratio and the modified RFDI as additional spectral information to train the classifier.

As mentioned above concerning coherence information, the sensitivity of the SAR signal to the structure of forest vegetation also depends on the wavelength used. Shorter wavelengths, such as C-band (5 cm) and the Xband (3 cm), are more sensitive to the canopy surface characteristics because comparable with the dimensions of needles and leaves, and therefore more helpful in differentiating between coniferous and broad leaves (Lapini et al., 2020). However, due to confusion with non-forest or secondary vegetation cover, misclassification is encountered (Lapini et al., 2020; Nicolau et al., 2021). Another factor to consider is the ease of saturation that the C-band has towards dense forest cover due to lower penetration capacities than longer wavelengths (Lapini et al., 2020; Meyer, 2019). Longer wavelengths (L-band and P-band) are proven to be better to estimate forest parameters (Morin et al., 2019), and therefore to better discriminate the forest vegetation (Lapini et al., 2020). Lapini et al. (2020), using only SAR data, proved that combining more wavelengths (multi-frequency approach), coming from different sources, leads to the highest accuracy of forest cover map.

It is expected that the imminent (in 2022) launch of the BIOMASS mission (Le Toan et al., 2011), consisting of a P-band polarimetric SAR satellite, will further improve forests biomass estimations. This could also concern other aspects such as forest type classification and other forest parameters estimation. The future objective will be to evaluate these new data as integrative information of the already consolidated optical spectral response.

Meanwhile, the approach proposed in this study demonstrated the effective potential of the combined use of S1 and S2 imagery in classifying forest cover in a fragmented and heterogeneous Mediterranean landscape. The applicability of remote sensing in these conditions has always been a complex task due to the anthropogenic influence on the landscape and the natural variability of plants structure and response to the climate-related typical events (e.g., summer aridity, higher fire severity, etc.) (Lapini et al., 2020). The situation is worsened by the topographic aspect of the study area. The roughness and irregular Earth's surfaces are more complicated to classify correctly than flat and homogeneous areas, mainly if SAR data are used, due to the effect of the slope exposure on both the sensor signal and on the characteristics of the vegetation cover (Inglada et al., 2017).



With this research, we demonstrated the reliability of our open workflow based on diverse free and opensource software to accurately map the forest cover, distinguishing the non-forest vegetation among the others LULC classes. Moreover, our workflow has been able to classify the vegetation cover more in-depth, discriminating between Eucalyptus, pine, and other forest types. This information could also be helpful in the framework of programmes aimed at long-term mapping and monitor of natural (or semi-natural) and planted forest cover. Future analysis dealing with sustainable forest management, habitat and biodiversity monitoring, carbon cycle estimation, and forest inventory could further exploit the reliability of our proposed research.

## **2.4. Conclusion**

The forest and plant composition mapping is essential to analyze ecosystems' quantitative and qualitative characteristics to facilitate various monitoring applications of their state and condition. In this context, remote sensing techniques and tools demonstrated to be very efficient, especially with the advent of easily accessible and open-source solutions (data and software). This study explored the potential of the combined use of SAR Sentinel-1 SAR and optical Sentinel-2 band and indices time-series, integrated the InSAR coherence measure and the optical biophysics variables to classify forest cover and discriminate it from the surrounding non-forest land covers. A new cloud detection tool, provided by the Sentinel Hub team, was implemented to optimize the cloud masking, followed by a temporal linear interpolation for gaps filling. This allowed us to effectively manage one of the main problems encountered in the analysis of optical images. Among the layers that have had greater importance in obtaining good results are the NBR and NDRE, mainly from the autumn, and interferometric coherence. This study aimed to optimize a supervised classification procedure for the quantitative and qualitative analysis of the forest vegetation cover in the Mediterranean region in the time period immediately prior to a wildfire occurred in August 2018. Obtaining a map of the vegetation cover, with a good level of accuracy achieved ( $> 90\%$ ), is a significant advantage to improve future monitoring and analysis of the study area and to be able to carry out an effective and more targeted management on specific ecosystems. This aspect is even more interesting if we consider that the approach presented by this study has been implemented with the combination of free imagery and open-source software, proving the efficiency of the interoperability of the various web platforms and open-source libraries, from download to final process (GEE, ASF, ESA SNAP, Scikit-learn, etc.). The spatial resolution offered by these satellites, although allowing classification at a good scale of detail, still does not allow the detection of small landscape elements, such as narrow roads and small patches of land cover, and still creates confusion where the land cover is not pure (e.g., commission errors were found where small nuclei of Eucalyptus settled in the autochthonous forest vegetation). In the distinction and classification of vegetation cover, the contribution of C-band backscatter was found not to be as decisive as the InSAR coherence itself or some optical bands, as already observed in the literature. It is expected that the imminent launch of new SAR satellite platforms, such as the SAR L-band mission BIOMASS, will improve the contribution of this type of information. Future studies should test and validate the proposed approach on different Mediterranean study areas, equally contributing to the poor state of the art on the use of multisensor data LULC classification in this biome. The results obtained in this work will be fundamental to set up a more focused investigation on the integrated use of SAR and optical data for monitoring over time the study area so as to assess the ecosystems' response to wildfires.

### 3. Unsupervised detection of burned area using SAR data

Adapted from

De Luca, G., Modica, G., Fattore, C., Lasaponara, R.: *Unsupervised Burned Area Mapping in a Protected Natural Site. An Approach Using SAR Sentinel-1 Data and K-mean Algorithm*. In: Gervasi O. et al. (eds) *Computational Science and Its Applications – ICCSA 2020. ICCSA 2020. Lecture Notes in Computer Science*, vol 12253 (2020). Springer, Cham. [https://doi.org/10.1007/978-3-030-58814-4\\_5](https://doi.org/10.1007/978-3-030-58814-4_5);

and

De Luca, G., Silva, J.M.N., Modica, G.: *A workflow based on Sentinel-1 SAR data and open-source algorithms for unsupervised burned area detection in Mediterranean ecosystems*. *GIScience Remote Sens.* 58, 516–541 (2021). <https://doi.org/10.1080/15481603.2021.1907896>.

GISCIENCE & REMOTE SENSING  
2021, VOL. 58, NO. 4, 516–541  
<https://doi.org/10.1080/15481603.2021.1907896>



#### A workflow based on Sentinel-1 SAR data and open-source algorithms for unsupervised burned area detection in Mediterranean ecosystems

Giandomenico De Luca <sup>a</sup>, João M.N. Silva <sup>b</sup> and Giuseppe Modica <sup>a</sup>

<sup>a</sup>Dipartimento di Agraria, Università degli Studi Mediterranea di Reggio Calabria, Reggio Calabria, Italy; <sup>b</sup>Centro de Estudos Florestais, Instituto Superior de Agronomia, Universidade de Lisboa, Lisbon, Portugal





##### ABSTRACT

This paper investigates the capability of the free synthetic aperture radar (SAR) Sentinel-1 (S-1) C-band data for burned area mapping through unsupervised machine learning open-source processing solutions in the Mediterranean forest ecosystems. The study was carried out in two Mediterranean sites located in Portugal (PO) and Italy (IT). The entire processing workflow was developed in Python-based scripts. We analyzed two time-series covering about one month before and after the fire events and using both VH and VV polarizations for each study site. The speckle noise effects were reduced by performing a multitemporal filter and the backscatter time averages of pre- and post-fire datasets. The spectral contrast between changed and unchanged areas was enhanced by calculating two single-polarization radar indices: the radar burn difference (RBD) and the logarithmic radar burn ratio (LogRBR); and two temporal differences of dual-polarimetric indices: the delta modified radar vegetation index ( $\Delta RVI$ ) and the delta dual-polarization SAR vegetation index ( $\Delta DPSVI$ ), all exhibiting greater sensitivity to the backscatter changes. The scene's contrast was enhanced by extracting the Gray Level Co-occurrence Matrix (GLCM) textures (dis-similarity, entropy, correlation, mean, and variance). A principal component analysis (PCA) was applied for reducing the number of the GLCM image layers. The burned area was delineated through unsupervised classification using the *k*-means clustering algorithm. A suitable number of clusters (*k* value) were set using a silhouette score analysis. To assess the accuracy of the resulting detected burned areas, an official burned area map based on multispectral Sentinel-2 (S-2) was used for PO, while for IT, a reference map was produced from S-2 data, based on the normalized burned ratio difference ( $\Delta NBR$ ) index. Recall (*r*), precision (*p*) and the *F*-score accuracy metrics were calculated. Our approach reached the values of 0.805 (*p*), 0.801 (*r*) and 0.803 (*F*-score) for PO, and 0.851 (*p*), 0.856 (*r*) and 0.853 (*F*-score) for IT. These results confirm the suitability of our approach, based on SAR S-1 data, for burned area mapping in heterogeneous Mediterranean ecosystems. Moreover, the implemented workflow, completely based on free and open-source software and data, offers high adaptation flexibility, repeatability, and custom improvement.

##### KEYWORDS

SNAP-python (snappy) interface; *k*-means clustering; scikit-learn libraries; radar vegetation index (RVI); dual-polarization sar vegetation index (DPSVI)

# Unsupervised Burned Area Mapping in a Protected Natural Site. An Approach Using SAR Sentinel-1 Data and K-mean Algorithm

Giandomenico De Luca<sup>1</sup> , Giuseppe Modica<sup>1</sup> , Carmen Fattore<sup>2</sup> ,  
and Rosa Lasaponara<sup>3</sup> 

<sup>1</sup> Dipartimento di Agraria, Università degli Studi Mediterranea di Reggio Calabria,  
Località Feo di Vito, 89122 Reggio Calabria, Italy  
{giandomenico.deluca, giuseppe.modica}@unirc.it

<sup>2</sup> DiCEM, Università degli Studi della Basilicata, Via Lanera 20, 75100 Matera, Italy  
carmen.fattore@imaa.cnr.it

<sup>3</sup> Istituto di Metodologie per l'Analisi Ambientale,  
Consiglio Nazionale delle Ricerche, C.da S. Loja, 85050 Tito Scalo, Italy  
rosa.lasaponara@imaa.cnr.it

**Abstract.** This paper is focused on investigating the capabilities of SAR S-1 sensors for burned area mapping. To this aim, we analyzed S-1 data focusing on a fire that occurred on August 10<sup>th</sup>, 2017, in a protected natural site. An unsupervised classification, using a k-mean machine learning algorithm, was carried out, and the choice of an adequate number of clusters was guided by the calculation of the silhouette score. The  $\Delta$ NBR index calculated from optical S-2 based images was used to evaluate the burned area delimitation accuracy. The fire covered around 38.51 km<sup>2</sup> and also affected areas outside the boundaries of the reserve. S-1 based outputs successfully matched the S-2 burnt mapping.

**Keywords:** Burned area detection · Sentinel-1 · SAR · Machine learning · K-mean clustering · Silhouette score · PCA · Radar burn difference (RBD) · Radar burn ratio (RBR) · Normalized burn ratio (NBR) · Protected natural site · Forest fire

In the Mediterranean basin, although wildfires are an integral part of natural ecosystems, their extent and impacts have increased in the last decades, with thousands of hectares of forest areas burned every year and with significant economic damages and landscape changes (Chuvieco, 2009; Gitas et al. 2012; Lanorte et al. 2012; Ruiz-Ramos, Marino, and Boardman 2018; SanMiguel-Ayanza et al. 2018; San-Miguel-Ayanza et al. 2019). Moreover, fires are a long-term threat, contributing to soil erosion and habitat degradation, releasing greenhouse gases (GHGs), affecting air quality and global climate (Chuvieco, 2009; Gitas et al. 2012; Rosa, Pereira, and Tarantola 2011). Timely and accurate detection and quantification of burned areas are necessary to assess the damages, address the post-fire management, and implement medium and long-term territorial and landscape restoration strategies (Chuvieco et al., 2019; Lasaponara and Tucci, 2019; Pepe et al., 2018). In this context, satellite remote sensing provides reliable tools and techniques for detecting and quantifying the extension of burned areas (Chu and Guo, 2013; Chuvieco et al., 2019; Filipponi, 2019; Lizundia-Loiola et al., 2020; Otón et al., 2019), permitting rapid, cost-effective, temporally constant coverage and monitoring of large and less accessible regions (Pepe et al., 2018). Several studies concerning the localization and mapping of fires' effects on vegetation were based on multispectral satellite data (Chuvieco et al., 2019; Filipponi, 2019; Imperatore et al., 2017; Lizundia-Loiola et al., 2020; Mouillot et al., 2014; Otón et al., 2019). These sensors are very efficient for the purpose due to their sensitivity in the visible, near and short infrared (NIR and SWIR) bands to changes in the state of vegetation and soil (Pereira et al., 1999; Chuvieco et al., 2019; Meng et al., 2017; Tanase et al., 2020; Miller et al., 2007; De Santis et al., 2009; Fornacca et al., 2018; Filipponi et al., 2018; Fernández-Manso et al., 2016). The optical spectral signature of the burned vegetation is unique and distinguishable from other disturbance factors or phenological changes in the short-term

period after a fire. This is mainly due to the combined effect of diverse factors: the reduction of vegetation amount, the presence of coal and ash, changes in the moisture content and temperature, and the reflectance of soil. However, some of these elements tend to be attenuated in a few weeks or months after the fire event, in particular where the fire severity was low (Pereira et al., 1999; Smith et al., 2005; Inoue et al., 2019), leading to a spectral confusion of burned areas with other disturbances or low unburned albedo surfaces (e.g., dark soils, water surfaces, shaded regions, ploughed fields, timber harvesting) (Imperatore et al., 2017; Kurum, 2015; Pepe et al., 2018; Fraser et al., 2000; Stroppiana et al., 2015; Dijk et al., 2021; Rodman et al., 2021). Moreover, optical signal data are influenced by different phenological and physiological vegetation phases (e.g., seasonal senescence, leaf-off conditions), especially in the case of burned vegetation detection and monitoring at larger time intervals after the event (Gallagher et al., 2020; Verbila et al., 2008; Fraser et al., 2000). In this context, the synthetic aperture radar (SAR) sensors are active systems that avoid some of these problems, proving to be an alternative or complementary data source for burned area detection and fire effects monitoring (Lehmann et al., 2015; Lasko, 2019; Kurum, 2015; Stroppiana et al., 2015; Tanase et al., 2011; Martinis et al., 2017; Chuvieco et al., 2019; Lasaponara et al., 2019). The response of the radar signal is affected by the ensemble of environmental variables (e.g., land cover, vegetation cover structure, moisture content, dielectric property of objects, size/shape and orientation of the scatterers in the canopy) and variables related directly to the sensor (e.g., polarisation, wavelength, orbit) or the local surface properties (e.g., topography, orientation, surface roughness, local incident angle) (Gimeno and San-Miguel-Ayanz, 2004; Hachani et al., 2019; Imperatore et al., 2017; Lapini et al., 2020; Santi et al., 2019, 2017; Tanase et al., 2011, 2020, 2010). SAR data are more sensitive to canopy structure than optical-based products (Martins et al., 2016). In detecting burned areas, SAR technology uses the variations in microwave backscatter caused by vegetation cover and soil structure and moisture content modifications, which implies a dielectric permittivity variation, thus providing an efficient system for discriminating events that cause changes in objects on the Earth's surface (Chuvieco et al., 2019; Donezar et al., 2019; Imperatore et al., 2017; Kurum, 2015; Pepe et al., 2018; Santi et al., 2017; Tanase et al., 2011, 2020, 2015, 2010; Zhou et al., 2019). Ruiz-Ramos et al. (2018) noted that, in dry conditions, the backscatter signal tended to decrease even after several weeks after the fire, indicating how degraded conditions can persist significantly after the event. This highlights the efficiency of SAR data in monitoring burned areas and justifying the need for timely interventions to counteract the ecosystem degradation and avoid desertification phenomena (Hill et al., 2008; De Luis et al., 2001; Chuvieco, 2009).

The variation of the backscattering signal due to the fire's effect on reducing the crown structure can be of different evidence depending on the polarisation. Generally, cross-polarised signals (vertical-horizontal, VH, and horizontal-vertical, HV) show a decrease in the backscatter response due to the consequent reduced volumetric dispersion contribution. Conversely, the change in the co-polarised backscatter coefficients (vertical-vertical, VV or horizontal-horizontal, HH) can be attributed to higher soil exposure (Imperatore et al., 2017). Due to this different interaction with the various aspects of the effects of fire on the environment, both types of polarisation can be decisive in detecting burnt forest areas (Tanase et al., 2014). For other purposes, this aspect is already employed in vegetation monitoring through the use of radar-based polarimetric indices in which both types of polarisation are used depending on the type of product and the SAR sensor used (Gururaj et al., 2019; Mandal et al., 2020; Nasirzadehdizaji et al., 2019). The radar vegetation index (RVI) (Kim et al., 2009), full- or dual-polarimetric, is a well-established SAR index (Szigarski et al., 2018) and generally used in studies related to vegetation biomass growth (Kim et al., 2014), in the LAI (leaf area index) estimation (Pipia et al., 2019) or in the

estimation of the water content of plants and soil (Kim et al., 2012; Trudel et al., 2015). Kim et al. (2012) demonstrated a high correlation between L-band RVI and other optical vegetation indices. The dual-polarisation SAR vegetation index (DPSVI) (Periasamy, 2018) also returned positive results for the study of plant biomass, demonstrating a good correlation with the normalised difference vegetation index (NDVI). However, single-polarisation indices were also used with excellent results to map the burnt areas or fire severity (Lasaponara and Tucci, 2019; Tanase et al., 2015).

More generally, most of the studies explored the backscattering behaviour after a fire in the Mediterranean environment (Imperatore et al., 2017; Kurum, 2015; Minchella et al., 2009; Tanase et al., 2015), but few of these have focused on the ability of SAR data to map the burned areas by measuring their accuracy with analytical methods (Belenguer-Plomer et al., 2019; Gimeno et al., 2004; Gimeno and San-Miguel-Ayanz, 2004; Lasaponara and Tucci, 2019; Martinis et al., 2017; Zhang et al., 2019).

Several space missions provide satellite constellations operating SAR imaging dedicated to environment observation useful for fire monitoring purposes (Chuvieco, 2009; Chuvieco et al., 2019; Mouillot et al., 2014). Copernicus missions by the European Space Agency (ESA) provides free high spatial and temporal resolution SAR (S-1) and multispectral (S-2) data (ESA Sentinel Homepage, 2020). The S-1 constellation comprises two polar-orbiting satellites (S-1A and S-1B) performing C-band (from 3.75 cm to 7.5 cm wavelength) radar imaging. The good spatial and temporal resolutions added to the free distribution make the Sentinel mission particularly suitable for risk monitoring and rapid mapping (Martinis et al., 2017). Several studies have demonstrated the sensitivity of the C-band to changes in the vegetation and environment affected by fire (Imperatore et al., 2017; Kurum, 2015; Tanase et al., 2020, 2010).

One of the strengths of the S-1 and S-2 data is their high spatial and temporal resolution. The spatial resolution has a considerable effect on the detection of burnt areas and their subsequent monitoring, lowering the omission errors typical of the coarser resolution data in detecting the smallest areas and improving spectral discrimination (Verhegghen et al., 2016; Boschetti et al. 2015; Stroppiana et al., 2015; Belenguer-Plomer et al. 2019; Mouillot et al., 2014). The advantages become more evident when the acquisition revisit time of these products is a few days, allowing the monitoring of temporal trends at an appropriate temporal scale (Boschetti et al., 2015; Verhegghen et al., 2016; Gitas et al., al., 2012; Tanase et al., 2020).

Furthermore, ESA itself distributes the Sentinel application platform (SNAP) (ESA SNAP Homepage, 2022), a free and open-source software platform containing the toolboxes necessary for pre-processing and processing Sentinel data. The SNAP toolboxes, initially Java-based, can also be accessed from the Python programming language (The Python Language Reference, 2020), one of the most popular languages for remote sensing and scientific analysis, widely used in both operational and scientific domains (Hao and Ho, 2019), through the ESA SNAP-Python (snappy) interface (ESA SNAP Cookbook, 2022).

The present work aimed to develop a semi-automatic procedure for mapping burned areas in Mediterranean regions using SAR S-1 data and based on the *k*-means clustering algorithm for an unsupervised image classification approach. Therefore, supporting the state-of-the-art of SAR-based burned area mapping.

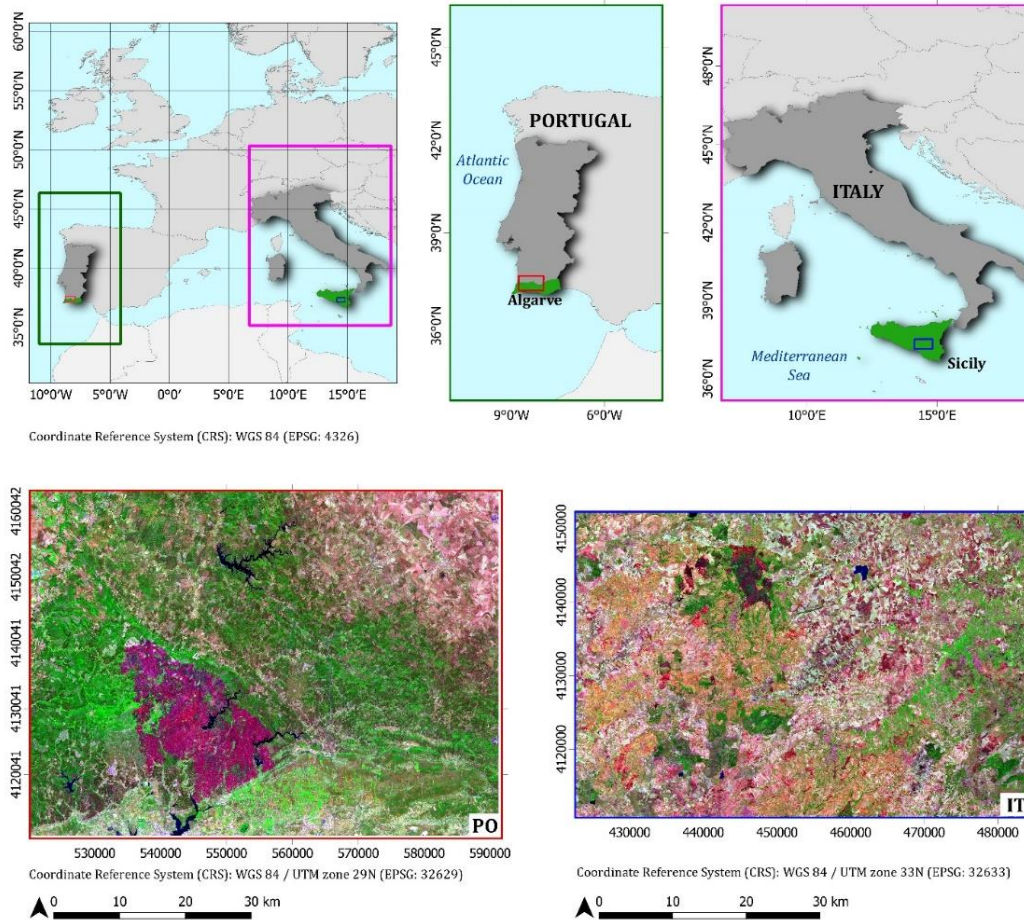
The *k*-means is one of the most straightforward iterative clustering algorithms, widely used in data mining and pattern recognition purposes (Dhanachandra et al., 2015; Nagpal et al., 2013, Jain 2010). One of the main difficulties for the *k*-means cluster analysis is to set the more suitable number of clusters (*k* value) in the initialisation phase. Among the different approaches proposed in the literature (Kodinariya and Makwana, 2013),

in our approach, we used the silhouette score (Rousseeuw, 1987) to set the value of the  $k$  parameter, which statistically measures the average separation distance (dissimilarity) between points within neighbouring clusters. The entire processing workflow (Figure 3.2), excluding accuracy assessment, was developed in Python-based open-source libraries and scripts, implementing ESA-snappy for image pre-processing and Scikit-learn (Pedregosa et al., 2011) processing and classification. It consists of the following fundamental steps: 1) speckle-noise reduction by calculating the backscatter time average of pre- and post-fire datasets and then applying a multitemporal filter; 2) calculation of the radar burn difference (RBD) and the logarithmic radar burn ratio (LogRBR) single-polarisation indices and the dual-polarimetric S-1 indices ( $\Delta RVI$  and  $\Delta DPSVI$ ) in order to emphasise the areas of change; 3) gray-level co-occurrence matrix (GLCM) texture features extraction; 4) data reduction using the principal components analysis (PCA) transformation; 5) silhouette score analysis in order to set the  $k$  parameter value; 6) unsupervised classification using the  $k$ -means clustering algorithm. To confirm the method's applicability, it was tested on two scenes representing two Mediterranean forest environments located in two different countries (Italy and Portugal). The validation of the classification maps was performed by comparison with reference maps based on S-2 Multispectral images and calculating accuracy metrics (recall,  $r$ , precision,  $p$ , and the  $F$ -score).

### 3.1. Materials and methods

#### 3.1.1. Study sites

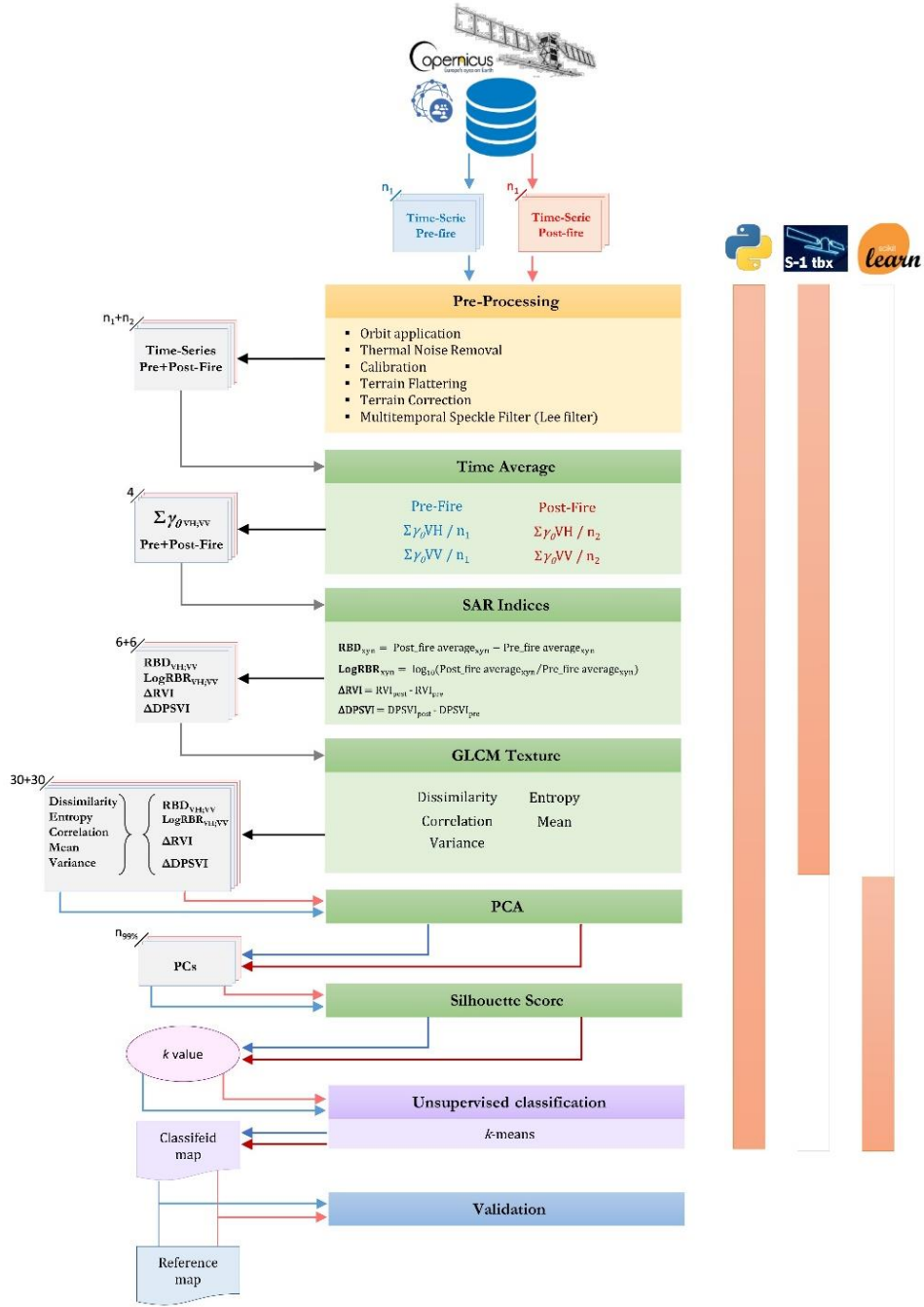
The implemented methodology was tested in two Mediterranean areas of Southern Europe (Figure 3.1). The first is located in Algarve, the southernmost region of Portugal (37° 18'N; 08° 30'W), a forest area in the Serra de Monchique Mountain range (study site PO). The second is located in the central area of Sicily (South of Italy, 37° 43'N; 14° 39'E), the “Rossomanno-Grottascuro-Bellia” regional nature reserve (study site IT). The extent of the two study sites was obtained manually based on the overlapping area of the tiles of the various orbits of S-1. The two study sites extend to approximately 2550 km<sup>2</sup> (IT) and 3600 km<sup>2</sup> (PO). The sites are located at the same latitude and present very similar and comparable typical Mediterranean vegetation contexts. Most parts of the two study areas were dominated by genus *Eucalyptus* species (*Eucalyptus* spp.) and typical Mediterranean conifers (*Pinus* spp.), deriving mainly from artificial planting during the end of the 19<sup>th</sup> century and the 20<sup>th</sup> century. However, both areas study sites are also covered by areas with dense typical Mediterranean forest vegetation of secondary broad-leaved (ex. *Quercus* spp.) and coniferous trees, interspersed with sclerophyllous shrublands (Camerano et al., 2011; San-Miguel-Ayaz et al., 2016). The PO study site also includes agricultural areas and pastures.



**Figure 3.1.** Study sites: in the top, location of the study sites in Europe and in the respective countries; in the bottom, the overviews of the two study sites (post-fire Sentinel-2 images, SWIR-NIR-Green false-colour composite) where the burned areas are clearly visible (the dark-purple area in PO; the darker area in IT).

The events occurred in August from the 3<sup>rd</sup> to the 10<sup>th</sup>, 2018, in the PO study site, covering 268.9 km<sup>2</sup>, while, in the IT study site, the fire occurred on August 6<sup>th</sup>, 2017, covering an area of 38.51 km<sup>2</sup>. Regarding the Sicilian natural reserve, the fire also affected neighbouring and similar forest areas outside its administrative boundaries. In the PO study site, fire affected the vegetation in a heterogeneous way at the spatial level, altering or removing the structure at various degrees, with a predominant crown fire occurrence, leaving residues of burns on the ground (ash and coal). In some places, where the severity was higher, the bare soil was exposed (Oom et al., 2018).





**Figure 3.2.** The workflow of the implemented approach.

## 3.2. Dataset

### 3.2.1. Sentinel-1 dataset

The Sentinel-1A/B high-resolution ground range detected (GRDH) dual-polarised (VV and VH polarisations) time series, acquired in interferometric wide (IW) mode, was searched through the Copernicus Open Access Hub (2022). The spatial resolution of the product is 20 m x 22 m (ground range x azimuth), with a pixel spacing of 10 m x 10 m (ground range x azimuth) on the image, corresponding to the mid-range value at mid-orbit altitude averaged over all sub-swaths (ESA Sentinel-1 User Guide, 2016). The bulk downloading process was carried out



using the aria2 command-line downloader (aria2 download utility Homepage, 2020), allowing to automate and speed up the acquisition of huge datasets. In total, we acquired two S-1 image datasets, one for each of the two study sites, respectively. The images were acquired to cover a time frame of about a month before and after the event date during the summer fire season (July-September), taking into account the need for the absence of rain that could affect the backscatter signal. For the PO study site, the dataset was formed by eight images for the pre-fire period and five images for the post-fire period; for the IT study site, the pre-fire and the post-fire images were nine and five respectively.

### 3.2.2. Reference data

As reference data for the PO study site, the burned area perimeters provided by Instituto de Conservação da Natureza e das Florestas (ICNF) based on S-2 satellite imagery (SIG-ICNF, 2021) were adopted. The minimum extent of the mapped fires is 0.5 km<sup>2</sup>. Due to the insufficient quality of the official data (see the Supplementary material), we downloaded two Sentinel-2B Level-1C images, acquired one before (sensing date: 2017/08/01, 09:50) and one after the fire (sensing date: 2017/08/11, 09:50), respectively, in order produce the reference map for the IT event.

The two images were pre-processed and the normalized burn ratio (NBR) (Eq. 3.1) for the pre- and post-fire S-2 data and, consequently, their temporal difference represented by  $\Delta NBR$  index (Eq. 3.2) (Key et al., 2006) was calculated:

$$NBR_{zj} = (NIR_{zj} - SWIR_{zj}) / (NIR_{zj} + SWIR_{zj}) = (B8A_{zj} - B12_{zj}) / (B8A_{zj} + B12_{zj}) \quad (3.1)$$

$$\Delta NBR = NBR_{prefire} - NBR_{postfire} \quad (3.2)$$

where  $zj$  represents a fire-related time period (pre- or post-fire); NIR is the near infra-red band that in this case was represented by the band B8A (865 nm) of S-2 data; SWIR is the short-wave infra-red band represented by the band B12 (2190 nm) of S-2 data. These two bands are very sensitive to burned vegetation (Lanorte et al., 2012). For this reason, this index is generally used as a reference layer since it allows to better identify the perimeter of the burned areas than other methods (Ban et al., 2020; Donezar et al., 2018; Tanase et al., 2015; Zhang et al., 2019; Kurum, 2015; Tanase et al., 2010), in the absence of good quality official data. The shapefile used as reference was obtained by converting the binary map composed of pixels with  $\Delta NBR$  values greater than 0.1 (conventional burned / not-burned threshold (Keeley et al., 2009). Moreover, the interpretation was visually strengthened and guided by using the RGB false-colour combination (SWIR-NIR-Red). The IT reference shapefile was filtered, deleting all the polygons with an area less or equal to 0.05 km<sup>2</sup> to reduce redundancy and make the data consistent with the PO.

### 3.3. Processing libraries

The S-1 data pre-processing was carried out using the Sentinel-1 Toolbox implemented in ESA-SNAP v.7.0.4 (ESA SNAP Homepage, 2022) and executed through Snappy (ESA SNAP Cookbook, 2022), the SNAP-Python interface which enables accessing and managing the SNAP Java application programming interface (API) from Python. The application script was built on Python v.3.6.8 (The Python Language Reference, 2022), a version compatible with the Snappy interface. The image processing and classification were implemented in Scikit-learn v.0.23.1 (Pedregosa et al., 2011, Scikit-learn Homepage, 2022), an open-source Python-based library that provides a collection of different data-processing modules concerning machine learning analysis and modelling (Pedregosa

et al., 2011). This library contains all the processing modules used in this study: the MinMaxScaler module, the sklearn.decomposition.PCA module, the sklearn.metrics.silhouette\_score module and the sklearn.cluster.KMeans module.

### 3.4. Image pre-processing and layers creation

The S-1 data pre-processing steps (Figure 3.2), carried out for both the two time-series datasets, started by applying the auto-downloaded orbit file, followed by thermal noise removal.

The images were then radiometric calibrated and converted to beta ( $\beta_0$ ) noughts backscatter standard conventions. Due to the rough terrain topography of both study areas and consequently the presence of geometric and radiometric distortions, a radiometric terrain flattening (RTC processing) and a terrain correction were performed using a digital elevation model (DEM) obtained from the shuttle radar topography mission (SRTM) (Farr et al., 2007; Small, 2011), presenting a spatial-sampling of 1 arc-second. The bilinear interpolation resampling method was used for both DEM and output image resampling. During the RTC processing, the images were converted from  $\beta_0$  to gamma ( $\gamma_0$ ) nought automatically. In contrast, in the terrain correction step, the images were projected to WGS84/UTM zone 29N and 33N for the PO study site and IT study site, respectively.

For each study site dataset, an image stack was made using the Create Stack Operator of Sentinel-1 Toolbox. The product geolocation was used as an initial offset method, and the extent of the master image was adopted on the slave images without resampling. The optimal master image for each dataset was chosen automatically by the tool. A multitemporal speckle Lee filter (Quegan et al., 2000; Santoso et al., 2015) of 15x15 pixel window size was carried out to apply a first reduction of the radar speckle noise. Subsequently, the speckle reduction was improved by calculating the backscatter time average (Lasaponara and Tucci, 2019), separately for the images before and after the fire, for each polarisation (VH and VV). Following the implemented pre-processing phase, four layers are obtained: i) Pre-fire time average VH; ii) Pre-fire time average VV; iii) Post-fire time average VH; iv) Post-fire time average VV.

For both study sites, these individual layers were used to compute two single-polarisation radar indices for change detection: the RBD (Eq. 3.3) (the difference between pre- and post-fire backscattered time average for each polarisation) and the LogRBR (Eq. 3.4) (log-scaled ratio of the backscattering coefficients between pre- to post-fire for each polarisation). This latter index is derived from the radar burn ratio (RBR) (Tanase et al., 2015) used in change detection or fire severity detection (Lasaponara and Tucci, 2019; Tanase et al., 2015), scaled to logarithmic in order to optimise the noise distribution (Dekker, 1998).,

The equations of the two indices are:

$$RBD_{xy} = \text{Post-fire TimeAverage}_{xy} - \text{Pre-fire TimeAverage}_{xy} \quad (3.3)$$

$$\text{LogRBR}_{xy} = \log_{10}(\text{Post-fire TimeAverage}_{xy} / \text{Pre-fire TimeAverage}_{xy}) \quad (3.4)$$

where  $xy$  represents a specific polarization (VV or VH).

Besides, two dual-polarimetric radar vegetation indices, the radar vegetation index (RVI) (Eq. 3.5) proposed by (Kim and Van Zyl, 2009) and modified for the S-1 dual-polarized SAR data (Gururaj et al., 2019; Mandal et al., 2020; Nasirzadehdizaji et al., 2019), and the dual-polarisation SAR vegetation index (DPSVI) proposed by (Periasamy, 2018) (Eq. 3.6) were computed for pre- and post-fire datasets, respectively:

$$RVI_{zj} = 4 \cdot \text{TimeAverageVH} / (\text{TimeAverageVV} + \text{TimeAverageVH}) \quad (3.5)$$

$$\text{DPSVI}_{zj} = (\text{TimeAverageVV} + \text{TimeAverageVH}) / \text{TimeAverageVV} \quad (3.6)$$

where  $z_j$  represents a fire-related time period (pre- or post-fire).

From these two vegetation indices, the relative temporal difference was calculated ( $\Delta RVI$  and  $\Delta DPSVI$ ) (Eq. 3.7, 3.8):

$$\Delta RVI = RVI_{post} - RVI_{pre} \quad (3.7)$$

$$\Delta DPSVI = DPSVI_{post} - DPSVI_{pre} \quad (3.8)$$

For the  $RBD_{VH}$ ,  $RBD_{VV}$ ,  $LogRBR_{VH}$ ,  $LogRBR_{VV}$ ,  $\Delta RVI$  and  $\Delta DPSVI$  index layers, five GLCM (Grey Level Co-occurrence Matrix) texture features (Haralick, 1979; Haralick et al., 1973) were computed for each of the two study sites (Tab 3.1) fixing the size of the search window to 11x11 pixels. The five GLCM textures were computed to exhibit a more marked contrast between changed and unchanged areas, adding extra spatial information to support classification accuracy performance (Hall-Beyer, 2017; Li et al., 2014).

**Table 3.1.** Name, group, and equation of used GLCM (Grey Level Co-occurrence Matrix) texture measures.  $P_{i,j}$  is the probability of values  $i$  and  $j$  occurring in adjacent pixels in the original image within the window defining the neighbourhood.  $i$  and  $j$  are the labels of the columns and rows (respectively) of the GLCM:  $i$  refers to the digital number value of a target pixel;  $j$  is the digital number value of its immediate neighbour.  $\mu$  is mean and  $\sigma$  the standard deviation.

GLCM Features	Group	Equation
Dissimilarity	Contrast	$\sum_{i,j=0}^{N-1} P_{i,j}  i - j $
Entropy	Orderliness	$\sum_{i,j=0}^{N-1} -\ln(P_{i,j})P_{i,j}$
Correlation	Statistics	$\sum_{i,j=0}^{N-1} P_{i,j} \left[ \frac{(i - \mu_i)(j - \mu_j)}{\sqrt{(\sigma_i^2)(\sigma_j^2)}} \right]$
Mean		$\mu_i = \sum_{i,j=0}^{N-1} i(P_{i,j}); \mu_j = \sum_{i,j=0}^{N-1} j(P_{i,j})$
Variance		$\sigma_i^2 = \sum_{i,j=0}^{N-1} P_{i,j} (i - \mu_i)^2; \sigma_j^2 = \sum_{i,j=0}^{N-1} P_{i,j} (j - \mu_j)^2$

The GLCM process originated a dataset consisting of 30 layers for each study-site, which constituted the input data for the next processing workflow step.

The S-2 images downloaded to generate the IT reference data were pre-processed using the Sentinel-2 Toolbox. These were first resampled to 10 m × 10 m pixel size using the band B4 (Red; 664.6 nm) as reference source size and the bilinear interpolation as an upsampling method. Subsequently, the images were reprojected and clipped on the same area of the correspondent S-1 data. The Level-2A products (Bottom-of-Atmosphere) were generated using Sen2Cor v2.8 processor (ESA sen2cor Homepage, 2022).

### 3.5. Data preparation

#### 3.5.1. Data normalization

The data normalisation in the same continuous scale range [0-1] was carried out for all the S-1 single layers (Eq. 3.9). This operation converts the original values of the input data into the new range through rescaling. This step aimed to equalise the input features, reducing the influence of differences in their intervals, making them

comparable in numerical values and optimising the learning algorithm process (Angelov and Gu, 2019, Subasi, 2020). The normalisation was carried out using the specific MinMaxScaler module contained in scikit-learn, given by:

$$x_{norm} = (x - x_{min}) / (x_{max} - x_{min}) \quad (3.9)$$

where  $x_{norm}$  is the new normalised value,  $x$  is the value to be normalised,  $x_{min}$  and  $x_{max}$  are the smallest and the highest value of the data (feature range).

### 3.5.2. *Data reduction: principal component analysis (PCA) transformation*

Considering the high number of input data layers, a principal component analysis (PCA) was performed to reduce the dimension of the dataset and select the optimum layer subset without losing the essential information (total variance) for image classification (Gimeno et al., 2004; Richards, 2013). The PCA module provides a linear dimensionality reduction based on singular value decomposition (SVD) in order to project the data in a lower-dimensional space (eigenspace) and derive the new principal components (PCs) representing the directions of maximum variance of the eigenspace (Subasi, 2020). In this study, the first transformed PCs that explained a high enough cumulative variance (greater than or equal to 99%) were considered the optimal reduced representation of the original dataset and used as input in the classification process.

## 3.6. Image classification

### 3.6.1. *Classification algorithm (k-means)*

The burned areas' classification was carried out using the popular  $k$ -means algorithm, a data clustering method introduced by James MacQueen (1967). It is known as one of the simplest and fastest unsupervised machine learning algorithms (Dhanachandra et al., 2015; Nagpal et al., 2013), widely used in remote sensing applications (Celik, 2009; Dhanachandra et al., 2015; M. Li et al., 2014; Phiri & Morgenroth, 2017; Rehman et al., 2019; Senthilnath et al., 2017). Given a dataset, the algorithm is based on the grouping (clustering) of the pixels with homogeneous characteristics in a predefined number ( $k$ ) of clusters. The homogeneity of the pixels is defined by the minimum distance between their value and the single cluster's centroid. The algorithm's initialisation starts with a first random definition of the  $k$  centroids, optimised by the  $k$ -means++ method, and is based on the weighted distribution probability for the definition of the centroids. Then, it proceeds with the first assignment of each pixel to the nearest centroid, in terms of values' Euclidean distance, and therefore with the first  $k$  clusters' generation. After the first initialisation of the  $k$  centroids, each of them is recalculated many times over so that the dataset belonging to a cluster can be reassigned to the new cluster, obtaining the most appropriate assignment of each pixel to the clusters. This process is repeated iteratively until the centroids' arrangement ceases to change, the tolerance or error value is satisfied, or until the maximum number of defined iterations is reached (Dhanachandra et al., 2015). The centroid of a cluster is the point to which the sum of distances from all the pixels in that cluster is minimised. Therefore, the  $k$ -means could be defined as an iterative algorithm that minimises the value of the sum of squared errors (SSE) of distances from each object to its cluster centroid (Dhanachandra et al., 2015). The  $k$ -means algorithm used in this work was based on a combination with the expectation-maximisation (EM) model (Dempster et al., 1977).

### 3.6.2. *Definition of a suitable number of clusters using the Silhouette Score*

One of the main issues at initialising a clustering algorithm is setting the optimal number of clusters ( $k$  parameter). To solve this issue, we used the silhouette score approach (Rousseeuw, 1987), which is based on the separation distance between clusters, according to the following formula (equation 3.10):

$$\text{Silhouette Score} = (b_i - a_i) / \max(a_i, b_i) \quad (3.10)$$

where  $i$  is the value of a single-pixel contained in a cluster,  $a$  is the average distance (dissimilarity) between  $i$  and all other objects of the same cluster, and  $b$  is the average distance between  $i$  and the nearest cluster of which  $i$  is not a part (Rousseeuw, 1987). This coefficient measures how close each point in a cluster is to the neighbouring clusters' points for a given number of clusters. The computation of its average results is a simple method to address  $k$  value (Rousseeuw, 1987). We calculated the mean of the silhouette score for different  $k$  values ( $k$ -space, from 2 to 20) using the “relative” module provided in scikit-learn. To save on computation time, the calculation was performed on a sample of 100,000 points randomly distributed over the entire area of the two datasets. The score value can vary in a range from 1 (maximum separation: well clustered, best  $k$ -value) to -1 (minimum separation: misclassified, worst  $k$ -value).

### 3.6.3. Classification application and post-process enhancement

For each of the two transformed and reduced datasets, an unsupervised classification was carried out using the  $k$ -means algorithm. The number of clusters ( $k$  parameter) was set according to the silhouette score analysis result, while the default number of iteration (300) was left.

In order to identify the classes representing the real burned areas, the mean value of each radar index for each class was computed and plotted.

Despite the noise reduction operations, the SAR data still presents some outliers, which are persistent due to the signal's intrinsic characteristics. Moreover, since we used several images for each dataset covering a time-frame of about one month before and one month after the fire event, different surface-changes could have occurred (small fires, agronomic operations, etc.), leading to an erroneous assessment of commission errors. Therefore, following the raster data's vectorisation, pre and post-fire scenes were filtered, eliminating clusters covering an area less or equal to 0.05 km<sup>2</sup> (minimum mapping unit of reference data).

## 3.7. Accuracy assessment

The resulting classification maps were compared to the respective reference burned areas to assess their accuracy. The accuracy analysis regarded only those classes corresponding to the actual burned area, excluding the other classes. We chose these classes by observing the distribution of the average value of each of the six radar indices for each class. The classes that did not correspond to the burned area were aggregated together as “unburned class”. Both the classified and the reference images were vectorised to facilitate their analytical comparison. Therefore, after their superimposing, each classified pixel was labelled into one of the following categories (pixel-based accuracy assessment) (Goutte & Gaussier, 2005; Giuseppe Modica et al., 2020; Shufelt, 1999; Sokolova et al., 2006):

- True Positive (TP): when a pixel classified as burned corresponded to burned class in the reference data (pixel correctly classified).
- False Negative (FN): when a pixel representing burned in the reference data was classified as not-burned (pixel not detected).

- False Positive (FP): when a pixel classified as burned did not correspond to burned class in the reference data (pixel erroneously detected).

After counting the number of pixels belonging to one of the three categories for each image, the recall ( $r$ ), Precision ( $p$ ) and  $F$ -score accuracy metrics were calculated (eq. 3.11-3.13) (Goutte & Gaussier, 2005; Shufelt, 1999; Sokolova et al., 2006; Sokolova & Lapalme, 2009):

$$r = |TP| / |TP + FN| \quad (3.11)$$

$$p = |TP| / |TP + FP| \quad (3.12)$$

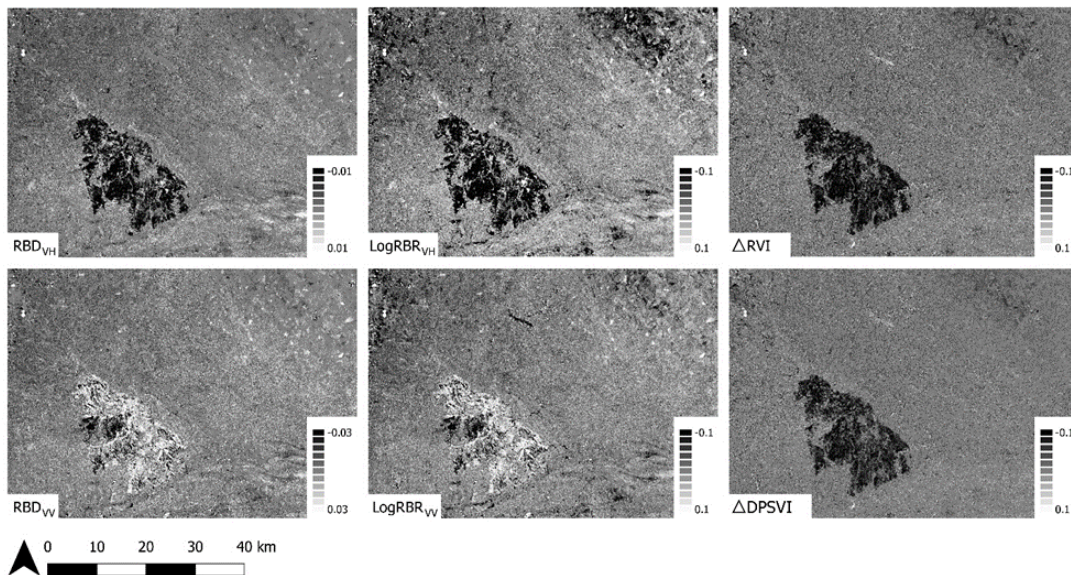
$$Fscore = 2 \cdot (r \cdot p) / (r + p) \quad (3.13)$$

where  $r$  and  $p$  are functions of omission and commission errors. Their opposites,  $1-r$  and  $1-p$ , indicate the omission and commission errors, respectively. The  $F$ -score measures the overall accuracy using the harmonic mean of commission and omission errors. The  $r$ ,  $p$ , and  $F$  can be in a range from 0 (total misclassification) to 1 (perfect classification) (Goutte and Gaussier, 2005; Modica et al., 2020; Sokolova and Lapalme, 2009).

### 3.8. Results

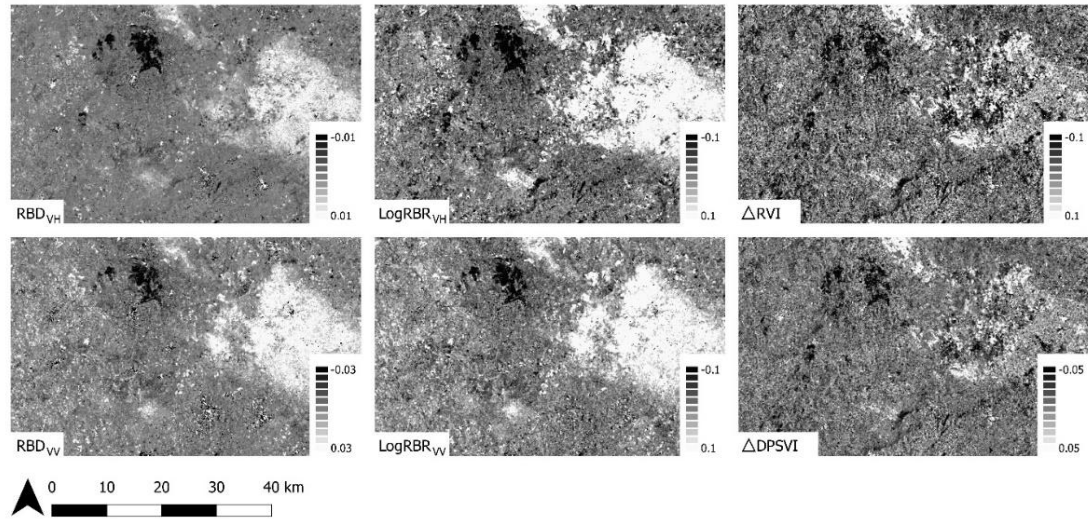
#### 3.8.1. Data preparation

To detect burned areas, the radiometric changes that occurred after the fire had to be highlighted. For this reason, radar vegetation indices were calculated, of which two were single-polarisation (RBD and LogRBR) and two dual-polarimetric (RVI and DPSVI). Unlike the RBD and LogRBR indices that already express temporal differences, the respective  $\Delta RVI$  and  $\Delta DPSVI$  indices had to be derived from the original RVI and DPSVI. The RBD, LogRBR,  $\Delta RVI$  and  $\Delta DPSVI$ , used as the input layer for successive GLCM computation step, are shown in Figures 3.3 and 3.4 for the PO, and IT study sites, respectively.



**Figure 3.3.** The S-1 indices (RBD<sub>VH</sub>, LogRBR<sub>VH</sub>, ΔRVI, RBD<sub>VV</sub>, LogRBR<sub>VV</sub>, and ΔDPSVI) were obtained in the PO dataset pre-processing steps. For each of these indices, the GLCM (Grey Level Co-occurrence Matrix) texture features were calculated.

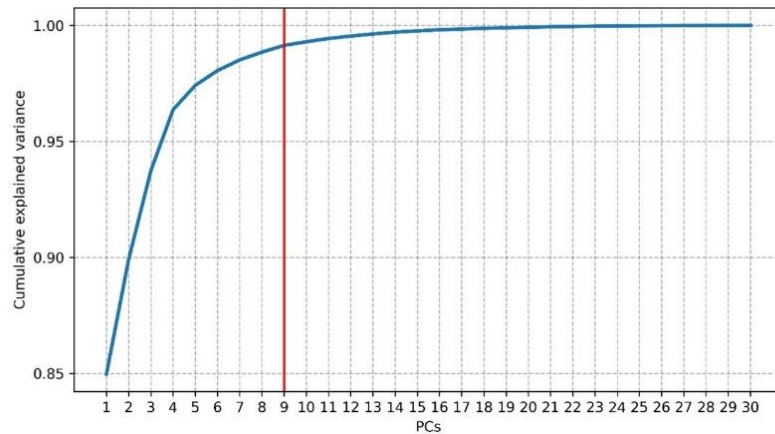




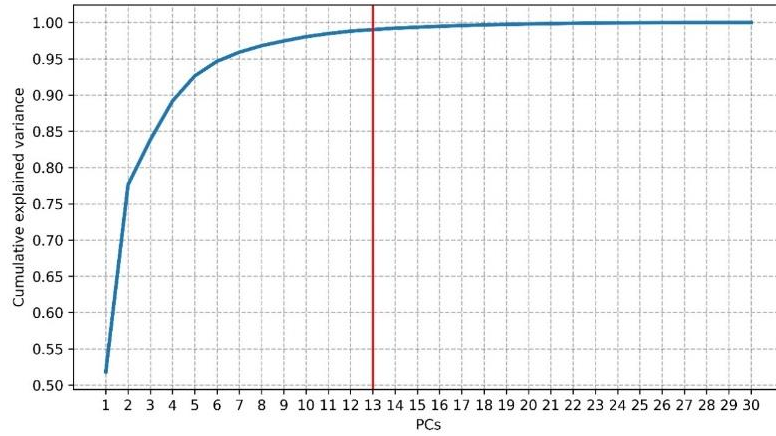
**Figure 3.4.** The S-1 indices (RBD<sub>VH</sub>, LogRBR<sub>VH</sub>, ΔRVI, RBD<sub>VV</sub>, LogRBR<sub>VV</sub> and ΔDPSVI) were obtained in the IT dataset pre-processing steps. For each of these indices, the GLCM (Grey Level Co-occurrence Matrix) texture features were calculated.

### 3.8.2. PCA transformation

The PCA was performed on the entire dataset to reduce their dimension. The cumulative variance explained by the PCs is reported in Figures 3.5 (PO) and 3.6 (IT). As shown, the PO dataset reached the threshold (0.99) at the 9<sup>th</sup> PC, while the IT dataset expressed the same cumulative variance value at the 13<sup>th</sup> PC. These PCs, which for each dataset have reached the threshold and are represented by transformed images, have been chosen as input layers in the subsequent related processes.



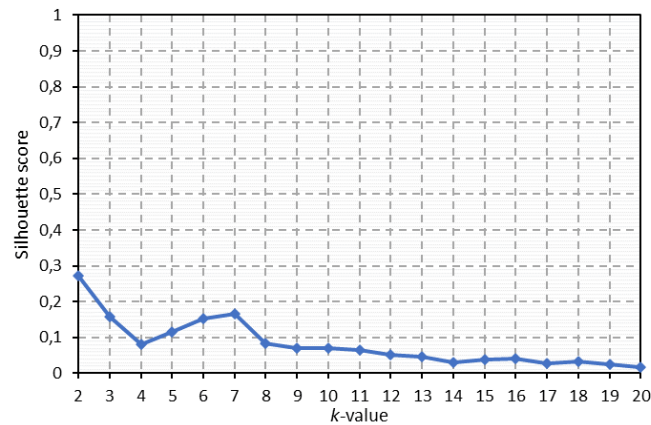
**Figure 3.5.** The cumulative variance explained by the principal components (PCs) for the PO study site. The red line identifies the first PCs that reached a cumulative variance of 0.99.



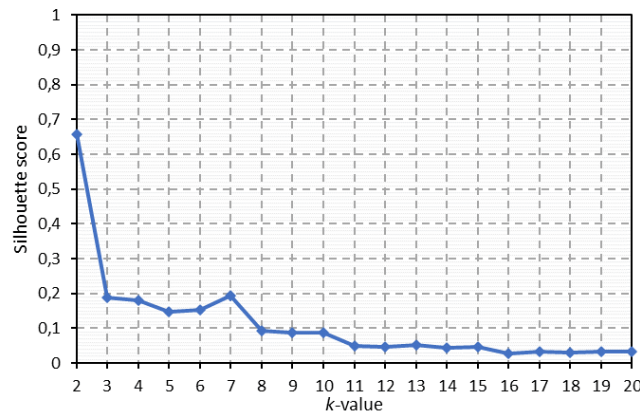
**Figure 3.6.** The cumulative variance explained by the principal components (PCs) for the IT study site. The red line identifies the first PCs that reached a cumulative variance of 0.99.

### 3.8.3. Silhouette score

Figures 3.7 (PO) and 3.8 (IT) show the trend of the averaged silhouette score calculated on relative PCA outputs for a  $k$ -space ranging from 2 to 20 clusters and for a sample of 100,000 random points. The highest values resulted from lower  $k$ -values, with the maximum value described by  $k = 2$  for both datasets. The next highest value was found when  $k = 7$  in both datasets with a Silhouette score of 0.166 and 0.191 for PO and IT, respectively.



**Figure 3.7.** Silhouette score values, for the PO dataset, for a  $k$ -space range ( $k$  values) between 2 and 20.

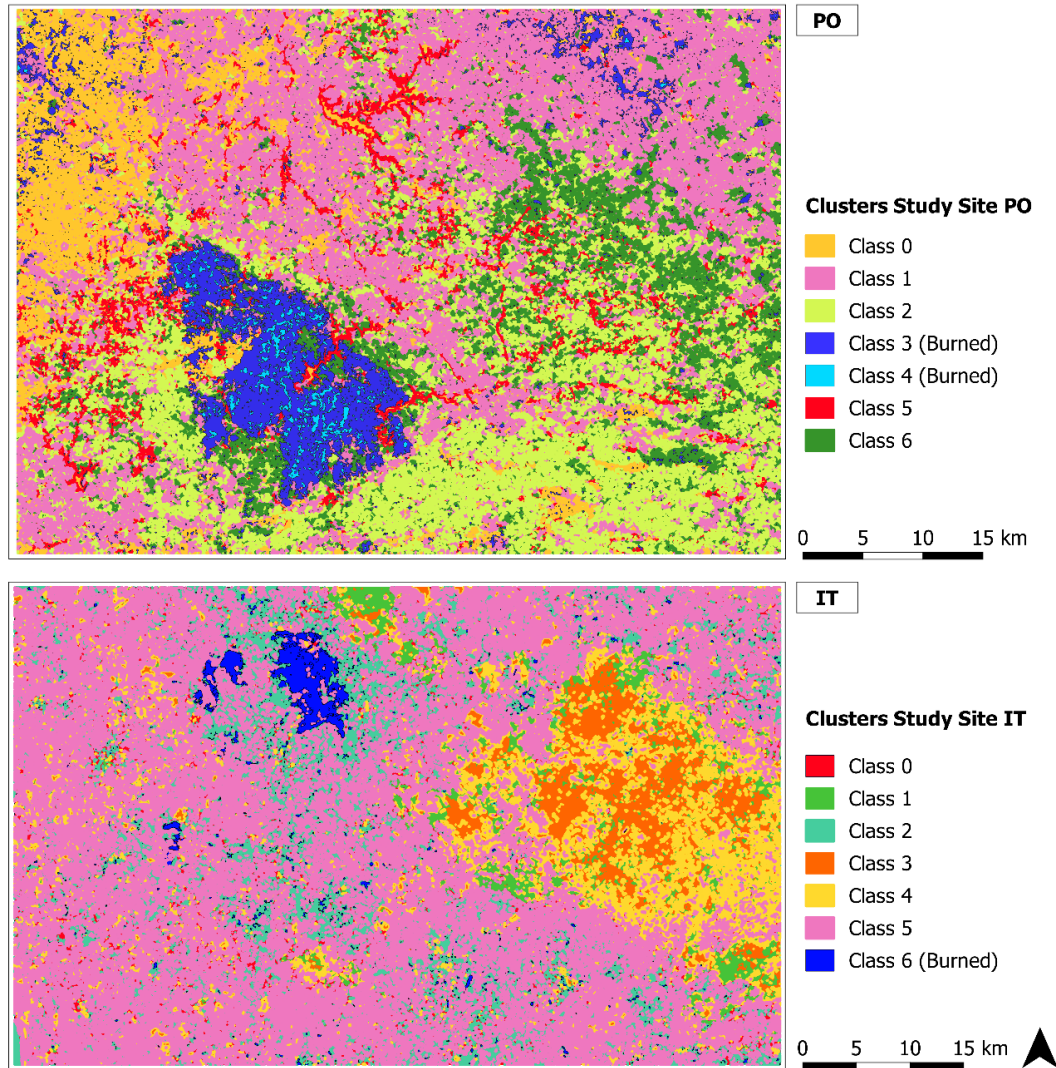


**Figure 3.8.** Silhouette score values, for the IT dataset, for a  $k$ -space range ( $k$  values) between 2 and 20.



### 3.8.4. Image classification and accuracy assessment

The clusters resulting from the two datasets are shown in Figure 3.9. The number of classes resulting from the classification was equal to seven for both study sites, resulting from the silhouette analysis, which defined k parameter setting.

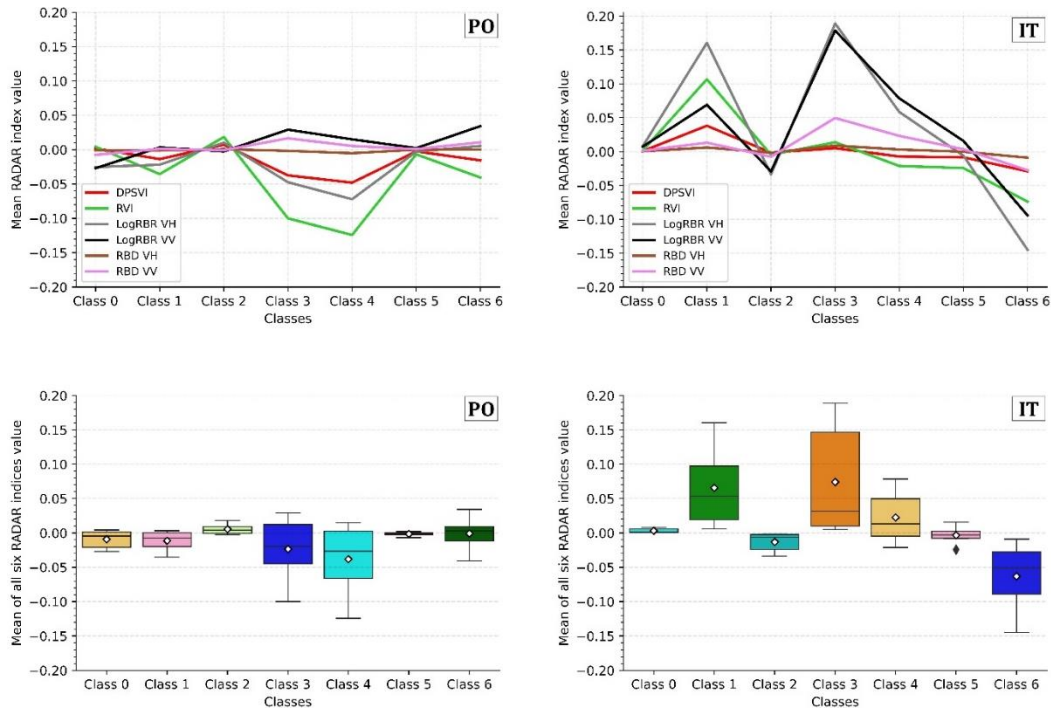


**Figure 3.9.** Classification results, showing the seven classes for both study areas. The blue clusters (classes 3-4 in the PO, and 6 in IT) represent the burned areas' classes.

From a first visual interpretation of the entire classified maps, the association between the resulting classes and the burned areas is evident if these are visually compared with the radar indices of Figures 3.3 and 3.4.

Figure 3.10 shows the distribution of the mean value of each of the six radar indices for each class (at the top). At the bottom is showed the mean of all the six indices for each class. For the PO study site, the RBD (both polarisations) and the LogRBR\_VV maintain stable behaviour for all classes and do not allow class discrimination. The LogRBR\_VV shows a slight increase in classes 3, 4 and 6, while the RBD\_VV in classes 3 and 4. The other three indices clearly show different behaviour in classes 3 and 4 with lower values, especially observing the RVI and observing the IT plots, the LogRBR (both polarisation), and the RVI lower value in class 6. Classes 1 and 3

are characterised by a positive peak given by some indices: DPSVI, RVI, LogRBR\_VH-VV and RBD\_VV, respectively. Also, in this case, the RBD\_VH had stable behaviour between the classes.



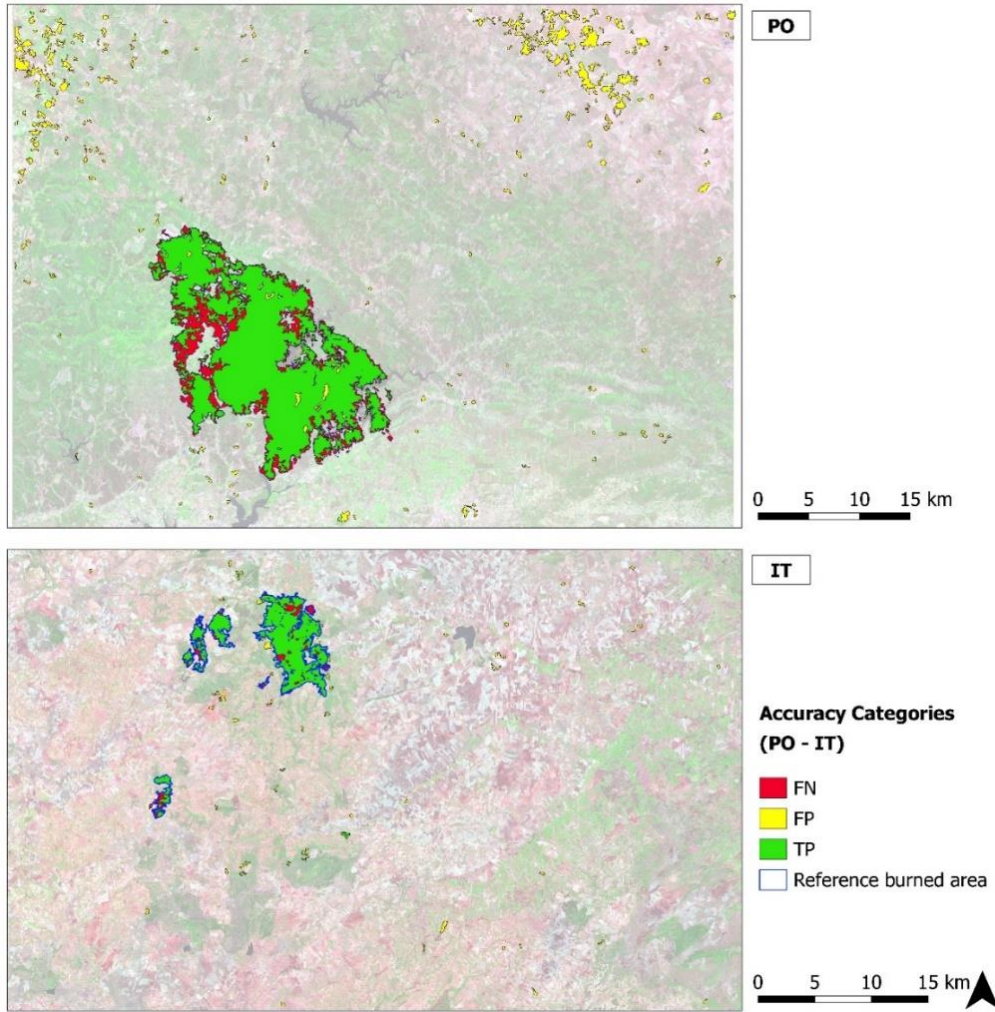
**Figure 3.10.** The figure shows the distribution of the mean value of each radar index across all six classes for both study sites (PO and IT) (at the top). At the bottom, boxplots of indices values for each class are reported (the white rhombus marker indicates the mean values).

In Figure 3.10, it is possible to clearly distinguish the classes that have lower and negative values and a mean below -0.02 for both study sites. Since we are using temporal difference indices, we assume that classes 3, 4 (PO) and 6 (IT) represent the burned areas. In total, considering only these fire-related classes, they covered an area equal to 300.10 km<sup>2</sup> in PO (classes 3 and 4 together) and 51.59 km<sup>2</sup> in IT (class 6). However, we noted the presence of several small areas distributed over all the scenes. For this reason, all the single clusters with a size less or equal than 0.05 km<sup>2</sup> belonging to the fire-related classes were excluded. This threshold corresponds to the minimum mapping unit of the reference data used in the accuracy assessment. The remaining filtered burned clusters covered an area of 269.67 km<sup>2</sup> in PO and 43.28 km<sup>2</sup> in IT.

**Table 3.3.** Distribution of each dataset's pixels and the three accuracy categories (true positive, TP; false negative, FN; false positive, FP) for both study sites (PO and IT).

GLCM Features	PO	IT
TP	80.47 %	85.57 %
FP	19.95 %	14.94 %
FN	19.53 %	14.43 %

A visual overview showing the spatial distribution of the accuracy assessment categories (TP, green; FP, yellow; FN, red) is presented in Figure 3.11 for both study areas. In the same figure, the perimeter of the S-2 based reference burned area, used for accuracy assessment, has been superimposed (blue border).



**Figure 3.11.** The maps show the spatial distribution of the three accuracy categories, true positive (TP, green), false positive (FP, yellow), false negative (FN), for IT and PO study sites, using the reference layer (blue) derived from S-2 data.

The  $r$ ,  $p$  and  $F$ -score accuracy metrics were calculated. The results show that the highest values for  $p$  and  $r$  and the  $F$ -score were reached by the IT classification, with 0.0851, 0.0856 and 0.853, respectively, compared to those produced by the PO dataset, which are 0.805, 0.801 and 0.803, respectively.

### 3.9. Discussion

#### 3.9.1. SAR dataset and indices

SAR data entails a more complicated extraction, management and understanding of the extracted information. Compared to the generally more stable accuracy performance of optical data, under optimal time conditions, it must be considered that the research on these is much more consolidated over time, and numerous methodologies of analysis and optimisations have been developed (Chuvieco et al., 2019; Pereira et al., 1999; Meng et al., 2017; Tanase et al., 2020; Miller et al., 2007; De Santis et al., 2009; Fornacca et al., 2018; Filipponi et al., 2018;

Fernández-Manso et al., 2016). Tanase et al. (2020) also stated that the development of methodologies for detecting burned areas from SAR sensors is infancy compared to the optical sensors. Further contributions in this field could improve the results. Some studies using deep learning with SAR data, have already shown that accuracy can be high (Ban et al., 2020). We consider that the two types of data should be used as complementary to fill each other's gaps and optimise their usage potential (Lehmann et al., 2015; Stroppiana et al., 2015; Lasko, 2019).

Concerning the number and dates of images used, we have decided to include approximately one month before and one month after the event, represented, in this case, by the more drastic months of the summer fire season (July and August). Since the events under study did not occur precisely on August 1st, this resulted in a different number of pre- and post-fire images. We have not included additional images (i.e., from September) to avoid rain interference, which would have involved further analyses in interpreting the noise. The imbalance in the number of pre- and post-fire images may affect their time average, an issue not explored in the present study. Nevertheless, even with a small number of post-fire images, the aim of reducing speckle noise has been fulfilled.

This study aimed to test and establish the workflow's functionality, focusing mainly on extracting valid and useful information from the SAR data. The approach has been applied only to two regions of the Mediterranean, presenting similar vegetation, climate, and latitude. If further tested and optimised, this method could be easily applicable and with good results, at least in the Mediterranean environments.

The S-1 radar indices (Equations 3.3, 3.4, 3.7, and 3.8), calculated from the time-averaged data layers and for both study sites (PO and IT), present a well-defined area of low backscatter (darker area), indicative of the fire occurrence. This is in agreement with several research works (e.g., Belenguer-Plomer et al., 2019; Carreiras et al., 2020; Imperatore et al., 2017; Tanase et al., 2015, 2010; Zhang et al., 2019) that show how a progressive fall in the cross-polarised intensity of the radar backscatter is always observed after a forest fire. This is related to the forest structure's loss, leading to a less reflection of the C-band signal (Carreiras et al., 2020; Chuvieco et al., 2019; Donezar et al., 2019; Imperatore et al., 2017; Kurum, 2015; Pepe et al., 2018; Santi et al., 2017; Tanase et al., 2010, 2011, 2020, 2015; Zhang et al., 2019), and the soil changes following the fire occurrence (Hachani et al., 2019; Kurum, 2015; Martinis et al., 2017; Ruiz-Ramos et al., 2018; Tanase et al., 2010).

A clear difference is observed in the PO study site in the co-polarised indices (RBD and LogRBR) obtained from VV polarisation. The corresponding burned areas are represented by lighter pixels (higher backscatter), but in any case, always distinguishable from the rest of the scene. This is partly observable in the upper plots of Figure 3.10. However, it must be taken into account that they represent the classes deriving from the classification and therefore affected by commission and omission errors. This particularity is not observed in the IT study site, demonstrating a different property of the signal from each polarisation and the possibility of having a different result, depending on a multitude of local conditions as stated in several studies (Belenguer-Plomer et al., 2019; Donezar et al., 2019; Imperatore et al., 2017; Tanase et al., 2010). This is because polarisations have a different interaction with vegetation scattering components based on their size and space orientation. Standing vertical tree trunks depolarise the incoming waves with different strengths than branches or leaves (Flores et al., 2019). The total backscatter coefficient from vegetation surface is the combination of the scattering components given by the volume of the stand, by the volume of the soil, and the combination of these two (Richards J.A., 2009; Flores et al., 2019). The backscatter from co-polarisation is typically stronger for rough surface scattering components (e.g., bare ground). The cross-polarised backscatter from vegetation is associated with the distribution of volume scatterers from leaves and small branches (Flores et al., 2019; Carreiras et al., 2020). So, the cross-polarised backscatter coefficient has



higher sensitivity for volume changes, decreasing with the increase of burn severity at all frequencies due to the destruction of the canopy volume component (Tanase et al., 2010; Imperatore et al., 2017; Carreiras et al., 2020). The co-polarised signal VV is not so markedly affected by the loss of the canopy components but is affected by greater exposure of the underlying soil after the destruction of the canopy. As hypothesised by other studies (Tanase et al., 2010; Imperatore et al., 2017), this can result in a different and opposite behaviour compared to the cross-polarised signal, with an increase in backscattering. The sensitivity of the signal to the vegetation structure also depends on the wavelength. It determines the signal's penetration capacity (the longer the band, the lower the frequency, the more the radar waves can penetrate the canopy of trees) and diffusion from the smaller or larger woody components of the forest. Therefore, it affects the degree of interaction of the signal with the underlying components such as the soil, whose contribution increases after disastrous events such as a fire (Saatchi et al., 2016; Hosseini et al., 2017; Flores et al., 2019). The combined use of both polarisations, using dual-polarimetric difference indices ( $\Delta RVI$ ,  $\Delta DPSVI$ ), represents an effective tool for integrating the information. In general, the use of both polarisations (VV, VH) allows capturing the volume and structure variability of different sizes and orientations of the vegetation (Flores et al., 2019). Polarisation impacts differently how each element of the surface affects the backscatter. Therefore, the use of combined polarisation can help improve the retrieval of more information (Santi et al., 2019; Tanase et al., 2014), and it has already been shown how polarimetric data have high sensitivity towards changes in vegetation conditions (Engelbrecht et al., 2017; Chang et al., 2018; Mandal et al., 2020). Chen et al. (2018) show how indices that combine cross- and co-polarised bands had better performance than single-polarisation when used to map post-fire regrowth in different recovery intervention conditions. Plank et al. (2019) investigated the different behaviours of the quad-polarimetric L-band SAR backscatter properties during active fire and post-fire conditions. Moreover, a series of polarimetric decomposition procedures, including the RVI index, were computed to map the burned scar with an overall accuracy similar to the one we obtained in this research. Martinins et al. (2016) used several dual- and quad polarimetric L-band indices for monitoring forest degradation after the fire, demonstrating that these are very sensitive to forest structure and its modifications. However, none of them was able to discriminate between the intermediate levels of degradation. Dos Santos et al. (2013) show that L-band polarimetric indices can be applied to quantify and monitor the carbon stocks in the tropical forest affected by the fire. Other studies investigated the capability of dominant scattering mechanisms in fully-polarimetric data to detect burned areas using polarimetric decompositions models (Engelbrecht et al., 2017; Goodnough et al., 2011; Czuchlewski et al., 2005; Martins et al., 2016; Tanase et al., 2014). All those researches obtained high accuracy values, demonstrating that polarimetric data increase SAR measurement sensitivity for scar detection and classification.

Although the potential of polarimetric indices and backscatter decomposition models has been proven in these mentioned research, some of these dealt with the L-band use (Chen et al., 2018; Plank et al., 2019; Martins et al., 2016; Dos Santos et al., 2013). Our research is the first to deal with  $\Delta RVI$  and  $DPSVI$  in mapping burned areas using S-1 C band data to our best knowledge. Therefore, more research should be carried out to investigate this issue deeply.

### ***3.9.2. GLCM texture extraction and PCA transformation***

For GLCM texture calculation, the square processing window size is crucial since it defines the number of neighbour pixels used for texture calculations (Coburn et al. 2004). GLCM analysis results largely depend on the

relationship between the processing window's size and the objects' size and variability across the image (Coburn et al. 2004).

Several studies confirmed that small sizes could miss important information for texture characterisation, failing to capture enough surface patterns, while too large windows could introduce systematic errors (Dorigo et al. 2012; Hall-Beyer et al., 2017; Coburn et al. 2004; Franklin et al., 2020; Murray et al. 2010; Caridade et al. 2008). This last hypothesis occurs when the window is too large, overlapping more land-use class edges (Franklin et al., 2000; Dorigo et al., 2012). Coburn et al. (2004) and Murray et al. (2010) demonstrated that using medium-high window size (between 7x7 and 15x15 pixels), there are improvements in the overall accuracy. In our case, small fires (i.e., less than 0.5 km<sup>2</sup>) were not considered. Moreover, given our research's purpose (i.e., a binary detection of burned/not burned areas), delta indices are useful, considering that they highlight only those areas where changes occurred. Indeed, these indices do not provide any information on the actual land use cover. We fixed the window size to 11x11 pixels following these considerations and based on Muthukumarasamy et al. (2019) research aimed at land cover classification using S-1 and S-2 data. However, if small and scattered burned areas have to be mapped, smaller window sizes should be considered. Similar consideration could be addressed about the window size used for the spatial averaging in each image of the time-series in multitemporal speckle filtering (Quegan et al., 2000).

The datasets transformed and reduced by the PCA can be considered an optimal representation subset of the original ones. On the one hand, it maintains the most useful information in a few layers, speeding up the calculation process. On the other hand, the linear transformation performed on the original images, as a function of the maximum variance expressed, created new, improved imagery, able to discriminate better the changes caused by the fire, and therefore, optimising the unsupervised classification, as already pointed out by Gimeno et al. (2004). The first PC represents the maximum proportion of the original dataset variance (Fung and Ledrew, 1987). In our case, we used the first PCs obtained that explained a cumulative variance larger than 99%, which revealed with high contrast the area affected by the fire. This aspect is important so that the various characteristics of the scene can be circumscribed and classified within the various classes, directly influencing the values obtained in subsequent analyses.

### **3.9.3. *k-means classification and accuracy assessment***

The silhouette score in the preliminary choice of the most suitable number of clusters has solved the well-known problem of parameter setting that allowed reducing the algorithm's implementation time, i.e., avoiding a series of trial-and-error tests. It is evident from the graphs shown in Figures 7 and 8 that for lower  $k$  values (<10), the silhouette score and, therefore, the clusters' separation is more significant. A value of 7 seemed to be optimal to discriminate the various areas that characterized the scene, which was an expression of the different surface change levels.

The  $k$ -means unsupervised classification was applied to the transformed dataset (PCs) to discriminate the burned areas without having prior knowledge of the characteristics and the number of classes characterising the surface background. Although the easy to use and speed execution time characterising the standard  $k$ -means algorithm has been widely recognised (Nagpal et al., 2013), extensions like the  $k$ -means++ (Arthur and Vassilvitskii, 2007) improved the reliability of the obtained classifications. Indeed, the standard  $k$ -means algorithm is very prone to the different numerical distribution of the individual layers' values, making up the datasets, to the so-called outliers with extreme values. The choice of a centroid is generally random in this algorithm, leading to the definition of

always different centroids, even in identical and repeated conditions, limiting the results' repeatability. Therefore, all data must be reported on the same scale. In our case, a normalisation (Eq. 3.9) of all layers values in the range [0, 1] has been carried out. Normalisation is a crucial step when the different input data have different values range. However, although MinMax normalisation is one of the most common ways to rescale the data, it keeps all the data values, including any outliers that can influence the result (Kandanaarachchi et al. 2020). These are very different values from the rest of the other data values, and the k-means algorithm is sensitive to them, affecting its performance (Gan et al., 2017; Hautamäki et al., 2005). These arise from common noise or errors in remotely sensed data (Liu et al., 2017) with anomalous values concerning the surrounding pixels (Alvera-Azcárate et al., 2012). Several methods of outliers detection and correction are present in the literature for general data analysis (Kandanaarachchi et al. 2020, Campos et al. 2016, Angelov et al. 2019, Gan et al. 2017, Hautamäki et al. 2005) and specific remote sensing contexts (Liu et al. 2017, Alvera-Azcárate et al. 2012). Gan et al. (2017) reported a series of related work concerning outliers detection, dedicated to cluster analysis and specific to the k-means algorithm. Given the good results of the first test of the classification, this topic has not been addressed in this study case, but it could be further investigated in future work developments.

Since the quality of the final clustering results depends on the arbitrary selection of initial centroid (Dhanachandra et al., 2015), the *k-means++* (Arthur and Vassilvitskii, 2007), and implemented in the scikit-learn module, optimise the standard *k-means* algorithm by choosing the initial cluster centroids basing on the weighted distribution probability metric and only the first centroid is randomly selected. This seeding method yields a better performing algorithm and consistently finds a better clustering with lower resources than the standard *k-means* (Arthur and Vassilvitskii, 2007).

To estimate SAR S-1 data accuracy in detecting burned areas, the classified maps were compared to the relative reference burned area obtained from S-2 images. From a first visual assessment of the classified maps (Figure 11), the 3, 4 (in IT) and 6 (in PO) classes seem to have detected a large part of the relative affected area, a condition confirmed by observing TPs' distribution in Figure 10. Nevertheless, the *F-score*, *p* and *r* accuracy metrics are those that give an analytic and objective picture of the classification algorithm performance (Modica et al., 2020; Shufelt, 1999). The results indicated a satisfying global accuracy, represented by the *F-score*, for both the study sites, similar to other works using only the SAR data (Belenguer-Plomer et al., 2019; Carreiras et al., 2020; Donezar et al., 2019; Gimeno et al., 2004; Gimeno and San-Miguel-Ayanz, 2004; Lasaponara and Tucci, 2019; Zhang et al., 2019; Goodnough et al., 2011).

However, some commission and omission errors occurred. It should be noted that the omission and commission errors, represented by the opposite of *r* and *p*, respectively, presented similar values in both study sites. Figure 10 shows how most FPs are located in scattered areas throughout the scene and probably represented by local surface changing conditions (i.e., topography, roughness, humidity, local incidence angle) affecting the backscatter signal (Belenguer-Plomer et al., 2019; Donezar et al., 2019; Gimeno et al., 2004; Gimeno and San-Miguel-Ayanz, 2004; Kurum, 2015). Concerning the effects of the terrain conformation and the sensor geometry, these were attenuated by using images deriving from both ascending and descending orbits (Tab. 1), allowing to observe the burned surfaces from multiple angles of incidence of radar beams. This is due to the reliefs' topographic characteristics that determine the radar beam's local incident angle, which plays a fundamental role in the radiometric radar response of the surface (Gimeno and San-Miguel-Ayanz, 2004; Kurum, 2015; Tanase et al., 2010). Also, Donezar et al. (2019) observed how the low detection of some burned areas could be since orography overshadowed these

areas facing the side opposite the radar beam, while this problem did not occur when using images of both orbits. This increases the chance that a burned surface that was shadowed in one image would be illuminated on another. The same behaviour was observed in Sayedain et al. (2020), where the use of both ascending and descending orbit directions improved the accuracy of land use classification with S-1 data.

Still, regarding the commission errors, it is necessary to consider the variations inherent in the observed scenario within the time considered from the first pre-fire acquisition date to the last post-fire image date. During this time-frame, other environmental and agricultural changes could also occur. More investigations should be carried out in these contexts. Taking these critical aspects into account, the time-series on which the backscatter was averaged has probably contributed to producing a better result, reducing the intrinsic noises of the radar data (Lasaponara and Tucci, 2019). Obviously, previous knowledge of the meteorological conditions present at the date of image acquisition must be taken into account to select an optimal time series or possibly consider the effects of rains (Gimeno et al., 2004). The multitemporal Lee filter's use allowed further reduction of the noise and amalgamated pixels with different intensities to be similar to their neighbours, thus eliminating small isolated regions (Imperatore et al., 2017).

#### **3.9.4. *Advantages and shortcomings of the implemented workflow***

The use of specific Python-based libraries allowed us to build a complete workflow and enclose it in a single script. Furthermore, the use of Python scripts offers the repeatability of the proposed model with high flexibility, allowing any further improvement (e.g., more reliable classification algorithm) with only small script changes. The process is not entirely automatic. Many steps require the user's intervention, such as the imagery selection and the analysis of the results for clusters related to the burned areas. However, the availability of free and open-source software dedicated to remote sensing image processing such as ESA snappy allow connecting the first pre-processing steps to a large number of free toolkits and libraries for exploration, in-depth analysis, data processing, implementing advanced algorithms and graphics (Hao and Ho, 2019; Pedregosa et al., 2011).

The main advantages of the approach developed here were related to (i) self-adaptation to local scattering conditions without the need for a priori information of the observed area; (ii) total free and open-source based workflow, from satellite data to the libraries used in the processing; (iii) possibility of adaptation and interchangeability of parts of the Python-based script (essential for custom improvements); (iv) ability to detect burnt areas during the summer period in territories with heterogeneous vegetation and topographical characteristics, typical in the Mediterranean environment. On the other hand, the main limitations concerned: (i) the misclassification of non-fire related modifications; (ii) dependence of accuracy on variables influencing radar scattering processes (e.g., type of ecosystem, topography). Therefore, there is a need for further improvements to reduce these limitations.

### **3.10. Conclusions and recommendations**

Our study showed the potential of the implemented approach, based on Sentinel-1 SAR data, for semi-automated and accurate detection of burned areas in Mediterranean contexts, which is the first and necessary operational step for any subsequent investigations the disturbing effects on vegetation and the environment. This sensor showed to be sensitive to fire-induced changes, and this has been enhanced through the use of radar difference indices. In particular, the dual-polarimetric vegetation indices, RVI and DPSVI, used as differences between pre- and post-



event ( $\Delta$ ), have never been used to the best of our knowledge for this purpose with S-1 data. Therefore, more investigation will have to be done to find out more about their behaviour. It could be interesting to study these two for the medium and long-term monitoring of post-fire effects and vegetative dynamics.

The pre-processing approaches adopted have made it possible to reduce the adverse geometric and radiometric effects of sensor characteristics and local surface conditions (topography, roughness, humidity, local incidence angle, etc.). These factors mentioned above are those that most affect the backscatter signal. Meanwhile, the combination of using a time-average of the pre- and post-fire time series with a multitemporal speckle-filter can reduce the intrinsic speckle noise of the SAR data. The PCA analysis, reducing the amount of data deriving from pre-processing steps, allowing to decrease the time and computational resources requesting.

Our findings confirm the reliability of open-source and Python-based processing solutions. On the one hand, they allow building an almost complete processing and analysis workflow, with a high degree of interchangeability and flexibility in the choice of components. On the other hand, they offer full repeatability when similar conditions arise or partially repeatability, in this case, using some parts of a process even if some steps requires user intervention.

The research was conducted in two Mediterranean areas with similar environmental characteristics, located in different countries, to test the operability of the methodological workflow and its various components. Future developments may involve testing our approach over larger study areas affected by large and small fires in order to assess the impact of the spatial pattern of burned areas on the classification accuracy. It is also planned to improve some workflow components, such as the use of other radar indices or the use of more robust machine learning techniques, to minimise the presence of commission errors, resulting from signal confusion between burned areas and other land cover types.

## 4. Regional-scale detection of burned area using a multicomposite process and GEOBIA

Adapted from

De Luca, G., Silva, J.M.N., Modica, G.: *Regional-scale burned area mapping in Mediterranean regions based on the multitemporal composite integration of Sentinel-1 and Sentinel-2 data*. *GIScience Remote Sens.* 59, 1678–1705 (2022). <https://doi.org/10.1080/15481603.2022.2128251>.

GISCIENCE & REMOTE SENSING  
2022, VOL. 59, NO. 1, 1678–1705  
<https://doi.org/10.1080/15481603.2022.2128251>



RESEARCH ARTICLE

OPEN ACCESS

### Regional-scale burned area mapping in Mediterranean regions based on the multitemporal composite integration of Sentinel-1 and Sentinel-2 data

Giandomenico De Luca <sup>a</sup>, João M. N. Silva <sup>b</sup> and Giuseppe Modica <sup>a</sup>

<sup>a</sup>Dipartimento di Agraria, Università degli Studi Mediterranea di Reggio Calabria, Località Feo di Vito, I-89122 Reggio Calabria, Italy; <sup>b</sup>Forest Research Centre, School of Agriculture, University of Lisbon, Tapada da Ajuda, 1349-017 Lisboa, Portugal

#### ABSTRACT

Wildland fires are among the main factors affecting the surrounding territory in terms of ecological and socioeconomic changes at different temporal and spatial scales. In the Mediterranean environment, although fire can positively influence some bio-physical dynamics of habitats, it acts as a pressing disturbance on ecosystems when the severity, spatial scale, and/or frequency are high, thereby determining their degradation. Therefore, knowing and mapping the accurate quantitative spatial distribution of all areas affected by fire during an entire high-frequency fire season and on a relatively large scale (regional/national scale) is an essential step to initialize the numerous subsequent effect monitoring analyses that can be carried out. This work proposes a reliable and open-access workflow to map burned areas on regional and national scales during the entire fire season. To achieve this, we integrated optical (Sentinel-2, S2) and Synthetic Aperture Radar (SAR; Sentinel-1, S1) free high spatial and temporal resolution data into a multitemporal composite criterion. Open-source software and Python-based libraries were used to develop the workflow. In particular, the second-lowest near infra-red (NIR) image composite (secMinNIR) criterion, based on the retrieval of the second minimum values that the NIR values reached in each pixel during the entire time frame considered, was applied to cloud-free S2 imagery to optimize the separability between burned and unburned areas. Subsequently, a second temporal composite criterion was developed and applied to the S1 time series, relying on the SAR capacity to detect vegetation fire-induced structural and humidity changes. It was based on retrieving the S1 pixel value of the first next (or the same) date to the corresponding date of the pixel value previously found by secMinNIR. The burned area map was created using an object-based geographic analysis (GEOBIA) process, using two optical and SAR composite images as input layers. The large-scale mean-shift (LSMS) algorithm was employed to segment the image, while the random forest (RF) classifier was the machine-learning model used to perform supervised classification. GEOBIA-based burned area classification was also performed using only the optical composite. The resulting accuracy values were compared using the precision (p), recall (r), and F-score accuracy metrics. The classification achieved high accuracy levels (F-score value greater than 0.9) in both cases (S1+ S2, 0.956; S2, 0.914), highlighting the increased effectiveness of this approach in detecting burned areas, heterogeneous in terms of amplitude, and affected site-specific characteristics that occurred during the fire season. Although the use of only optical data is sufficient to map the fire-affected areas early, some commission errors, represented by small regions scattered over the entire study area, remain, proving that the integration of SAR data improves the quality of the obtained results.

#### ARTICLE HISTORY

Received 1 March 2022  
Accepted 13 September 2022

#### KEYWORDS

Wildland fires; geographic object-based image analysis (GEOBIA); Orfeo toolbox (OTB); random forest (RF) classifier; multitemporal composite integration; sentinel-1 and sentinel-2

Remote sensing techniques and optical satellite imagery have been extensively used for burned area detection on a regional/national scale (Barbosa et al., 1999; Crowley et al., 2019; Eva & Lambin, 1998; Filippini, 2019; Kasischke et al., 1993; Pulvirenti et al., 2020; Setzer & Pereira, 1991) and globally (Chuvieco & Martin, 1994; Chuvieco et al., 2016; Giglio et al., 2018; Knopp et al., 2020; Otón et al., 2019; Tansey, Gre, et al., 2004), promoted by the increasing availability of numerous satellite platforms and more robust algorithms and software (Chuvieco, 2009; Chuvieco et al., 2019). The efficiency of these sensors is due to the high sensitivity of the visible (VIS), near-infrared (NIR), and short-infrared (SWIR) spectral regions to changes in the surface affected by fire (Chuvieco, 2009; Chuvieco et al., 2019; Pereira et al., 1999). In the period immediately after a fire, burned vegetation presents an unequivocal spectral signature owing to the cumulative effects of the loss of green biomass,

bare soil unveiling, ash and coal presence, and temperature and moisture changes (Inoue et al., 2019; Miettinen & Liew, 2008; Pereira et al., 1999; Smith et al., 2005).

#### **4.1. The compositing criteria: principles and literature review**

Among the methodologies provided in the literature aimed at large/regional-scale burned area mapping, the multitemporal image compositing criteria enable the mapping of fires that occur at different and progressive times, such as during an entire fire season, which is adequate to maintain the spectral discrimination between unburned and burned pixels in longer timeframes (Barbosa et al., 1998; Chuvieco et al., 2005; Qi & Kerr, 1997; Sousa et al., 2003). Furthermore, several studies have demonstrated the ability of this method to deal with the influence of external factors such as clouds, cloud shadows, and high-brightness surfaces (Barbosa et al., 1998; Cabral et al., 2003; Emilio Chuvieco et al., 2005; Mayaux et al., 2000; Qi & Kerr, 1997; Sousa et al., 2003). The multitemporal compositing criteria initially proposed with the aim of optimizing land cover classification because of its capacity to maximize the spectral reflectance of healthy vegetation (Cabral et al., 2003; Holben, 1986; Qi & Kerr, 1997), have been subsequently adapted for burned area detection by numerous authors (Barbosa et al., 1998; Chuvieco et al., 2005; Fernández et al., 1997; Miettinen & Liew, 2008; Pereira et al., 2017; Pereira et al., 1999; Silva et al., 2004; Sousa et al., 2003; Tansey, Gre, et al., 2004; Tansey, Grégoire, et al., 2004). The main approaches used for land cover classification, such as the multitemporal normalized difference vegetation index (MNDVI), are unsuitable for burned surfaces because of their spectral characteristics, resulting in the worst discrimination (Chuvieco et al., 2005; Pereira et al., 1999), returning a low spectral separability between unburned and burned areas (Miettinen & Liew, 2008; Sousa et al., 2003), underestimating the results, and generating a large number of false positives (Barbosa et al., 1999; Cabral et al., 2003; Pereira et al., 2016). Other authors have improved the criteria for dealing with various artifacts. For example, the lowest reflectance value of red or short-wave infrared (SWIR) bands, coupled with the MNDVI criterion, has been used to reduce the presence of clouds in composite images, with the disadvantage of causing an increase in the presence of cloud shadows (Cabral et al., 2003; Chuvieco et al., 2005; Mayaux et al., 2000; Qi & Kerr, 1997). For these reasons, several alternative criteria have been proposed for multitemporal compositing in burn mapping. Barbosa et al. (1998), followed by other studies (Chuvieco et al., 2005; Miettinen & Liew, 2008), selected pixels with minimum NIR reflectance in the time series using low/coarse resolution satellite data, considering that burned vegetation has low reflectance in these spectral bands. The minimum NIR reflectance highlights the separability of charred fuels deposited over the ground, characterized by very low VIS and NIR reflectance, preventing the misinterpretation of clouds and vegetated areas. Therefore, burned territory unity (pixels) represents the minimum NIR value in a time series. The lowest NIR criteria produce higher separability between burned and unburned vegetation (Sousa et al., 2003). However, this emphasizes cloud shadows when used in more local-scale studies (Chuvieco et al., 2005; Pereira et al., 1999; Sousa et al., 2003) and requires supplementation with efficient cloud shadow removal approaches (Miettinen et al., 2013). Miettinen et al. (2008) evaluated several composite methods and considered the lowest value of NIR as one of the more permeants, but only if the dataset was cloud shadow masked before the process. The criteria of the third lowest NIR value selection were demonstrated to deal with this issue, achieving better performance in removing shadows. At the same time, the quality of the image and the spectral differences between vegetation covers were maintained without fine-grained spatial heterogeneity typical of other criteria (Cabral et al., 2003; Stroppiana et al., 2002). Researchers have also used the thermal infrared (TIR) band to detect burned areas (Chuvieco et al.,

2005; Miettinen & Liew, 2008; Pereira et al., 1999; Sousa et al., 2003). In fact, recently burned areas are warmer than unburned surfaces, clouds, and shadows (Pereira et al., 1999; Pereira et al., 1999). Chuvieco et al. (2005) concluded that maximizing the TIR criteria was more accurate than maximizing other NIR-based criteria. Miettinen et al. (2008) highlighted the problem of using this band, including the underestimation of smaller burned areas owing to its lower spatial resolution. When the thermal band is not available, several authors (Cabral et al., 2003; Chuvieco et al., 2005; Stroppiana et al., 2002) have suggested using the highest NIR value among the three minimum red reflectance values of the daily images because, as seen above, although minimizing NIR may be suitable, the presence of cloud shadows needs to be dealt with extra processing. This technique has been further integrated with the use of SWIR, which, similar to TIR behavior, avoids the selection of colder pixels (e.g., occupied by cloud shadows) more than NIR. Pereira et al. (2017) and Pereira et al. (2016) evaluated different criteria, the first, second, and third lowest NIR value and the maximum SWIR value among the three lowest NIR values (minNIRmaxSWIR criteria), in terms of spectral separability between burned/unburned areas and the presence of clouds and shadows. The final conclusions were that, although the lowest NIR presented higher separability between burned and unburned areas, it caused the identification of a large number of cloud shadows owing to the spectral similarity between burned vegetation and shadows at this wavelength, as also observed by Miettinen et al. (2008); the second lowest NIR criterion achieved the best results, followed by the minNIRmaxSWIR criterion, maintaining burn separability with a low incidence of cloud shadows.

#### **4.2. The opportunity for higher resolution data**

These approaches have been successfully applied for the regional to continental/global mapping of burned areas using coarser spatial resolution satellite data (e.g., NOAA/AVHRR, PROBA-V, SPOT-VEGETATION, and NASA Terra/Aqua MODIS). This could involve underestimating smaller burned areas and increasing omission errors (Roteta et al., 2019). Kasischke et al. (1993) observed that only 89.5% of burned areas larger than 20 km<sup>2</sup> were detected, without false positives, using AVHRR satellite data. An additional shortcoming of coarse-resolution data is their inability to distinguish medium/small unburned areas within the fire perimeter (unburned “islands”), representing potential areas of high biodiversity from which vegetation recovery can spread in a post-fire scenario (through speed dispersion and/or agamic regeneration) (Christopoulou et al., 2014; Meddens et al., 2016), overestimating the actual damage. The advent of sensors with increasingly better spatial and temporal resolutions has allowed the development of approaches that ensure a more accurate mapping of burned areas. Several authors have shown that using Landsat-7/8 multispectral satellite platforms (Axel, 2018; Boschetti et al., 2015; Christopoulou et al., 2014; Goodwin & Collett, 2014; Hawbaker et al., 2017; G. H. Mitri & Gitas, 2004; João M.N. Silva et al., 2019; Storey et al., 2021), high performance can also be achieved for larger burned area detection scales, improving the level of detail and accuracy obtained from coarse resolution sensors, particularly for smaller burned areas and unburned islands. Their higher temporal resolution, combined with finer spatial resolution, allowed a broad application of successful approaches based on single or multitemporal Sentinel-2 data for mapping burned areas. Recent studies have exploited the spectral endowment of sensors and the combination of derivable spectral indices (Filipponi, 2019; Knopp et al., 2020; Llorens et al., 2021; Mpakairi et al., 2020; Navarro et al., 2017; Pulvirenti et al., 2020; Roteta et al., 2019; Sali et al., 2021; Smiraglia et al., 2020; Vanderhoof et al., 2021). Multispectral Sentinel-2 data were recently integrated into the fire detection procedure adopted by the European Forest Fire Information System (EFFIS) (EFFIS Rapid Damage Assessment, 2022), thus allowing the refinement

of the map of burned areas obtained from coarser-resolution sensors and the detection of fires below 30 hectares. However, the literature lacks the use of NIR-based multitemporal composite techniques applied to the higher temporal and spatial resolution Sentinel data to optimize the mapping of burned areas.

### **4.3. Integration of SAR information**

In addition to optical data, synthetic aperture radar (SAR) active sensors have achieved good performance in burned area mapping and fire effect estimation (Belenguer-Plomer, Chuvieco, et al., 2019; De Luca, Silva, & Modica, 2021b; Donezar et al., 2019; M. Gimeno et al., 2004; Kurum, 2015; Lasaponara & Tucci, 2019; Lehmann et al., 2015; Pepe et al., 2018a; Stroppiana et al., 2015; M. Tanase et al., 2011; Mihai A. Tanase et al., 2020; P. Zhang et al., 2019). The Earth's microwave backscatter is affected by variations in the structural parts and dielectric permittivity of the surface, triggered by vegetation cover, shape, size, and orientation of the canopy scatterers, soil structure, and moisture content modifications, making it a suitable system for discriminating alterations on the Earth's surface. Factors such as wavelength, polarization, the orbit of the satellite sensor, and local topographic properties of the Earth's surface can influence the SAR backscatter (De Luca et al., 2021; Gimeno et al., 2004; Hachani et al., 2019; Imperatore et al., 2017; Kurum, 2015; Tanase et al., 2011; 2010a; 2020). Polarization is an intrinsic feature of the primary sensor that influences the behavior of the SAR signal scattered by burned vegetation. Generally, after a fire event in a Mediterranean context, characterized by drier seasons, cross-polarized backscatter [vertical-horizontal (VH) and horizontal-vertical (HV)] decreases owing to its higher sensitivity to the reduced contribution of volumetric dispersion and moisture content. In contrast, the co-polarized signal [vertical-vertical (VV) or horizontal-horizontal (HH)] might show an increased backscatter attributable to higher soil exposure after the fire event (Imperatore et al., 2017). Although several studies have confirmed this finding (Carreiras et al., 2020; De Luca et al., 2021; Ruiz-Ramos et al., 2018; Tanase et al., 2010a; 2010b), the literature shows how several different backscatter behaviors can be observed for vegetation affected by fire and influenced by local environmental variables (Ban et al., 2020; F. S. R. V. Martins et al., 2016; Stroppiana et al., 2015). Some authors have used multi-polarimetric indices to maintain the information provided by two different polarizations for various research purposes concerning environmental monitoring (Kim et al., 2012, 2014; Yunjin Kim & Van Zyl, 2009; Martins et al., 2016; Periasamy, 2018; Pipia et al., 2019; Szigarski et al., 2018; Trudel et al., 2012), including the radar vegetation index (RVI), which is one of the most widespread. De Luca et al. (2021) successfully used a dual-polarimetric RVI index to map burned areas in Mediterranean environments. Martins et al. (2016) used several dual-polarimetric SAR indices to analyze and monitor the temporal effects of fire in a Mediterranean environment.

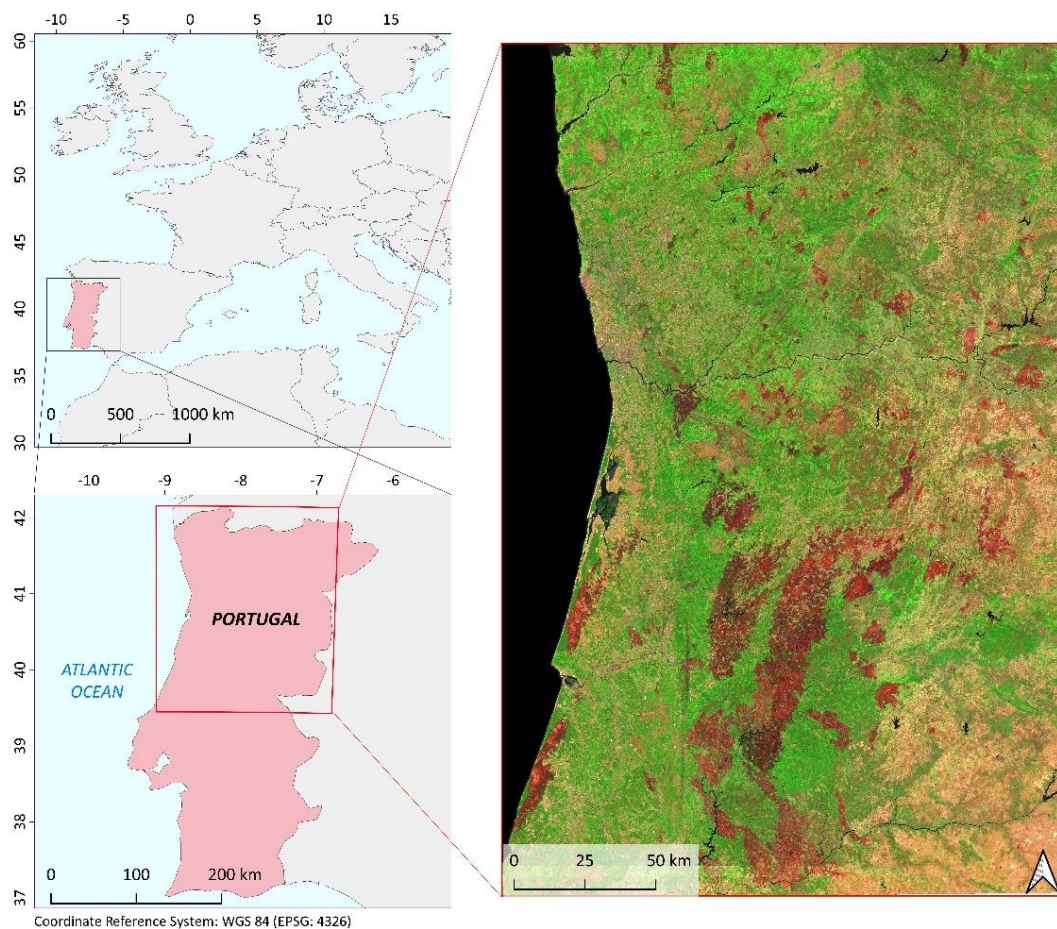
### **4.4. Aim and structure of the study**

This research maps a series of fires throughout the 2017 fire season, covering most of Portugal, using a multitemporal composite and supervised geographic object-based classification approach (GEOBIA). The main objective was to develop an open-source workflow based on optical and SAR multitemporal composite data for burned area mapping at a regional scale in Mediterranean regions, assessing the contribution of SAR data, given that most studies of burned area mapping in this region are based only on coarser optical data. Specifically, the aim and novelty of our proposed workflow rely on the following key points.

- To optimize an optical-based multitemporal composite processing criterion using higher temporal and spatial multispectral data (Sentinel-2) and integrating SAR data (Sentinel-1) to accurately map the burned areas that occurred during the entire fire season.
- To compare the accuracy of burned area maps derived from S1 and S2 data with those derived from S2 data only.
- To assess the effectiveness of GEOBIA over a large region using open-source software and freely available datasets.

#### 4.5. Study area

The analyses focused on a study area (Figure 4.1), including Portugal's northern and central parts (between the 39.5° and 42.1° parallels), expanding to 55,441.44 km<sup>2</sup>. This represented the area where major fires occurred during the exceptional fire season (June–October) of 2017 (ICNF, 2017; European Environment Agency, 2022). According to statistics provided by the Instituto da Conservação da Natureza e das Florestas (ICNF, 2017), the total burned area from January 1 to October 31 was 442,418 ha. Almost all burned areas (>95% of the national burned surface) occurred inside the present study area. The southern part of Portugal was excluded because it was unaffected by significant events (in terms of the total surface area that affected the country during the fire season analyzed). Only one large fire (defined by ICNF as a fire exceeding 100 ha) occurred outside the study area in southern Portugal.



**Figure 4.1.** Location of the burned study area in Europe (top-left), in Portugal (bottom-left). The image on the right shows the overview of the study area (Sentinel-2 composite image based on the second-lowest NIR criterion, false-color composite SWIR-NIR-RED); the red areas represent the burned surfaces.

## 4.6. Materials and methods

### 4.6.1. Satellite dataset and pre-processing

A multitemporal compositing approach was tested on different progressive fire events in the central and northern parts of Portugal during the fire season in 2017, from June to October. In Mediterranean European regions, this period is considered one of the most severe fire seasons in recent years in terms of the total area burned and environmental and civil damages (San-Miguel-Ayanz et al., 2018). The size of each event was very different, and the spatial distribution over the entire area was considered. Most of the surface (52.37 %) was affected during the fire events in October (ICNF, 2017).

#### 4.6.1.1. Sentinel-2 dataset

The S2 Level-2A (Bottom of the Atmosphere) dataset was preprocessed and downloaded using the Google Earth engine (GEE), which sped up the process considering that most parts of the images are unavailable online in the Copernicus Open Access Hub owing to the long-term policy adopted, which allows only 12 months of the online retention period of the images (Copernicus Long Term Archive Access, 2021).

Focusing on image research in the study area, the first period considered was from June 1 to November 15, 2017. Extending the image search period by a few weeks was necessary so that the number of images covering the last fire season to be analyzed was sufficient. Otherwise, applying the composite criterion could discard the last images of the fire season in which fires could be present. The number of available images for the study area with less than 7.5% cloud cover was 227. After selecting only the red (B4), NIR (B8), and SWIR (B12) bands, the latter was resampled from a 20 m to a 10 m pixel space using bilinear interpolation to relate it to the first two bands. Each of these images was grouped per day of acquisition, and, according to this, a large image mosaic for each acquisition date, covering the entire study area, was produced. The GEE *imageCollection.mosaic()* function was used for mosaicking.

On some acquisition dates, very few images were taken over the study area; therefore, some mosaics mainly consisted of unavailable pixels. These mosaics were excluded from the final dataset to reduce the time and memory process demand without affecting it. Considering this reduction, the final dataset consisted of three-monthly dates, represented by 15 image mosaics for the entire study area.

As illustrated in the following sections, the change in the detection technique between the pre- and post-fire scenes was implemented to map the burned areas. To do this, a pre-fire composite image was constructed by applying the same pre-processing steps as for the post-fire image, to the images acquired from April 1 to May 31.

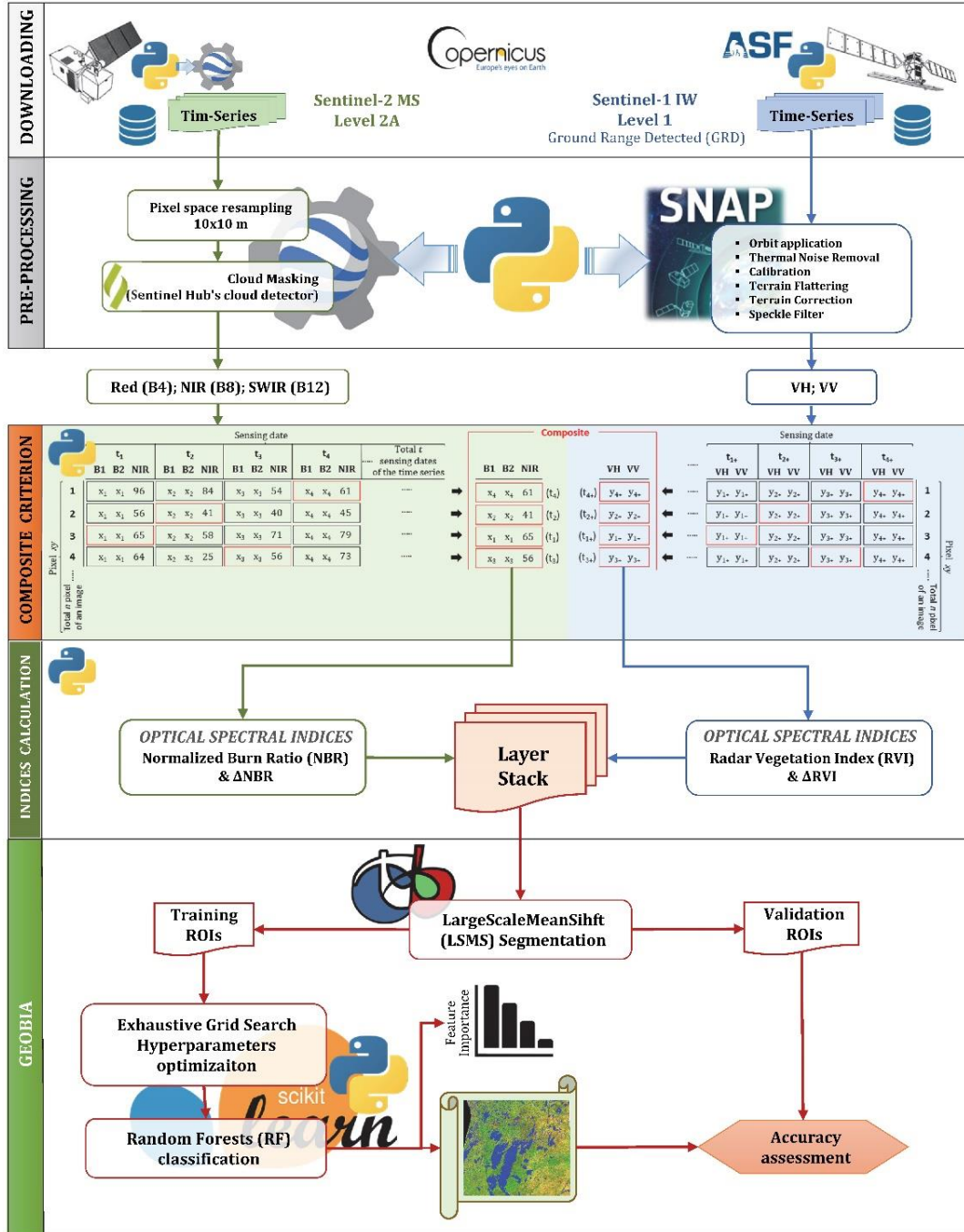
#### 4.6.1.2. Sentinel-1 dataset

The S1 images were downloaded using the Alaska Satellite Facility (ASF, 2022) interface. The S1-A/B high-resolution ground range detected (GRDH), acquired in interferometric wide (IW) mode, and dual-polarized [vertical-horizontal (VH) and vertical-vertical (VV) polarizations] were used. To cover the entire study area, 45

images of the same flight path (path 147, ascending flight direction), consisting of three images for each sensing date (15 sensing dates) and covering the same sensing period adopted for the S2 dataset, were downloaded.

The S1 pre-processing workflow commenced by applying precise orbit information and removing thermal noise. This workflow involved radiometric calibration (to beta,  $\beta^0$ , nought backscatter standard conventions) (Small, 2011) and radiometric terrain correction (RTC) processes, through which the images were radiometrically flattened and geometrically corrected using the shuttle radar topography mission (SRTM) 1 arc-second (Farr et al., 2007) digital elevation model (DEM). All S1 images were mosaicked as a function of the acquisition date, resulting in a final dataset of 15 large image mosaics covering the entire study area, and stacked, relying on the geolocation product to initialize the offset method. A multitemporal Lee filter with a  $5 \times 5$  pixel of window size was employed to reduce the speckle noise (Lee & Pottier, 2009). To align each pixel of both datasets, consisting of a 10 m space sampling, the S1 and S2 mosaic datasets were finally stacked, choosing the extent of the S1 dataset as master data for the geolocation and the bilinear as the interpolation method.





**Figure 4.2.** The flowchart illustrates the second-lowest NIR (secMinNIR) scheme, SAR criteria, and their placement within the workflow.

#### 4.6.2. Multitemporal compositing

##### 4.6.2.1. Optical (Sentinel-2) part

The second lowest NIR composite criterion (secMinNIR) (Figure 4.2) was adopted in this study for the optical dataset. Considering a time series in which each image corresponds to an acquisition date, each pixel of the final composite image contains the second-lowest value of NIR among the corresponding pixels (exactly aligned  $xy$  position in the image) of the entire image time series. For each  $xy$  pixel, the process searches for the sensing date where the pixel has the second lowest NIR value.

#### 4.6.2.2. SAR (Sentinel-1) part

To obtain an SAR composite image, information on the acquisition date of the image to which each pixel of the S2 composite belongs was created, that is, the date when the second lower value of NIR was observed. According to the literature, a fire event does not always correspond to a decrease in the SAR backscatter (Ban et al., 2020; Hosseini & McNairn, 2017; F. S. R. V. Martins et al., 2016; Stroppiana et al., 2015). In the Mediterranean environment, the results depend on different environmental (e.g., humidity and land cover) or sensory (e.g., frequency and polarization) factors (Mihai A. Tanase, Santoro, De La Riva, et al., 2010; Mihai A. Tanase, Santoro, Wegmüller, et al., 2010). This is why a similar compositing approach was not applied to the S1 data. Instead, based on the layer with the date of S2 compositing, for each pixel of the S1 data, the value recorded in the image with the first date of acquisition subsequent to the one corresponding to S2 compositing was chosen. Thus, both the optical and SAR datasets corresponded to information acquired at a similar moment. The S1 and S2 compositing procedure was written in a Python script and could be adapted to be performed on different time frames (monthly, bimonthly, during the entire fire season, etc.). In our case, the criterion was applied for the entire fire season (June-October) and, separately, for the pre-fire period (April-May).

#### 4.6.3. Object-based burned area mapping

Burned area mapping was carried out by performing supervised object-based geographic object-based image analysis (GEOBIA) classification. The large-scale mean shift (LSMS) algorithm for image segmentation (Michel et al., 2015) and random forest (RF) machine learning algorithm for classification (Breiman, 2001; Cutler et al., 2007) were used. The two methods were implemented in Orfeo tool-box v.7.0.0 (OTB) (OTB Homepage, 2021) and Scikit-learn Python library v. 0.23.1 (Pedregosa et al., 2011), respectively.

##### 4.6.3.1. Input layer creation

From the two optical bands, NIR and SWIR (B8 and B12 bands, respectively), the normalized burn ratio (NBR; eq. 4.1) for the pre- and post-fire periods was computed. From the VH and VV layers, the dual-polarized radar vegetation index (RVI; eq. 4.2) was also calculated for the pre- and post-fire periods. The differences between the post-fire and pre-fire values were computed as  $\Delta NBR$  (eq. 4.3) and  $\Delta RVI$  (eq. 4.4) to allow a change detection approach. Two datasets were created and used as inputs for segmentation and image classification. One was formed by the four layers derived from optical and SAR data (S1+S2):  $\Delta NBR$  and post-fire NBR for the optical data, and  $\Delta RVI$  and post-fire RVI as SAR layers. The second included only two optical layers (S2):  $\Delta NBR$  and post-fire NBR.

$$NBR_t = (NIR - SWIR) / (NIR + SWIR) \quad (4.1)$$

$$RVI_t = 4 \cdot VH / (VV + VH) \quad (4.2)$$

$$\Delta NBR = NBR_{postfire} - NBR_{prefire} \quad (4.3)$$

$$\Delta RVI = RVI_{postfire} - RVI_{prefire} \quad (4.4)$$

Before stacking, each layer band was normalized in the same continuous scale range [0–100] (eq. 4.5) to equalize and make them comparable as well as reduce the influence of their different scale ranges on the following segmentation process (De Luca et al., 2019b; De Luca, Silva, & Modica, 2021b):

$$X_{norm} = (X - X_{min}) / (X_{max} - X_{min}) \quad (4.5)$$

where  $X_{norm}$  is the normalized value,  $X$  is the original value, and  $X_{min}$  and  $X_{max}$  are the lower and highest pixel values of the layer band (original range), respectively.

#### 4.6.3.2. Image segmentation

The large-scale mean shift (LSMS) is a non-parametric segmentation algorithm introduced by Fukunaga and Hostetler (1975) and developed and improved by Michel et al. (2015). It is a tile-based approach, optimized for extensive and/or high-resolution imagery, comprising four successive steps: a) smoothing (filtering), for image noise reduction; b) segmentation, for image subdivision in segments; c) segment merging: for small-size segment reduction; d) vectorization: transformation in vector format, including spectral feature extraction (mean and variance). The first and second steps require setting the two parameters that most influence the final result: range radius and spatial radius. In terms of Euclidean distance, the range radius is the spectral threshold for regrouping two neighboring pixels. The spatial search distance of the neighboring pixels was set based on the spatial radius (measured in the number of pixels). While the spatial radius was set to 25, the range radius was set based on the minimum Euclidean distance between burned and unburned pixels calculated on 300 regions of interest (ROIs) (150 for burned and 150 for unburned areas) scattered over the entire study area. These ROIs, with a size of  $4 \times 4$  pixels, were chosen to cover all the most representative land covers (forest, mainly composed of native *Quercus* species, Mediterranean *Pinus* and *Eucalyptus* plantations; shrublands; pastures; agricultural orchards and crop areas), through visual interpretation supported by several ancillary pieces of information: the high spatial resolution Esri ArcGIS World Imagery map (Esri ArcGIS World Imagery, 2021) and Google Earth Satellite Imagery (Google Earth, 2021), the land use/land cover map of Portugal (Carta de Uso e Ocupação do Solo) (COS, 2018), and the official burned area map of Portugal (ICNF, 2017). The mean value of the pixels in each ROI was computed separately for each optical and/or SAR layer band. The Euclidean distance was calculated for each combined pair of mean ROI values.

The value of the 35<sup>th</sup> percentile resulting from the entire Euclidean distance list (composed of each Euclidean distance value between every combination of ROIs) was chosen as the range radius value for the smoothing step. To initialize the segmentation step, the process was repeated on the smoothed images by selecting a series of values around the 10<sup>th</sup> percentile of the Euclidean distance list calculated for the smoothed image. To finalize the parameter value set, we carried out a careful trial-and-error procedure to select a suitable range radius value for the segmentation step. The results were visually evaluated at each step of the segmentation process by using a composite optical image of the burned areas. We applied a criterion according to which the burned area was successfully segmented when it was completely “encapsulated” within one or more polygons. There must be no unburned parts in the same polygon. This approach was carried out for both datasets (S1+S2 and S2), and the final range radius parameter was set as follows: for S1+S2, 6 (smoothing) and 2 (segmentation); for S2, 12 (smoothing) and 5.8 (segmentation).

In terms of space and radiometry, segments of less than 10 pixels were merged into adjacent segments.

#### 4.6.3.3. Object-based classification

A well-known RF machine learning algorithm was implemented to classify the segments resulting from the LSMS segmentation. The training polygons were derived by selecting segments that matched the previously selected ROIs used in the segmentation step. In total, 300 training polygons were selected, with 150 for each of the two classes: unburned and burned. The mean ( $m_s$ ) and variance ( $v_s$ ) spectral data were used as spectral features to fit and predict the RF model.

The algorithm parameters were set by using the initial out-of-bag (OOB) error estimated by the RF model during the training step as a predictor of the final accuracy level. A set of values was chosen for each RF parameter, and the classification process was initiated for every possible combination of parameter values (Table 4.1). The combined values that reached the highest OOB were used in the RF model.

Finally, the Gini feature importance was computed to assess the contribution of each input spectral feature image layer to classification.

**Table 4.1.** Parameter values of the Random Forest (RF) classifier tested through an exhaustive grid search approach to set the optimal combination.

Parameter name	Values set	Description
n_estimators	100, 650, 1200, 1750, 2300, 2850, 3400, 3950, 4500, 5050, 5600, 6150, 6700, 7250, 7800, 8350, 8900, 9450, 10000	The number of trees in the RF model
max_depth	10, 20, 30, 40, 50, 60, 70, 80, 90, 100, 110, 300, 500, 800, 1000	The maximum depth of the tree
min_samples_split	2, 5, 10	The minimum number of samples required to split an internal node
min_samples_leaf	1, 2, 4	The minimum number of samples required to be at a leaf node
max_features	"auto", "None", "log2"	The number of features to consider when looking for the best split

#### 4.6.4. Accuracy assessment

The accuracy assessment was implemented using 1,000 validation sampling points distributed in the study area so that they did not overlap with the training polygons and were labeled following a stratified random approach (Congalton & Green, 2019). The official ICNF burned area map was used to initialize stratified sampling, from which 500 points were randomly distributed for each of the two classes (unburned and burned). Subsequently, the distribution of points was optimized through a careful visual assessment supported by the ancillary information already used for the training step (Esri ArcGIS World Imagery, 2021; Google Earth Homepage, 2022; COS, 2018) and by each pre- and post-fire Sentinel-2 mosaic image. In addition to avoiding the overlapping of the training polygons, this enabled the improvement of the ICNF map, namely the identification of unburned islands, which were frequently not mapped in the ICNF map. The ICNF maps of the burned area were based on field surveys and complemented with semi-automatic image classification of satellite imagery. Landsat and Sentinel-2 data from 2017 were used (ICNF, 2017). True positive (TP), false negative (FN), and false positive (FP) accuracy categories were computed using the following criteria:

- TP: the sum of burned and unburned corrected classified polygons.
- FP: when an unburned validation polygon corresponds to a polygon classified as burned.
- FN: when a burned validation polygon corresponds to a polygon classified as unburned.

Subsequently, the *precision*, *recall*, and *F-score* accuracy metrics (eqs. 4.6, 4.7, and 4.8) were computed to evaluate the accuracy of the classified map (Goutte & Gaussier, 2005; Shufelt, 1999; Sokolova et al., 2006).

$$precision = |TP| / |TP+FP| \quad (4.6)$$

$$recall = |TP| / |TP+FN| \quad (4.7)$$

$$F\text{-score} = 2 \cdot \text{precision} \cdot \text{recall} / (\text{precision} + \text{recall}) \quad (4.8)$$

#### 4.6.5. Spectral separability

Some descriptive statistics of the classified product, namely the total weighted (involving the number of pixels of each polygon) average ( $\mu_{sw}$ ) and standard deviation ( $\sigma_{sw}$ ) of the values of the spectral feature mean ( $\mu_s$ ) and variance ( $v_s$ ) of all the resulting polygons, separately for class (burned/unburned), were calculated to further investigate and characterize the resulting output.

The relationship between the differently classified polygons was further analyzed by calculating their spectral separability. The modified M-statistic (Kaufman & Remer, 1994) was implemented using the weighted average of the mean values of the spectral polygons (eq. 4.9):

$$M\text{-statistic} = |\mu_1 - \mu_2| / (\sigma_1 + \sigma_2) \quad (4.9)$$

where  $\mu_1$  and  $\mu_2$  are the weighted averages of the spectral mean values ( $\mu_{sw}$ ) for burned and unburned polygons, respectively, and  $\sigma_1 + \sigma_2$  are the weighted standard deviations of the spectral mean values ( $\sigma_{sw}$ ) for burned and unburned polygons, respectively. The spectral separability between the two targets increased with an increasing M-statistic.

## 4.7. Results

### 4.7.1. Optical multitemporal composite image

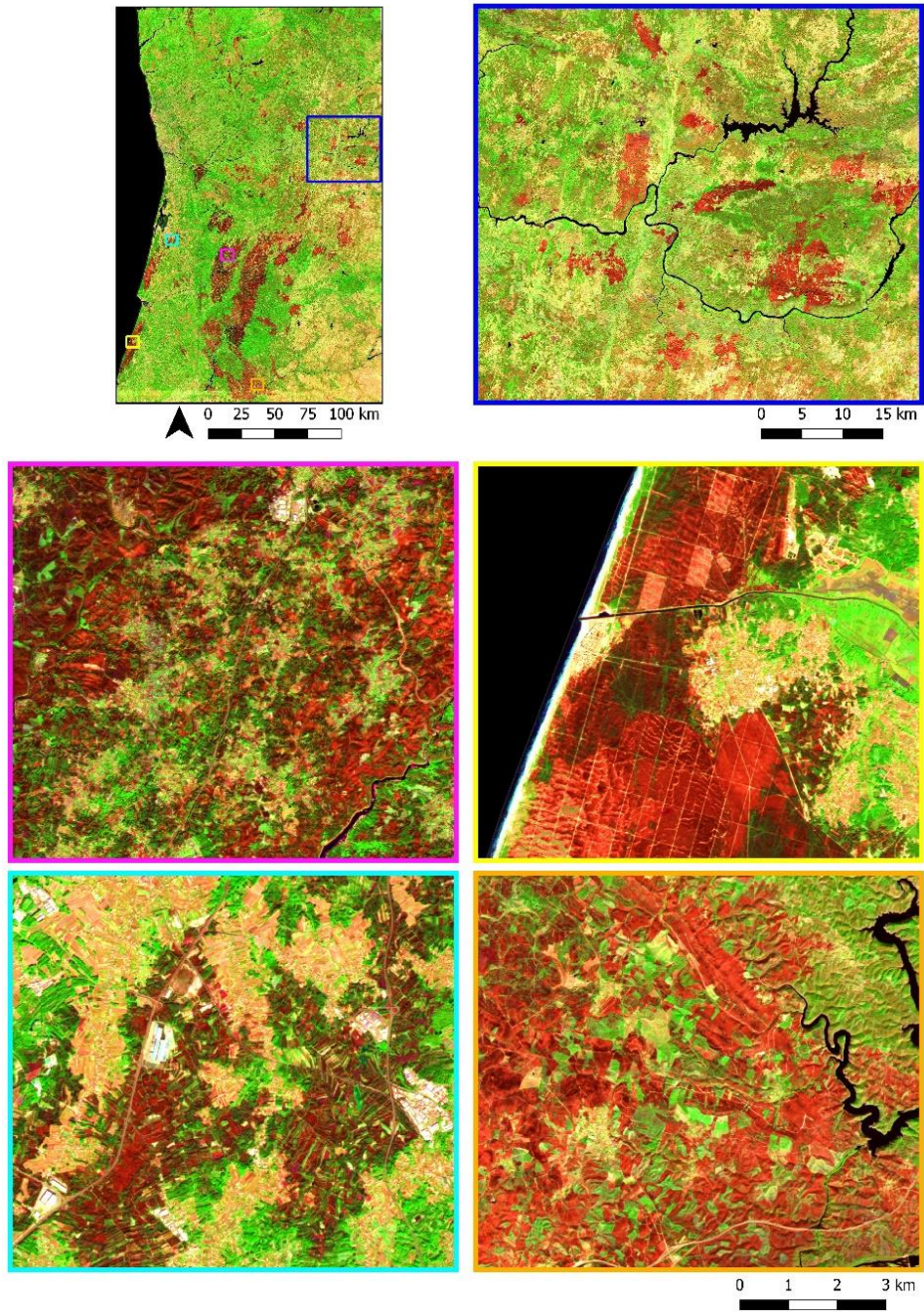
Figure 4.3 shows an overview of the multitemporal compositing for the study area and the five illustrative areas. A composite image resulting from the application of the secMinNIR criterion is shown.

This image consists of Sentinel-2 values observed on the date corresponding to the second-lowest NIR value, considering the time frame from June to October 2017. The RGB image combination (R = B12; G = B8; B = B4) highlights the areas where NIR is lower than the surrounding pixels, making them appear red. These areas are expected to represent the surfaces affected by fire events during the entire fire season.

The destruction of the vegetative part (therefore, of the chlorophyll content) involves a decrease in the reflectance of NIR, followed by a simultaneous increase in red and SWIR; the latter was caused by reduced absorption by water (Miettinen et al., 2013; Pereira et al., 1999). The  $\Delta$ NBR image, shown in Figure 4.4, was computed as the difference between the NBR composite image derived for the fire season time series (June–October) by applying the secMinNIR criterion and the NBR image derived for the time series covering the pre-fire period (April–May) by applying the same compositing criterion.

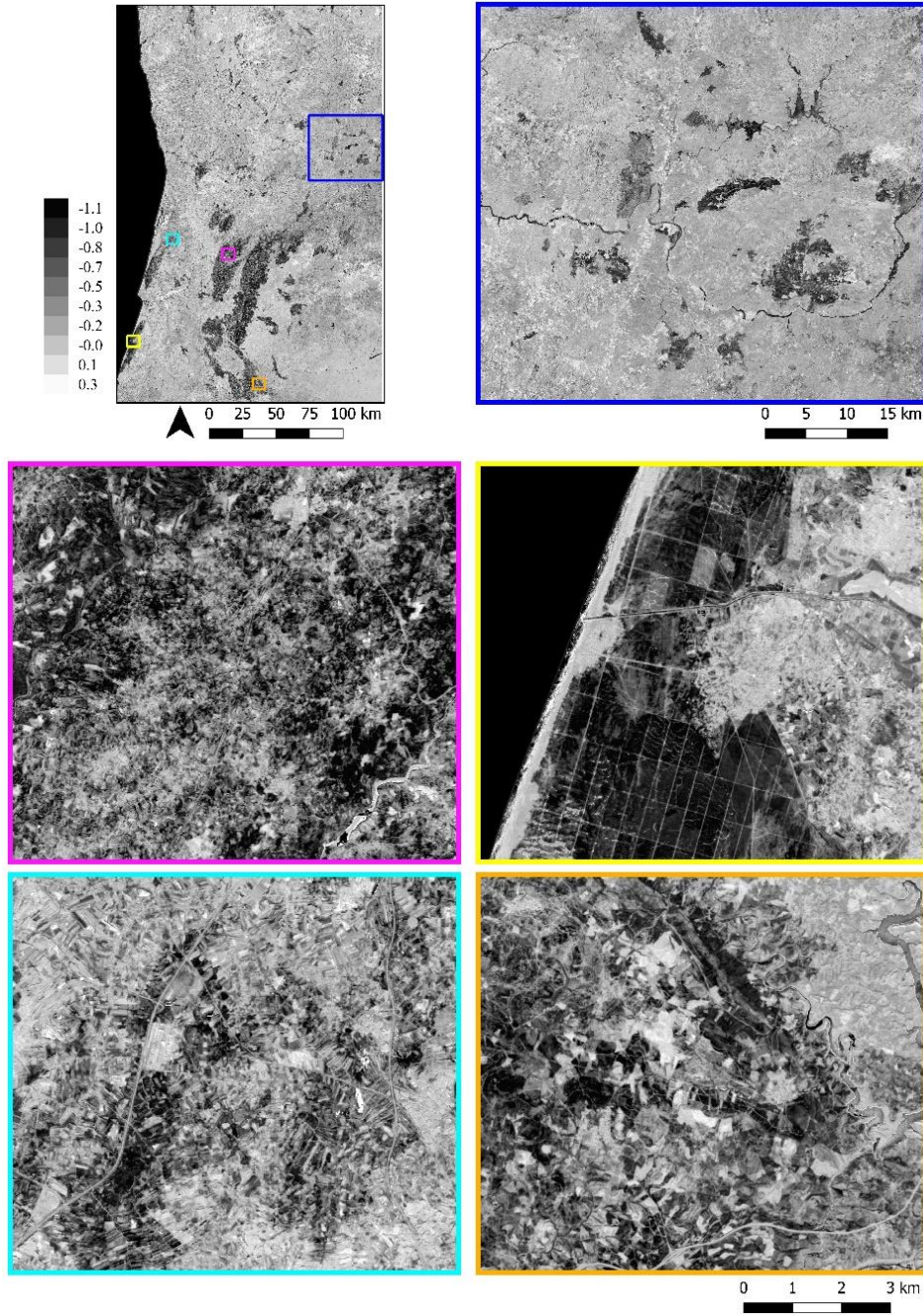
Using the “*post- less pre-fire*” formula, the darker areas in the image correspond to lower values of the  $\Delta$ NBR index, representing a high level of change between the two dates with a decline in NIR and an increase in SWIR.





**Figure 4.3.** Multitemporal composite output relative to the optical part of the dataset (Sentinel-2) that resulted from processing fire season images (June-October). Five illustrative areas are shown on a more detailed scale beside the overview of the entire study area (top left). The images are shown in RGB combination (R = B12; G = B8; B = B4).





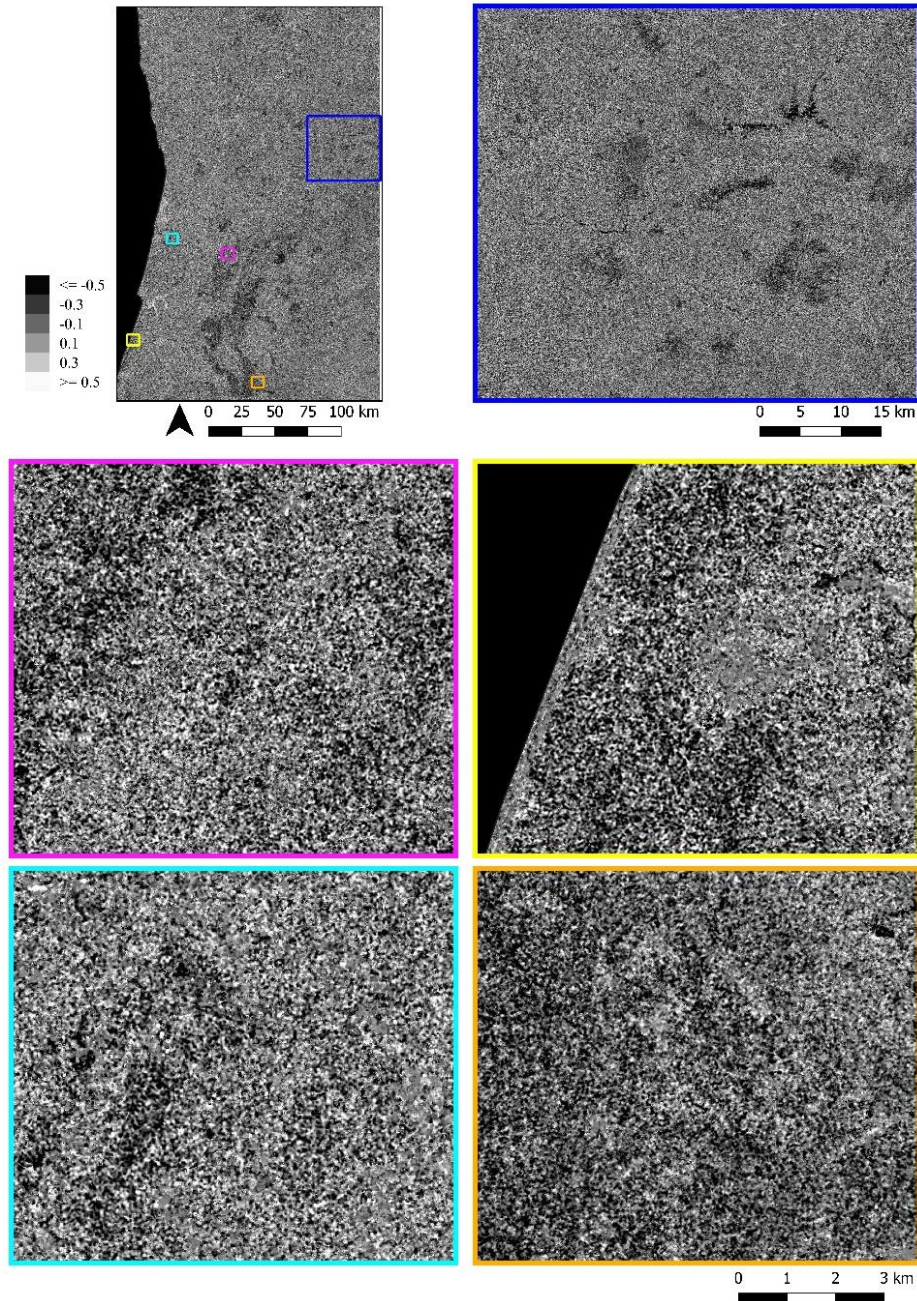
**Figure 4.4.** The Figure shows the  $\Delta\text{NBR}$  index map calculated by applying the subtraction  $\text{NBR}_{\text{post-fire}} - \text{NBR}_{\text{pre-fire}}$ . The darker areas correspond to lower index values, while the brighter pixel means represent higher values. The overview of the entire study area is shown on the top-left; five illustrative areas are shown on a more detailed scale.

#### 4.7.2. SAR multitemporal composite image

For each optical pixel chosen using the secMinNIR composite criterion, the SAR pixel with the same or the next closest acquisition date was associated with the optical data and used to create a SAR composite image for the same pre- and post-fire periods (April-May and June-October, respectively). The dual-polarized  $\Delta\text{RVI}$  derived from the VH and VV composite SAR images relative to the difference between the pre- and post-fire periods is shown in Figure 4.5. Considering the gray scalar used in Figure 4.5, the pixels tend to darken as much as the  $\Delta\text{RVI}$  value is lower, and vice versa. The datasets formed by the optical indices ( $\Delta\text{NBR}$  and  $\text{NBR}_{\text{post-fire}}$ ) and SAR indices



( $\Delta RVI$  and  $RVI_{\text{post-fire}}$ ) were segmented using the LSMS algorithm. Segmentation was performed on the S1+S2 and S2 datasets, which resulted in 2,136,807 and 2,238,504 objects, respectively. The area of the objects for the S1+S2 and S2 datasets ranged from 0.15 ha to 154,969.23 ha (mean = 2.78 ha; standard deviation = 186.40) and from 0.15 ha to 291,812.03 ha (mean = 2.81 ha; standard deviation = 265.98), respectively.



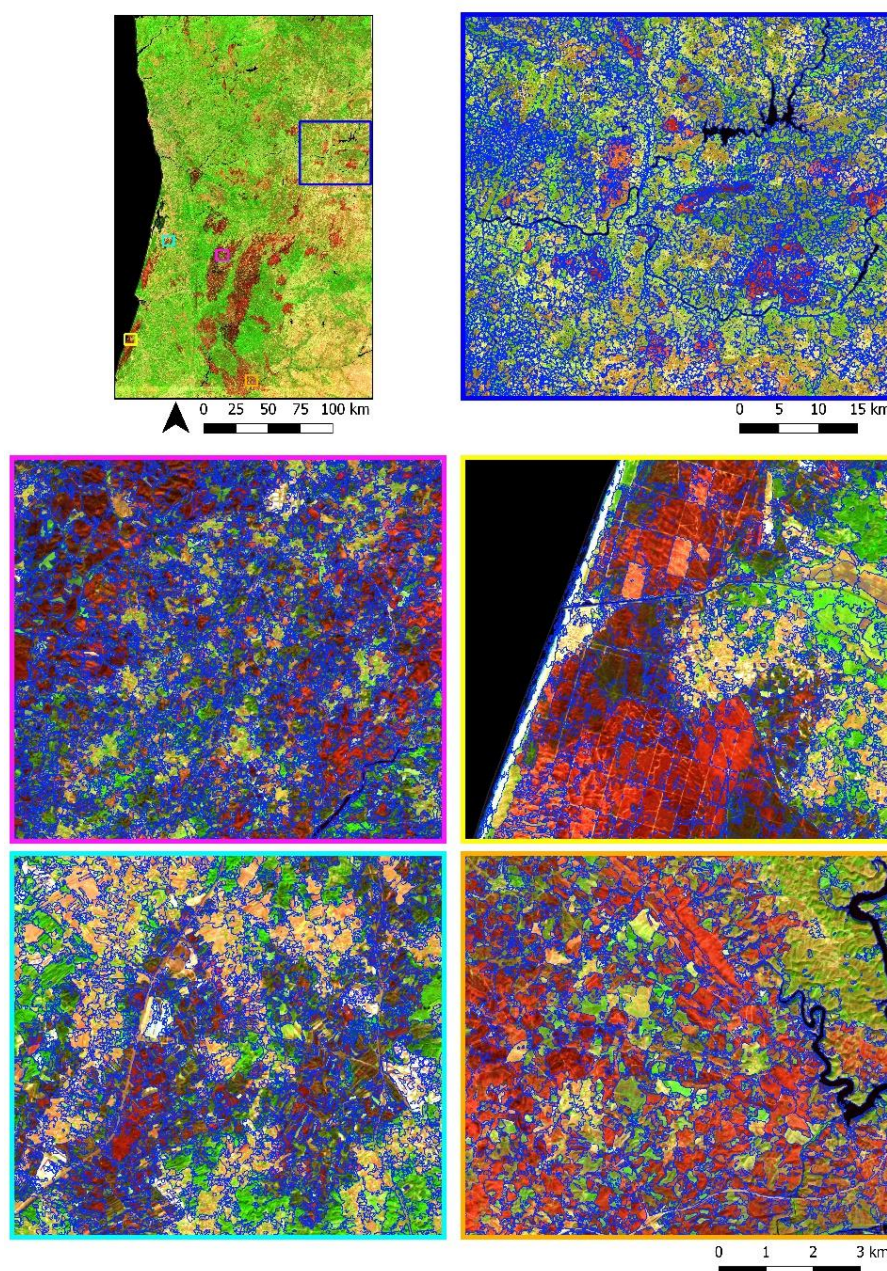
**Figure 4.5.** The  $\Delta RVI$  index map, calculated by applying the subtraction  $RVI_{\text{post-fire}} - RVI_{\text{pre-fire}}$ . The darker areas correspond to lower index values, while the brighter pixels represent higher values. The overview of the entire study area is shown on the top-left; five illustrative areas are shown on a more detailed scale.

#### 4.7.3. Segmentation results



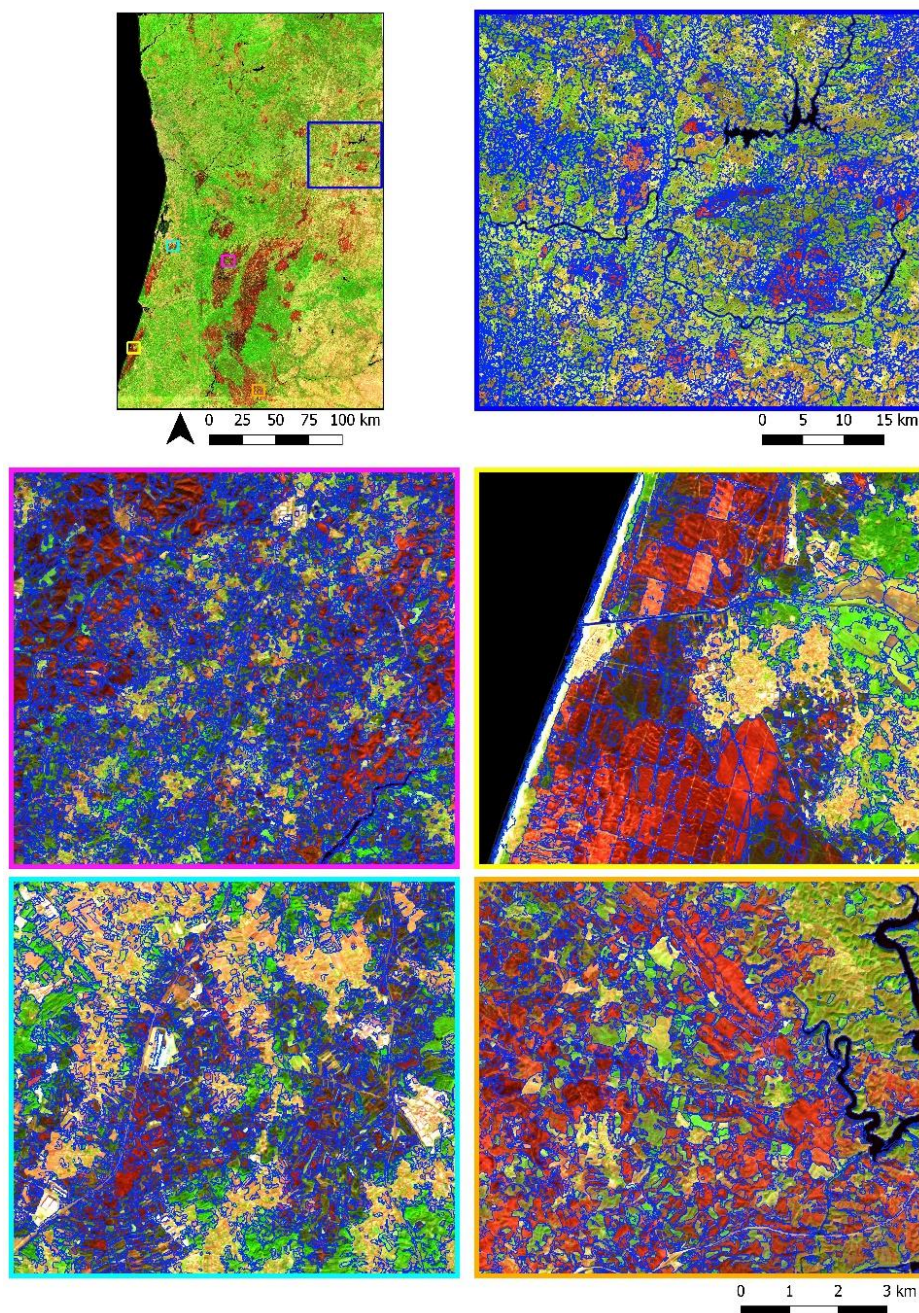
The segmentation results for the S1+S2 and S2 datasets are presented in Figures 4.6 and 4.7, respectively. The segments enclose groups of adjacent spectrally homogeneous pixels and, considering only the optical and/or SAR bands sensitive to fire, correspond to the same level of fire severity and are different from the surrounding segments representing burned or not-burned segments.

The unburned part is represented both by most of the study area (unburned surface surrounding the burned areas) and by the small areas not reached by the fire, but which are within the burned areas (“unburned islands”). The Figures also show that the transition areas between burned and unburned areas, where the fire caused low-severity damage, were segmented separately from the higher-severity burned areas in both sensor combinations (S1+S2 and S2).





**Figure 4.6.** Segmentation output that resulted from applying the Large-Scale-Mean-Shift (LSMS) algorithm to the S1+S2 dataset. The segments are presented in a blue border, while the base map is the S2 composite image based on the second-lowest NIR criterion (false-color composite B12-B8-B4). The segmentation is shown for the entire study area (top left) and five detailed illustrative areas.



**Figure 4.7.** Segmentation output that resulted from applying the Large-Scale-Mean-Shift (LSMS) algorithm to the S2 dataset. The segments are presented in a blue border, while the base map is the S2 composite image based on the second-lowest NIR criterion (false color composite B12-B8-B4). The segmentation is shown for the entire study area (top left) and five detailed illustrative areas.

#### 4.7.4. *GEOBIA classifications and accuracies*

Subsequently, the segmented data results were classified using the RF algorithm. The values of the RF parameters, set using the OOB estimated error as a predictive accuracy indicator, are listed in Table 4.2. As observed, the three

parameters did not vary between the two-sensor combinations, maintaining their default original values (*min\_samples\_split*:2; *min\_samples\_leaf*:1; *max\_features*: “auto”). Reaching an OOB error of 0.924, the set values for *n\_estimators* and *max\_depth* parameters were 1,200 and 110, respectively, using a combination of both sensors (S1+S2). Using only S2 and an OOB value of 0.908, the values were 1,750 and 65.

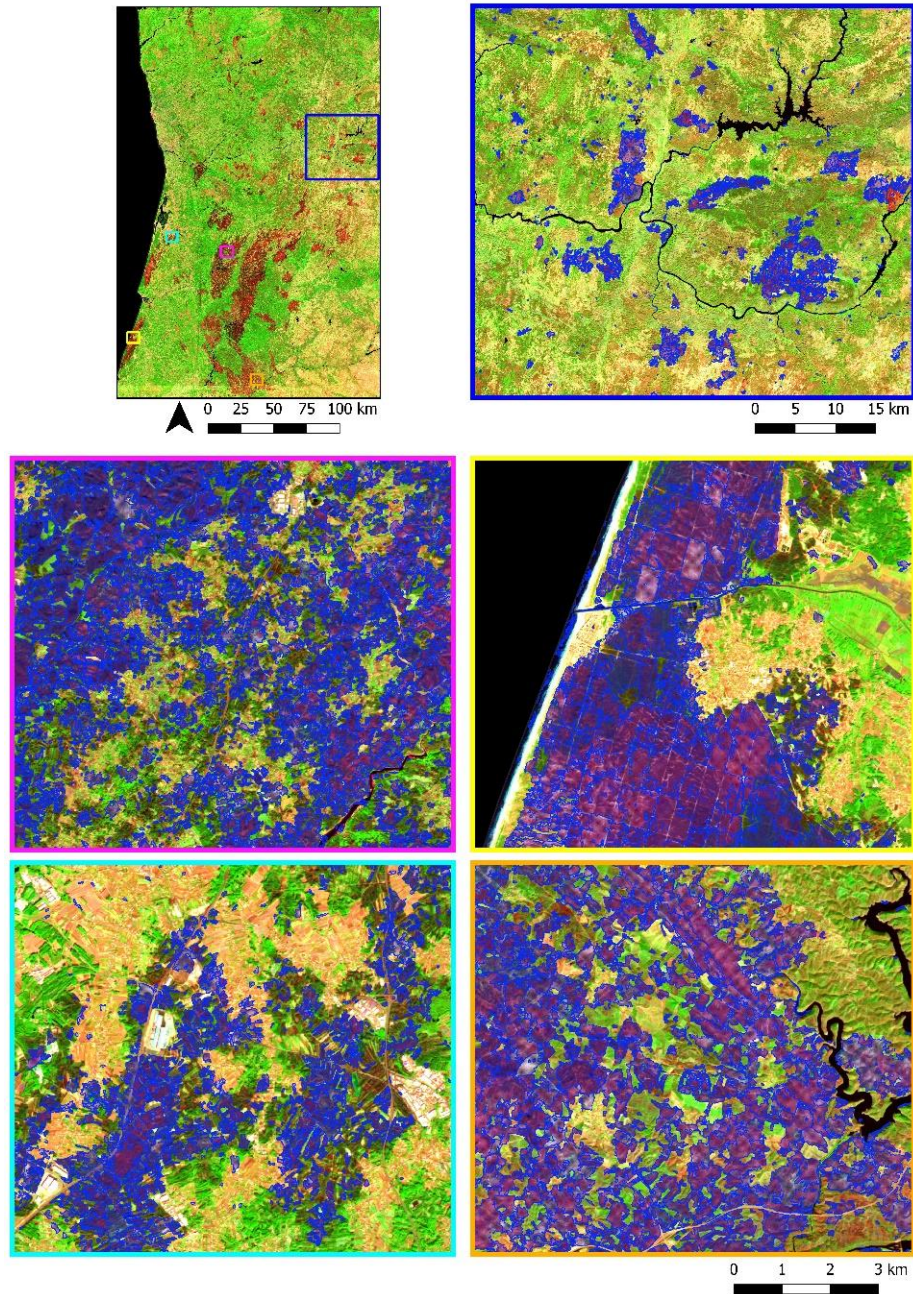
**Table 4.2.** The final combination of Random Forest (RF) parameter values that resulted from the exhaustive grid search-based test and was used in the classification approach for both datasets (S1+S2 and S2).

Parameter name	Values (S1+S2)	Values (S2)
n_estimators	1200	1750
max_depth	110	65
min_samples_split	2	2
min_samples_leaf	1	1
max_features	“auto”	“auto”

The classifications resulting from the GEOBIA process for the S1+S2 and S2 datasets are shown in Figures 4.8 and 4.9, respectively. The images show the segments classified as burned in the entire scene and five representative sample areas. Based on the images, a few differences appear between the sensor combinations. The classified segments encircle the regions affected by the fire. Only a minor confusion is noticeable at the level of some transition areas (e.g., Figures 4.8–4.9, bottom left), mainly where the low-severity fire occurred, as observed by comparing the respective  $\Delta$ NBR maps (Figure 4.4, bottom left). Some commission errors were also noticeable, involving very small agricultural fields (Figures 4.8–4.9, bottom left). The S2 classified map shows that, although it incorporated small transitional areas omitted with the S1+S2 combination, it made more commission errors by including agricultural and unburned regions adjacent to these areas.

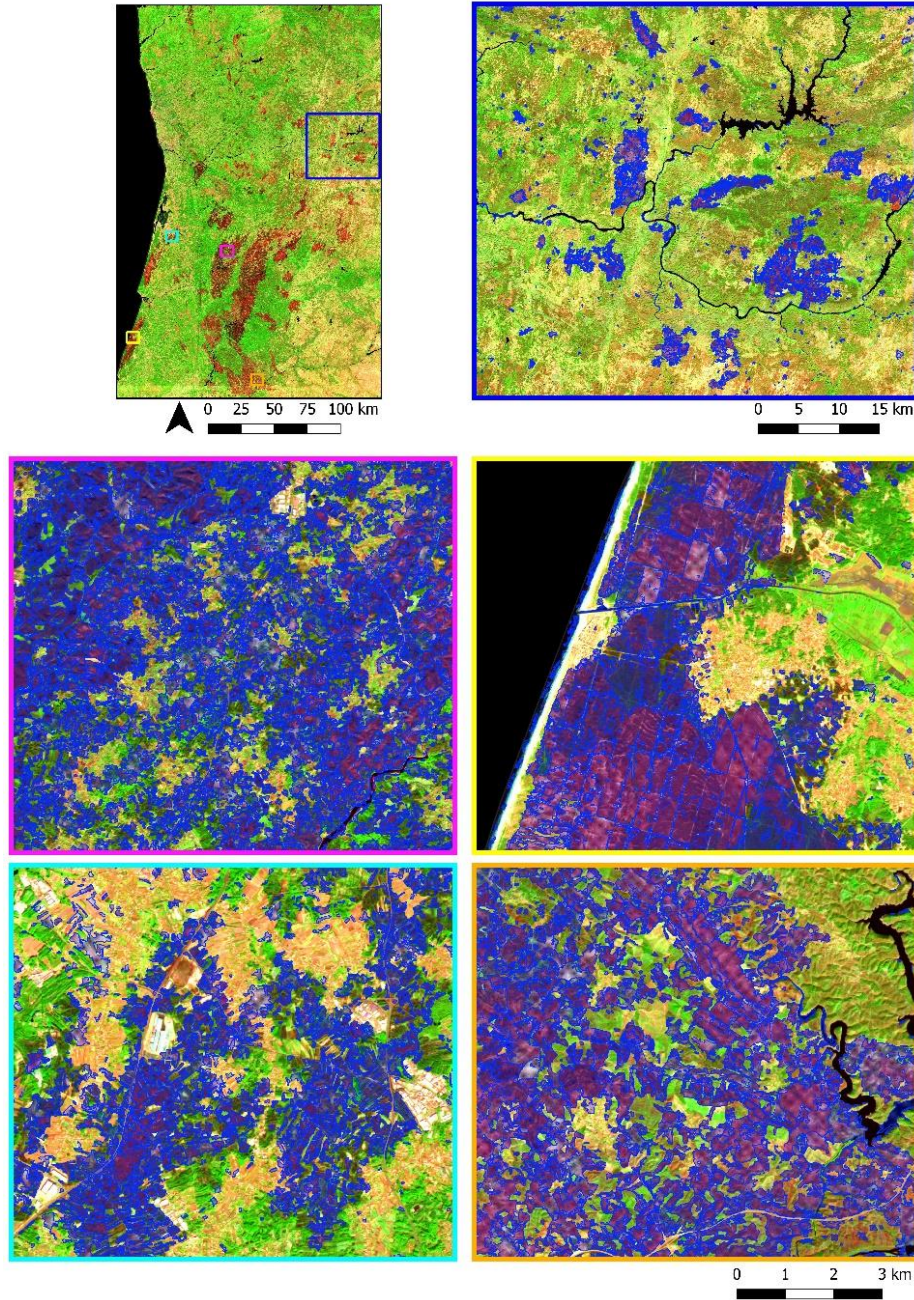
The Gini feature importance was calculated to express the influence of the spectral features (mean and variance) of each image layer during the model prediction process (Figure 4.10). In both dataset combinations and corresponding burned area classification, the mean spectral feature of  $NBR_{post}$  reached the highest values (0.413 for S1+S2 and 0.515 for S2), followed by the mean spectral features of  $\Delta$ NBR (0.256 and 0.305), highlighting the importance of optical data for burned area mapping. When both optical and SAR data were used (S1+S2), the third and fourth most important features were derived from the SAR data: the mean spectral features of  $\Delta$ RVI (0.125) and  $RVI_{post}$  (0.048). Below the mean spectral feature importance values, the variance achieved a lower importance value in both dataset combinations, with the lowest absolute variance values reached with the SAR indices (0.035,  $\Delta$ RVI, and RVI).





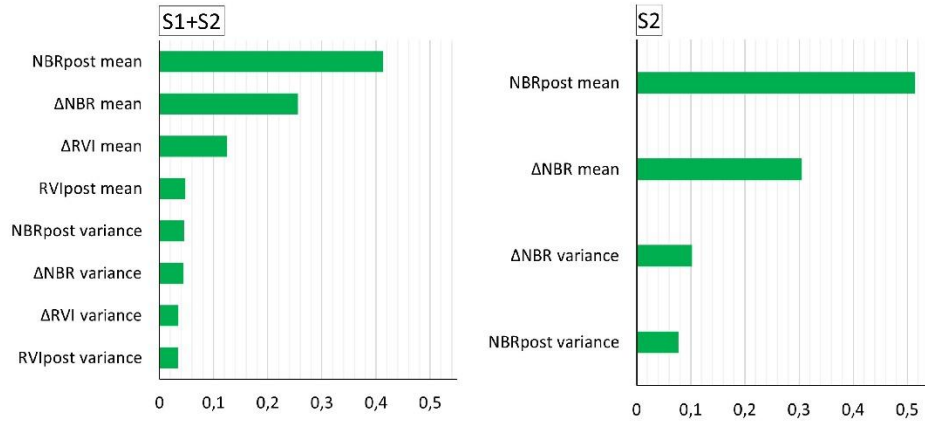
**Figure 4.8.** Classification output, based on the S1+S2 dataset. Segments showing only the burned class (blue) are overlaid on an S2 composite image based on the second-lowest NIR criterion (false color composite B12-B8-B4). The classification is shown for the entire study area (top left) and five detailed illustrative areas.





**Figure 4.9.** Classification output, based on the S2 dataset. Segments showing only the burned class (blue) are overlaid on an S2 composite image based on the second-lowest NIR criterion (false color composite B12-B8-B4). The classification is shown for the entire study area (top left) and five detailed illustrative areas.

The weighted descriptive statistics ( $\mu_{sw}$  and  $\sigma_{sw}$ ) calculated for the values of the spectral features ( $m_s$  and  $v_s$ ) of all classified polygons, separately for burned/unburned classes and the image layer, are reported in Table 4.3. Specifically, only the statistics calculated for the S1+S2 dataset were reported because the values retrieved for S2 (referable to  $\Delta NBR$  and  $NBR$ ) are similar.



**Figure 4.10.** Feature importance for burned area mapping (Gini importance), expressed by each spectral feature (mean and variance) used in the classification process for both dataset combinations: S1+S2 and S2.

**Table 4.3.** Weighted descriptive statistics (average,  $\mu_{sw}$ ; standard deviation,  $\sigma_{sw}$ ), computed using the values of the spectral features (mean,  $m_s$ ; variance,  $v_s$ ) of all the classified polygons of each S1+S2 input layer ( $\Delta$ NBR, NBR,  $\Delta$ RVI, RVI), separately for burned and unburned classes.

Image layer	Spectral features	Weighted average ( $\mu_{sw}$ )		Weighted standard deviation ( $\sigma_{sw}$ )	
		Burned	Unburned	Burned	Unburned
$\Delta$ NBR	$m_s$	29.7601	45.8026	4.8992	3.8137
	$v_s$	2.4165	1.4901	2.8745	2.1497
NBR	$m_s$	12.3907	23.8265	2.8068	4.1501
	$v_s$	1.1457	1.5632	1.9540	1.8859
$\Delta$ RVI	$m_s$	47.4288	49.5496	1.7230	1.0755
	$v_s$	0.8201	0.7188	1.5703	1.5541
RVI	$m_s$	17.5369	20.3481	3.8364	3.9241
	$v_s$	2.6855	3.2240	5.6704	4.2363

As expected, the weighted average of the spectral mean ( $m_s$ ) for both optical and SAR image layers was higher for the unburned class (45.8026,  $\Delta$ NBR; 23.8265, NBR; 49.5496,  $\Delta$ RVI; 20.3481, RVI) than the burned class (29.7601,  $\Delta$ NBR; 12.3907, NBR; 47.4288,  $\Delta$ RVI; 17.5369, RVI), and the respective weighted standard deviation was in the range between 1.7230 ( $\Delta$ RVI) and 4.8992 ( $\Delta$ NBR) for the burned class, and 1.0755 ( $\Delta$ RVI) and 4.2363 (RVI) for the unburned class. The second spectral feature, namely the variance ( $v_s$ ), did not exceed 2.6855 (RVI) and 3.2240 (RVI) for the burned and unburned classes, respectively. The total burned area that occurred during the considered fire season, resulting from classification, was 3,471.75 km<sup>2</sup> using the S1+S2 dataset and 3,648.17 km<sup>2</sup> using the S2 dataset. The accuracy overview of the obtained burned area map was expressed as precision (proportionally inverse to commission errors), recall (proportionally inverse to omission errors), and F-score (representing the overall accuracy of the map). Using the S1+S2 dataset, the recall, precision, and F-score metrics were 0.954, 0.957, and 0.956, respectively. Using the S2 dataset, the recall, precision, and F-score metrics were 0.969, 0.865, and 0.914, respectively.

## 4.8. Discussion

### 4.8.1. Image compositing



The final images were composed of all pixels affected by the fire events that occurred during the fire season considered (June–October). This means that all the single events that occurred in the period considered, even in the first month, were potentially equally highlighted in the image. Generally, when a single post-fire image is used to map a long time series of fires, less spectral discrimination of burned areas that occur during the starting and farthest periods of the fire season is expected. This is due to various environmental factors (climatic events, vegetation regrowth, biochemical changes in the burned material, etc.) that could lead to possible confusion with vegetation affected by phenological senescence and/or stress (Dijk et al., 2021; Fraser et al., 2000; Gallagher et al., 2020; Jukka Miettinen et al., 2013; Pereira et al., 1999; Rodman et al., 2021; Verbyla et al., 2008). The high discrimination between burned and unburned areas observed in the composite image is given by the lower NIR reflectance that the vegetation fire induces immediately after the event and in the first few weeks afterward. The minimum NIR values commonly occur on the dates closest to fire extinction. Under these conditions, the difference between the spectral signal from the surrounding background and the discriminability of the burn area was higher. However, choosing the NIR to its minimum value implies that in the final composite, the reflectance values of the surrounding vegetation background are among the lowest in the time series. Cabral et al. (2003) discuss this aspect. However, this makes the image compositing approach less appropriate for some specific applications (e.g., temporal growth monitoring, analysis of the spectral behavior of post-fire vegetation, etc.), the signal reduction is consistent throughout the image, and the relative differences between vegetation types are maintained. This procedure is particularly suitable for qualitative analyses, such as image classification. Choosing a low NIR value ensures that the pixel that best corresponds to the burned area is selected. However, when cloud shadows are present, this involves a substantial reduction in the NIR reflectance on the affected surface, which becomes an obvious problem if we directly choose the pixel with the lowest NIR value, as demonstrated in several studies (Barbosa et al., 1998; Chuvieco et al., 2005; Miettinen & Liew, 2008; Pereira et al., 2017; Pereira et al., 2016; Sousa et al., 2003). The same authors demonstrated a method to choose the second-lowest NIR to solve this problem. This is because the strong reduction in optical reflectance caused by cloud shadows has a higher magnitude than that caused by fire. Pereira et al. (2017) showed that the second NIR also overcame the criterion in which the highest SWIR value among the three pixels with the lowest NIR was used. This problem arises when the shadow occupies the same surface twice (or more). The advantage of the latter approach is that SWIR interacts with fire and shadows in a mutually opposite manner. The reflectance values of SWIR increase in the case of vegetation affected by fire because the absorption of electromagnetic waves at these wavelengths by the water is lacking (Pereira et al., 1999). Using  $\Delta\text{NBR}$  boosted the sensitivity of these two bands to the burned vegetation. This well-known index, which is used in burned area mapping, severity estimation, and post-fire monitoring purposes, has been widely explored and its efficacy proven in the literature (Crowley et al., 2019; Donezar et al., 2019; Epting et al., 2005; Fernández-García et al., 2018; Fornacca et al., 2018; Key & Benson, 2006; Kurum, 2015; Miller & Thode, 2007; Pulvirenti et al., 2020; Roteta et al., 2019; Schepers et al., 2014; Vanderhoof et al., 2021; P. Zhang et al., 2019), is also used for the creation of reference maps of burned areas (Ban et al., 2020; De Luca, Silva, & Modica, 2021b).

Concerning the SAR data on the dual-polarimetric  $\Delta\text{RVI}$  image, the burned areas were visually evident (Figure 4.5), highlighting the efficiency of the data for visually detecting burned areas. The dual-polarimetric  $\Delta\text{RVI}$  integrates the information of both polarizations (VH and VV), improving the backscatter interception of the variability of volume, structure, and size of the different components of the vegetation canopy and soil (De Luca,

Silva, & Modica, 2021b; Saatchi, 2019b). The combined contribution of these two elements forms the total SAR signal backscattered from the Earth's surface, which is covered by vegetation (Saatchi, 2019b). Cross-polarization presents a higher sensitivity for the distribution of vegetation volume scatterers associated with small branches and leaves. Therefore, it is more efficient in detecting variations in the structure and volume of objects placed on the Earth's surface, depending on the severity of the disturbance and the length of the wave used (Carreiras et al., 2020; Imperatore et al., 2017; Saatchi, 2019; Tanase, Santoro, Wegmüller, et al., 2010). Cross-polarized backscatter tends to decrease when drought conditions persist on the surface (Ruiz-Ramos et al., 2018). On the other hand, co-polarization intercepts the signal backscattered from the rough surface of bare ground, which is more exposed to the destruction of the canopy after the fire component (Carreiras et al., 2020; Saatchi, 2019b).

#### **4.8.2. *GEOBIA application***

Several studies have successfully applied GEOBIA to map burned areas for mapping purposes (Gitas et al., 2004; Mitri & Gitas, 2004; Polychronaki & Gitas, 2010, 2012; Sertel & Alganci, 2016; Shimabukuro et al., 2015) as an alternative classification technique to the pixel-based approach, observing that the former mitigates common biases provided by the pixel-based approach. Georgopoulos et al. (2019) presented an OBIA methodology based on mean-shift and support vector machine (SVM) algorithms for segmentation and classification, respectively, to map burned areas using Sentinel-2 data. The advantage of the GEOBIA approach is that, using the average value of the set of pixels contained within a segment, instead of any single value, the pixel variance caused by possible outliers is reduced, increasing the reliability of the classification (Radoux & Defourny, 2008). Considering only the spectral mean pixel value of the objects is a more efficient approach in the case of SAR data where, even if the speckle filter is applied, speckle noise remains in the images (Anastasia Polychronaki et al., 2013). The integration of both spectral features used in the present work (mean and variance) was thus expected to provide an advantage in classifying the two burned/unburned binary classes as additional information on the variability of the objects inside the polygons compared with using only the mean. However, the importance of the resulting features demonstrated that the former feature was not as decisive as the spectral mean for both optical and SAR data. This was because the spectral separability expressed by the mean was sufficiently discriminatory (Table 4.4). An M-statistic higher than 1 means that the discrimination is relatively strong (De Luca et al., 2019b; Kaufman & Remer, 1994). Furthermore, the weighted statistics (Table 4.3) demonstrated that the variance did not differ significantly between the burned and unburned classes.

A combination of uncorrelated feature spaces (e.g., shape and topological features) is considered to be able to avoid classification confusion and improve accuracy (Gitas et al., 2004; Mitri & Gitas, 2004; Polychronaki et al., 2013; Polychronaki & Gitas, 2010).

#### **4.8.3. *Map accuracy***

The classification accuracy assessment results reached high levels in both cases (S1+S2 and S2), as represented by an F-score value of more than 0.9. Although there was an effective distinction between most agricultural areas (plowed fields) and burned areas, some commission errors distributed over the entire study area remained when only an optical dataset was used. Tillage exposed the underlying soil layers on the surface, eliminating the vegetation present and causing a spectral response in some cases comparable to that caused by a low-severity fire (Dijk et al., 2021). When  $\Delta$ NBR was used, which was the most “important” layer for the learning model (Figure 4.10), the spectral separability was indeed higher between agricultural fields and unburned polygons than between

the former and the burned surface (Table 4.5). However, the extent of these errors remained low, considering the size of the study area and minimal amount of spectral information used. Conversely, SAR achieved low separability in all cases ( $<1$ ). Separability was sufficiently high if agricultural fields were compared with the burned class and when using the SAR layer with the highest importance in the RF learning process. Speckle noise may also play a dual role in this issue. Even after the filtering process, the SAR image layers presented persistent speckle outliers (Figure 4.5) owing to the intrinsic characteristics of the SAR signal (De Luca et al., 2021). At smaller scales (such as those of agricultural fields), this implies higher mixing with the background (Figure 4.5, bottom left). This could decrease the distinguishability of agricultural fields and affect small burned areas or transition areas between burned and unburned areas (Figure 4.5, bottom left). However, this would be relevant when using only SAR data, rather than integrating both optical and SAR information. Several studies (De Luca, Silva, & Modica, 2021b; Anastasia Polychronaki et al., 2013; Verhegghen et al., 2016) have addressed false positives and negatives using only SAR-based datasets caused by either the strong influence of moisture changes in bare soil or speckle noise. Considering the results of the present study, the feature importance demonstrates how the SAR product contributes to the final accuracy at a lower level than the optical product. However, the accuracy results indicate that the integrated use of optical and SAR datasets reduces commission errors, correcting the erroneous identification of burned areas that could occur using individual types of sensors, as already observed in Stroppiana et al. (2015). This confirms what other authors have considered using SAR as complementary data, rather than a substitute for optical data (De Luca, Silva, & Modica, 2021b; Lasko, 2019; Lehmann et al., 2015; Anastasia Polychronaki et al., 2013; Stroppiana et al., 2015). Optical sensors are more effective for burned area mapping because of the more robust relationship between the optical wavelengths and the effects of fire on vegetation.

However, SAR data are fundamental not only for proven complementary information that improves classification, but also for fire detection in unfavorable atmospheric conditions, owing to the ability of microwaves to penetrate cloud cover (Richards, 2009c). However, this latter aspect is less important in the Mediterranean climate context than in the tropical zone.

#### **4.8.4. *Final considerations and limitations***

Burned area maps, covering regional to continental/global territory, derived from coarse and medium spatial resolution satellite sensors (e.g., NASA Terra/Aqua MODIS, SPOT-VEGETATION, NOAA/AVHRR) have certainly been an important source of information for the fire science and application communities (Boschetti et al., 2015). As demonstrated in this and other studies, the free availability of Sentinel satellites with enhanced spatial and temporal resolution offers new opportunities that guarantee the fast distribution of burned area products at very high accuracy and large scales. This can only be achieved if all fire events, including small fires (between 0.1 and 1 km<sup>2</sup>), and small unburned islands are detected. The use of improved spatial resolutions guarantees more precise monitoring, even within the same burned areas, because all the details (e.g., unburned spots) can be surveyed. The increase in time and processing consumption required by higher resolution is also overcome by the development of open-source software solutions and cloud platforms that allow the easy processing of large amounts of data (Chuvieco et al., 2019).

The findings of this approach open a debate regarding the quality of official reference data. Official maps based on coarse data tend to overestimate burned areas. They fail to classify many unburned islands, rendering the produced map almost unusable as a reference. In our case, this problem was overcome by integrating freely

available high-resolution images with accurate visual analysis. However, in our opinion, this method is laborious. For this reason, there is a need for increasingly accurate mapping methods for relatively large territories (and/or specific fire seasons) that lack accurate maps of burned areas.

The results of this study showed that using only the NIR and SWIR bands, already known to be the most sensitive bands for discriminating burned areas (Chuvieco et al., 2005; Pereira et al., 1999), with or without the integrated use of given SAR, it is possible to achieve high values of accurate burned area mapping quality (accuracy >90%). This is an essential aspect favoring a more rapid and effective practical operability of the approach.

Although the integration of the SAR data slightly increased the accuracy, it did not overcome the importance expressed by the information of the optical indices during the learning process.

Although this was not the case in this study, the method might be hindered by the frequent presence of cloud shadows on the same pixels, which is typical in more temperate European climates. The advantages of SAR should be investigated and possibly raised in these cases. Integrating the highest SWIR might be another valid solution, considering the already addressed weaknesses compared with the secoMinNIR.

#### **4.9. Conclusions and recommendations**

The objective of this study was to optimize a method of detecting burned areas that occurred during an entire fire season, based on a multitemporal compositing criterion and image segmentation, through the integration of optical and SAR data, open-source software, and algorithms. This study contributes to the development and harmonization of accurate methods used for the detection of burned areas at national and continental levels. These objectives were pursued based on the robustness and spatial adaptability of the algorithm. The approach was tested and validated on a large regional scale in a heterogeneous Mediterranean territory with fire conditions of varying severity and different burned vegetation and temporal progression. We believe that this method could be extended to other European ecosystems. Future studies might involve verifying the performance of the proposed classification workflow in other Mediterranean regions or ecosystems. However, the efficiency of SAR information when cloud shadows occupy the same pixel for more scenes should be tested and compared, especially in more temperate climates, as should the eventual integration of the highest SWIR value into the composite process.

Our findings suggest that optical data can only achieve high levels of accuracy. However, optical and SAR imagery synergy can improve the accuracy of burned-area mapping. Despite this, we believe that optical data alone can be used as the first effective solution for the detection of burned vegetation areas, allowing easier data management and less time-consuming processing. These aspects are fundamental in operational scenarios in which disaster mapping methodologies such as fires are used. The utilization of other bands, frequencies, polarization combinations, or indices may provide improvements for further analysis. In particular, many optical indices have been implemented and proposed as optimized for the detection of burned areas compared to standard NBR [e.g., BAIS2 (Filipponi, 2018) or the recent NBR+ (Alcaras et al., 2022)]. Supplementary analyses should integrate, test, and compare these data to optimize the approach proposed in this study further.




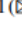

Further optimizations might entail using open-source cloud computing platforms, such as the Google Earth Engine (GEE), where an extensive database of satellite imagery and computational power is accessible to all users.

## 5. Fire severity estimation and mapping: an approach using machine learning and the combined optical and SAR data

Adapted from

De Luca, G., Silva, J.M.N., Oom, D., Modica, G.: *Combined Use of Sentinel-1 and Sentinel-2 for Burn Severity Mapping in a Mediterranean Region*. In: *Computational Science and Its Applications – ICCSA 2021. Lecture Notes in Computer Science*. pp. 139–154 (2021). [https://doi.org/10.1007/978-3-030-87007-2\\_11](https://doi.org/10.1007/978-3-030-87007-2_11).

### Combined Use of Sentinel-1 and Sentinel-2 for Burn Severity Mapping in a Mediterranean Region

Giandomenico De Luca<sup>1</sup> , João M. N. Silva<sup>2</sup> , Duarte Oom<sup>2,3P</sup> ,  
and Giuseppe Modica<sup>1</sup>  

Dipartimento Di Agraria, Università Degli Studi Mediterranea Di Reggio Calabria,  
Località Feo di Vito, 89122 Reggio Calabria, Italy

{giandomenico.deluca, giuseppe.modica}@unirc.it

Forest Research Centre, School of Agriculture, University of Lisbon, Tapada da Ajuda,  
1349-017 Lisboa, Portugal

joaosilva@isa.ulisboa.pt

<sup>3</sup> European Commission, Joint Research Centre, Ispra Site, Ispra, Italy

Duarte.Oom@ec.europa.eu

**Abstract.** The present study is focused on investigating the capabilities of the combined use of synthetic aperture radar (SAR) Sentinel-1 (S1) and optical Sentinel-2 (S2) for burn severity mapping. For this purpose, a fire that occurred in August 2018 in southern Portugal was analyzed. The composite burn index (CBI) was used to visually classify geo-referenced photographs in the field and create the training data for image classification. A supervised classification was carried out using the machine learning random forests (RF) algorithm, on which the optimization of the parameters setting was carried out through an exhaustive grid search approach. In order to assess the advantages of combining optical and SAR data, and the importance of each band, the approach was tested separately on three data combinations (S1, S2 and S1 + S2) and feature importance was computed to evaluate the contribution of each input layer. The multi-class F-score, used to assess the accuracy of the map, reached a value of 0.844 when both the datasets were combined (S1 + S2), compared with the values 0.514 and 0.805 achieved by only SAR (S1) and only optical (S2), respectively.

**Keywords:** Composite burn index (CBI) · Random forest (RF) · Exhaustive grid search (GridSearchCV) · Scikit-learn · SNAP-Python (snappy) interface

Wildfires are one of the most important ecological factors in Mediterranean ecosystems, with different degrees of impact depending on the severity and distribution of burns (Emilio Chuvieco, 2009; Fernández-García et al., 2018; Lanorte et al., 2013; San-Miguel-Ayanza et al., 2019; Saulino et al., 2020; João M.N. Silva et al., 2019). These effects determine, at different spatial and temporal scales, microclimatic and ecological changes that rearrange the habitats assets, positively (i.e., regeneration, regrowth, vegetation composition enrichment) or negatively (i.e., degradation, desertification, higher exosystemic vulnerability) (Emilio Chuvieco, 2009; Di Fazio et al., 2011;

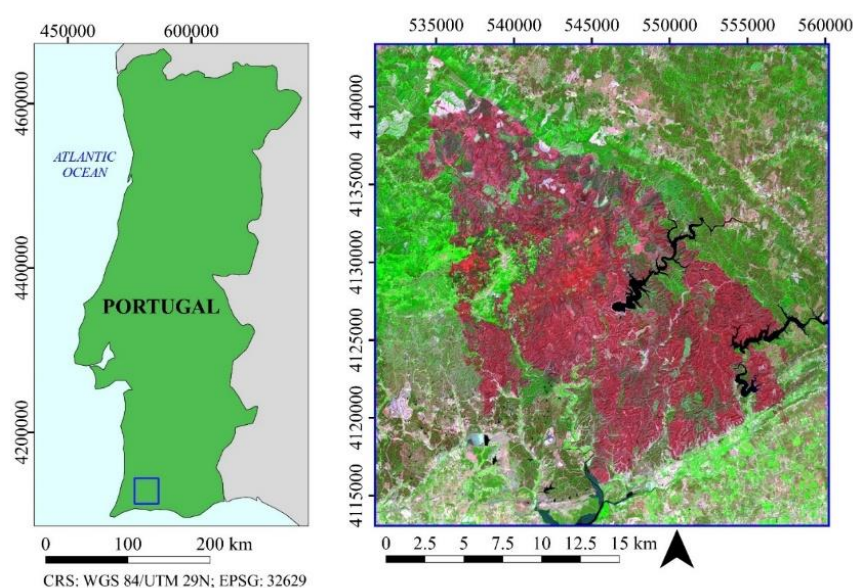
Häusler et al., 2018; George H. Mitri & Gitas, 2012; Giuseppe Modica et al., 2015; Morresi et al., 2019; Saulino et al., 2020; Semeraro et al., 2019). Burn severity is defined as the degree of environmental change caused by fire. Analytically, it can be measured as the degree of chemical-physical changes, decomposition and loss of above/below-ground organic matter (Keeley, 2009; Key & Benson, 2006). It influences and determines, at various degrees, the transformation of the organic and mineral components of the soil, the conversion of biomass into inorganic carbon, structural transformation of habitats and, at the most extreme degree, the destruction of the biological communities of an ecosystem (Key & Benson, 2006). The knowledge on the spatial distribution of the burn severity is a crucial and essential step for assessing and monitoring the impacts of fire on ecosystems and to address optimal and timely post-fire management operations (De Luca et al., 2020; Fernández-García et al., 2018; I. Gitas et al., 2012a; Meng et al., 2018; George H. Mitri & Gitas, 2012; Morresi et al., 2019). Key & Benson (2006) proposed the composite burn index (CBI) for determining the burn severity, becoming a standard metric in literature. This index is based on the qualitative/quantitative measurement of ecosystem alterations, carried out through visual interpretation in sample field plots, comparing the aboveground biomass and necromass after the fire with their pre-fire conditions. In the CBI protocol, several ecological attributes are measured to estimate the effect of fire in the post-fire environment in five vertical structural layers (strata), from litter and duff consumption, canopy cover reduction, branch and wood consumption and plant mortality (De Santis & Chuvieco, 2009; Keeley, 2009; Key & Benson, 2006).

Remote sensing techniques and satellite data are effective when retrieving the spatial distribution over large areas of the burn severity information carried out in the field plots, with a high level of correlation (De Santis & Chuvieco, 2007; Fernández-García et al., 2018; I. Gitas et al., 2012a; Keeley, 2009; Otón et al., 2019; M. A. Tanase et al., 2015b). Their use was encouraged by the availability of open-source data, acquired from satellite sensors with increasing spatial and temporal resolutions (Emilio Chuvieco et al., 2019), and software that provides advanced process and analysis tools. In this context, the Sentinel constellation (Copernicus mission) launched by the European Space Agency (ESA) provides free high temporal and spatial resolution data acquired by several sensors. The Sentinel-1 (S1) and Sentinel-2 (S2) missions consist, respectively, of a C-band synthetic aperture radar (SAR) and an optical multispectral sensor, both composed of two polar-orbiting satellites (S1A/B and S2A/B) (ESA Sentinel Homepage, 2022). The high sensitivity in the visible, near infrared (NIR) and short-wave infrared (SWIR) spectral bands to the effects of fire on ecosystems (José M. C. Pereira et al., 1999, 1999; J. M.N. Silva et al., 2004) allowed the rapid development and diffusion of optical-based approaches for this purpose, achieving efficient results (Cansler & McKenzie, 2012; Emilio Chuvieco et al., 2019; Epting et al., 2005; Fornacca et al., 2018; Mallinis et al., 2018; Morresi et al., 2019). Numerous authors, in the past decades, proposed different methods aimed at estimating and mapping burn severity using remotely sensed data (Cansler & McKenzie, 2012; De Santis et al., 2009; Fernández-García et al., 2018; Lanorte et al., 2013; Meng et al., 2018; Carmen Quintano et al., 2013; Saulino et al., 2020; Schepers et al., 2014) and effective vegetation indices using optical sensors (Fernández-García et al., 2018; A. Fernández-Manso et al., 2016; Filipponi, 2018; Miller et al., 2009; Parks et al., 2014; Zheng et al., 2016). SAR data have also been explored in recent years for burn severity mapping (Addison & Oommen, 2018; Kurum, 2015; Lasaponara & Tucci, 2019; Mihai A. Tanase et al., 2014). Tanase et al. (2010) and Tanase et al. (2010) explored the suitability of different frequency SAR sensors for burn severity purposes in Mediterranean vegetation. Tanase et al. (2015) proposed a SAR index to estimate fire severity in temperate forests, based on the ratio between post and pre-fire SAR images. The sensitivity of SAR signal is given by the variation

in vegetation and soil structure and moisture content, which affect the dielectric properties of the surface and influence the level of microwave backscatter, in synergy with various environmental factors and/or intrinsic sensors characteristics (e.g. wavelength and polarization) (Imperatore et al., 2017; Mihai A. Tanase, Santoro, De La Riva, et al., 2010). Therefore, this type of active sensor may be a complementary source for monitoring the fire impacts on ecosystems, considering that it is not sensitive to cloud cover conditions (Lasko, 2019; Lehmann et al., 2015; Stroppiana et al., 2015). However, few studies focused on integrating the two types of sensors for the estimation of burnt area (Stroppiana et al., 2015; Verhegghen et al., 2016) and, even less, for burn severity (M. A. Tanase et al., 2015a). This study aims to contribute to the state of the art by evaluating the capability of the integrated use of S-1 and S-2 to estimate burn severity using the random forest (RF) machine learning algorithm and the field-based CBI measurements as training data. A series of processing steps anticipated the severity estimation: a) download and pre-processing of optical and SAR time series and subsequent creation of input image layers; b) creation of three dataset combination: S1, S2 and S1+S2, in order to evaluate the contribution of each sensor to the final accuracy; c) search and setting of optimal values of RF parameters using an exhaustive grid search approach. The single- and multi-class F-score was calculated to assess the accuracy of the maps. The feature importance was extracted to evaluate each of the input variables' contribution to the final map accuracy. All the processes were carried out through the use of open-source softwares and libraries executed in python-script language (The Python Language Reference, 2022).

## 5.1. Study site

The study area is located in the south of Portugal (Algarve, 37° 18'N; 08° 30'W), in the Serra de Monchique mountain range. The site is characterized by typical Mediterranean vegetation. The forest areas were composed of coniferous (*Pinus pinea* L., *Pinus pinaster* Aiton.), broad-leaves trees (*Quercus suber* L., *Quercus ilex* L., other secondary Mediterranean native species), and Eucalyptus plantations (*Eucalyptus globulus*, Labill. 1800). A large part of the territory is covered by sclerophyllous shrublands or pastures, interspersed with agricultural and urban landscapes (SNIG, 2021). The fire event occurred in August from the 3<sup>rd</sup> to the 10<sup>th</sup> of 2018, covering 268.9 km<sup>2</sup>.





**Fig. 5.1.** Location of the study burned area in Portugal (on the left). On the right, overview of the study area (Sentinel-2 image on August 13<sup>th</sup>, 2018 false-colour composite SWIR-NIR-RED), where the red area represents the burned area.

## 5.2. Materials and methods

### 5.2.1. Satellite dataset

The SAR dataset was composed of a temporal series of Sentinel-1A/B ground range detected (GRD), acquired in interferometric wide (IW) mode, dual-polarized (vertical-vertical VV, and vertical-horizontal VH polarizations). Five images for the pre-fire period (covering around the month before the starting date of the event) and five images for the post-fire period (covering the period from the end of the event until the end of the same month), including both the ascending and descending orbits.

The optical dataset was composed of a temporal series of Sentinel-2A/B Level 2A (Bottom of Atmosphere reflectance), composed of three images before and three images after the fire (accounting for a similar time frame to that considered for the S1 dataset).

### 5.2.2. Field data and ROIs selection

The field sampling involved capturing post-fire conditions through geo-referenced photographs in different points sampled on the burned surface. Field data were collected in November of the same year of the fire (2018), before the growing season, to avoid confusion between regenerated and unburned vegetation. Fire severity quantification was based on the visual interpretation of the photographs, supported by the Esri ArcGIS World Imagery (2021) map, providing post-fire medium/high-resolution images and by the field-notes taken during the on-field surveys. The protocol used in this study to quantify fire severity was the Composite Burn Index (CBI), consisting of visually estimation of post-fire change in several ecological variables for each of the five vegetation stratum (inert understory substrate and fuel; herbs, low shrubs and <1m high trees; tall shrubs and <5m high trees; subcanopy intermediate trees; dominant and codominant cover trees). The level of changed inducted by the fire was ranked between 0 (unburned) and 3 (highest level of severity). The average of all the index values for each variable and stratum represented the severity CBI value of the entire single plot observed. Based on the CBI values obtained, six fire severity categories were created: 1) Unburned soil/rock; 2) Unburned vegetation; 3) Low severity; 4) Moderate severity; 5) Moderate-High severity; 6) High severity.

During the field surveying, 200 sampling photographs were taken, from which 185 sampling plots were observed. Each of these points was the centre of a 20 m x 20 m square sampling area (region of interest, ROI), homogeneous in terms of burn severity, matching 2x2 pixel areas on Sentinel images (considering resampling of the pixels at 10 m; see Subsection 3.3). Each ROI was finally labelled with one of the six severity categories.

### 5.2.3. Satellite data pre-processing and layers creation

The data pre-processing was carried out using the Sentinel-1 and Sentinel-2 Toolboxes implemented in the SNAP v.8.0.1 open-source software (*Snap*, n.d.) (ESA SNAP Homepage, 2022) provided by ESA and executed through Snappy (*Snap Cookbook*, n.d.) (ESA SNAP Cookbook, 2022), the SNAP-Python interface.

#### 5.2.3.1. Sentinel-1

The S1 pre-processing workflow started from the auto-downloaded orbit file application and the thermal noise removal. After the radiometric calibration to beta ( $\beta_0$ ) noughts backscatter standard conventions, the radiometric terrain correction (RTC) process was applied to the dataset, flattening (radiometric terrain flattening) and geometrically correcting (terrain correction) the images using the shuttle radar topography mission (SRTM) digital elevation model (DEM), presenting a spatial-sampling of 1 arc-second. The bilinear interpolation resampling method was used for both DEM and output image resampling. All the S1 images were stacked using the product geolocation as the initial offset method. To reduce speckle noise effects, a multitemporal Lee filter (Quegan et al., 2000; Santoso et al., 2015), with a 5x5 pixel window size, was applied. The backscatter time average (BTA) was computed separately for the images before and after the event and for polarization to improve speckle reduction (De Luca et al., 2020; Lasaponara & Tucci, 2019; M. A. Tanase et al., 2015b). At the end of the S1 pre-processing steps, we had four resulted image layers: 1) BTA\_VH<sub>pre-fire</sub>; 2) BTA\_VV<sub>pre-fire</sub>; 3) BTA\_VH<sub>post-fire</sub>; 4) BTA\_VV<sub>post-fire</sub>. From these image layers, three dual-polarimetric SAR indices were computed to have layers expressing the two polarisations' combination. The dual-polarimetric SAR indices were the adapted version for S1 sensor (Mandal et al., 2020; Nasirzadehdizaji et al., 2019; Nicolau et al., 2021).

$$RVI_t = 4 \cdot BTA\_VH_t / (BTA\_VV_t + BTA\_VH_t) \quad (5.1)$$

$$DPSVI_t = (BTA\_VV_t + BTA\_VH_t) / BTA\_VV_t \quad (5.2)$$

$$RFDI_t = (BTA\_VV_t - BTA\_VH_t) / (BTA\_VV_t + BTA\_VH_t) \quad (5.3)$$

Where  $t$  represents one of the two time periods: before or after the fire.

Moreover, the difference between pre- and post-fire of each respective image layer was computed ( $\Delta$  = pre-fire – post-fire).

At the end, the BTA\_VH<sub>post-fire</sub>,  $\Delta$ BTA\_VH, BTA\_VV<sub>post-fire</sub>,  $\Delta$ BTA\_VV, RVI<sub>post-fire</sub>,  $\Delta$ RVI, DPSVI<sub>post-fire</sub>,  $\Delta$ DPSVI, RFDI<sub>post-fire</sub>,  $\Delta$ RFDI formed the SAR-based input image layers in the next classification steps.

#### 5.2.3.2. Sentinel-2

The S2 pre-processing concerned the pixel resampling to 10 m x 10 m pixel size. As with the S1 dataset, the time average was computed for the images before and after the fire. All 10 m and 20 m spatial resolution, and their respective pre- and post-fire difference ( $\Delta$ ), were used as image input layers in the classification processes: B2 (Blue),  $\Delta$ B2, B3<sub>c</sub> (Green),  $\Delta$ B3, B4 (Red),  $\Delta$ B4, B5 (RedEdge1),  $\Delta$ B5, B6 (RedEdge2),  $\Delta$ B6, B7 (RedEdge3),  $\Delta$ B7, B8 (NIR),  $\Delta$ B8, B8A (NarrowNIR),  $\Delta$ B8A, B11 (SWIR1),  $\Delta$ B11, B12 (SWIR2),  $\Delta$ B12.

The two S1 and S2 datasets, clipped on the same area, were stacked together using the S1 dataset as the master extent. The bilinear interpolation was performed to resample the pixels between master and slaves.

#### 5.2.4. Image classification

The random forests (RF) algorithm (Breiman, 2001; Cutler et al., 2007) was used to perform a supervised pixel-based classification, using a part (2/3) of the pixels contained and labelled in the ROIs as training data. Three different dataset combinations were evaluated: only optical (S2); only SAR (S1); optical and SAR (S1+S2). To assess each image layer's contribution to the classification, the feature importance (Gini importance) was computed for each of the three dataset combinations. The classification algorithm was implemented in the scikit-learn library (*RFclassifier* module) (Pedregosa et al., 2011) and executed via a Python script.

The optimal values of the algorithm parameters were determined using an exhaustive grid search approach. The exhaustive grid search is based on testing and cross-validation of each possible combination of the set of values

given for each parameter, returning the best combination for a given training input set. The *GridSearchCV* algorithm implemented in scikit-learn was used for this purpose. The combination of parameters tested is reported in Table 5.1.

**Table 5.1.** Sets of parameters values tested and combined for exhaustive grid search-based optimization. The name and the definition of each parameter are the original ones reported in the *RFclassifier* module user guide (for deeper description, see <https://scikit-learn.org/stable/modules/generated/sklearn.ensemble.RandomForestClassifier.html>).

Parameter name	Values set	Description
n_estimators	100, 650, 1200, 1750, 2300, 2850, 3400, 3950, 4500, 5050, 5600, 6150, 6700, 7250, 7800, 8350, 8900, 9450, 10000	The number of trees in the RF model
max_depth	10, 20, 30, 40, 50, 60, 70, 80, 90, 100, 110, 300, 500, 800, 1000	The maximum depth of the tree
min_samples_split	2, 5, 10	The minimum number of samples required to split an internal node
min_samples_leaf	1, 2, 4	The minimum number of samples required to be at a leaf node
max_features	"auto", "None", "log2"	The number of features to consider when looking for the best split

### 5.2.5. Accuracy assessment

The remainder part of ROIs pixels (1/3) was used to validate the classification accuracy of the three burn severity maps (S2, S1 and S1+S2). The confusion matrix was carried out, from which the *producer's* accuracy (defined as the ratio between the correctly classified pixels in a given class and the number of validation pixels for that class) and the *user's* accuracy (the ratio between the correctly classified pixels in a given class and all the classified objects in that class) were calculated (Congalton & Green, 2019). From these measures, we calculated the single-class F-score ( $F\text{-score}_i$ ) (eq. 5.4) (De Luca et al., 2020; Goutte & Gaussier, 2005; Giuseppe Modica et al., 2020; Ok et al., 2013; Shufelt, 1999; Sokolova et al., 2006) and the multi-class F-score ( $F\text{-score}_M$ ) (eq. 5.5) (Sokolova & Lapalme, 2009), representing a form of overall accuracy. The F-score is the harmonic mean of *recall* and *precision* measures, which have the same respective meaning of *producer's* and *user's* accuracy. Therefore they were replaced in the equations (eq. 5.4, 5.6, 5.7) (G. Modica et al., 2021a).

$$F\text{-score}_i = 2 \cdot (\text{producer}'s_i \cdot \text{user}'s_i) / (\text{producer}'s_i + \text{user}'s_i) \quad (5.4)$$

$$F\text{-score}_M = 2 \cdot (\text{producer}'s_M \cdot \text{user}'s_M) / (\text{producer}'s_M + \text{user}'s_M) \quad (5.5)$$

Where  $i$  is a single class;  $\text{producer}'s_M$  and  $\text{user}'s_M$  metrics are expressed as follows (eq. 5.6, 5.7):

$$\text{producer}'s_M = (\sum_{i=1} \text{producer}'s_i) / n \quad (5.6)$$

$$\text{user}'s_M = (\sum_{i=1} \text{user}'s_i) / n \quad (5.7)$$

Where  $n$  is the total number of classes.

## 5.3. Results

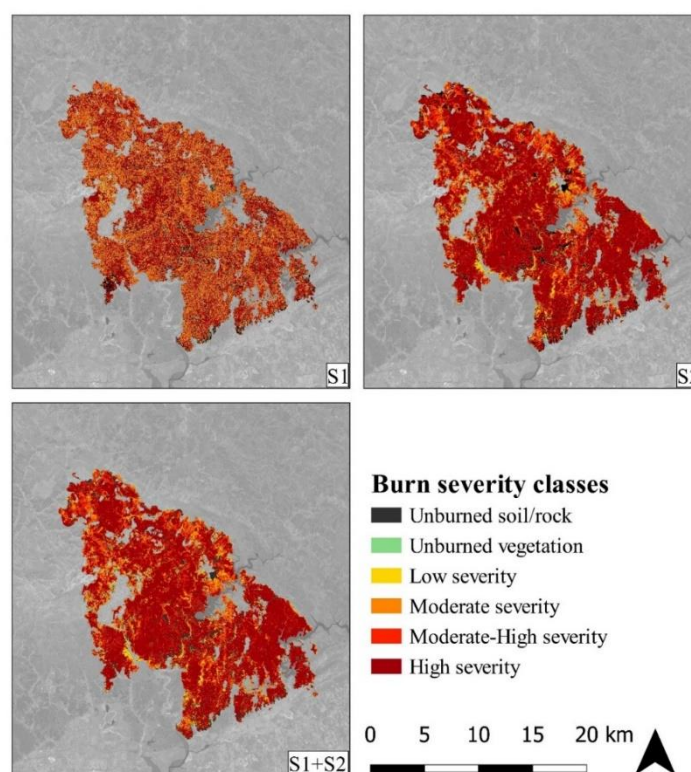
### 5.3.1. Classified burn severity map

Table 5.2 shows the RF classification algorithm's optimal parameters values, set using an exhaustive grid search approach. This was carried out for each of the three data combination (S1, S2 and S1+S2) separately.

**Table 5.2.** Random forests (RF) parameters values used for each of the three data combination (S1, S2 and S1+S2) and set using an exhaustive grid search approach.

Parameter name	Values set		
	S1	S2	S1+S2
n_estimators	650	1200	1200
max_depth	1000	90	110
min_samples_split	2	2	2
min_samples_leaf	1	1	1

Figure 5.2 shows the three burn severity maps resulted from the classification processes tested. Respectively, they represent the map resulting from using only the SAR image layers, the map resulting from using only the optical bands and, finally, the burn severity map obtained using the SAR and optical datasets together.



**Fig. 5.2.** Burn severity maps resulted from the classification of the three data combination: Sentinel-1 dataset only (S1); Sentinel-2 dataset only (S2); Sentinel-1 and Sentinel-2 data (S1+S2).

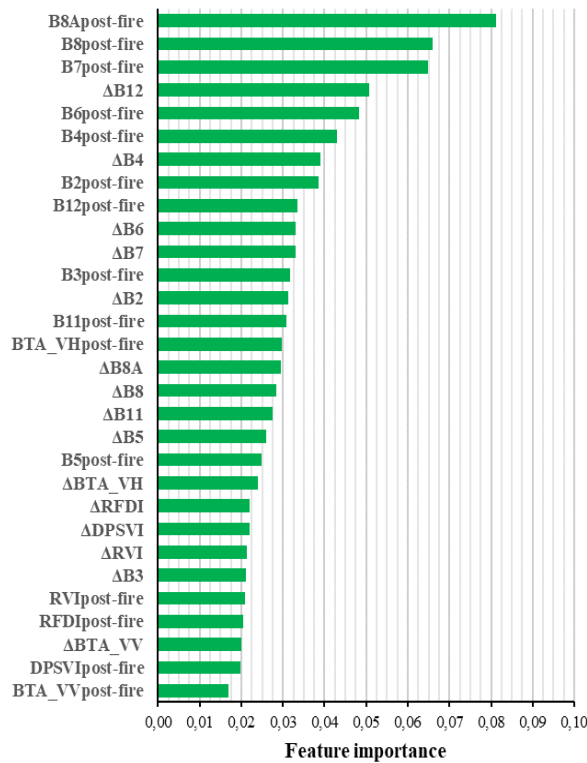
In Table 5.3, the distribution (%) of the area of each burn severity classes is reported.

**Table 5.3.** Distribution (%) of the area of each burn severity class for each data combination: Sentinel-1 dataset only (S1); Sentinel-2 dataset only (S2); Sentinel-1 and Sentinel-2 data stack (S1+S2).

Burn severity classes	Distribution (%)		
	S1	S2	S1+S2
Unburned soil/rock	6.55	8.35	8.31
Unburned vegetation	11.92	1.85	2.15
Low severity	6.83	2.90	3.03
Moderate severity	17.67	12.54	13.15
Moderate-High severity	16.29	16.84	16.02
High severity	40.74	57.51	57.34

### 5.3.2. Feature importance

The influence that each image layer gave to the classification of each of the three respective data combination is expressed by the feature importance, whose results are presented below by dividing them by dataset combination. The result of dataset S1+S2 is reported in Figure 5.3; the other two data combinations present almost the same behavior.



**Fig. 5.3.** Feature importance (Gini importance) expressed by each image layer used in the classification process of the Sentinel-1 and Sentinel-2 data stack (S1+S2).

#### 5.3.2.1. Sentinel-1

The BTA\_VH<sub>post-fire</sub> had the highest value of importance (0.1431), followed by its respective ΔBTA\_VH image layer (0.1349) and by the VV bands (0.1125 and 0.0983 for ΔBTA\_VV and BTA\_VV<sub>post-fire</sub>, respectively). The Δ of the dual-polarimetric indices presented close values of feature importance (from 0.0924 to 0.0886), while the post-fire dual-polarization indices reached a range of values between 0.0814 and 0.0788.

#### 5.3.2.2. Sentinel-2

The two-NIR, RedEdge2/3,  $\Delta$ SWIR2 and Red bands for post-fire ( $B8A_{\text{post-fire}}$ ,  $B8_{\text{post-fire}}$ ,  $B7_{\text{post-fire}}$ ,  $\Delta B12$ ,  $B6_{\text{post-fire}}$ ,  $B4_{\text{post-fire}}$ ) reached the highest values of feature importance: 0.0913, 0.0798, 0.0785, 0.0592, 0.0591 and 0.0554, respectively, followed by the Blue and SWIR2 post-fire (0.0481 and 0.0444). The lowest values are achieved mainly by the NIR-based  $\Delta$  layers and the RedEdge1 bands (0.0384 to 0.0346).

### 5.3.2.3. Optical+SAR

The feature importance values roughly reflect what has already been seen for individual datasets. The  $B8A_{\text{post-fire}}$ ,  $B8_{\text{post-fire}}$ ,  $B7_{\text{post-fire}}$ ,  $\Delta B12$ ,  $B6_{\text{post-fire}}$ ,  $B4_{\text{post-fire}}$  image layers reported highest values: 0.0812, 0.0660, 0.0648, 0.0506, 0.0483, 0.0431, respectively. The  $B2_{\text{post-fire}}$  (0.0298) preceded the  $B12_{\text{post-fire}}$  (0.0334). The  $BTA\_VH_{\text{post-fire}}$  reached the fifteenth value of importance (0.0316); the other SAR based, especially both the  $BTA\_VV$  layers, returned the lowest values.

### 5.3.3. Map accuracy

The accuracy of each map was evaluated using several accuracy metrics, and the resulted values are reported below. The F-score was calculated both for the single classes ( $F\text{-score}_i$ ) to have a more comprehensive measure for each of them and for all the classes ( $F\text{-score}_M$ ), thus expressing the map's overall accuracy. The initial out-of-bag (OOB) error, representing a forecast accuracy performance estimated by the RF model during the training step, was also reported.

#### 5.3.3.1. Sentinel-1

Considering the  $F\text{-score}_i$  for each class, the values are 0.732 (unburned soil/rock), 0.372 (unburned vegetation), 0.267 (low severity), 0.434 (moderate severity), 0.489 (moderate-high severity), 0.721 (high severity). The overall accuracy expressed by the  $F\text{-score}_M$  is 0.513. The OOB error was equal to 0.5101.

#### 5.3.3.2. Sentinel-2

The  $F\text{-score}_i$  for each class is 0.933 (unburned soil/rock), 0.879 (unburned vegetation), 0.615 (low severity), 0.683 (moderate severity), 0.773 (moderate-high severity), 0.898 (high severity). The  $F\text{-score}_M$  is 0.805. The OOB error was 0.7805.

#### 5.3.3.3. Optical+SAR

For each single class, the values of  $F\text{-score}_i$  reached are 0.933 (unburned soil/rock), 0.899 (unburned vegetation), 0.696 (low severity), 0.738 (moderate severity), 0.818 (moderate-high severity), 0.916 (high severity). The  $F\text{-score}_M$  resulted 0.838. The OOB error was equal to 0.7996.

## 5.4. Discussion

The burn severity maps obtained in this study provided a different level of accuracy. Although the optical information could already suffice to map burn severity, thanks to the univocal spectral properties that characterize these effects (José M. C. Pereira et al., 1999; José M.C. Pereira, 1999; J. M.N. Silva et al., 2004), the use of both types of sensors, with the integration of SAR data, leads to better accuracy values. This confirms what other authors had already observed in their studies, such as Stroppiana et al. (2015) for burn area mapping, and Tanase et al. (2015b) for burn severity mapping, proving the importance of an integrated information in burned areas monitoring

framework. When using only optical data, however, several factors can be a source of spectral confuse, especially at medium-low severity classes, such as the presence of mixed spectral characteristics within the pixels due, for example, to the mixture of unburned and partially unburned vegetation (Carmen Quintano et al., 2013). Tanase et al. (2015b) noted that the joint use of optical and SAR data improved the classification of areas unburned or affected with low severity. Other authors also considered the phenological status of vegetation as an element that can lead to errors (e.g. low photosynthetic activity, summer drought stress, leaves fall) (Gallagher et al., 2020; Inoue et al., 2019; Picotte & Robertson, 2011; Verbyla et al., 2008). Moreover, ash and smoke encrustations on the green leaves surface can alter the optical spectral reflectance (Saulino et al., 2020).

Considering the performance of only SAR data, we achieved the worst result. In other studies using SAR data, such as Addison et al. (2018), a level of 60% of overall accuracy is considered high for this type of data. The better performance of VH polarization, compared to VV polarization, in both data configuration (S1 and S1+S2) confirmed what literature reported (Imperatore et al., 2017; Lasaponara & Tucci, 2019; M. A. Tanase et al., 2015b). We achieved these results using mono-temporal image layers (pre- or post-fire) in order to understand the contribution of each of those to fire severity estimation, although the bi-temporal spectral indices resulted more correlated to CBI field measurements (Fernández-García et al., 2018; Key & Benson, 2006). Moreover, the CBI index could present different correlation performance with different vegetation cover type. Studies demonstrate that the CBI is more correlated with forest areas than with shrubs and herbs (De Santis & Chuvieco, 2009; Epting et al., 2005; Key & Benson, 2006), indicating that the performance of burn severity assessment may vary as vegetation type varies (Schepers et al., 2014).

The contribution of each input layer was explained using the feature importance analysis. The sensitivity of the NIR and SWIR bands was confirmed (José M. C. Pereira et al., 1999; José M.C. Pereira, 1999; Schepers et al., 2014). However, it is interesting to observe how the RedEdge, Red and Blue bands were also fundamental in achieving the result. Some authors had already hypothesized this aspect. Filipponi et al. (2018) proposed a second version of the burn area index (BAI2), built also using the S2 RedEdge (B6, B7) and the NarrowNIR bands. Fernández-Manso et al. (2016) tested the suitability of RedEdge-based indices for burn severity estimation, achieving good results. Fernández-García et al. (2018) use more spectral information than the other NBR type indices, combining Red, Blue, NIR and SWIR bands, considering them very suitable for initial burn severity assessments across different climatic gradients due to their respective sensitivity to atmospheric aerosols, chlorophyll levels, the cellular structure of the leaves and canopy density, and soil and vegetation moisture.

## 5.5. Conclusions

This study aims to assess the potential of integrating SAR data to optical datasets to estimate and map burn severity and contribute to the state of the art. The integration improved the accuracy of the results. A more in-depth investigation would be helpful to understand how these data can effectively complete the derived information.

In the present work, the various types of vegetation cover were not distinguished. For example, a high severity was attributed without distinction to both pastures, shrubs and forests, as required by the CBI protocol. Future studies could investigate the correlations between severity mapped and vegetation type, an essential key in post-fire monitoring and management of forest regeneration processes and spatial patterns.





## 6. Fire severity estimation and mapping: an approach using deep learning and the combined optical and SAR data

Adapted from

De Luca, G., Modica, G.: *Canopy fire effects estimation using Sentinel-2 imagery and deep learning approach. A case study on the Aspromonte National Park*. In: *Communications in Computer and Information Science (CCIS) – AII2022: International Conference on Applied Intelligence and Informatics*. Springer (2022). Accepted.

### Canopy fire effects estimation using Sentinel-2 imagery and deep learning approach. A case study on the Aspromonte National Park

Giandomenico De Luca<sup>1</sup>[0000-0002-4740-6468] and Giuseppe Modica<sup>1</sup>[0000-0002-0388-0256]

<sup>1</sup> Department of Agriculture, University *Mediterranea* of Reggio Calabria, Località Feo di Vito, 89122 Reggio Calabria, Italy {giandomenico.deluca, giuseppe.modica}@unirc.it

**Abstract.** The accurate estimation of fire severity, in terms of physical effects occurred on the tree's canopies, as well as the accurate mapping of its spatial distribution, is a necessary information to optimally quantify and qualify the damage caused by the fire to ecosystems and address the most correct remedial procedures. The development of even more accurate learning algorithms and higher resolution satellite multispectral data have become essential resources in this framework. This study proposes a deep learning approach, exploiting remote sensed satellite data, to produce the accurate severity map of the effects caused by the devastating fires affecting the Aspromonte national Park forests during the 2021 fire season. Two multispectral Sentinel-2 data, acquired before and after the fires, were classified using an artificial neural network-based model. All the multispectral fire-sensitive bands (visible, near infra-red, short-infrared) and the respective temporal difference (post-fire – pre-fire) were involved, while the selection of the training pixels was based on field-based observations. Despite the preliminary nature of this study, the map accuracy reached high values (> 95%) of  $F\text{-score}_M$  (representing the overall accuracy) already since the first test of this configuration, confirming the validity of this approach. The quanti-qualification of the fire effects reported that 35.26 km<sup>2</sup> of forest cover was affected, of which: 41.03% and the 26.04% of tree's canopies were low and moderately affected respectively; the canopies killed but structurally preserved were the 12.88%; the destroyed trees (very-high severity), instead, were the 20.05%.

**Keywords:** fire severity, remote sensing, machine learning

Forest fires are among the principal factors affecting the Mediterranean environment, both from an ecological and a socio-economic aspect (Moreira et al., 2020). The spatial distribution of burned area, the frequency of the fires and the amount of structural and physical-chemical modifications that they cause on the affected habitats activate subsequent ecological transformations and alterations of the vegetation cover and of the organic-mineral components of the soil. These factors that impact, at different temporal and spatial scales, the physiologic dynamics, the microclimate and the water balance of ecosystems might be either degradative or positive (Morresi et al., 2019; Rosa et al., 2011; Semeraro et al., 2019). Indeed, if on the one hand the fire can induce decomposition

of biomass into inorganic carbon, desertification, sterility of ecosystems and their loss of resilience, up to the destruction of entire biotic communities, on the other hand, and at the right doses of frequency and severity, the fire can stimulate the interaction and competitiveness of some Mediterranean species, activating regeneration processes and enriching biodiversity (De Luis et al., 2006; Mitchell et al., 2009; Montès et al., 2004; Moreira et al., 2020; Riaño et al., 2002). The accurate quantitative estimation and qualitative categorization of the short-term effects induced by fire on forest vegetation are therefore fundamental analysis to predict and understand their ecological and socio-economic evolution over the time and therefore to be able to plan suitable post-fire management policies.

The application of remote sensing data and techniques, especially optical satellite imagery, have been providing increasingly efficient outcomes in the characterization and mapping of the burn consequences (such as fire severity) on ecosystems (e.g. (Han et al., 2021; Meng et al., 2015; Morresi et al., 2019, 2022; Saulino et al., 2020)). The availability of free optical imaging systems with high spatial and temporal resolution, such as the multispectral Sentinel-2 satellites of the Copernicus mission managed by the European space agency (ESA) (ESA Sentinel Homepage, 2022), have encouraged the advancements in this framework. Sentinel-2 platforms (two different satellites, A and B) provide the wavelengths mainly sensitive to the fire effects, namely visible, near infrared (NIR), red-edge and short-wave infrared (SWIR) (José M. C. Pereira et al., 1999), at a native pixel resolution of 10x10m or 20x20m and with a revisit time of 2-3 days at mid-latitudes.

Simultaneously, the development of open-source and user-friendly libraries and software performing complex machine learning algorithms (e.g. OTB, Scikit-learn, TensorFlow+Keras, etc.) increased the opportunities of draw up efficient prediction and classification workflows (Bot & Borges, 2022; G. Modica et al., 2021b). Classic supervised machine learning models (principally random forest and support vector machine) rendered performing results in terms of accuracy (between 70% and 90%) when tested on high resolution optical satellite data for supervised classification of fire effects severity e.g. (e.g. Amos et al., 2019; Bot & Borges, 2022; De Luca, Silva, Oom, et al., 2021; Sali et al., 2021). Most of these works were based on the associating spectral information and field based measurements carried out using well-established protocols (e.g. CBI (Key & Benson, 2006)) for fire severity gradient estimation. In recent years, some studies went as far as to test advanced deep learning models based on artificial neural networks (ANN) in order to improve burned areas detection (Hu et al., 2021; Knopp et al., 2020), overcoming the 90% of accuracy in most of the cases. However, to the best of our knowledge, few experiments attempted to exploit deep learning models for estimating fire effects on vegetation (Farasin et al., 2020; Monaco et al., 2020).

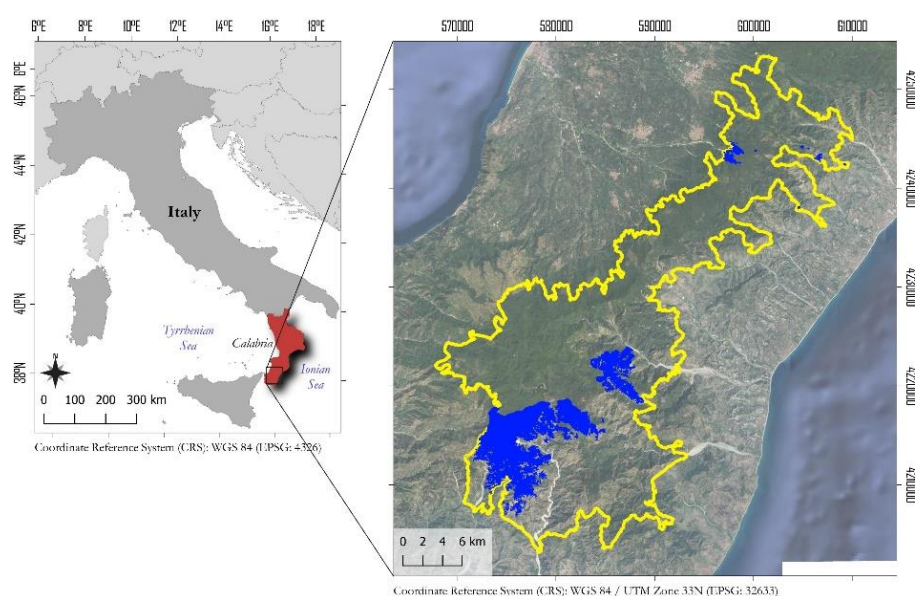
The aim of this study was to contribute to the lacking state of the art by proposing a deep learning-based approach to categorize the level of fire effects severity that have affected the forest canopies of the Aspromonte national Park (2021 fire season) using Sentinel-2 multispectral imagery. In particular, taking as training information four field-based visual physical effects that can affect canopy forest (low affected, moderately affected, highly affected and very-highly canopy), the level of fire severity was classified by performing a artificial neural network (ANN) model formed by a sequential of Dense hidden layers implemented in Keras library (Keras Homepage, 2022). The contribution of each single image layer band to the learning process was estimated by operating a feature importance based on a weighted linear regression. The single-class  $F-score_i$  accuracy metric was used to compute the accuracy performed by the classification model for each fire effect severity category. The overall accuracy was instead carried out using the multi-class  $F-score_M$ . The analysis continued by comparing the fire effects severity

result with a vegetation cover map of the Aspromonte Park (Spampinato et al., 2002) so that it was possible to investigate their distribution among the different affected forest types.

## 6.1. Study area

The fire events considered in this study involved the Aspromonte National Park (Aspromonte Park, 2022), located in the southernmost continental Province of Italy (Reggio Calabria, 38° 16'N; 15° 84'E), affecting a total area of about 70 km<sup>2</sup> and occurring between July and August 2021 (Figure 6.1). The examined events were part of a larger (>160 km<sup>2</sup>) ensemble of fire events striking the entire Province territory during the assessed fire season.

The Aspromonte Park, extending for 641.53 km<sup>2</sup> NE-SW and constituting the last continental extension of the Apennine Mountain range, is characterized by a wide phytoclimatic range (from *Lauretum* to *Fagetum*) and high heterogeneity of flora, resulting from the combination of different environmental and topographic factors (latitude, altitude range, proximity to the sea, slope exposition, etc.). Moreover, it contains 21 special habitat sites afferent to the Natura2000 network ([https://ec.europa.eu/environment/nature/natura2000/index\\_en.htm](https://ec.europa.eu/environment/nature/natura2000/index_en.htm)), pointing out its ecological and socio-economic substantial role for the territory. An exhaustive description of the Aspromonte vegetation could be found in (Spampinato, 2014). In this work, only the fire affecting forest vegetation was taken into consideration (35.26 km<sup>2</sup>), discriminated using the Aspromonte Vegetation Cover Map (Spampinato et al., 2002).



**Fig. 6.1.** Location of the study area (left). On the right, the yellow line delimits the Aspromonte national Park perimeter, while the total burned area falling inside the Park are represented in blue.

## 6.2. Materials and methods

### 6.2.1. Dataset and pre-processing

The multispectral Sentinel-2 dataset was composed of two Level 2A (Bottom of Atmosphere reflectance) (ESA Sentinel Homepage, 2022) cloud-free images acquired before (28/07/2021) and after all the fires occurred

(16/09/2022) respectively, downloaded through the Copernicus Open Access Hub (Copernicus Access Hub, 2022), the official ESA platform for the distribution of Sentinel satellite data.

All the image bands at native resolution of 10x10m (blue, B2; green, B3; red, B4; NIR, B8) were directly involved to construct the final dataset, while the image bands at native resolution of 20x20m (red-edge<sub>704</sub>, B5; red-edge<sub>739</sub>, B6; red-edge<sub>780</sub>, B7; NIR<sub>864</sub>, B8A; SWIR<sub>1610</sub>, B11; SWIR<sub>2186</sub>, B12) were resampled to 10x10m pixels spacing using the red band (B4) as pixel spacing reference and the bilinear interpolation as resampling method.

For each image band; the respective difference between post and pre-fire (delta,  $\Delta$ ) images was carried out. All the post-fire and  $\Delta$  image bands formed the final dataset employed in subsequent analysis. This according to what was done in a previous work (De Luca, Silva, Oom, et al., 2021) by the same research group in which a dataset formed by post-fire and delta Sentinel-2 image bands was modelled through random forest algorithm to estimate the fire severity in a Mediterranean site.

### **6.2.2. Field measurements and sampling points collection**

Several geo-referenced photos and descriptive notes were taken during the field sampling campaign in the period immediately after the fire events (September 2021). Supported by Google Satellite high resolution images (Google Earth Homepage, 2022), the selection of suitable sampling points (one point = one pixel) was subsequently carried out on the basis of those field data. The method of fire effects severity estimation was inspired by the CBI protocol, based on the quantification of structural and physical alterations occurred on several vegetation layers (Key & Benson, 2006). However, in this study, only the dominant and co-dominant trees cover was assessed, directly categorizing the observed alterations into one of the four severity classes: low, moderate, high and very-high. In total, 1,000 sampling points for each severity class were retrieved. Moreover, additional 250 samplings points were reserved to trace the bare soil, since it might be present between the canopy ground projection edges, leading to commission errors.

### **6.2.3. Artificial Neural Network (ANN) construction and image classification**

#### **6.2.3.1. ANN architecture and hyperparameters optimization**

The ANN structure was characterized by a sequential model of simple Dense hidden layers, in which each neuron is densely connected with each neuron of the previous/next layer. The *relu* (rectified linear unit) function was applied to activate all the hidden layers, except for the last one which was activated with the *softmax* function in order to retrieve the probability distribution of the output data. Each pixel of the dataset is labeled with the class that had reached the highest probability coefficient for that pixel. The weight regularization was implemented using a *L2 kernel regularizer* (based on the square of the value of the weight coefficients) to reduce overfitting. The *RMSProp*, *sparse\_categorical\_crossentropy* and *accuracy* finally compiled the model as optimizer, loss and metric functions respectively.

The most suitable model hyperparameters values (dimensionality of the output tensor of each hidden layer, epoch, number of batches and kernel regularizer) were determined by testing several possible combinations of pre-choose values and assessing, for each test, the training and test accuracy metric resulted. The best combination of hyperparameters, defined by the reaching of the highest validation accuracy, was kept as final configuration for subsequently prediction step. The tested hyperparameters values were: dimensionality of the layers output tensor (units for all the hidden layers) [50, 100, 250, 500, 1000]; epoch [5, 10, 20, 30, 40]; number of batches (50, 100,

150, 200, 250); kernel regularizer weight coefficient [0.001, 0.002, 0.003, 0.004]. The number of hidden layers was also tested in arrange between 2 and 5 after having set the hyperparameters.

#### 6.2.3.2. Model training and feature importance calculation

A part (1/2) of the sampling points were randomly choose, equally for each fire effect class, and used to train the ANN model. The remaining part (1/2) of sampling points were used as validation set.

The importance of each image band was estimated by performing a weighted linear regression approach on a smaller sample (20%) of relative training and validation points. The pre-built model *KernelExplainer*, implemented in SHAP library (SHAP, 2022), was used for this purpose, in which the returned coefficients and values from game theory determine the crude indicators of importance

#### 6.2.4. Accuracy assessment

Beside the accuracy metric provided by the ANN model, a confusion matrix was constructed using the same validation sampling points (1/2 of the total number of sampling points). For each severity class, the *producer's<sub>i</sub>* and *user's<sub>i</sub>* (*i* = single severity class) accuracy metrics were retrieved from the confusion matrix, and their respective single-class (*F-score<sub>i</sub>*, Eq. 6.1) and multi-class (*F-score<sub>M</sub>*, Eq. 6.2) harmonic means were calculated.

$$F\text{-score}_i = 2 \cdot (\text{producer's}_i \cdot \text{user's}_i) / (\text{producer's}_i + \text{user's}_i) \quad (6.1)$$

$$F\text{-score}_M = 2 \cdot (\text{producer's}_M \cdot \text{user's}_M) / (\text{producer's}_M + \text{user's}_M) \quad (6.2)$$

Where *i* is a single class; *producer's<sub>M</sub>* and *user's<sub>M</sub>* metrics are expressed as follows (eq. 6.3, 6.4):

$$\text{producer's}_M = (\sum_{i=1} \text{producer's}_i) / n \quad (6.3)$$

$$\text{user's}_M = (\sum_{i=1} \text{user's}_i) / n \quad (6.4)$$

Where *n* is the total number of classes.

### 6.3. Results

#### 6.3.1. Final structure of the ANN

The ANN optimal hyperparameters used in the classification process, retrieved by implementing a comparison the accuracy and loss metrics values restituted after having tested the different parameters hyperparameters combinations, are reported in Table 6.1.

**Table 6.1.** Artificial Neural Network optimal hyperparameters used in the classification process, retrieved by comparing the accuracy and loss metrics of various values combinations tested.

Hyperparameter name	Optimal value set
<i>Number of hidden layers</i>	6 Dense layers (5 activated with <i>relu</i> + 1 activated with <i>softmax</i> )
<i>Units</i> (for each Dense hidden layer)	500 ( <i>relu</i> layers) 5 ( <i>softmax</i> layer)
<i>Kernel regularizer</i>	0.0025
<i>Epochs</i>	40
<i>Batch size</i>	250

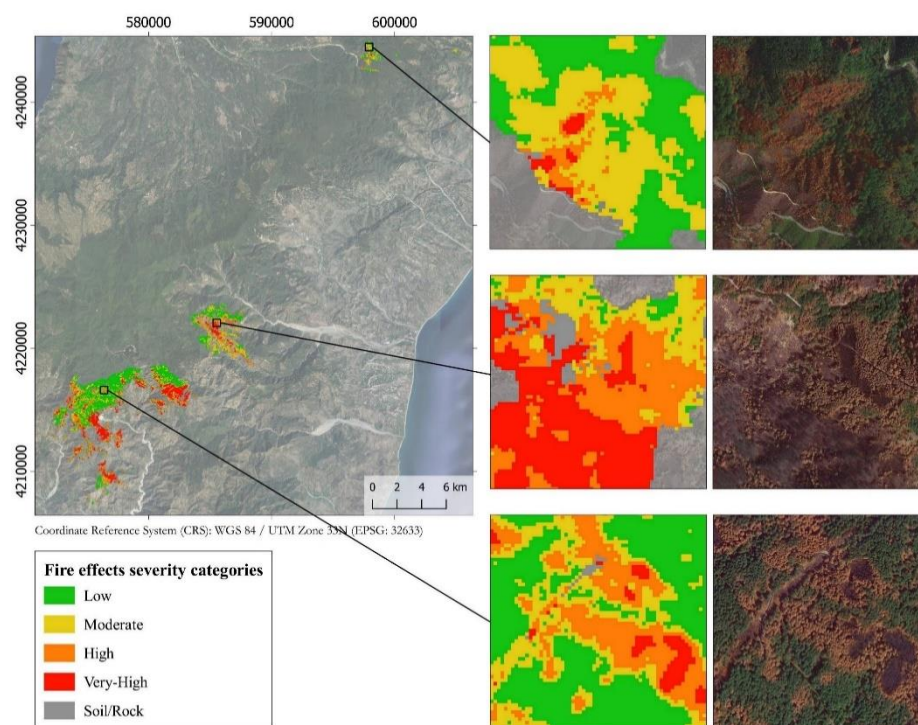
The final structure of the ANN was formed by a concatenation of layers ordered as follows: an input layer (shape: number of input image bands); five Dense hidden layer (units: 500; activation: *relu*) each of which regularized by a *Kernel regularizer* function (weight coefficient: 0.0025); a final Dense hidden layer (units: fire effect categories; activation: *softmax*).

### 6.3.2. Classified fire effects map

Figure 6.2 shows the spatial distribution of the fire effect categories resulted from the classification process (low, green; moderate, yellow; high, orange; very-high, red).

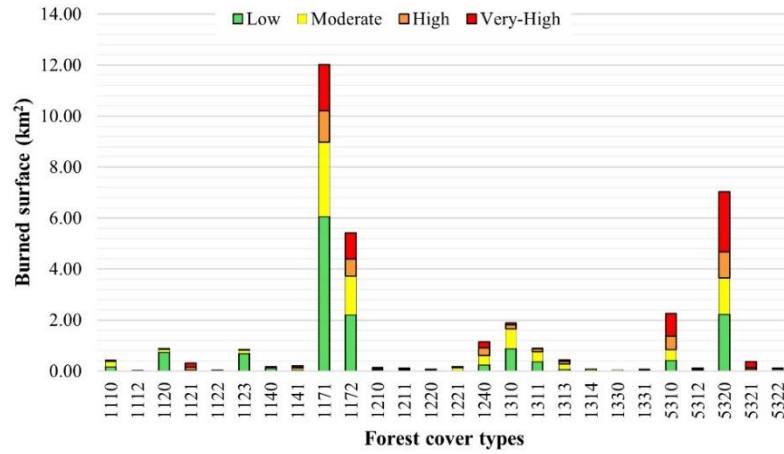
The distribution of the four fire effects among the affected forest cover types (forest cover type labels legend according to (Spampinato et al., 2002)), inside the Aspromonte Park, is illustrated in Figure 6.3.

On 35.26 km<sup>2</sup> of total forest cover burned, the fire had a lower and moderate impact on 14.47 km<sup>2</sup> (41.03%) and 9.18 km<sup>2</sup> (26.04%) of forest vegetation, respectively. A surface equal to 4.54 km<sup>2</sup> (12.88%) and the 7.07 km<sup>2</sup> (20.05%) were instead affected by high and very-high effects severity. Observing the apportionment of the fire effects categories among the forest types (burned surface > 2 km<sup>2</sup>), it is noticeable as the most affected were the areas naturally or artificially covered by coniferous, in particular by *Pinus nigra* spp. *Laricio*: “Natural pine *Laricio* forest” (Low, 6.06 km<sup>2</sup>; Moderate, 2.92 km<sup>2</sup>; High, 1.24 km<sup>2</sup>; Very-High, 1.80 km<sup>2</sup>), the “Mountain artificial (reforestation) coniferous forest with a prevalence of pine *Laricio*” (Low, 2.23 km<sup>2</sup>; Moderate, 1.43 km<sup>2</sup>; High, 1.02 km<sup>2</sup>; Very-High, 2.35 km<sup>2</sup>), the “Degraded natural pine *Laricio* forest” (Low, 2.20 km<sup>2</sup>; Moderate, 1.53 km<sup>2</sup>; High, 0.67 km<sup>2</sup>; Very-High, 1.02 km<sup>2</sup>) and the “Hilly artificial (reforestation) coniferous forest with a prevalence of pine *Laricio*” (Low, 0.42 km<sup>2</sup>; Moderate, 0.43 km<sup>2</sup>; High, 0.52 km<sup>2</sup>; Very-High, 0.88 km<sup>2</sup>).



**Fig. 6.2.** Fire effects severity map resulted from the classification process showing the spatial distribution of the four fire effects severity categories (Low, Moderate, High and Very-High) on the forest vegetation of the Aspromonte national Park.

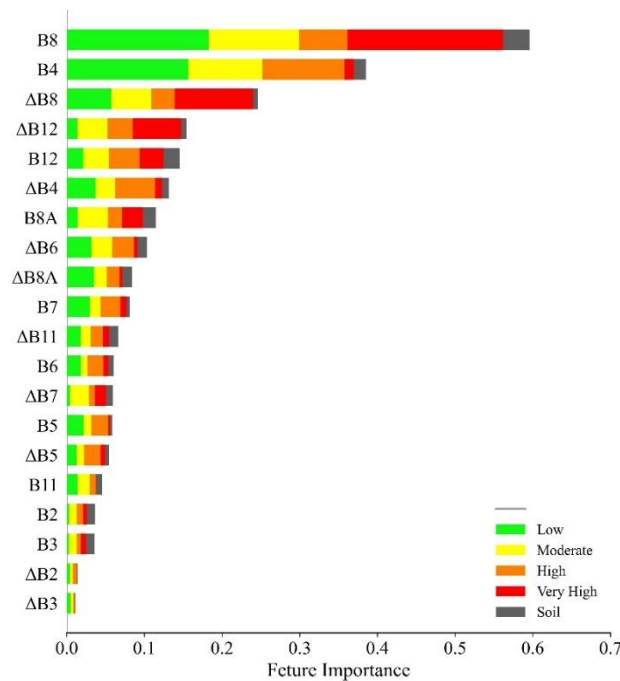




**Fig. 6.3.** Surface distribution of the four fire effects severity (Low, Moderate, High and Very-High) among the affected forest types (the legend of forest cover type is according to (Spampinato et al., 2002)).

### 6.3.3. Feature importance

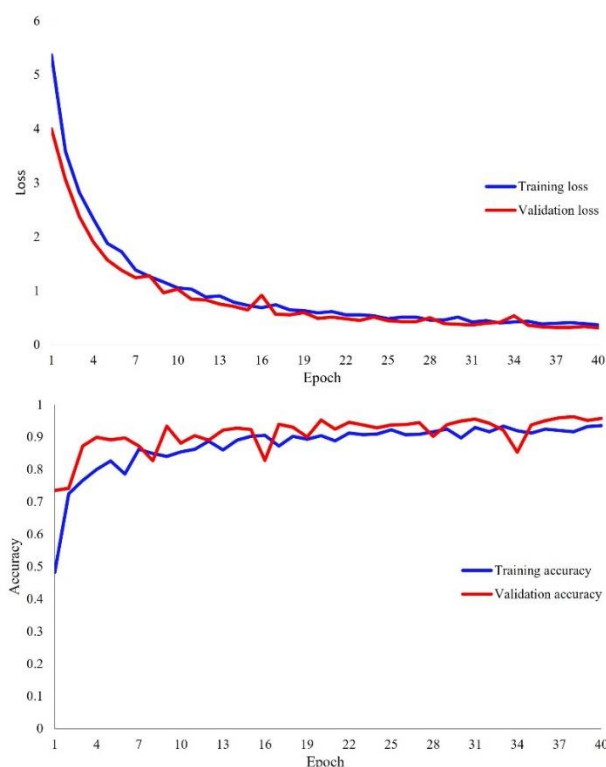
Figure 6.4 reports the importance that each image input layer exerted during the learning processing, for each of the four fire effect categories, resulted from the weighted linear regression approach. The highest importance ( $> 0.6$ ) was achieved by the post-fire NIR band, followed by red band (0.43), the  $\Delta$ NIR (0.28), the  $\Delta$ SWIR<sub>2186</sub> (0.18) and the SWIR<sub>2186</sub> (0.17). On the other hand, the green and blue image bands, and the respective  $\Delta$ , resulted to render lowest influence ( $< 0.05$ ).



**Fig. 6.4.** Feature importance (SHAP *Kernel Explainer*) exerted by each image band layer.

## 6.4. Map accuracy

Figure 6.5 report the training and validation loss (upper) and accuracy (bottom) metrics calculated directly by the ANN model.



**Fig. 6.5.** Plots displaying the values of the loss (top) and the accuracy (bottom) of training and validation processes calculated at each epoch of the classification process.

The confusion matrix retrieved in order to assess the accuracy of the map is shown in Figure 6.6. From the confusion matrix, the single-class  $F\text{-score}_i$  accuracy metric values computed for each fire effect category were 97.52% (Low), 93.01% (Moderate), 95.33% (High), 99.18% (Very-High) and 89.92% (Soil). The multi-class  $F\text{-score}_M$ , representing the overall accuracy of the map, was 95.12%.

	Low	Mod	High	Very-High	Soil	$User's_i$	$F\text{-score}_i$
Low	491	16	0	0	0	96.84%	97.52%
Mod	9	466	17	0	10	92.83%	93.01%
High	0	17	480	2	9	94.49%	95.33%
Very-High	0	0	1	486	5	98.78%	99.18%
Soil	0	1	1	0	116	98.31%	89.92%
$Producer's_i$	98.20%	93.20%	96.19%	99.59%	82.86%		

$Producer's_M$	94.01%
$User's_M$	96.25%
$F\text{-score}_M$	95.12%

**Fig. 6.6.** Confusion matrix reporting the accuracy of the classified map. The single-class  $user's_i$ ,  $producer's_i$ ,  $F\text{-score}_i$  and the multi-class  $user's_M$ ,  $producer's_M$ ,  $F\text{-score}_M$  accuracy metrics are reported.

## 6.5. Discussions

This study qualitatively and quantitatively estimated the fire effects severity that affected the forest vegetation of Aspromonte Park during the 2021 fire season. The analysis showed as conifers (*Laricio* pine) forests were the most affected, both in terms of surface and the severity. Although the high susceptibility to fire widespread is common for these forest type (A. Fernández-Manso et al., 2021; Moreno et al., 2021), other unknowns may have played a relevant role in this case: the location of the ignition points and the arrangement of the firefighting teams. The only canopy damages were considered because, though the sub-foliage layers are important from an ecological point of view (as also provided in the CBI protocol), this is not adaptable to the use of optical radiometric information due to their inability to penetrate the foliage.

The methodology for fire effects severity estimation proposed in this study based on a simple ANN model resulted to be reliable in terms of accuracy. Considering the spatial resolution of Sentinel-2, the accuracy resulting from the confusion matrix is very high and no particular case of overfitting can be found in the curves of Figure 5. The classified map spatial distribution of the four fire effects severity categories confirms what emerged from accuracy metrics. Minor exceptions are observable for soil class that was confused with moderately affected forest cover, as also proved by the confusion matrix outcomes. This could be due to the lower number of sampling points used for this class. However, the discriminations of bare soil and rocks in burned areas needs more accurate stratagems, such as the use of a longer observations (time series) (Pereira-Pires et al., 2020). In general, spectral confusion is ever expected at moderate severity gradients, caused by the concomitant presence of affected and unburned covers (De Luca, Silva, Oom, et al., 2021; Fernandez-Manso et al., 2016; Carmen Quintano et al., 2013; A M S Smith et al., 2007) and/or by the presence char and ash posed on the underlying slight exposed layers or on the foliage (De Santis & Chuvieco, 2007; Key & Benson, 2006; Rogan & Franklin, 2001). Further investigations involving spectral mixture analysis for mixed pixels accounting (Carmen Quintano et al., 2013), as well as the use of higher resolution optical images (although not free-available at the moment) could be tested to deal with the above mentioned issues.

Accounting the performance of the feature importance, the red, NIR and SWIR bands (and their respective temporal difference) are the most influent wavelengths for fire effects severity estimation, corroborating what has been widely proved in literature since earlier applications (De Santis & Chuvieco, 2007; García-Llamas et al., 2019). These are indeed the spectral bands used to construct two of the main vegetation indices already used in this context, the normalized burn ratio (NBR) and the normalized difference vegetation index (NDVI). Observing the Figure 5, the red band seems more related to the Moderate and High fires, at the expense of Very-High category. The latter appear to have been better managed by NIR and (followed by) SWIR, two chlorophyll and moisture-related wavelengths. The red-edge bands (at 739 nm and 780 nm) also expressed a medium importance. Other studies pointed out the relevance of red-edge for post-fire effect investigations (De Luca, Silva, Oom, et al., 2021; A. Fernández-Manso et al., 2016; Filipponi, 2018). In De Luca et al. (De Luca, Silva, Oom, et al., 2021), using the Gini coefficient to calculate the feature importance of Sentinel-2 bands for fire severity estimation, the B6 and B7 bands resulted decisive for the classification process. Filipponi et al. (Filipponi, 2018) proposed a new spectral indices for burned areas detection based on Sentinel-2 red-edge wavelengths. In this work, the blue and green resulted to be the less influent image bands.

## 6.6. Conclusions

This study presented an effective deep learning-based procedure to accurately estimate and map the fire effects severity that affected the Mediterranean forest vegetation of a national park. The use of these advanced artificial intelligence algorithms has been not as investigated in literature as the classic machine learning models (e.g., random forest, support vector machine, etc.). For these reasons, the proposed approach, based on a very simple ANN, was a preliminary trial which was set to test its reliability for the purpose. This study confirmed as the use of a simple Dense ANN achieves very good results and might be taken into consideration in future applications. This represents an optimal compromise between accuracy level and ease of implementation. The use of the python-based open-source and user-friendly Keras interface (on the TensorFlow architecture), in fact, enabled to exploit the calculation operations of the deep learning algorithms without requiring special programming skills. The outcomes were very promising, and next experimentation might involve more robust models for incrementing precision, such as the convolutional neural networks widely employed for image processing.

## 7. Spectral mixture analysis of forest crown fire damage

Remote sensing techniques have been extensively employed to detect and estimate the effects of fire on ecosystems (Chu & Guo, 2013; Emilio Chuvieco et al., 2019; Corona et al., 2008; I. Gitas et al., 2012a). Several scholars applied satellite multispectral optical imagery to detect burnt areas (Emilio Chuvieco et al., 2016; Filippini, 2019; Mpakairi et al., 2020; Otón et al., 2019; Pulvirenti et al., 2020; Santos et al., 2020; J. M.N. Silva et al., 2004; João M.N. Silva et al., 2019; Sousa et al., 2003), estimate the degree and the spatial distribution of burn severity (De Luca, Silva, Oom, et al., 2021; Fernández-García et al., 2018; Morresi et al., 2022; Saulino et al., 2020), and assess other consequences of the fire on environmental biological and structural features, such as biomass consumption (Garcia et al., 2017) and greenhouse gas emissions (Ostroukhov et al., 2022; Rosa et al., 2011). Most of the methodologies presented in those studies relied on the use of optical spectral indices (e.g. normalized burn ratio, NBR) and/or their temporal difference (e.g.  $\Delta$ NBR), in which the fire-sensitive infrared based bands are involved, such as near-infrared (NIR), typically related to photosynthetic tissues and chlorophyll content, and shortwave-infrared (SWIR), related to vegetation moisture content (José M. C. Pereira et al., 1999). Although highly effective for those purposes, spectral indices present some limitations for the direct estimation and quantification of the physical elements constituting the vegetation affected by fire at various degrees (De Santis et al., 2009; De Santis & Chuvieco, 2007; Leigh B Lentile et al., 2009; Carmen Quintano et al., 2013). Their empirical non-linear and non-physical relationship with real field fire consequences, based on the indirect models for combining optical reflectance to material burn consequences (Daldegan et al., 2019), does not allow the actual quantification of the elements typically present in a post-fire environment (Hudak et al., 2007; Y. E. Shimabukuro & Ponzoni, 2019; A M S Smith et al., 2007; Sander Veraverbeke & Hook, 2013). Scorched tissues, foliage and wood consumed, remaining green vegetation, and substrate color change, are some standard visual parameters generally associated to post-fire vegetation conditions and used for field-based burn severity estimation (Key & Benson, 2006; Sander Veraverbeke & Hook, 2013). Simplifying, fire affected vegetation surfaces are usually composed of a mixture of combustion products (ash and charcoal), scorched vegetation, and green live vegetation (Carmen Quintano et al., 2017). The relative abundance of each of these elements is related to the degree of burn severity (Tane et al., 2018). Assuming the image pixel as surface unit, it is clear that the assessment of post-fire effects and regeneration constitutes a sub-pixel issue that could be resolved by quantifying the proportion of each the abovementioned elements (I. Gitas et al., 2012a).

In this context, spectral mixture analysis (SMA) has been widely used for satellite-based analysis and monitoring approaches in different environmental application and in several biomes (Drake et al., 1999; Fernández-García et al., 2021; Franke et al., 2018; Y. E. Shimabukuro & Ponzoni, 2019). Similarly, applications of SMA for fire effects characterization have proven to be effective, providing some advantages in burned area detection (Daldegan et al., 2019; C Quintano et al., 2006; Sunderman & Weisberg, 2011) and as burn severity indicator (Fernandez-Manso et al., 2016; Ó. Fernández-Manso et al., 2009; Hudak et al., 2007; Kokaly et al., 2007; L.B. Lentile et al., 2006; Leigh B Lentile et al., 2009; Carmen Quintano et al., 2013, 2017, 2020; Robichaud et al., 2007; Rogan & Franklin, 2001; Alistair M S Smith et al., 2005; Tane et al., 2018; Sander Veraverbeke & Hook, 2013) and providing explicit physical meaning of post-fire components, comparable to field-based measurement protocols (Fernández-García et al., 2018; L.B. Lentile et al., 2006; Leigh B Lentile et al., 2009). The assessment of fire effects and their severity can be based on mixture composed of these three typical post-fire fractional cover components, given they directly comparability to the burn severity parameters traditionally assessed on field monitoring standard protocols (L.B.

Lentile et al., 2006; Leigh B Lentile et al., 2009; A M S Smith et al., 2007; Sunderman & Weisberg, 2011; Sander Veraverbeke & Hook, 2013), for example that proposed by Key & Benson (2006), aimed to standardize the measurements of fire effects across space and time, in a context that is otherwise characterized by its variability (Key & Benson, 2006; Sander Veraverbeke & Hook, 2013). Spectral Mixture Analysis applications for the monitoring of post-fire recovery, on the other hand, are scarcer (Fernandez-Manso et al., 2016; Riaño et al., 2002; Röder et al., 2008; Sankey et al., 2008; A M S Smith et al., 2007; Solans Vila & Barbosa, 2010; Souza et al., 2003; S Veraverbeke et al., 2012), incomparable to those based on spectral indices. The advantages of SMA for fire effects characterization relies on the accounting of sub-pixel spectral features, which enable the estimation of the direct proportion of these physical features within each pixel, and thus a more accurate delineation of real heterogeneity of fire scars (Daldegan et al., 2019; Ó. Fernández-Manso et al., 2009; Carmen Quintano et al., 2017). This makes the approach applicable to any type of optical sensor, both in terms of spectral and spatial resolution (Fernández-García et al., 2018; Leigh B Lentile et al., 2009).

The reliability of SMA results depends on endmembers (pure component) selection, these should indeed be as representative as possible of pure components constituting the spectral fraction of all image pixels (Somers et al., 2011). The selection of endmembers constitutes a key role in determining the reliability of the results of the SMA approach, being incisive in accurately fractional cover estimation (Carmen Quintano et al., 2012, 2013, 2020; Somers et al., 2011). These should indeed be as representative as possible of pure components constituting the spectral fraction of all image pixels (Somers et al., 2011). In literature is highlighted the importance of using ad-hoc techniques to define the optimal spectral endmembers (Fernandez-Manso et al., 2016; Carmen Quintano et al., 2017, 2020; Roth et al., 2012; Tane et al., 2018; Tompkins et al., 1997), even if each endmembers-selection technique might show a slight different balance between the efficiency of the created spectral library and the maintenance of the spectral variability (Tane et al., 2018). Several automatic endmember selecting algorithms were developed (Boardman et al., 1995; C. Chang et al., 2010; Dennison et al., 2004; Dennison & Roberts, 2003; Roberts et al., 2003; Tompkins et al., 1997; Winter, 1999) and common used in SMA approaches (Daldegan et al., 2019; Fernandez-Manso et al., 2016; Ó. Fernández-Manso et al., 2009; Nascimento & Dias, 2005; Carmen Quintano et al., 2020; Tane et al., 2018). A pioneer method is represented by the purity pixel index (PPI) (Boardman et al., 1995), widely exploited in literature (C. Chang et al., 2010; C -I. Chang & Wu, 2015; Chein-I Chang & Plaza, 2006; Ó. Fernández-Manso et al., 2009; Heylen & Scheunders, 2013; Nascimento & Dias, 2005; Plaza & Chang, 2005; Suryoprayogo et al., 2018).

The launch of Copernicus Sentinel-2A/B constellation by the European Space Agency (ESA) (ESA Sentinel Homepage, 2022), providing free high temporal and spatial multispectral images, enabled to fill some gaps maintained by coarser spatial resolution data. Nevertheless, few studies have applied SMA on Sentinel-2 images to analyse burned areas (Montorio et al., 2020; Carmen Quintano et al., 2019b, 2020).

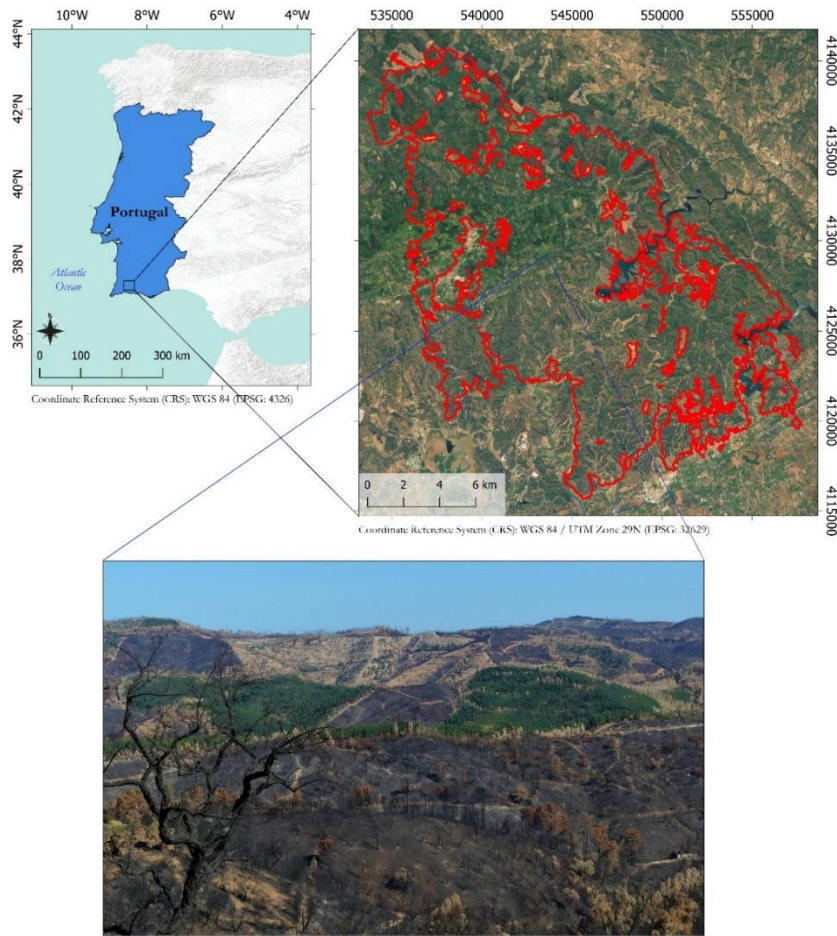
The purpose of this work was to estimate the proportion of the three fraction components indicative of the main physical effects observable immediately after a forest fire. In this regard, the present study aimed to quantitatively estimate and map three levels of physical alterations caused by the fire on tree crowns, in a large fire occurred in a Mediterranean area composed by different tree species and forest types, through the application of a linear SMA (LSMA) on multispectral Sentinel-2 data.

## 7.1. Study site

The study area is located in the Algarve (Figure 7.1), southwestern Portugal (37° 18'N; 08° 30'W), at Serra de Monchique (max. elevation 902 m). The area has a typical Mediterranean climate, with cool, rainy winter, and hot, dry summer (Köppen-Geiger climate type Csa) and is partly included in the European Natura2000 network as Special Area of Conservation (SAC) (Natura2000 Site Code: PTCON0037). Most of the forest cover is composed by eucalypt (*Eucalyptus globulus*, Labill. 1800) short-rotation plantations and evergreen cork oak woodlands composed by *Quercus* (spp. *suber* L. and *ilex* L.) and representing the typical Iberian agro-forestry systems (*dehesa* and *montado*), whose purposes are the economic activities such as cork production and grazing, in some cases mixed with secondary native species conforming the meso-Mediterranean forest ecosystem. Few isolated groups of Mediterranean coniferous (*Pinus pinea* L., *Pinus pinaster* Aiton.) plantations are also present on the study area. The remainder and larger part of the study site is covered by heathlands and/or pastures, composed by typical herbaceous and sclerophyllous shrubby species, in some areas accompanied by anthropic land covers (agriculture, urban) (Alves et al., 2007; De Luca, Silva, Di Fazio, et al., 2022; Häusler et al., 2018; Mitchell et al., 2009; J. San-Miguel-Ayán et al., 2016).

A fire event occurred on the first days (3<sup>rd</sup> - 10<sup>th</sup>) of August 2018, affecting 268.9 km<sup>2</sup> of the study area (De Luca, Silva, & Modica, 2021a). The forest cover was impacted at various degrees of severity: at highest severity only the combustion residues of biomass (ashes, charcoal and torches) remained, while the bare soil below was exposed; where the severity of the fire event was lower the canopy structure was less affected, in part consumed by direct burn or killed by proximal heating, with the (partially or totally) dead trees, and respective canopies, remained standing (scorched), while the undercover vegetation was killed and/or in part consumed; at lower severity degrees tree canopies, or at least their upper parts remained green.





**Figure 7.1.** Location of the study area in Portugal (top left). Overview of the study area (top right), with the burned area perimeter highlighted by the red line. On the bottom, a panoramic view of the landscape showing the heterogeneity of the crown damage level on the forest vegetation.

## 7.2. Data and methods

### 7.2.1. Satellite dataset and pre-processing

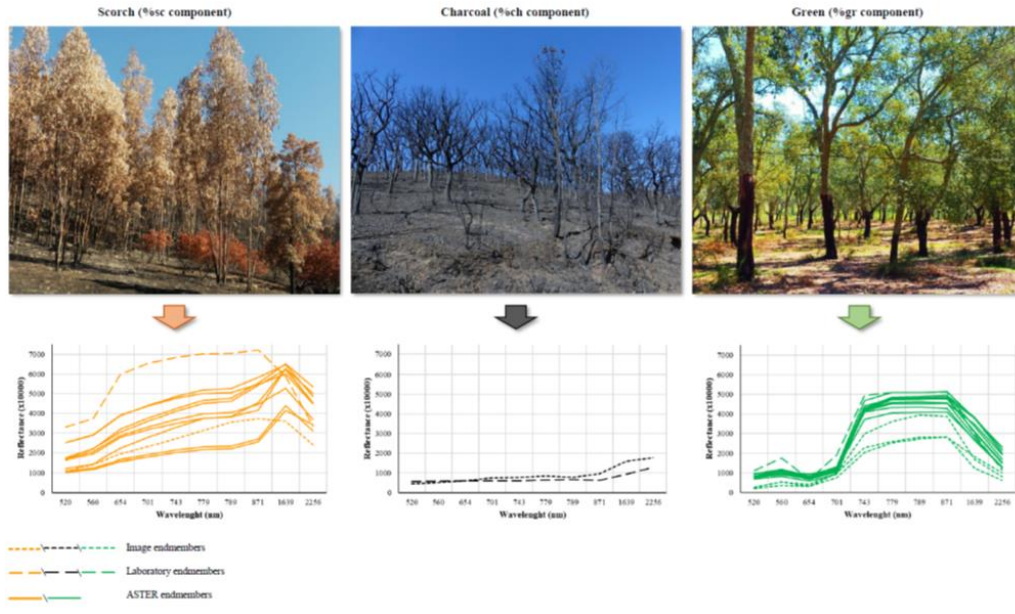
The Sentinel-2A Level 2A (Bottom of Atmosphere reflectance) optical imagery was employed to implement the LSMA. Two separated free-cloudy images, one representing the pre-fire condition (19<sup>th</sup> July 2018) and one the early post-fire condition (18<sup>th</sup> August 2018) was downloaded. Moreover, three additional free-cloudy images, each acquired every August of 2019 (13<sup>th</sup>), 2020 (27<sup>th</sup>) and 2021 (22<sup>nd</sup>) years, were retrieved in order to carry out a preliminary analysis of recovery status of forest vegetation across the first years after the event. The dataset was downloaded through the Copernicus Open Access Hub (Copernicus Open Access Hub 2022) and pre-processed using the Sentinel-2 Toolbox implemented in ESA-SNAP v.8.0.9 (ESA SNAP Homepage 2022) and executed by Snappy, the SNAP-Python interface (ESA SNAP Cookbook 2022). The pre-processing consisted of a bilinear pixel resampling to 10 m x 10 m followed by a of all the images in order to align each pixel.

### 7.2.2. Spectral endmember definition and selection

Three fraction components, indicative of the main physical effects observable in an immediate post-fire forest environment (Figure 7.2 top), were defined: % char component (%ch), representing the solid residues from vegetation combustion, with charred combustion products prominent at the surface; % scorched component (%sc), brown dead plant tissues, mostly leaves, killed by heat radiated and convected from the surface fire, with the structural elements unconsumed by fire (trunk, branches and foliage); % green vegetation component (%gr), composed by the unaffected green foliage cover. These represent the three main elements characterizing post-fire forest surface. The proportions in which they are present reflect the real heterogeneity of fire effects occurred (L.B. Lentile et al., 2006; A M S Smith et al., 2007; Sander Veraverbeke & Hook, 2013). The three pure endmembers (%ch, %sc, %gr) involved in the LSMA were chosen applying a semi-automatic hybrid selection algorithm, the purity pixel index (PPI) on a set of previously selected spectral signatures (Figure 2 bottom). For this purpose, three different sorts of sources were used to retrieve the selection of signatures: image endmembers, namely signatures directly chosen from the image; signatures taken from the ASTER v. 2.0 spectral library (Baldrige et al., 2009); a set of laboratory measured signatures using a ASD FieldSpec 3 spectroradiometer (Analytical Spectral Devices Inc., Boulder, CO, USA), carried out by the Pyrogeography Laboratory of the Instituto Superior de Agronomia (CEF/ISA), University of Lisbon. A set of pixels adequately representing the three pure components (%ch, %sc, %gr) were visually selected as image endmembers. The careful visual interpretation of the image was supported by the use of Esri ArcGIS World Imagery high-resolution satellite map (Esri ArcGIS World Imagery, 2021) and georeferenced photos took during fieldworks, hence driven by the direct knowledge of the study areas. From the ASTER spectral library, four cork oak leaf signatures and two eucalyptus leaf signatures were considered as green endmembers; the scorched component, instead, was accounted by six signatures of mixed-vegetation leaf and grass litter and three signatures of cork oak litter (no photosynthetic vegetation). The use of the spectral reflectance of dead vegetation or litter as a valid representative of the spectrum of the scorched component was used by De Santis & Chuvieco (2007). The endmembers collected with the field spectrometer were green and scorched eucalyptus leaves, and charred wood.

To ensure strict comparability between all spectral signatures used in the analysis, those ones retrieved from CEF/ISA and ASTER spectra libraries were convolved with the Sentinel-2 Spectral Response Functions v.3 (S2-SRF), for each Sentinel-2 band, in the spectral range from 300 to 2600 nm, with an interval of 1 nm.

Next, the three purest endmembers were found through PPI, to be used in LSMA of the Sentinel-2 images. The PPI algorithm repeatedly projects the spectral information on a large number of random vectors (*skewers*) counting the number of times each pixel is an extreme for each skewer, and choosing the pixels most often recorded as extreme (C. Chang et al., 2010; Nascimento & Dias, 2005). The number of skewers was set to 1000, following Nascimento et al. (2005), who found no improvements in pixel purity above this threshold.



**Figure 7.2.** The three main vegetation conditions observable in an immediate post-fire forest environment, representing the three pure components present in the image pixels (top): charred (%ch), scorched (%sc), and green (%gr). At the bottom, there are the respective spectral signatures retrieved from three different sources and converted to Sentinel-2 spectral bands: CEF/ISA spectral library, ASTER spectral library, and image endmembers.

### 7.2.3. Spectral unmixing and fraction image extraction

Once chosen the three final spectral endmembers, the proportion (relative abundance) of each pure component contained within each mixed pixel of the image was estimated by applying a non-negative constrained least squares (NN-CLS) model. The Least-squares approach family is a common mathematical procedure used by LSMA to estimate abundance (Y. E. Shimabukuro & Ponzoni, 2019; Y E Shimabukuro & Smith, 1991). This method estimates the proportion of each endmember within the pixel minimizing the sum of squared errors (residuals) (Y. E. Shimabukuro & Ponzoni, 2019). For each of the three endmembers searched, the LSMA decomposed each pixel of the multispectral input image as a weighted linear combination of the pure component spectral responses and generated an image (commonly defined as a fraction image or abundance map) whose pixels contain the abundance (the proportion, expressed in grayscale pixel value), of the respective spectral component (Carmen Quintano et al., 2012, 2013; Roberts et al., 1993; Settle & Drake, 1993; Y. E. Shimabukuro & Ponzoni, 2019; Tane et al., 2018).

### 7.2.4. Forest area masking

Since the analysis of fire effects was focused on tree crowns, it was necessary to delineate the forest areas contained within the fire perimeter in order to avoid confusion with surrounding surfaces (Daldegan et al., 2019). The integration of two masks was applied in this study in order to refine the result. First, the LULC map, retrieved as in Chapter 2, was used to select the forest cover. Afterwards, the pixels were further filtered using the tree cover density map for 2018, provided by European Environment Agency (EEA), where each pixel shows tree cover density in a range from 0-100%. A 10% was applied as threshold above which the land was considered forest, in accordance with the Food and Agriculture Organization (FAO) definition (FAO, 2020).

### 7.2.5. Relationship between fraction images and $\Delta NBR$

After the calculation of the normalized burn index (NBR) (eq. 7.1) for the pre-fire and the early post-fire images respectively, their temporal difference (pre-post,  $\Delta$ NBR) was computed.

$$NBR = (NIR - SWIR) / (NIR + SWIR) = (B8 - B12) / (B8 + B12) \quad (7.1)$$

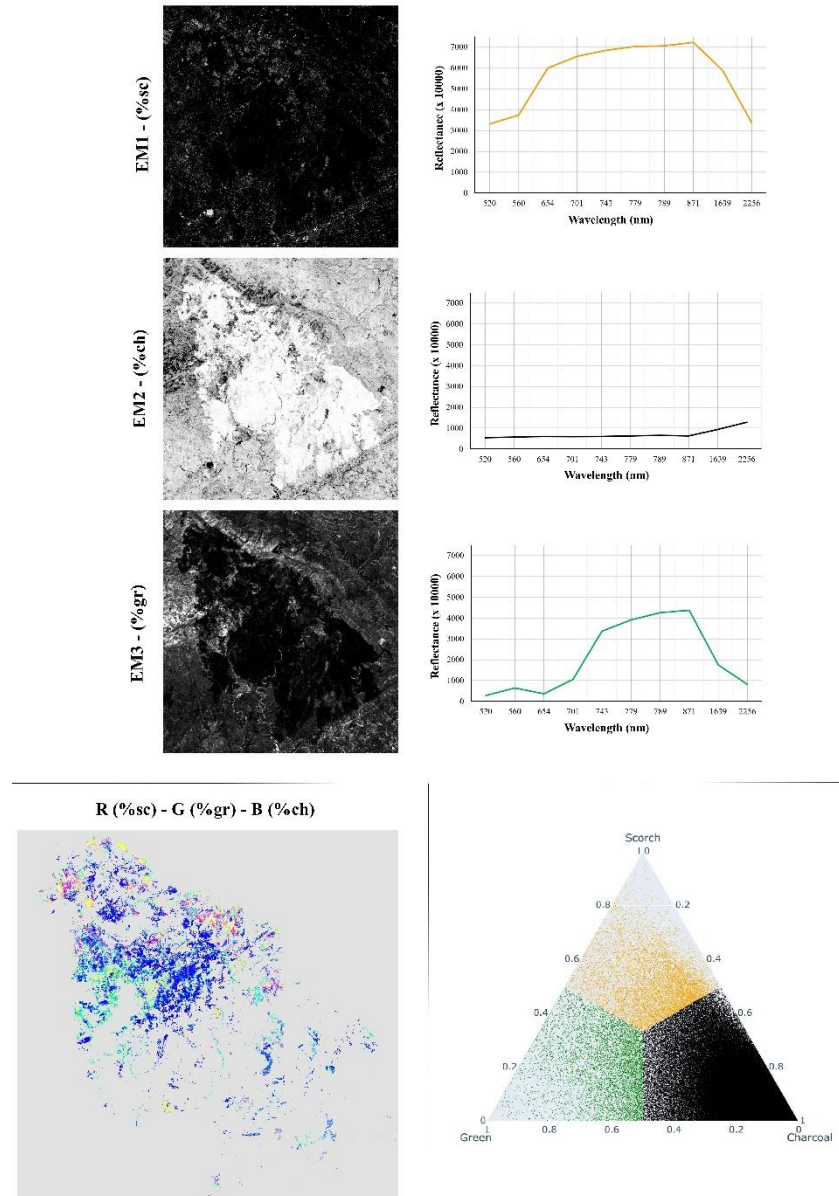
Where NIR and SWIR represent the respective bands (B8 and B12 in Sentinel-2, respectively). This index has been widely used as a spectral reference data of consequence of fire on vegetation (Ban et al., 2020; De Luca et al., 2020; De Luca, Silva, & Modica, 2021a; Donezar et al., 2019; Morresi et al., 2019) because the high fire sensitivity of its composing bands (José M.C. Pereira, 1999). For this reason, the bivariate relationship between the fraction images and the corresponding  $\Delta$ NBR pixels was investigated by plotting the respective scatter plots. Additionally, the distribution of  $\Delta$ NBR pixels into the respective resulted clusters was also investigated.

### 7.3. Result

#### 7.3.1. Selected endmembers and derived fraction images

Figure 7.3 reports the three endmembers, in the form of spectral signature, selected by the PPI index. All the signatures have been adapted to the Sentinel-2 wavelength centres using the S2-SRF function. The EM1 represents the scorch component of the spectre, characterized by a general higher reflectance in all the bands compared to the other two components, especially to the green component (EM3); minimum pics of reflectance ( $p$ ) at 490 nm (Blue) and 2190 nm (SWIR) with, respectively, 3319.59  $p$  and 3363.84  $p$ ; oppositely, the maximum pic is observed at 865 nm (NIR) reaching 7220.60  $p$ . In the SWIR domain, the EM1 maintained a decreasing trend as the wavelength increase, similarly to the EM3 trend. The former differs, in addition to the aforementioned greater reflectance, due to the absent inflection at the level of the Green band, typical of photosynthesizing vegetation spectral behaviour. The EM3n in fact, presents the typical patterns of green vegetation, with a higher absorption of Blue (289.00  $p$ ) and Red (360.00  $p$ ) opposed to a slight reflection in Green wavelength (346.00  $p$ ), and a maximum pic at 865 nm (4374.00  $p$ ) followed by a decrease to 819.00  $p$  at higher SWIR wavelength (2190 nm). The charcoal component, represented by EM2, is characterized by a linear and slightly increasing pattern, with a minimum at 490 nm (546.70  $p$ ) and a maximum at 2190 nm (1288.85).

The fraction images, generated from the application of the NN-CLS spectral mixture model to the image acquired in 2018, and representing the proportion of each of the three endmembers (scorch, charcoal and green), are shown in Figure 3 alongside the respective endmember. The value of each pixel is directly associated with the proportions (abundance) (in a range between 0 and 1) of each of the three respective endmembers of the scene selected through PPI index. The grey-scale colour makes perceptible the prevalence of charcoal component (EM2), in terms of both occupied area and proportion, considering the higher the proportion the brighter the colour of the pixel. This more evident observing the RGB map located in the lower left corner (representing the proportion of the three components for only the areas occupied by forest vegetation after masking the land cover classes, as defined in Section 3.4), where the %ch component (Blue) occupied most of the surface compared to %gr (Green) and %sc (Red). The ternary plot (lower right corner), finally, illustrates the proportion of each single pixels among the three components (relative to only the forest areas showed by RGB map) as potion in an equilateral triangle. The observed result corroborates what has just been said, with the point cloud shifted mainly towards the vertex representing the charcoal component.



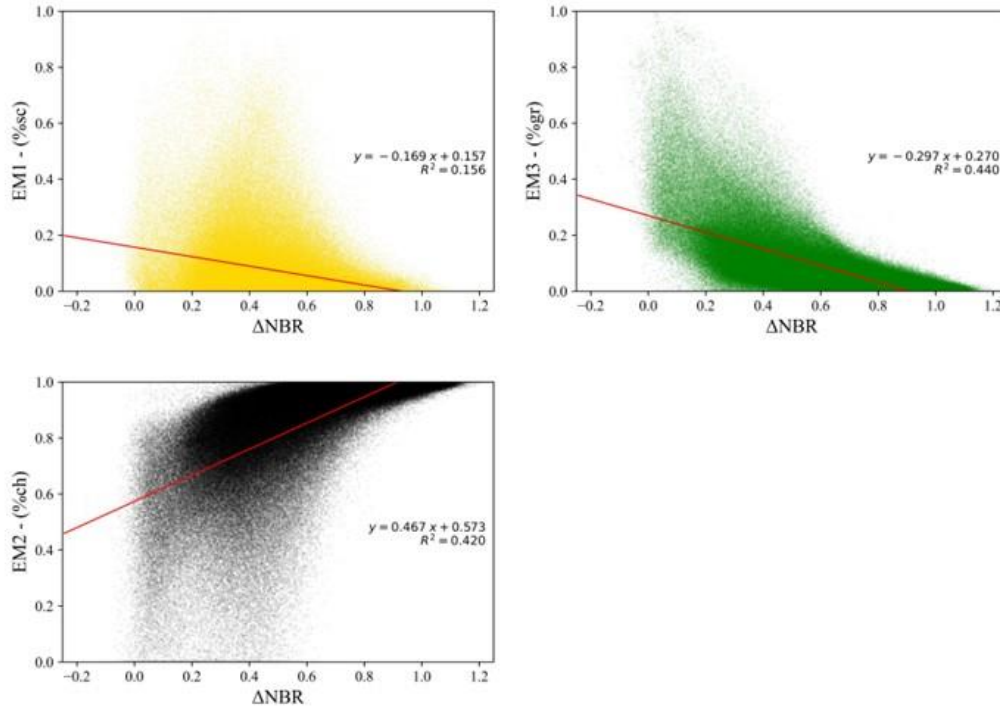
**Figure 7.3.** At the top, the three endmembers (EM1, %sc; EM2, %ch; EM3, %gr) selected through PPI analysis and the respective fraction images extracted by means of NN-CLS spectral mixture model for the post-fire 2018 Sentinel-2 image. At the lower left corner, the RGB map constructed using the three components %sc (Red, R), %gr (Green, G) and %ch (Blue, B) on the pixels occupied by only forest vegetation after the background had been masked (Section 3.4). At the lower right corner, a ternary plot is presented in which the proportion of each single pixels among the three components is accounted as portion in an equilateral triangle. The ternary plot was computed using the pixels occupying forest areas already illustrated in the RGB map; the colour palette follows that of the respective EM.

### 7.3.2. Relationship with $\Delta NBR$

The scatterplots representing the bivariate relationship between the three EMs and the  $\Delta NBR$  data are shown in Figure 7.4. The regression curve was calculated for each plot and reported, as well as the relative  $R^2$ . The EM2 and the EM3 show an expected opposite behaviour. The  $\Delta NBR$  has higher value where the %ch component is more abundant. Conversely, %gr and NBR are inversely related also. The relationship between %sc and  $\Delta NBR$



presented inverse proportionality, although low values of EM1 did not correspond to such high values of  $\Delta\text{NBR}$  as seen for EM3, while medium and higher EM1 values had also a sparser average distribution in the scatter plot.



**Figure 7.4.** Scatterplots showing the bivariate relationship between each EM (EM1, top; EM2, middle, EM3, bottom) and the  $\Delta\text{NBR}$  pixel values. For each scatterplot, the linear regression curve (red line) was calculated and the relative  $R^2$  was reported.

## 7.4. Discussion

### 7.4.1. Endmembers selection

Endmembers should be spectrally representative of the features of interest. Several authors suggest (Fernández-García et al., 2021; Carmen Quintano et al., 2013, 2017; Shimabukuro & Ponzoni, 2019) that the selection of the endmembers from the image is more convenient because there are no problems of spectrum scale divergence, that the selection of the endmembers from the image is more convenient because: i) are easy to retrieve, ii) are in the same radiometric scale of the analyzed image, iii) incorporate the same spectral corrections of the analyzed image, iv) involve the specific spectral variability of the scene. The highest spectral purity of target components can, instead, be obtained from signatures measured in field or laboratory although they do not account for the atmospheric influence and/or image noise generally addressed with calibration and correction techniques (Drake et al., 1999; Carmen Quintano et al., 2013, 2017). On the other hand, is difficult to find the ideal conditions in which image pixels are fully occupied by a pure component. This difference is observable in Figure 2, where the signatures deriving from the two different ASTER and CEF/ISA spectral libraries had very close values even if they were taken in different areas and at different times. Oppositely, the signatures of the image endmembers, which inevitably have to contend with impurities, show higher intra-variability, which generally is as apparent as

the lower the resolution (Tane et al., 2018). Some authors have effectively exploited the advantages of the combined use of endmembers deriving from different sources (e.g. image and laboratory (Rogan & Franklin, 2001); image, field and laboratory (Tane et al., 2018) field and/or laboratory). Fernandez-Manso et al. (2016) incorporated both image and reference endmembers to build the initial spectral library, to then define the optimal spectra through the use of selection indices.

Observing the resulting three endmembers (EM1, EM2 and EM3) in Figure 7.3, the semi-automatic hybrid method of endmember selection proposed in this study (based on both image and laboratory endmembers sources) demonstrated to be appropriate for its purpose. The initial step of spectral signature filtering and selection, using the PPI index, enabled to minimize the potential noise caused by signatures not conforming to the searched components (%sc, %ch, %gr). Moreover, the multi-source origin of the spectral library made it spatially and temporal generalized, a key prerogative to reduce the slight variability in reflective characteristics of a specific cover across the scene which could be caused by different environmental and site-specific variables (sunlight angle, topographic effects, site-specific soil characteristics, canopy exposition, plant-plant specific characteristics) (Carmen Quintano et al., 2013; Y. E. Shimabukuro & Ponzoni, 2019; Somers et al., 2011). Nevertheless, the eventual effects of the different spectral scales caused by the different spectral sources used should be deeply investigated. Tane et al. (2018) reported that the use of spectra collected at different location and spatial scales is a common practice to model cover fractions and suggested that it could be easily converted for fire scar assessment, at least a regional scale. Actually, the same authors found some biases when study areas-specific endmembers were used at coarse spatial resolutions. In Quintano et al. (2013) are reported some other authors affirming that the three post-fire components (%sc, %ch and %gr) are quite similar across a large range of ecosystems. Vereverbeke et al. (2013) also simplified the research on the main three components that reached a high correlation to GeoCBI (brown, black and green), pointing out that pure pixels do not occur for many land cover classes in post-fire environments. Although, on one hand, Sunderman & Weisberg (2011) suggest that the use of endmembers directly measured on the field immediately after the fire by using a spectroradiometer might improve the results, on the other hand, the use of specific field-measured spectral signatures excludes more the applicability of the methods to other generic study areas, or at least sharing similar Mediterranean biome, which was the purpose of this study. The second step, finally, using the automatic PPI algorithm to reduce the size of the just created large spectral library, was able to keep endmembers variability and their coherence with respective post-fire true field-elements reflectance signatures (Figure 3).

Concerning the choice of considering together the main species representing the vegetation LULC types present on the scene (*Q. suber*, *Q. ilex*, *Eucaliptus*, *Pine*) as unique component %gr, this was possible since these targets exhibited similar spectral responses (Figure 7.2). Considering the %sc component, the comparison of the curves confirms that the spectral signature of dead leaf litter is very similar to the spectrum of a scorched tree canopy, as already mentioned by De Santis et al. (2007).

#### **7.4.2. Fraction images analysis**

The LSMA applied on Sentinel-2 imagery successfully characterized the effects of fire on Mediterranean forest vegetation. The satellite spectral information was translated into physical information proportions of the three post-fire related components analyzed in each pixel: scorch (dead or non-photosynthetic vegetation, characterized by brown/ochre colour), charcoal (biomass totally carbonized, characterized by black color) and green vegetation, unaffected by fire.



Observing the post-fire short-term fraction images (Figure 7.3), the preponderance of %ch fraction over the other two components is noticeable. Indeed, most of the study area was covered by shrubs and/or herbaceous vegetation, besides the undergrowth settled under the forest cover (De Luca, Silva, Di Fazio, et al., 2022; De Luca, Silva, Oom, et al., 2021), inducing the formation of a charcoal and ash layer constituted by burned vegetation and litter. The charcoal (black) is the fraction more directly correlated to the biomass portion lost/consumed and to the carbon emission (Carmen Quintano et al., 2020), an effective quantitative indicator of the real physical effects of fire on vegetation (L.B. Lentile et al., 2006). For this reason, several studies proved that it could be used as unique estimator of burn severity, enabling a higher accuracy than vegetation indices (Ó. Fernández-Manso et al., 2009; Hudak et al., 2007; L.B. Lentile et al., 2006; Leigh B Lentile et al., 2009; Carmen Quintano et al., 2013, 2017, 2020; A M S Smith et al., 2007; Sander Veraverbeke & Hook, 2013). Quintano et al. (2020) observed as the proportion of charcoal, together with the evapo-transpiration driver, were the variables that most contributed to model the burn effect.

Observing the bivariate relationship with  $\Delta NBR$  (Figure 7.4), some of the pixels belonging to the %gr and %sc are superimposable. This is admissible considering the similarity that the two classes might have, for example when the fire-induced stress affect the surrounding alive green vegetation weakening its spectral response; or, inversely, due to the presence of still green foliage among scorched canopy (A M S Smith et al., 2007). The superimposition with %ch component should be mainly caused by the exposure of the char carpet covering the ground (De Santis & Chuvieco, 2007; Rogan & Franklin, 2001). Commonly, the higher severity classes are associated to high value of  $\Delta NBR$ , and vice versa. The bivariate relationship carried out in this study corroborate this aspect.

#### **7.4.3. Additional general observations**

The findings of this study showed a high effectiveness of SMA methods to delineate the high heterogeneity that characterize the crown damage level (L.B. Lentile et al., 2006). The ways in which the fire disturbs forest vegetation, in fact, are very variable due to several local environmental factors strongly influencing fire spread and intensity, and driving the formation of diversified conditions and degrees of burn and unburned patterns (Daldegan et al., 2019; Key & Benson, 2006; L.B. Lentile et al., 2006). The sub-pixel level analysis performed with spectral unmixing allows to account the different fire-related elements contained in each of these mixed pixels, which otherwise would not be representative of any of the objects present inside the portion of surface. This is obviously also applied to post-fire recovery monitoring. As stated by Veraverbeke et al. (2012), typical mixed composition of satellite pixels that characterize the post-fire vegetation regrowth establishes a sub-pixels issue. Daldegan et al. (2019) observed that sub-pixel SMA is able to detect recurrent fire scars occurred a few time previously, for which, if simple spectral indices were used, the reflectance signal would be so faint as to be confused with the fractions of vegetation spectral response that has grown back in the meantime.

Fraction images are based on full multispectral dimensionality information of sensor data, exploiting all the available reflective wavelengths, instead of a ratio between few bands like as vegetation indices (Carmen Quintano et al., 2020; Sunderman & Weisberg, 2011; Sander Veraverbeke & Hook, 2013).

As observed by Veraverbeke et al. (2013), the use of SMA is a necessary information, rather than complementary, when quantitative physical parameters relative to post-fire effects on vegetation need exanimating (e.g. the biomass lost). The estimation of biomass consumption or carbon emission, for example, requires the quantification of

complex physical indicators, among which the charcoal fraction could be included for its directly relationship, difficult to obtain through the only empirical relationship offered by vegetation index-based models.

## **7.5. Conclusions**

Post-fire immediate consequences quantification and mapping, with the essential distinction of crown fire from surface fire, is an important step in allowing inferences on fire behavior and ecosystems responses, which are important both for fuel management and for fire suppression.

This paper investigated the utilization of LSMA on multispectral Sentinel-2 satellite imagery, to analyze, quantify and map three main physical components observable at the forest tree crown level as effects of the occurrence of a fire: charcoal component, scorch component, and green component. Results complement the findings of a small set of previous studies that support the use of SMA in mapping fire effects and severity due to its ability to produce fractions representative of subpixel components directly related to fire severity.

The main challenge for SMA to become a global means of objective post-fire condition analysis is to determine an adequate basic spectral library (Tane et al., 2018). In this study, the application of LSMA involved a semi-automatic hybrid method to select the most suitable endmembers. The effectiveness of a post-fire effects analysis method is also dependent on its ability to capture the great variability of the phenomenon. LSMA fraction products, being more related to the field-based parameters such as those revealed in CBI (scorched canopy, canopy consumed, charred wood, green canopy, etc.), is more suitable to deal with heterogeneity (Sander Veraverbeke & Hook, 2013). Their physical meaning makes this information adequate for the construction of general standard models for evaluating the effects of fire, at least in the same biome (in this case, the Mediterranean), to be integrated with common methods based on spectral indices.

In this study only a heterogeneous study area was evaluated, however further analyzes are needed on different Mediterranean study areas in order to better evaluate their effectiveness and to encourage the development of improved techniques involving the increasing availability of free images at finer spatial and temporal resolutions (eg Sentinel-2) and open-source software. Considering this last aspect, noticeable is the advantageous operability and increased sharing capacity that Python-based libraries guarantee.

## 8. Temporal vegetation recovery post-fire

Adapted from

De Luca, G., Silva, J.M.N., Modica, G.: *Short-term temporal and spatial analysis for post-fire vegetation regrowth characterization and mapping in a Mediterranean ecosystem using optical and SAR image time-series*. *Geocarto Int.* 1–35 (2022). <https://doi.org/10.1080/10106049.2022.2097482>.

GEOCARTO INTERNATIONAL  
<https://doi.org/10.1080/10106049.2022.2097482>



OPEN ACCESS

### Short-term temporal and spatial analysis for post-fire vegetation regrowth characterization and mapping in a Mediterranean ecosystem using optical and SAR image time-series

Giandomenico De Luca<sup>a</sup> , João M. N. Silva<sup>b</sup> and Giuseppe Modica<sup>a</sup>

<sup>a</sup>Dipartimento di Agraria, Università degli Studi Mediterranea di Reggio Calabria, Reggio Calabria, Italy; <sup>b</sup>Forest Research Centre, School of Agriculture, University of Lisbon, Lisboa, Portugal

#### ABSTRACT

In the present study, the temporal and spatial dynamics of the post-fire recovery of different Mediterranean vegetation types during the three years after the fire event were analyzed, according to different fire severity categories, integrating the use of Synthetic Aperture Satellite Radar (SAR) (Sentinel-1) and optical (Sentinel-2) image time series. The results showed that Mediterranean forest species and shrub/herbaceous species are adapted to fire, with high efficiency in restoring the vegetation cover. Differently, the ecological vulnerability of non-native eucalyptus plantations was found in a lower recovery trend during the observation period. The use of optical short-wave infrared (SWIR) and SAR C-band-based data revealed that some ecological characteristics, such as the woody biomass and structure, recovered at slower rates, comparing to those suggested by using near-infrared (NIR) and red-edge data. An optimized burn recovery ratio (BRR) was proposed to estimate and map the spatial distribution of the degree of vegetation recovery.

#### ARTICLE HISTORY

Received 27 February 2022  
Accepted 29 June 2022

#### KEYWORDS

Random forest (RF) regressor; fire severity mapping; burn recovery ratio (BRR); optical and SAR time-series; vegetation recovery rate

Mediterranean ecosystems are critical at the European level due to their high biodiversity and intense interaction with human activities (Aragones et al., 2019; Moreira et al., 2020). The typical climatic regime of the Mediterranean region, characterized by long periods of summer drought, entails an increasing wildfire risk in terms of frequency, extension, and severity (Emilio Chuvieco, 2009; Moreira et al., 2020). This latter factor, defined as the degree of environmental chemical-physical alterations, decomposition, and loss of above/belowground organic matter caused by fire (Keeley, 2009; Key & Benson, 2006), plays a critical role in the sustainability of Mediterranean habitats, influencing the competitive interactions between species and their post-fire recovery capability (Fernández-García et al., 2018; Frazier et al., 2015; Lacouture et al., 2020; Morresi et al., 2019; Tanase et al., 2011). Moreover, the widespread accumulation of woody fuel, consequent to the abandonment of the semi-natural and agricultural areas that have been occurring in Mediterranean territories, causes suitable conditions for the ignition and the progress of such high intensity/severity fires (Xofis et al., 2022). After a forest fire, the spatial

and temporal analysis of both the fire severity and the vegetation response and recovery is a crucial step for assessing the fire impact on ecosystems and their capacity to reestablish the ecosystem services partially lost due to the fire (Huang et al., 2020; Ryu et al., 2018; Semeraro et al., 2019). The post-fire recovery of vegetation cover structure promotes the restoration of numerous ecosystem services, such as the carbon sequestration induced by the regenerating process of forest vegetation, which mitigates the carbon emissions to the atmosphere due to fire (Frolking et al., 2009; Huang et al., 2020; Morresi et al., 2019; Semeraro et al., 2019).

The efficiency of remotely sensed data applied to wildfire assessment has increased significantly in the last decade, thanks to the availability of satellite imagery at increasing spatial, spectral, and temporal resolutions (Chu & Guo, 2013; Emilio Chuvieco et al., 2019; García-Llamas et al., 2019; I. Gitas et al., 2012a; Mallinis et al., 2018). Remote sensing techniques based on time-series of optical vegetation indices (VIs) have been widely used for post-fire analysis and monitoring (Chompuchan & Lin, 2017; Chu & Guo, 2013; Frazier et al., 2015; I. Gitas et al., 2012a; Gouveia et al., 2010; Huang et al., 2020; Meng et al., 2018; Morresi et al., 2019; Ryu et al., 2018; Semeraro et al., 2019). VIs maximize the sensitivity to plant biophysical characteristics and reduce the effects of atmosphere, surface topography and soil variability (Morresi et al., 2019; Xofis et al., 2022). The normalized difference vegetation index (NDVI) is widely employed to detect and examine the post-fire vegetation recovery using a multi-temporal approach (Fernández-García et al., 2018; Goetz et al., 2005; Lacouture et al., 2020; George H. Mitri & Gitas, 2012; Morresi et al., 2019; A Polychronaki et al., 2014; Ryu et al., 2018; Semeraro et al., 2019). Other VIs based on shortwave infrared (SWIR) bands are also applied for long-term post-fire vegetation monitoring (Chen et al., 2011; Chompuchan & Lin, 2017; Epting et al., 2005; Grabska et al., 2020; Kennedy et al., 2012; Morresi et al., 2019; Ryu et al., 2018; Semeraro et al., 2019). Semeraro et al. (2019) showed that integrating NIR and SWIR data improved vegetation water content retrieval. Morresi et al. (2019) also used the NDVI and SWIR-based indices (normalized burn ratio, NBR and normalized difference moisture index, NDMI) to analyze the post-fire recovery dynamics in Mediterranean landscapes; the latter indices are more sensitive to those purposes.

Despite their proven efficiency in fire effects analysis, optical data have some limitations, namely the presence of clouds (Huang et al., 2020; Lacouture et al., 2020; Minchella et al., 2009; Morresi et al., 2019). Also, the spectral confusion between cloud shadows and burned areas creates considerable difficulties in discriminating one from the other (Emilio Chuvieco et al., 2005; José M. C. Pereira et al., 1999). Furthermore, NIR-based VIs can be affected by earlier saturation already at relative low conditions of vigorous photosynthetic activity and growth of the leaf structure due to their high sensitivity to the chlorophyll content and their high correlation with the leaf area index (LAI) (Chompuchan & Lin, 2017; Huang et al., 2020; Minchella et al., 2009; Q. Wang et al., 2005). Moreover, the optical waves do not penetrate the canopy, only providing information on the regeneration of the most superficial vegetation layers (Chompuchan & Lin, 2017). In the context of post-fire monitoring, this translates into a fast recovery of the VIs values, close to those of pre-fire conditions, corresponding to an overestimation of full recovery of the ecosystem and a not entirely realistic relationship between fire severity and post-fire regrowth dynamics (Meng et al., 2015, 2018; Tanase et al., 2011; Wang et al., 2005; Zhou et al., 2019). Some studies (e.g., Morresi et al., 2019; Ryu et al., 2018), analysing long-term post-fire spectral dynamics, observed that SWIR-based VIs express a more gradual temporal recovery rate than NDVI. The latter was 1-5 years earlier due to its greater sensitivity to photosynthetically active vegetation, combining the red and NIR bands. However, other scholars stated that spectral optical signals remain coherent only when restricted to the first decade after the disturbance (Frazier et al., 2015; Kennedy et al., 2012; Tanase et al., 2011).

In this context, active synthetic aperture radar (SAR) can integrate optical information in vegetation recovery analysis and mapping (Chen et al., 2018; Martins et al., 2016; Minchella et al., 2009; Tanase et al., 2015). Its high sensitivity to the structural properties of the vegetation, with a generally linear correlation between backscatter and vegetation biomass (Chen et al., 2019; Martins et al., 2016; Quegan et al., 2000; Saatchi, 2019; Saatchi et al., 2012; Yu & Saatchi, 2016), and its capabilities for all-weather and solar radiation independency, make the SAR backscatter complementary information with optical data (Minchella et al., 2009; Polychronaki et al., 2014; Tanase et al., 2011; Zhou et al., 2019). SAR data, however, has its challenges. The complex interactions between the backscatter and scattering components of the soil and vegetation affected by the fire are influenced by intrinsic SAR sensor/signal parameters (e.g., wavelength, polarization, incidence angles, look direction), structural/geometrical (objects structure, amount of scattering elements, surface roughness, geometry and topography of study area) and dielectrics characteristics of the affected surfaces, as well as environmental conditions (e.g., soil moisture, rain, wind) (Ban et al., 2020; Chen et al., 2018; De Luca, Silva, & Modica, 2021a; Tanase et al., 2014; Tanase, Santoro, De La Riva, et al., 2010; Tanase, Santoro, Wegmüller, et al., 2010). Among these factors, the wavelength is the one that most influences the ability of waves to penetrate vegetation cover, and thus the type and amount of information that can be derived about the impact of disturbance on it (Tanase et al., 2011). SAR shorter wavelengths (e.g., C-band, 3.8-7.5 cm) mainly interact with vegetation scattering elements such as leaves/needles, twigs and small branches, or herbaceous vegetation; this reduces the capacity to penetrate the regrowing dense forest canopy, meanwhile becoming less sensitive to structural modifications of vegetation strata (Chen et al., 2018; Minchella et al., 2009; Paloscia et al., 1999; Saatchi, 2019; Santi et al., 2017; Tanase et al., 2011). Moreover, the different polarizations of the SAR signal affect the interaction with the forest surface. Immediately after a disturbing event and for the first year after, the scattering effect of the damaged vegetation structure is lacking/decreasing. At the same time, the contribution to the back diffusion by the humidity and the roughness of the exposed soil is higher. In Mediterranean ecosystems, this generally results in a lowering of the cross-polarized signal, interacting with multiple scattering within the forest canopies (volume scattering), and an increase in the co-polarized signal, interacting with small branches, stems and, principally, the ground surface (direct and specular backscatter) (De Luca, Silva, & Modica, 2021a; Imperatore et al., 2017; Richards, 2009b; Saatchi, 2019a). The backscatter, indeed, typically increasing with forest biomass, has been found more directly correlated to above-ground biomass at cross-polarization than co-polarizations (Saatchi, 2019a; Saatchi et al., 2012; Yu & Saatchi, 2016). Both polarizations can be decisive in detecting better the different effects of fire on vegetation (Chen et al., 2018; Tanase et al., 2014). SAR polarimetric indices were generally employed for environment monitoring (De Luca, Silva, & Modica, 2021a; De Luca et al., 2021; Kim et al., 2014; Mandal et al., 2020; Nasirzadehdizaji et al., 2019; Periasamy, 2018; Pipia et al., 2019; Saatchi, 2019).

This work builds on previous research based on Sentinel-1 (S1) adapted dual-polarimetric SAR indices (dual-polarization SAR vegetation index, DPSVI; the radar vegetation index, RVI) applied to burned areas detection (De Luca, Silva, & Modica, 2021a), with the addition of the radar forest degradation index (RFDI), for burn severity estimation and mapping (De Luca, Silva, Oom, et al., 2021).

Among the several space agencies providing satellites platforms operating both optical and SAR sensors at different spatial, temporal and spectral resolutions (Emilio Chuvieco et al., 2019), the Copernicus missions by European Space Agency (ESA) include in its fleet both C-band band (centre wavelength of 5.6 cm) SAR (S1), with both cross- (VH) and co- (VV) polarizations, and multispectral (Sentinel-2, S2) sensors, each of which

consists of two polar-orbiting satellites (S1A/B and S2A/B, respectively) (ESA Sentinel Homepage 2022). The high spatial and temporal resolution makes the Copernicus constellation particularly suitable for mapping, quantitative-qualitative characterization, and temporal monitoring of the effects of fire on ecosystems; its free availability, moreover, is a fundamental attribute in risk management and monitoring framework (De Luca, Silva, & Modica, 2021a; De Luca, Silva, Oom, et al., 2021; Gitas et al., 2012; Martinis et al., 2017; Tanase et al., 2011; Tanase et al., 2020; Verhegghen et al., 2016).

Although numerous studies are using SAR C-band S1 or/and optical S2 imagery for burned area detection (Ban et al., 2020; Carreiras et al., 2020; De Luca, Silva, & Modica, 2021; Donezar et al., 2019; Pulvirenti et al., 2020; Roteta et al., 2019; Tanase et al., 2020) or burn severity estimation (Amos et al., 2019; De Luca, Silva, & Modica, 2021a; A. Fernández-Manso et al., 2016; Mallinis et al., 2018; Morresi et al., 2022; Carmen Quintano et al., 2019a), the contributions concerning their combined use in assessing and monitoring the temporal response of ecosystems to fire effects and the subsequent recovery patterns are very scarce (Evangelides & Nobajas, 2020; Han et al., 2021; Zhang et al., 2021); even less in Mediterranean ecosystems.

Understanding the spectral interactions between these patterns and the main factors that influence the damage and recovery processes is also important. Depending on fire severity, type of vegetation and climate conditions, recovery processes can be very heterogeneous, with large changes in forest structure and species composition (Lacouture et al., 2020; Morresi et al., 2019). Considering the post-fire recovery as a homogeneous and predictable process is almost unrealistic, as stated by Morresi et al. (2019). Understanding the quantitative relationship between post-fire vegetation recovery and fire severity allows the assessment of the temporal effects of fire on ecosystem characteristics such as biodiversity, evapotranspiration, carbon cycling, soil chemical and physical properties (Emilio Chuvieco, 2009; Emilio Chuvieco et al., 2014; Häusler et al., 2018; Hill et al., 2008; Kasischke et al., 2011; Meng et al., 2018). Some authors evaluated post-fire recovery processes in relation to the fire severity category (Fernandez-Manso et al., 2016; Martins et al., 2016; Meng et al., 2018; Ryu et al., 2018; Viana-Soto et al., 2017). However, few studies have analysed both S1 and S2 data on different fire severity categories and different types of forest cover in the Mediterranean region.

The spatial assessment of the post-fire recovery temporal rates was also explored by several authors proposing and applying recovery indices to both optical (Chompuchan & Lin, 2017; Chou et al., 2008; Lin et al., 2004; Meng et al., 2018; Morresi et al., 2019; Ryu et al., 2018) and SAR (Minchella et al., 2009). Some of these indices considered the effects of delayed vegetation mortality (Chompuchan & Lin, 2017), of annually varying meteorological effects (Ryu et al., 2018), or inter-annual modifications of natural phenological cycles (Morresi et al., 2019) by adding approximate parameters based on the generalization of the surrounding unburned vegetation. However, further investigations are needed given the increased availability of better resolution satellite images, such as S1 and S2, and performant open-source prediction algorithms based on machine learning.

The present study aims to:

- Assess post-fire forest recovery dynamics and their spatial patterns in a Mediterranean ecosystem, using S1 and S2 spectral vegetation indices.
- Assess the relationship between the recovery rate, the type of vegetation, and the fire severity level, by also taking into consideration the climatic conditions.
- Estimate and map the spatial distribution of recovery degree through the burn recovery ratio (BBR), based on pre- and post-fire conditions and optimized through machine learning regressors.



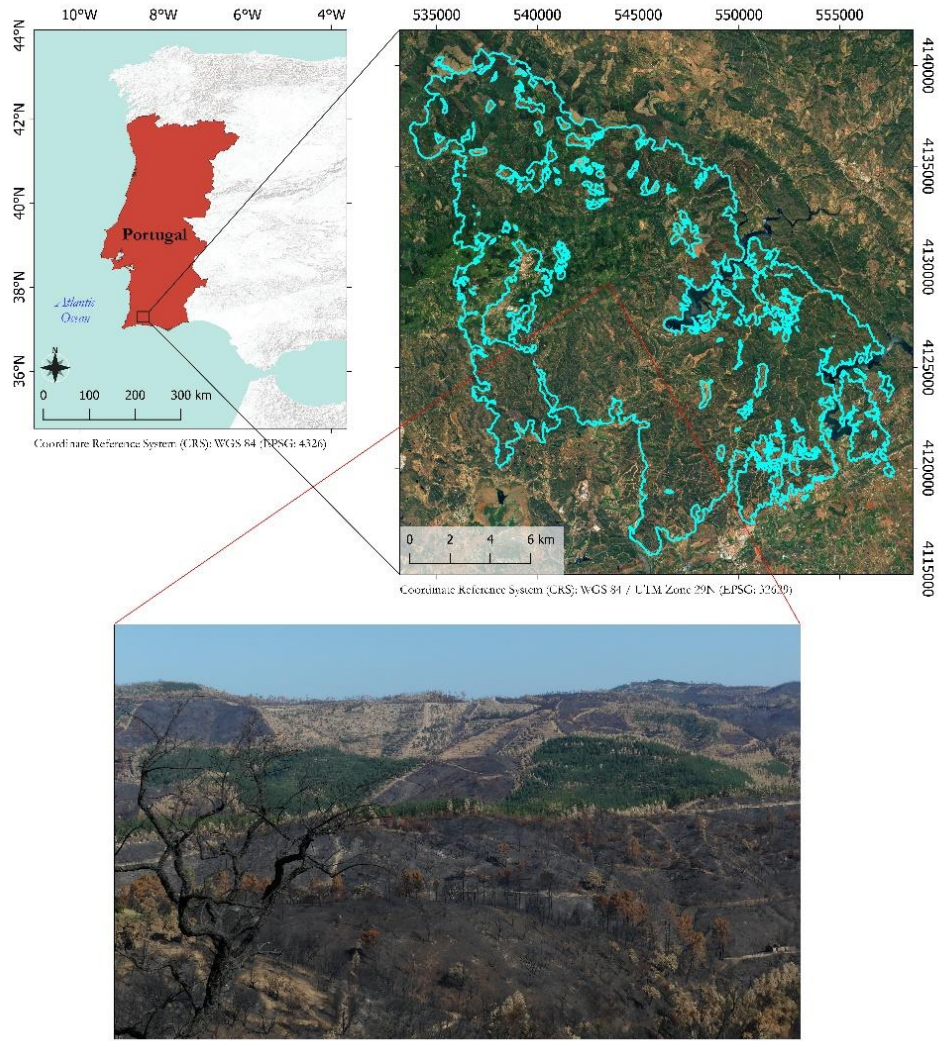
## 8.1. Masterials and methods

### 8.1.1. Study area

The study area is the Serra de Monchique mountain chain, located in the Algarve region, south of Portugal (37° 18'N; 08° 30'W), part of which is included in the European Natura 2000 network as a Special Area of Conservation (SAC) (Natura 2000 Site Code: PTCON0037). The climate is typically Mediterranean, with hot, dry summers and mild humid winters, with oceanic influences given by the relative proximity of the Atlantic Ocean and the heights of the mountain range that intercept the humidity (Martins et al., 2015). Considering the surface occupied, the forest cover is mainly composed of Eucalyptus plantations (*Eucalyptus globulus*, Labill. 1800) and cork oak forests (*Quercus suber* L.), part of which consists of the typical semi-natural agro-forestry system (*montado* in Portuguese), and part consisting of more close forest stands. Typical meso-Mediterranean forest ecosystem with other Mediterranean oaks species (e.g., *Quercus ilex* L.) and other secondary Mediterranean autochthonous broad-leaves trees are also present. A small part of the forest cover is also composed of isolated areas of Mediterranean conifers (*Pinus pinea* L., *Pinus pinaster* Aiton.) (Alves et al., 2007; Catry et al., 2015; De Luca et al., 2022; Häusler et al., 2018; San-Miguel-Ayanz et al., 2016). However, the largest part of the study area is covered by heathlands and pastures, composed of typical herbaceous and sclerophyllous shrubby flora alternating with agricultural fields surrounding small urban areas (De Luca, Silva, Di Fazio, et al., 2022; Mitchell et al., 2009; J. San-Miguel-Ayanz et al., 2016).

### 8.1.2. Description of the fire event

The fire event (Fig. 8.1) occurred in August 2018 from the 3<sup>rd</sup> to the 10<sup>th</sup>, affecting 268.9 km<sup>2</sup>, almost entirely represented by herbaceous, shrub and forest areas (De Luca, Silva, & Modica, 2021a). For most of the burnt surface (> 50%), the event was of high severity where, regardless of the type of vegetation, only the residues of the burned biomass (ash and coal) remained on the ground, and the bare ground was left exposed. Where the fire had moderate-high severity, the vegetation structure was, however, affected at various levels, with the consumption of the lower layers (grass and shrubs) and a predominant crown fire occurrence, which did not destroy all the canopy structure. In moderate and low severity categories, representing less than 15% of the burned surface, the fire affected the vegetation partially, with part of the canopy killed by heat proximity and the other amount remaining alive (De Luca, Silva, Oom, et al., 2021; Oom et al., 2018).



**Figure 8.1.** Location of the study area in Portugal (top-left). Overview of the study area (top-right) using the Google Earth Satellite map as a base map; the wildfire perimeter of August 2018 is overlaid in light blue. The landscape of the burned area (bottom) where all the categories of fire severity are observable.

### 8.1.3. Dataset and pre-processing

#### 8.1.3.1. Sentinel-1 dataset and pre-processing

The SAR dataset was composed of S1-A/B Level-1 high-resolution ground range detected (GRDH) time-series, acquired in interferometric wide (IW) mode, dual-polarized available: co-polarized VV and cross-polarized VH. The time series covered a period of four years (April 2017-Jun 2021) and, considering that the fire event time occurred in the first days of August 2018, the timeframe was split into a pre-fire (from April 2017 to July 2018) and post-fire (from the second half of August 2018 to June 2021) periods. Moreover, the Long-Term Access policy of the ESA (Copernicus Long Term Archive Access, 2021) makes very time-expensive the massive download of images from the official Copernicus Open Access Hub platform. Therefore, the S1 images were downloaded using the Alaska Satellite Facility (ASF) interface (ASF, 2022), which also provides the python code for bulk-downloading. The S1 time series comprised 273 images, including ascending (51 pre-fire and 88 post-fire) and descending (49 pre-fire and 85 post-fire) flight paths.

The pre-processing of the S1 dataset was carried out using the Sentinel-1 Toolboxes, implemented in the SNAP v.8.0.3 open-source software (ESA SNAP Homepage, 2022), and performed via the SNAP-Python interface (Snappy), the access provider to SNAP Java API (ESA SNAP Cookbook, 2022). Starting by applying the auto-downloaded orbit information file and the removal of the thermal noise, the SAR data pre-processing involved the radiometric calibration to beta ( $\beta_0$ ) noughts backscatter standard conventions (Small, 2011) and the radiometric terrain correction (RTC) process. RTC consists of the radiometric terrain flattening and the geometric terrain correction of the images using a digital elevation model (DEM) to reduce the geometric and radiometric distortions due to the rough surface topography. The shuttle radar topography mission (SRTM) DEM at 1 arc-second spatial resolution (Farr et al., 2007) was resampled using the bilinear interpolation method (De Luca, Silva, & Modica, 2021a; Mendes et al., 2019); no pixel resampling was instead necessary to the GRDH image products, already available in 10 m x 10 m resampled pixel spacing (ground range x azimuth) (ESA Sentinel-1 User Guide 2016). Subsequently, the stack of all the time series was carried out separately for each of the two flight paths. The geolocation of a master image (automatically chosen by the model among the time series) was adopted in this phase. An image Refined-Lee speckle filter (Lee & Pottier, 2009), with a 7x7 pixel window size, was applied to reduce the first speckle-noise effects. Finally, a backscatter monthly time average was computed for each month. The backscatter time average, besides reducing the massive amount of the images compositing the time series, further minimize the adverse effects of speckle noise and environmental variables affecting the SAR signal (De Luca, Silva, & Modica, 2021a; Lapini et al., 2020; Tanase et al., 2015; Zhang et al., 2019).

#### *8.1.3.2. Sentinel-2 dataset and pre-processing*

The optical time series was composed of 253 (60 pre-fire and 193 post-fire) S2-A/B Level-2A (Bottom-Of-Atmosphere, BOA) multispectral images. These images cover the same period of the S1 dataset (April 2017-Jun 2021), excluding the first half of August 2018 (when the fire occurred). Due to the same problem concerning the oldest-acquisition image accessibility from the official Copernicus database (section 2.3.1), the S2 dataset was downloaded from the Google Earth Engine (GEE) collections database and executed through the GEE Python API (Google Earth Engine Guides, 2022). The GEE Python API was also employed for S2 image pre-processing before the download, including resampling all S2 bands to 10 m of GSD using the nearest neighbour resampling algorithm. Additionally, the S2-Cloud Probability was used to mask each pixel of the time-series images by cloudiness probability (scaled from 0 to 100). The S2-Cloud Probability mask is available in the GEE Data catalog (GEE Data Catalog: Copernicus S2-Cloud Probability, 2022), sampled to 10 m of GSD, generated using the automatic pixel-based sentinel2-cloud-detector package (s2cloudless) (Sentinel2-cloud-detector repository, 2022), developed by Sentinel Hub's research team (Sentinel Hub Homepage, 2022) and based on the LightGBM machine learning library (LightGBM documentation, 2022). Higher values of cloud probability have a higher ability to detect dense clouds or highly reflective surfaces, but the omission of less dense clouds could be equally high. Lower values allow the possibility of detecting all the clouds on the scene; however, they increase the risk of more frequent commission errors due to the confusion between clouds and medium-high reflectance surfaces, masking them from the resulting image. To this end, a pixel probability threshold of 10 was set based on previous experiences in the same study area (De Luca, Silva, Di Fazio, et al., 2022). The masked pixels are replaced by applying a temporal linear interpolation involving all the time-series images, differentiating pre-fire and post-fire sub-sets. After the cloud masking, the images were averaged each month using the criterion adopted for the S1 time series.

#### 8.1.4. Land cover and fire severity maps

The temporal analysis of post-fire vegetation recovery was applied to three main LULC classes representing the vegetation of the study area: the eucalyptus (Euc) plantations; the autochthonous forest (AuFor), both natural and the semi-natural, consisting of two dominant species, *Quercus suber* and *Q. ilex*, and other secondary broadleaves; heathlands, shrublands or pastures vegetation (Pas/Shr). The pine class was excluded in this study due to its limited representativeness in the study area. The definition of the primary reference LULC classes was carried out using a classified LULC map retrieved from a supervised machine learning-based classification processing developed in Chapter 2 and based on the combined use of both SAR S1 and optical S2 data. The LULC map has a spatial resolution of 10 m x 10 m, and its overall accuracy is higher than 90%.

The burned vegetation was monitored based on the fire severity. The spatial distribution of fire severity, retrieved as explained in Chapter 5, was obtained applying the random forest (RF) machine learning model on a dataset constituted by an S1+S2 dataset and derived indices, and trained using a set of field measurements of the composite burn index (CBI) (Key & Benson, 2006). Based on the CBI sampling protocol, six conventional fire severity categories were detected (Key & Benson, 2006), and five of them were considered in the further analyses: a) unburned soil/rock (not taken into consideration); b) unburned vegetation; c) low severity: low impact of the fire, which was mainly kept at ground level with low levels of alteration of the shrub and/or tree cover; d) moderate severity: level of alteration of the vegetation higher than in low severity category, with the fire reaching the lower layers of the forest canopy, resulting in a mixture of scorch and green vegetation; e) moderate-high severity: predominance of burnt vegetation with a high percentage of tree foliage affected by scorch, and a part of the woody components of the canopy partially or totally consumed by fire; f) high severity: the short vegetation is consumed, as well as most of the tree's foliage, the surface is mainly covered with ash and charcoal.

#### 8.1.5. Climate variables

Two datasets with monthly climate variables series were retrieved, from April 2017 to January 2021, to analyse the relationship with the temporal profiles of vegetation affected by fire: monthly rainfall (mm) and average monthly temperature (°C). After analysing the meteorological stations' spatial distribution, the data were retrieved from 16 stations distributed over the study area (SNIRH, 2022).

#### 8.1.6. Data preparation and analysis

##### 8.1.6.1. Vegetation indices calculation

Three S1-adapted dual-polarimetric SAR indices were computed for each resulting month averaged image of the S1 time series: the RVI (Eq. 8.1), the RFDI (Eq. 8.2) and the DPSVI (Eq. 8.3) (Mandal et al., 2020; Nasirzadehdizaji et al., 2019; Nicolau et al., 2021; Saatchi, 2019a).

$$RVI_t = 4 \cdot VH_t / (VV_t + VH_t) \quad (8.1)$$

$$RFDI_t = (VV_t - VH_t) / (VV_t + VH_t) \quad (8.2)$$

$$DPSVI_t = (VV_t + VH_t) / VV_t \quad (8.3)$$

Where  $t$  represents the corresponding image date (months) constituting the time series (April 2017 - June 2021), and VV and VH represent the respective single-polarized backscatters. Besides the SAR VIs, computed separately for orbit path (RVI\_As, RVI\_Ds, RFDI\_As, RFDI\_Ds, DPSVI\_As, DPSVI\_Ds), the backscatter time-series for

the single co- and cross-polarization (VH\_As, VH\_Ds, VV\_As, VV\_Ds) were also involved to compose the final SAR dataset.

A similar procedure was carried out for each month image of the S2 time-series, for which five spectral indices were calculated: the NDVI (Eq. 8.4), the green normalized vegetation index (GNDVI) (Eq. 5), the normalized red-edge vegetation index (NDRE) (Eq. 8.6), the normal burn index (NBR) (Eq. 7) and the normalized difference water index (NDWI) (Eq. 8.8).

$$NDVI = (B8_t - B4_t) / (B8_t + B4_t) \quad (8.4)$$

$$GNDVI = (B8_t - B3_t) / (B8_t + B3_t) \quad (8.5)$$

$$NDRE = (B6_t - B5_t) / (B6_t + B5_t) \quad (8.6)$$

$$NBR = (B8_t - B12_t) / (B8_t + B12_t) \quad (8.7)$$

$$NDWI = (B8A_t - B11_t) / (B8A_t + B11_t) \quad (8.8)$$

B3, B4, B5, B6, B8, B11 and B12 represent the S2 bands conventionally named (ESA Sentinel Homepage 2022). The final optical dataset was composed of the monthly time series of the VIs above.

#### 8.1.6.2. ROIs collection and temporal profiles extraction

The temporal analysis of vegetation dynamics affected by the fire was divided according to the LULC class and the fire severity category. A series of square 3x3 pixel regions of interest (ROIs) were collected to fulfil these criteria. Each ROI was homogeneous regarding LULC class and fire severity; the whole dataset covered the spatial distribution of the land cover and fire severity. The ROIs were retrieved by visual assessment of LULC and fire severity maps and the Esri ArcGIS World Imagery high-resolution satellite map (Esri ArcGIS World Imagery, 2021). A total of 700 ROIs were collected and distributed: 50 ROIs for each fire severity category for both forest LULC classes and the high severity category of Past/Shr class; 25 ROIs for each low, moderate and moderate-high fire severity category for Past/Shr LULC. The choice of 25 ROI was due to the difficulty of finding homogeneous areas of Past/Shr vegetation belonging to these three severity categories. Using the mean value of ROIs allows to examine the overall change occurring inside these sampling units through the entire observation period and compare the different profiles, avoiding the influence of the values of single pixels (Lacouture et al., 2020).

#### 8.1.6.3. Correlation between temporal profiles and climate variables

The monthly temporal profiles of rainfall and temperature were constructed and compared to the temporal profiles of each S1 and S2 spectral index to investigate the influence that the climate variables had on the dynamics of post-fire vegetation recovery. To define the relationship with the vegetation dynamics of post-fire recovery, we implemented a Pearson's correlation analysis ( $r$ ) between the temporal profiles of each S1 and S2 index and the climate variables.

#### 8.1.6.4. The burn recovery ratio (BRR)

The spatial distribution of the degree of vegetation recovery was estimated and mapped using the burn recovery ratio (BRR) (Eq. 8.9), proposed by Chompuchan et al. (2017), in turn inspired by the recovery index of Chou et al. (2008) and Lin et al. (2004), which represents the ratio between the value of a given VI at the time of assessment ( $VI_{\text{post-fire}}$ ) and its value at the reference pre-fire time ( $VI_{\text{R\_pre-fire}}$ ).

$$BRR = VI_{\text{post-fire}} / VI_{\text{R\_pre-fire}} \quad (8.9)$$

As further explained below,  $VI_{\text{post-fire}}$  and  $VI_{\text{R,pre-fire}}$  values falling inside the burned perimeter were predicted by the mean of a regression algorithm to minimize the inter-annual biases.

Due to the natural inter-annual variations that may have occurred in unburned vegetation, if an image taken in the pre-fire period was used for BRR calculation, it would lead to biases for each year of its estimation. Morresi et al. (2019), for example, exploiting the concept already used in Miller (2007) for the computation of the relative NBR, integrated their recovery index with a coefficient calculated by averaging the difference between pre-fire median and annual post-fire VI values of unburned vegetation to account the inter-annual phenological changes. In this study, to cope with this aspect, the unburned reference values for each index and each year of BRR assessment were estimated using the RF machine learning regression model (Breiman, 2001). To this end, 250 additional sample ROIs ( $ROI_{\text{SBRR}}$ ) ( $3 \times 3$  pixels) were selected for each of the three LULC classes in areas not affected by the fire (outside the fire perimeter). Their pixel values were used as reference unburned training points for the RF model. For each year of calculation of the BRR, the respective  $ROI_{\text{SBRR}}$  pixels of the same year were used as trainers; meanwhile, all the pixels falling within the burned area were reconstructed by interpolating them with the individual pre-fire image values (June 2018). This month was chosen since it was the closest to the fire event to also be present for all the observed following years (2019, 2020 and 2021), implicating that the conditions of the vegetation were more similar to those at the time of the fire event, as already considered by De Luca et al. (2022). Furthermore, the cloud-free seasonal period was optimal to avoid using those pixels reconstituted from cloud gaps and the rain noise on the SAR signal. Thus, the new unburned pixels for the BRR calculation have been predicted. The RF regressor parameters values were set using those already calculated in Chapters 2 and 5 and optimized for the study area through an exhaustive grid search approach.

Based on the BRR results, six recovery rate categories were created, similar to those proposed by Chompuchan et al. (2017): very low (condition worse than before the fire) ( $BRR < 0$ ), low ( $0 < BRR < 0.25$ ), moderate ( $0.25 < BRR < 0.50$ ), moderate-high ( $0.50 < BRR < 0.75$ ), high ( $0.75 < BRR < 1$ ) and very high ( $BRR > 1$ ). The BRR was calculated in June (springer greenness peak) of each year after the fire (2019, 2020, 2021) for NBR ( $BRR_{\text{NBR}}$ ), NDVI ( $BRR_{\text{NDVI}}$ ), NDRE ( $BRR_{\text{NDRE}}$ ) and RVI (ascending and descending;  $BRR_{\text{RVI\_As}}$  and  $BRR_{\text{RVI\_Ds}}$ ).

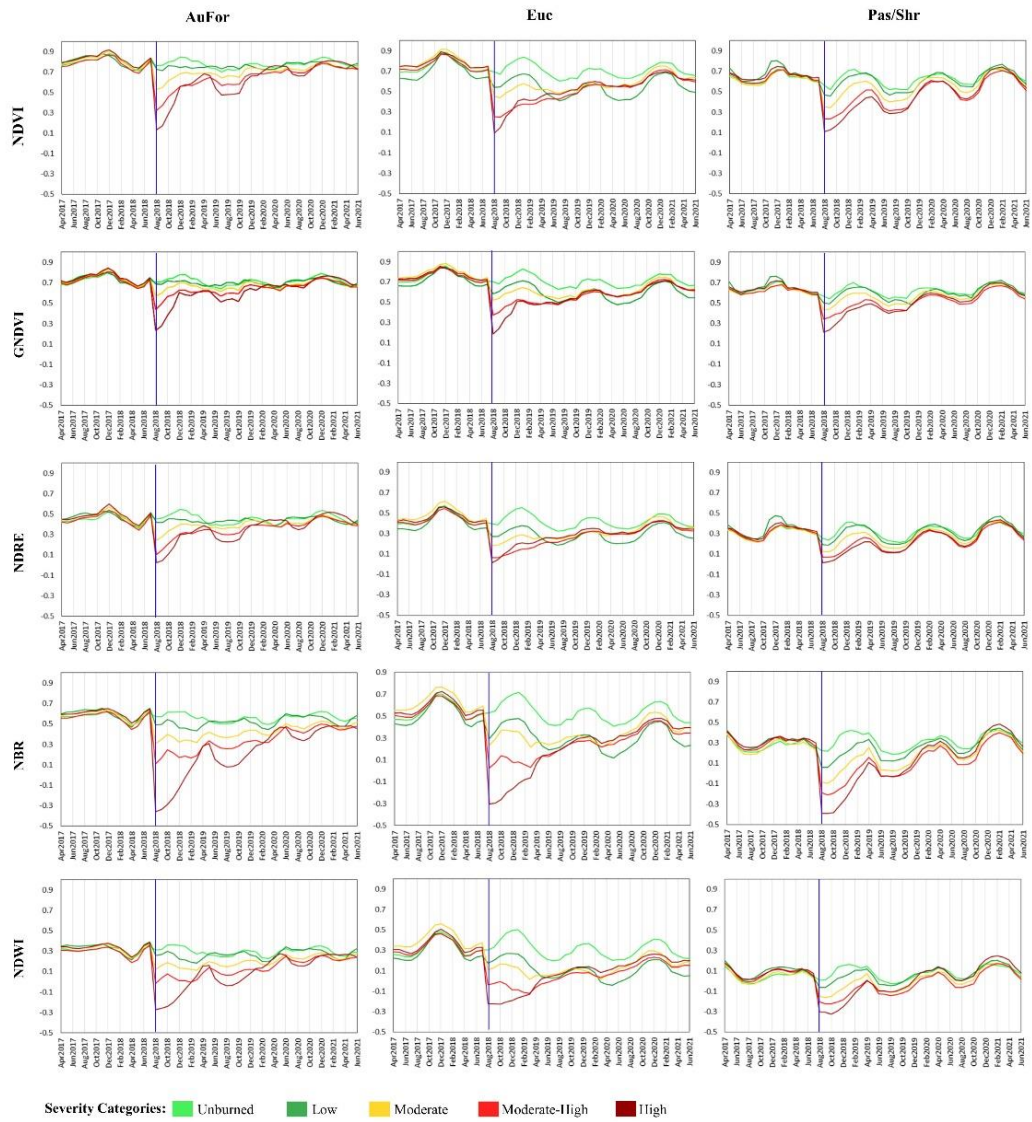
## 8.2. Results

### 8.2.1. Temporal profiles

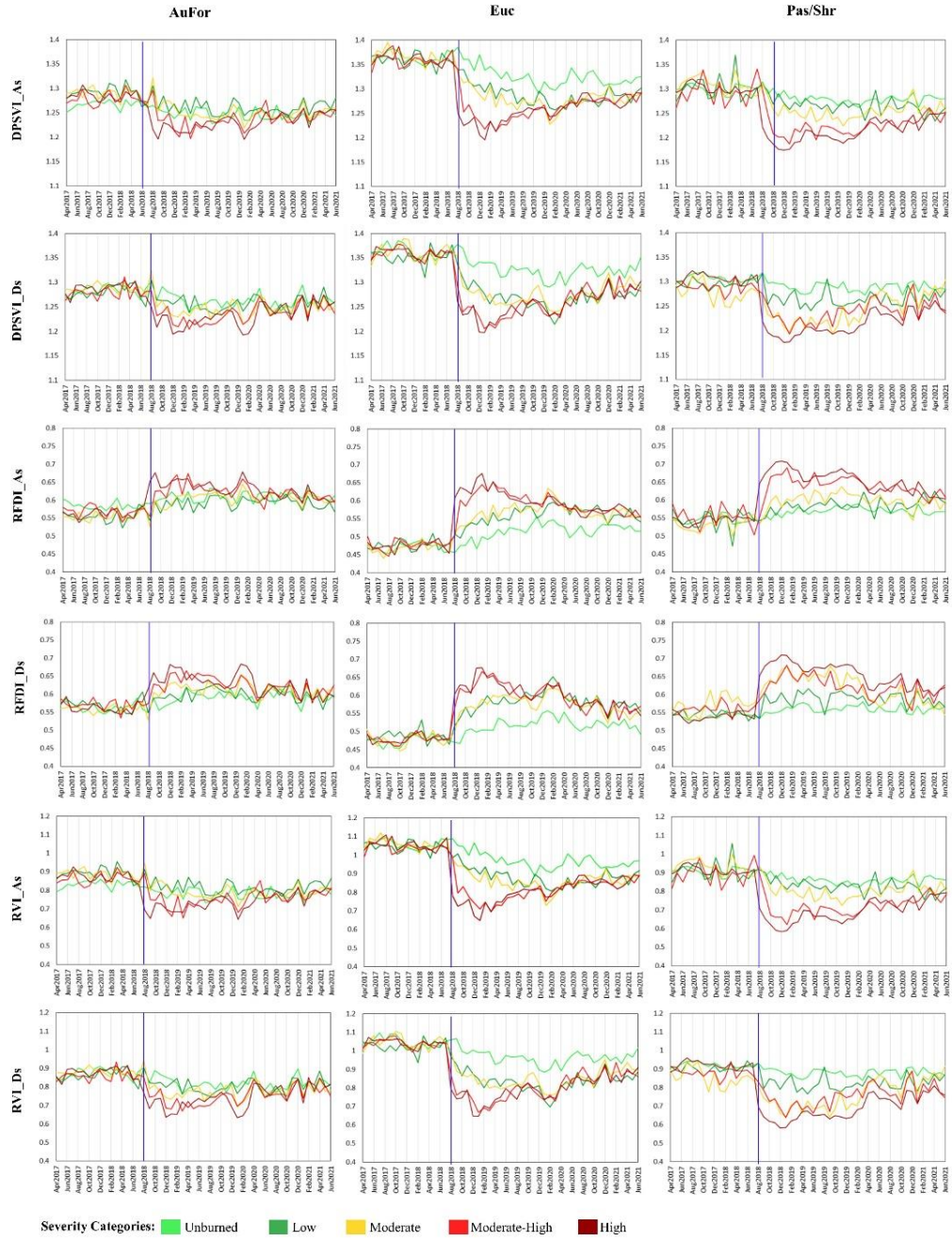
The temporal profiles of S1 and S2 spectral indices (Figures 8.2-8.4) show the mean reflectance value of the pixels retrieved from ROIs, separated by LULC class and fire severity category. The time series, divided between the pre-fire period (April 2017 - Jul 2018) and the post-fire period (second half of August 2018 - Jun 2021), is composed of images representing the monthly averages of the observed timeframe.

Different patterns are distinguishable in each temporal profile, with a common breakpoint denoting the fire event in August 2018. An evident and expected difference between the two types of sensors is also found. Other noticeable differences in the LULC class, fire severity category, seasonal variability, and long-term trend are also observed. Large variability in the short-term post-fire behaviour (within the first year after the fire) is evident in both S1 and S2 indices but is significantly attenuated during the second and the third post-fire year in the S2 time series.

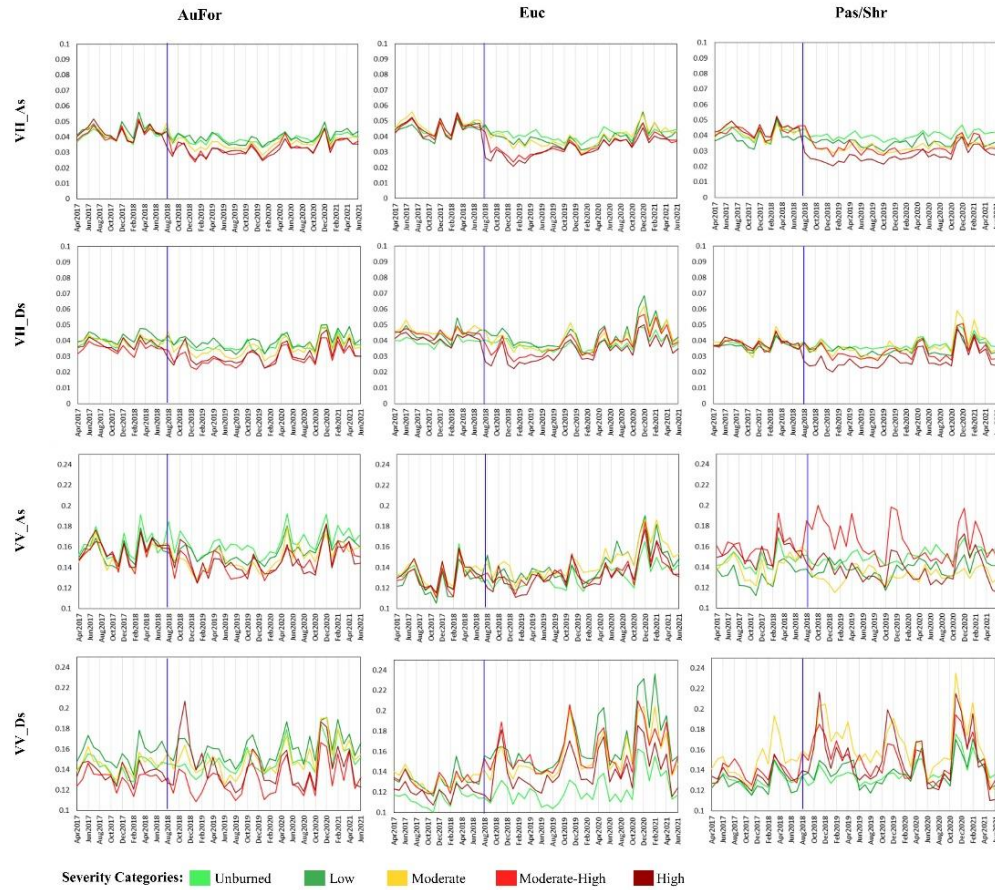




**Figure 8.2.** Temporal profiles of optical vegetation indices, for each of which a comparison between the three different LULC classes is displayed.



**Figure 8.3.** Temporal profiles of SAR dual-polarized vegetation indices, for each of which a comparison between the three different LULC classes is displayed.



**Figure 8.4.** Temporal profiles of SAR single-polarization backscatter, for each of which a comparison between the three different LULC classes is displayed.

### 8.2.2. Optical Sentinel-2 profiles

As expected, for each LULC class, similar behaviour is observed between the different temporal profiles divided by fire severity category in the time frame preceding the fire event. Such profiles thus outline LULC-specific spectral signatures, an aspect much more evident in optical-based profiles than in SAR-based profiles (Figures 8.2-8.4).

After the fire event, different recovery patterns are recognizable according to the severity category in all the optical indices. Two common patterns are observed among all the profiles. A pronounced drop of the Vis values, with a magnitude related to the fire severity, in the period immediately following the fire event and maintained for about a year; a recovery of the pre-fire levels of spectral response (positive increasing trend) after the first year.

Observing the unburned category, the three vegetation classes had specific seasonal patterns during the observed period, with slight variations in the temporal dynamics between the different spectral indices in specific years. The highest index values occur in the same period for all the LULC classes: the autumn-winter period with peaks observed in December in almost all periods of all spectral indices, with some variation found in the two SWIR-based indices. The AuFor class showed less pronounced seasonal fluctuations and lower amplitude of the curve, opposite to the Euc profiles characterized by higher amplitude. Keeping the minimum values higher than the other classes, the AuFor secondary growth phase takes place in the earlier summer period between June and July, attributable to the growth of new leaves, with the only exception for the year 2019, in which there is no summer

increase in the values of all the analysed spectral indices. This phase is anticipated by a minimum value occurring during the second half of May (NDVI, GNDVI, NDRE) or April (NBR, NDWI). The Pas/Shr class, generally characterised by lower VIs values compared to the forest classes, presents its single and regular period of annual growth that goes from September-October (minimum value), when the autumnal rains break the summer drought, through the whole winter, reaching the maximum peaks in December-January, and until they start to dry again at the end of spring.

The AuFor and Past/Shr post-fire profiles relative to the low severity category profiles present values very close to the reference unburned vegetation profiles in all the spectral indices. The intra-annual variability of phenology is clear in the time series even after the fire occurrence. The periods of growth and decrease are comparable between the two severity categories along almost the entire post-fire period. The impact of the low severity fire on the surface occupied by eucalyptus trees led to a lowering of the values of all the calculated optical indices. However, the magnitude of the recovery is the same as the corresponding unburned profile. Noticeable is the higher amplitude of the Euc low-severity profile compared to those falling into the other severity categories of the same LULC class. After a detachment the first year after the fire event, the moderate-high and high fire severity profiles showed similar values and followed the cyclical trend already observed for the unburnt category. However, the spectral response of the high fire severity category showed a steeper decrease immediately after the fire, more pronounced in SWIR-related VIs. Concerning the recovery degree observed in the temporal profiles, a complete recovery seems to be recorded for AuFor and Pas/Shr classes in all the VIs, except for the SWIR-based indices, highlighting a slower recovery of AuFor vegetation. Unlike what was observed for the other two classes, Euc profiles failed to restore the respective pre-fire Vis values within the analysed post-fire period.

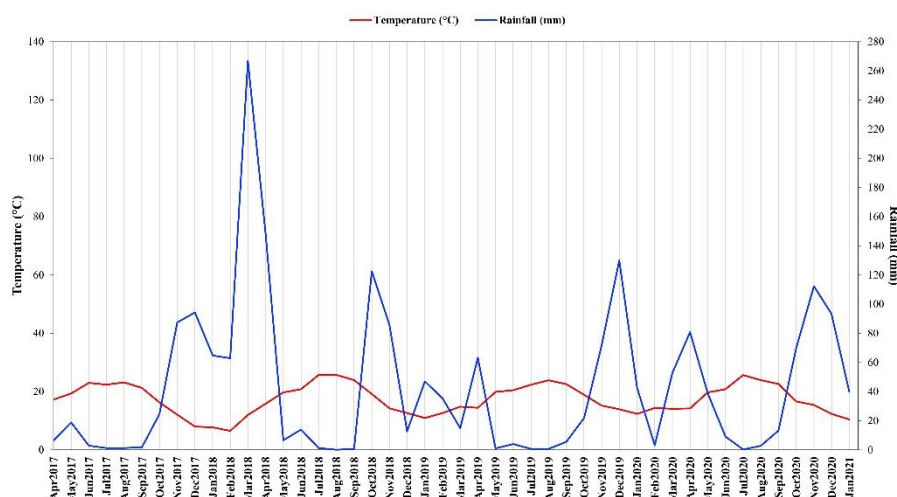
### **8.2.3. SAR Sentinel-1 profiles**

The comparison of SAR-based profiles denotes significant differences in the interactions between SAR indices and each LULC class, including those related to the ascending or descending orbit paths (Fig 8.3). The characterization of specific pre-fire seasonality and post-fire recovery patterns is complex in most profiles, mainly in the case of the single-polarized VV backscatter signal (Fig 8.4). Indeed, the fire event is visually perceptible, observing the profiles. A distinction between pre- and post-fire patterns is observed for all the LULC and fire severity combinations except the VV-related profiles. Furthermore, co-polarized profiles tend to slightly increase values in the post-fire period in all severity categories, but with an amplitude of the curve fluctuations that increase with fire severity. The profiles of dual-polarized SAR indices (Fig 8.3) are similar to those of the optical indices, exhibiting a better relationship between the fire severity category and the SAR signal (Fig 8.2). The RFDI represents an exception, which shows an expected increase after the fire. The post-fire response of the SAR indices is more evident for high and moderate-high severity categories than for moderate or low severity and stronger for Euc and Pas/Shr. Indeed, the SAR response of vegetation affected by low severity fire does not present distinguishable traits from the unburned vegetation profile in most cases. Conversely, Euc low severity profiles differ from unburned and high severity profiles during the first post-fire year. The common characteristic of all SAR profiles for all the LULC classes and fire severity categories is a slower recovery trend than optical profiles. In the case of Euc, even after three years, the indices' values do not reach those of pre-fire situations (Fig 8.3). In the case of pre-fire or unburned vegetation, a general slight decrease is visible over the whole period when DPSVI and RVI are used (resulting in an increasing trend for RFDI), as observed in optical indices profiles. For the Euc class, the decreasing trend can be observable until November 2019 - February 2020, after which a slight increase

is detectable. The same behaviour appears in ascending and descending VH backscatter profiles for all LULC classes and ascending VV backscatter for AuFor.

#### 8.2.4. Climate variables and relationship with satellite temporal profiles

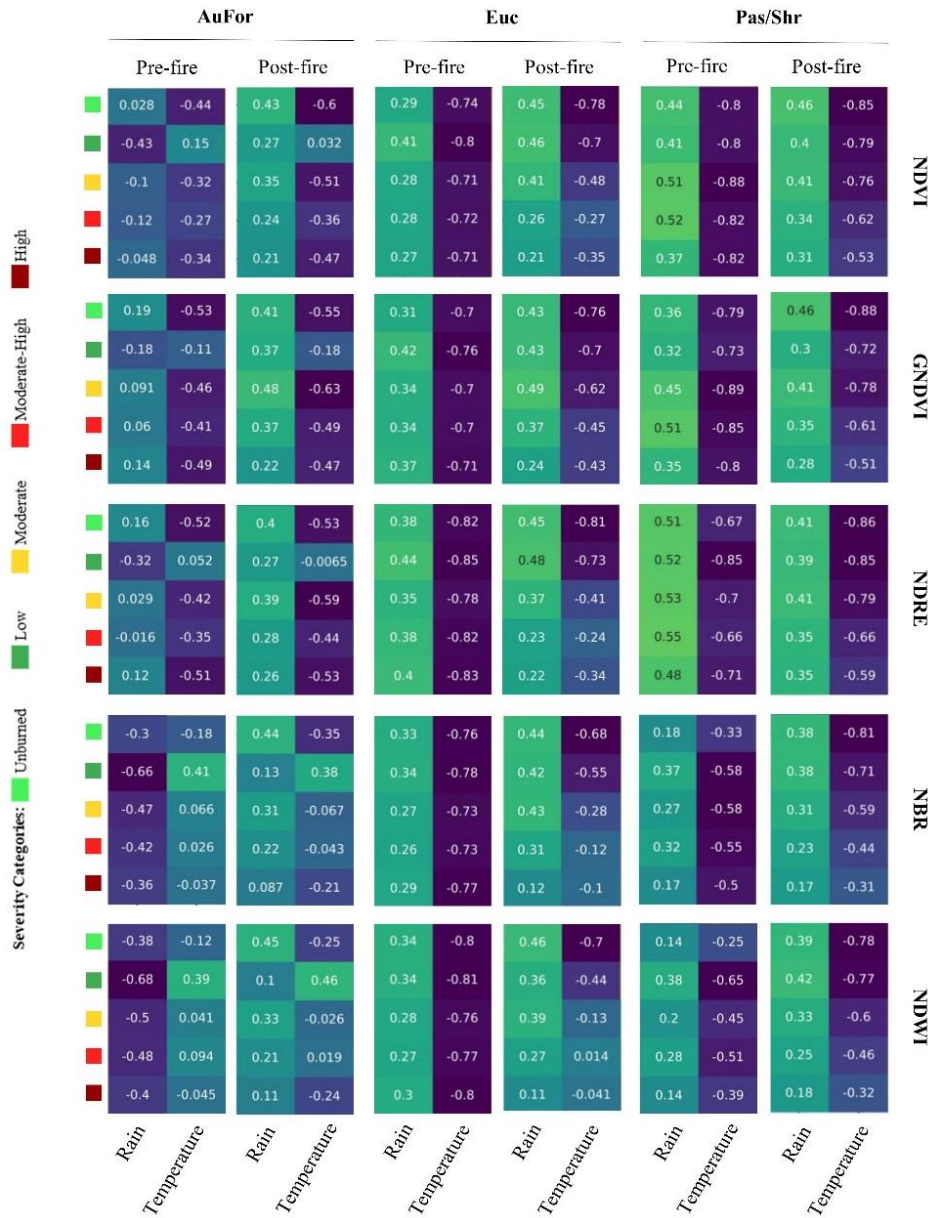
The Bagnouls-Gaussen Thermo-pluviometric diagram in Fig. 8.5 shows the temporal profiles (April 2017 - January 2021) of the monthly rainfall and monthly mean temperatures, highlighting the Mediterranean climate of the study area (mild and rainy autumn, winter and early spring seasons, dry summers). Notable decreases in rainfall are observed in December 2018 (12.6 mm), March 2019 (14.8 mm) and February 2020 (3.96). Another exceptionality is given by the maximum peak recorded in March 2018 (266.7 mm); other maximum peaks were observed in October 2018 (122.5 mm), December 2019 (129.84 mm) and November 2020 (112.2 mm). The seasonal thermal variation is not high, and this is due to the oceanic influence that mitigates the average temperature during the year.



**Figure 8.5.** Bagnouls-Gaussen Thermo-pluviometric diagram reporting the temporal profiles of the monthly rainfall and monthly average temperatures. The precipitation axis (right) has an interval double compared to the temperature axis (left).

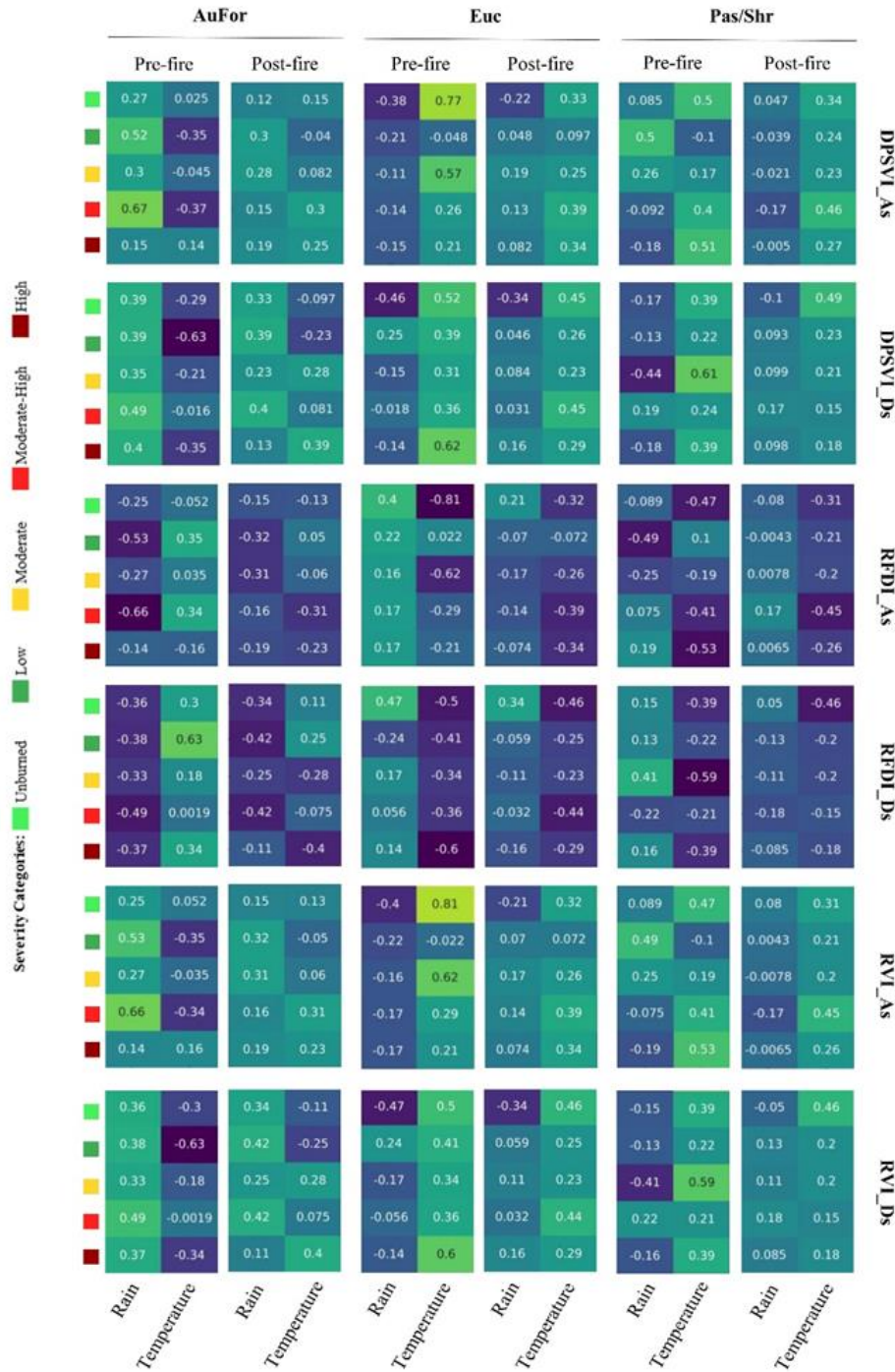
The Pearson's correlation coefficient between climate variables and temporal trends of both SAR and optical data was computed to investigate their linear relationship, considering the fire severity category, the LULC class and period considered (pre- or post-fire). The resulting Pearson's coefficient values are reported in the heatmaps of Figures 8.6-8.8.



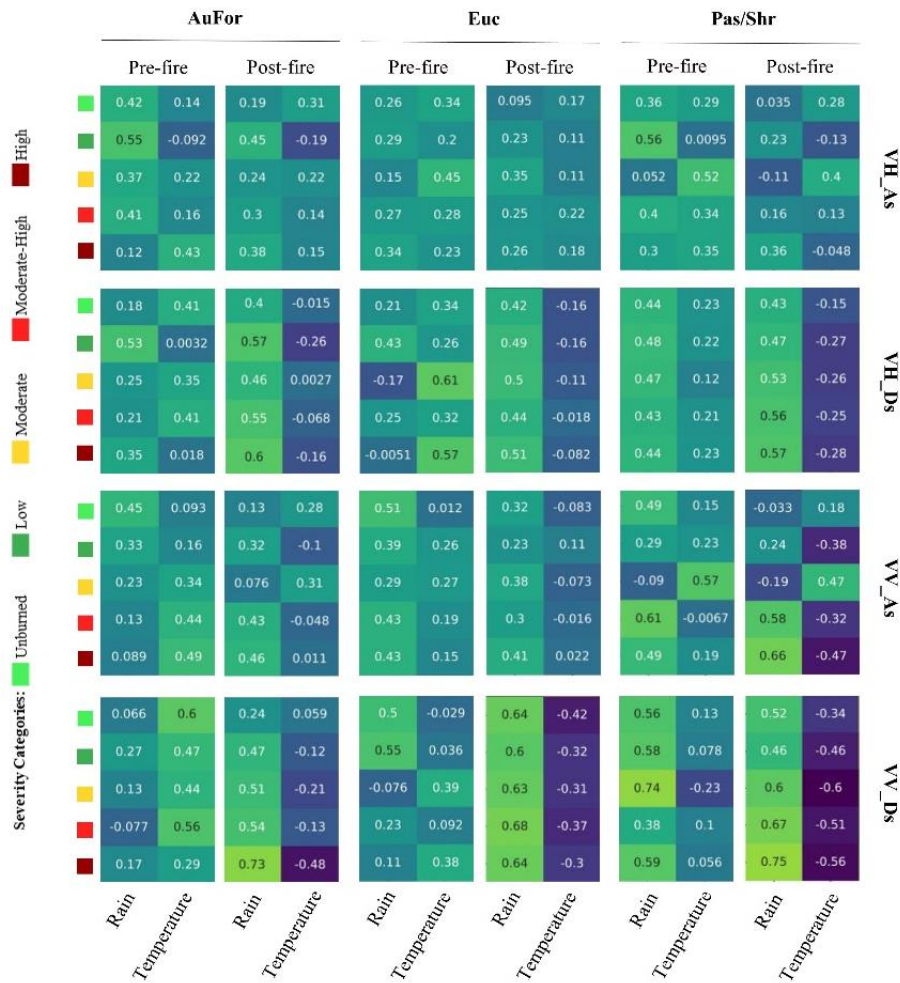


**Figure 8.6.** Heatmaps reporting the Pearson's correlation coefficient performed between optical vegetation indices (NDVI, GNDVI, NDRE, NBR and NDWI) and climate variables monthly rainfall (Rain) and monthly mean temperature (Temperature). The correlation was carried out separately between the pre- and post-fire period and fire severity categories. The heat map colour palette gradient describes the Pearson's values range from lower (dar blue) to higher (yellow-light green).





**Figure 8.7.** Heatmaps reporting the Pearson's correlation coefficient performed between SAR single polarizations (RVI\_As, RVI\_Ds, RFDI\_As, RFDI\_Ds, DPSVI\_As, DPSVI\_Ds) and climate variables monthly rainfall (Rain) and monthly mean temperature (Temperature). The correlation was carried out separately between the pre- and post-fire period and fire severity categories. The heat map colour palette gradient describes the Pearson's values range from lower (dar blue) to higher (yellow-light green).



**Figure 8.8.** Heatmaps reporting the Pearson's correlation coefficient performed between SAR dual-polarized vegetation indices (VH\_As, VH\_Ds, VV\_As, VV\_Ds) and climate variables monthly rainfall (Rain) and monthly mean temperature (Temperature). The correlation was carried out separately between the pre- and post-fire period and fire severity categories. The heat map colour palette gradient describes the Pearson's values range from lower (dark blue) to higher (yellow-light green).

For optical datasets (Fig 8.6), a general positive correlation between rainfall and spectral indices can be observed for most LULC classes and fire severity categories, higher for Pas/Shr and the post-fire period. The NDRE index of non-forest vegetation was most correlated with the rainfall in the pre-fire period, with values not lower than +0.48. The degree of correlation for the post-fire period decreases with increasing fire severity, with the minimum value recorded for the NBR profile used AuFor class affected by high severity (+0.087). The AuFor class mainly showed a lower correlation with rainfall than the other two LULC classes. Oppositely, most of the correlations with temperature were negative, with values that reached -0.89 (Pas/Shr-GNDVI-moderate severity-pre-fire). The AuFor class had some exceptions, presenting positive correlations for the SWIR-based indices (NBR and NDWI), with a higher positive correlation (+0.38 to +0.46) for low fire severity.

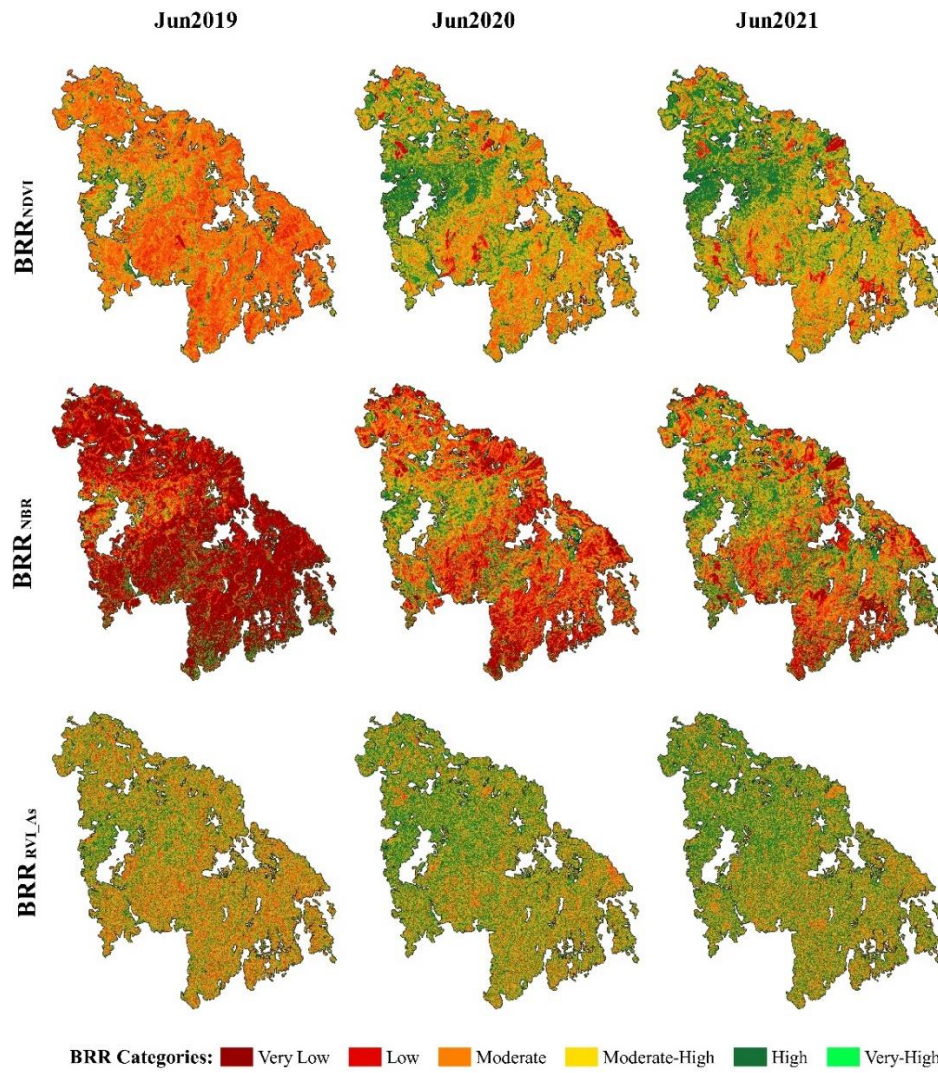
Concerning SAR datasets (Fig 8.7), the RVI and DPSVI indices reached a similar correlation in their respective orbit path. For AuFor class, these indices had a higher correlation with the rainfall variable in the pre-fire condition, showing values between +0.14 (RVI ascending) and +0.67 (DPSVI ascending). This class reached a higher correlation in the two indices in post-fire conditions. For Euc and Pas/Shr the highest positive and/or negative correlation was observed in pre-fire conditions, ranging from -0.47 (RVI descending) to +0.5 (DPSVI ascending).

During the post-fire period, both Euc and Pas/Shr achieved values not exceeding +0.2 in any case. The RFDI showed values of opposite correlations to RVI for both orbit paths in Euc and Pas/Shr classes. Considering the AuFor class, the RFDI reached a similar and opposite to the DPSVI. A higher correlation was found between single-polarization profiles and the rain variable. Noticeable is the high level of  $r$  reached by VV\_Ds in all three LULCs during the post-fire period ( $0.24 < r < 0.75$ ). Except for some cases (e.g., VV\_Asc for Pas/Shr; VH\_Ds for Euc), the other single-polarized combinations followed this trend in both pre-fire and post-fire periods. A divergence was observed between dual-polarized indices and single-polarized backscatter and between ascending and descending orbit paths when correlated with the monthly mean temperature. After the fire event, the unburned and low severity categories correlated to the pre-fire period using dual-polarized VIs in descending mode. With ascending VIs, a slight divergence was observable for the low severity category. The other fire severity categories registered similar behaviour, except AuFor, which changed signs from negative (pre-fire) to positive (post-fire) or vice versa (RVI\_Ds). Generally, pre-fire condition guaranteed highest correlation coefficient (e.g.,  $r = 0.81$ , RVI\_As, Euc;  $0.77$ , DPSVI\_As, Euc;  $0.61$ , DPSVI\_Ds, Pas/Shr). Dissimilar behaviours were found using single-polarized backscatter profiles. The unburned vegetation did not maintain its correlation level with the climatic variable in all the cases. The VH\_As was an exception, although this data presented the highest continuity between pre-fire and post-fire values in almost all the categories. The VV\_Ds showed the highest negative correlation with temperature in the post-fire period, totally contrasting with the values expressed before the fire event.

#### 8.2.5. *Spatial distribution of recovery rate: the BRR*

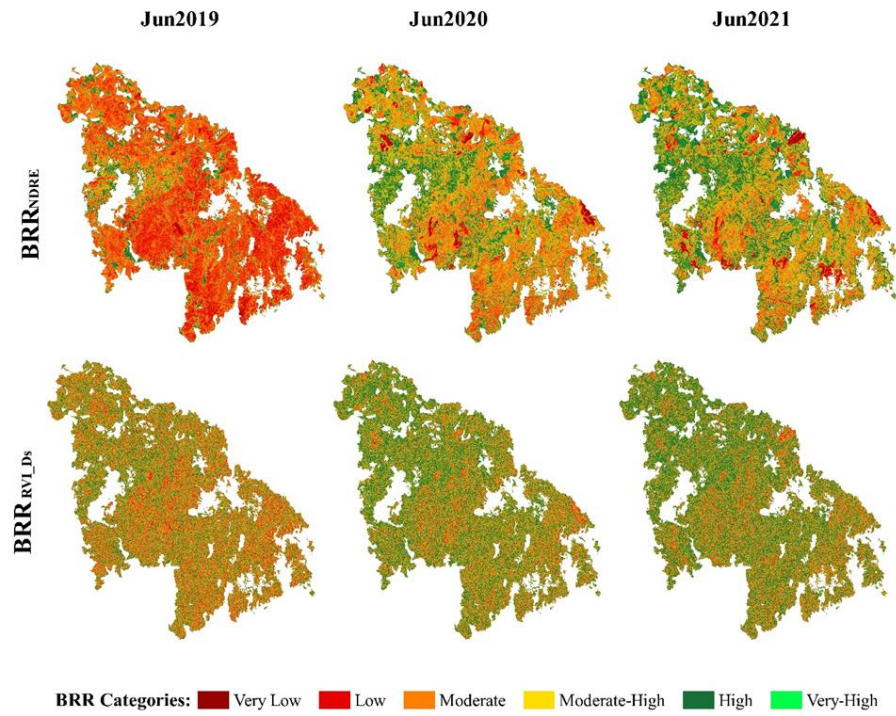
Figures 8.9 and 8.10 show the spatial distribution of the general recovery rate of vegetation for the NDVI, NBR and RVI\_As, and for NDRE and RVI, respectively. Areas in dark red ( $BRR < 0$ ) denote slow/absent recovery, with values of the VIs lower than in the pre-fire conditions; conversely, where the BRR was more than one (light green areas), the recovery condition was higher than the pre-fire condition. Considering the different VIs, the three maps showed noticeable differences, with  $BRR_{NBR}$  reporting recovery levels much lower than  $BRR_{NDVI}$ . This disparity is kept during subsequent years, although the spatial pattern of re-greenness is quite similar, with a recovery distribution starting from the area around the unburned island (Monchique town) located on the west side of the study area toward the easter and north part/side of the study area. Other high-recovery areas are patchy and spread throughout the 2021 map. Concerning SAR BRR, the recovery level has higher absolute values starting from 2019, and its spatial distribution is more homogeneous across the area. However, comparing the two highest recovery categories during the temporal progression from 2019 to 2021, the SAR shows a lower and more gradual regrowth rate than  $BRR_{NDVI}$ . Some dark red areas are viewable in the year after the fire, recognizable by a sudden decrease in BRR values compared to the previous year, resulting from other fires' recurrence after August 2018. Although present on the map (Figures 8.9 and 8.10), these fires have been detected in advance and excluded from any calculation ( $ROI_{BRR}$  and pixel distribution).

Figure 8.11 reports the proportion of the area occupied by each BRR category for each LULC class and year, assessed for the NBR, NDVI and RVI\_As indices;  $BRR_{NDRE}$  and  $BRR_{RVI\_Ds}$  are not shown since they displayed similar values of  $BRR_{NDVI}$  and  $BRR_{RVI\_As}$ , respectively.

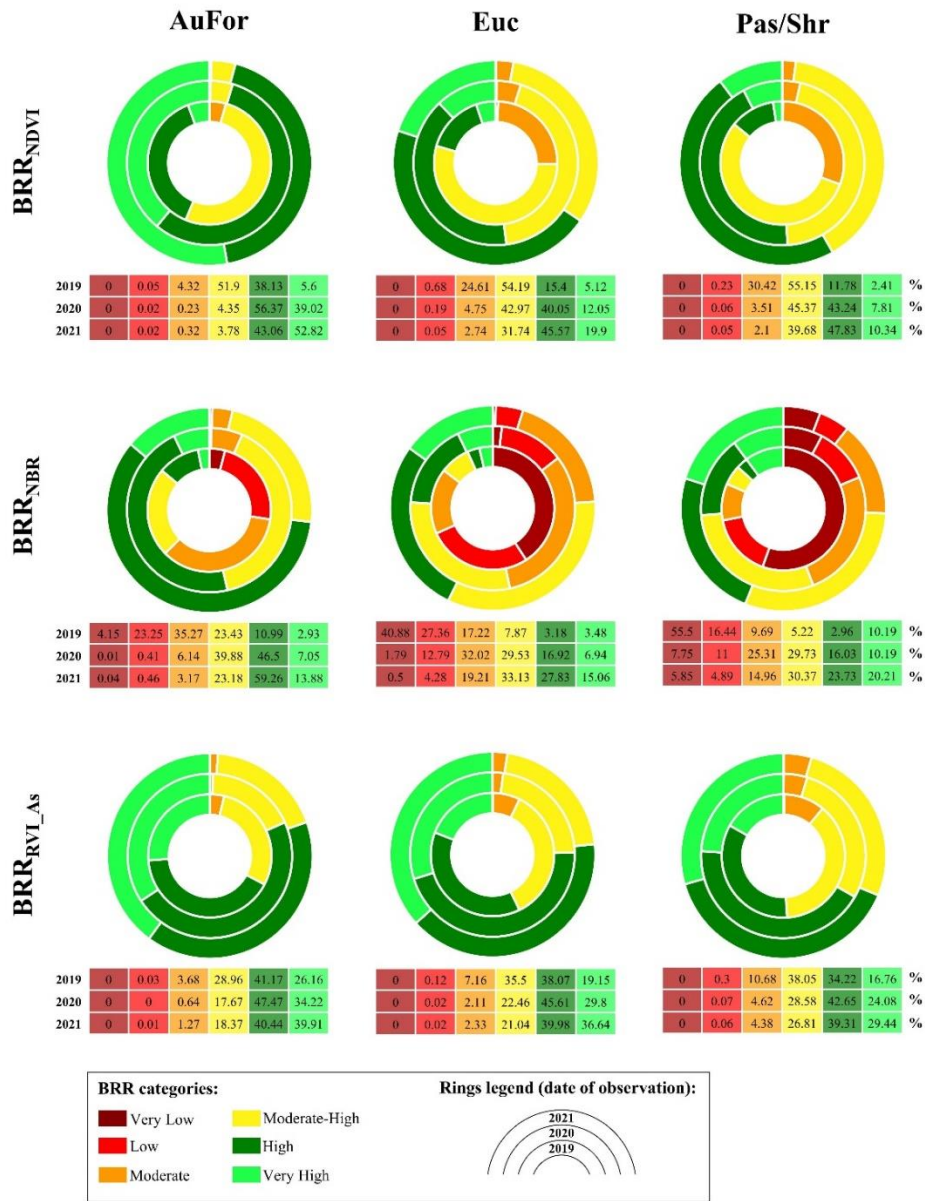


**Figure 8.9.** Burn recovery ratio (BRR) was separately calculated for NDVI ( $BRR_{NDVI}$ ; first row), NBR ( $BRR_{NBR}$ ; second row) and RVI\_As ( $BRR_{RVI\_As}$ ; third row). The columns separate the three post-fire dates of observation: June 2019 (first column), 2020 (second column), and 2021 (third column). The colour palette represents a recovery gradient from very low (dark red) to very high (light green).





**Figure 8.10.** Burn recovery ratio (BRR) separately calculated for NDRE (BRRNDRE; first row) and RVI\_Ds (BRRRVI\_Ds; second row). The columns separate the three post-fire date of observation: June 2019 (first column), 2020 (second column), 2021 (third column). The colour palette represents a recovery gradient from very low (dark red) to very high (green).



**Figure 8.11.** Distribution of the number of pixels (%) falling in every burn recovery ratio (BRR) category, separately calculated for: vegetation index, NDVI (BRR<sub>NDVI</sub>; first row), NBR (BRR<sub>NBR</sub>; second row) and RVI<sub>As</sub> (BRR<sub>RVI<sub>As</sub></sub>; third row); date of observation, June 2019 (internal ring), June 2020 (medium ring), 2021 (external ring); LULC class, AuFor (first column), Euc (second column) and Pas/Shr (third column). The colour palette represents a recovery gradient from very low (dark red) to very high (light green).

Figures 8.9 and 8.11 show that the BRR<sub>NBR</sub> points out lower degrees of recovery for all the LULC classes. The substantial difference is denoted in the percentage values of pixel distribution in the two lowest recovery classes (very low and low), for Euc (40.88% and 27.36%) and Pas/Shr (55.50% and 16.44%) classes on the first date after the fire (Jun 2019). For AuFor class, the pixels falling in the Very low category were only 4.15%, but the 23.25% resulted in low recovery on the same date. The other optical and SAR VIs did not classify pixels into the very low BRR category, while the number of pixels labelled as low recovery was less than 1%. However, as expected, in all the cases, a positive recovery trend was detected; indeed, a shift in the distribution of pixels from lower to



higher recovery categories when increasing years after the fire is observable. Concerning SAR-based  $BRR_{RVI_{As}}$ , although it appears that most of the pixels fell within higher recovery levels already starting from the first year after the fire, the relative increase in the number of pixels within the same BRR category for each observation year is significantly lower than that observed in the optical data. Looking at the categories of high and very high recovery, respectively, the AuFor went from 10.99% (2019) to 59.26% (2021) and from 2% (2019) to 13% (2021) for  $BRR_{NBR}$ ; from 38.13% (2019) to 43.06% (2021) and from 5.60% (2019) to 52.82% (2021) for  $BRR_{NDVI}$ ; while for  $BRR_{RVI_{As}}$  from 41.17% (2019) to 40.44% (2021) and from 26.16% (2019) to 39.91% (2021).

### 8.3. Discussion

#### 8.3.1. Optical time-series

This study reveals a strong relationship between vegetation recovery rate and fire severity category (Figure 8.2), as expected based on existing literature (Meng et al., 2018; Morresi et al., 2019; Ryu et al., 2018). In higher severity categories the maintenance of lower values of the profiles during most of the observation period is due to the double effect of the loss of photosynthetic vegetation and the presence of charcoal and ash (José M. C. Pereira et al., 1999). Each LULC class showed a specific temporal pattern. Typically, tree species' predisposition to fire resistance and/or adaptation affects the recovery rate and patterns (Catry et al., 2012; Filipe X Catry, Pausas, et al., 2013; Chompuchan & Lin, 2017; Gouveia et al., 2010), especially for low and moderate fire severity. The seasonal stability of AuFor vegetation, characterizing the unburned vegetation, and the highest annual variability of Pas/Shr, with the relative differences detected by NIR- or SWIR-based VIs, comply with what was observed by Soares et al. (2022) concerning the phenology adaptation strategies of Portuguese cork oak ecosystems.

Generally, a gradual spectral post-fire recovery is displayed in almost all cases at the end of the observing period, mainly when the species are characterized by a high regeneration capacity and vegetative growth (Semeraro et al., 2019). In the final monitoring year, the optical profiles no longer present dynamic patterns and differences between the various severity categories. Similar behaviour of recovery patterns of the photosynthetic activity and the ecosystem's physiological cycles after a few years from the fire event was reported in other studies (Chompuchan & Lin, 2017) using optical profiles based on NIR and SWIR bands. As expected, the lower and moderate severity categories faster achieved advanced recovery stages in AuFor and Pas/Shr, near or equal to the initial unburned VIs values. This is supposed to be due to vegetation generally remaining totally or partially unburned, contributing positively to the optical reflectance. Meng et al. (2018) observed that a low level of fire-induced damage does not induce such a significant reconstruction action by tree species to be detected by the VIs. This statement could justify the Euc low severity profile behaviour, characterized by a parallel pattern to the unburned profile; however, further and longer-time investigations are needed to explain these aspects.

Additionally, Catry et al. (2013) demonstrated in their study that although *Eucalyptus* spp. has a general fire-resistant behaviour, it presents higher fire-susceptivity when placed in artificial plantations. It should be considered the result reported by Hausler et al. (2018), where it was observed that four years after the fire event, many eucalyptus surfaces have not yet fully recovered the levels of evapotranspiration, thus suggesting that it may take longer for a full recovery. These results highlight the higher efficiency of native species in restoring the ecological equilibrium. These observations are corroborated by the spatial distribution of recovery rate, represented by the BRR.

Regarding the interpretation of forest LULC classes profiles, a specific influence of the underlying vegetation should be considered (Meng et al., 2018). Where plant structural layers are vertically superimposed, gaps between the dominant foliage that leave the underlying vegetation uncovered make it very difficult to distinguish the unique spectral signatures of each vegetation layer by optical sensors. (Lacouture et al., 2020). This is commonly observable in moderately burnt areas, where the gaps in the foliage caused by the fire expose the underlying vegetation that has regrowth in the meantime (Meng et al., 2018; A Polychronaki et al., 2014). This behaviour can be ascribed to the ability of optical sensors to detect only the external reflective surface of objects and to the saturation of the optical VIs at relatively low levels of LAI, with an increased rate that could be induced by the rapid colonization of herbaceous and shrubby vegetation. (Frazier et al., 2015; Zhao et al., 2016).

The gradual declension of the VIs profiles perceptible in the unburned forest classes (AuFor and Euc), opposite to the increasing trend associated with a frequent and growing fire disturbance regime, was already observed and described in other studies (Goetz et al., 2005; Ryu et al., 2018; Semeraro et al., 2019). The stasis in the physiological trend may be due to a combination of different factors. The reaching of the point of maximum vegetation increase in which the levels of competition between plants are lowered, and the rainfall decrease, lengthening the drought period (Figure 5).

Although annual optical fluctuations seem more influenced by season-specific phenological dynamics than by rainfall's direct effect, it should be considered that plant phenology is closely related to the climatic variables, and this is reflected in all-optical VIs (Fernández-García et al., 2018; Morresi et al., 2019; Poon & Kinoshita, 2018; Ryu et al., 2018; Song & Woodcock, 2003). The correlation indices displayed in the heatmaps (Fig 8.6) show that precipitation positively impacts physiological activity, especially for Pas/Shr and Euc vegetation. Significant drops in optical VIs occurred in these two LULCs classes between the end of June and August, corresponding to a sharp decrease in total rainfall during these months, highlighting that some vegetation types may be more sensitive to a meteorological parameter than another. The lower correlation with rainfall regimes of AuFor describes the low susceptibility to water stress that characterized Mediterranean corks, corroborating what was found by the recent study of Soares et al. (2022) and what was observed by Vidal-Macua (2017). The former study observed a high sensitivity of herbaceous species and shrubs belonging to the cork oak ecosystems to high temperatures (negatively) and precipitations (positively), supporting our findings (Figure 8.6).

Concerning the temperatures, the greater susceptibility to high summer temperatures is confirmed, concomitant with a phase of vegetative stasis.

Focusing on the observation, the NIR- and RedEdge-based VIs showed faster recovery trends than SWIR-based VIs. This confirms what other scholars (Frazier et al., 2015; Morresi et al., 2019; Ryu et al., 2018; M. Tanase et al., 2011; Q. Wang et al., 2005; Zhao et al., 2016) stated concerning, on the one hand, the greater sensitivity of the combination of the Red and NIR bands to photosynthetically active vegetation and the LAI, induced by the rapid regrowth of vegetation canopy; on the other hand, the complementary SWIR-based VIs sensitivity the immediate damage caused by the fire on the forest cover and to the gradual development of the canopy cover, which might take even a few years longer (1-4) than the NIR-based ones, as observed in other studies.

### **8.3.2. SAR time-series**

The comparison of the different profiles shows how the interactions of the SAR signal, both individual polarized backscatter (Figure 8.4) and dual-polarimetric VIs (Figure 8.3), are not so easy to interpret as in the case of optical reflectance. Generally, our results show that the cross-polarized backscatter and dual-polarized index (RVI and

DPSVI) values of the burned areas initiate an incremental trend phase, representing the beginning of the vegetation recovery phase, starting from the first year after the fire event in a way that is directly proportional to the fire severity category and as a function of the type of vegetation (LULC class). This was after an initial decrease immediately after the fire event, which was also proportional to the fire severity. However, the recovery dynamics are different between the type of VI used, and the characterization of specific phenological patterns is complex. This was expected given the greater sensitivity of the SAR signal to local environmental parameters. In particular, surface and soil moisture can heavily influence SAR recovery backscatter (Hachani et al., 2019; Kasischke et al., 2011; Tanase et al., 2011; Zhou et al., 2019), while less influential seems to be the biochemical composition of the exposed soil (Minchella et al., 2009). Nonetheless, geomorphology and topography can directly or indirectly affect hydrological processes and, consequentially, vegetation recovery dynamics (José Vidal-Macua et al., 2017). The drainage or retention capacity of the rock basement or the slope's orientation towards the sun's direct radiation determines local ground water balance and evapotranspiration (Christopoulou et al., 2019; Röder et al., 2008; Viana-Soto et al., 2017).

The indirect effects that fires of this size and severity can cause surrounding unburned vegetation should also be considered. The micro-climatic conditions and the hydrological balance are altered by the destruction of the proximal coverings, whose mitigating and balancing properties are well known (shading, wind repair, humidity balance, rainfall interception, etc.). The artificial ecosystems (such as eucalyptus plantations) used for biomass production are more susceptible to these alterations, both for their ecological vulnerability and higher nutritional needs (Catry et al., 2015; Häusler et al., 2018). This could partly explain the decline in the unburned SAR curve of the Euc. Differentially, native species in a natural or semi-natural environment are predisposed to adaptive strategies to environmental adversities (Catry, Pausas, et al., 2013; Soares et al., 2022).

The results of the interactions between SAR polarization and surface dynamics can have different meanings depending on the observation biome (Chen et al., 2018; Tanase et al., 2011). For this reason, coupling climate variables profiles (Figure 8.5) to spectral SAR response is helpful. The interception of rain by vegetation, especially by the forest cover, plays a fundamental role in the water balance of the ecosystem, resulting in a difference between the total rainfall recorded and that reached the ground, which would greatly influence the SAR signal (Ban et al., 2020; Frison et al., 2018). Although few intra-seasonal dynamic fluctuations were found in the SAR profiles, many of them (e.g., all the dual-polarization combinations: RVI, DPSVI, and RFDI ascending for AuFor and Pas/Shr; RVI, DPSVI and RFDI descending for AuFor class) showed evident inter-seasonal patterns driven by humidity conditions, in particular by rain (Figure 8.5) when compared to the relative plot (Figure 8.4). Noticeable are the effects of the exceptional amount of rain that fell in March 2018 and of that rainfall that fell in November-December 2017 on the response of the SAR signal, observable in all combinations. The peak of the SAR curve relative to June 2017, noticeable in most of the profiles, is difficult to interpret; this behaviour, among other things, is not found in the patterns following the fire event both for the unburned vegetation and that affected by low/moderate severities. A notable detail is a minimum value that is observed in many SAR profiles (VH, DPSVI, RFDI, RVI\_As/Ds for AuFor and Euc; VV\_Ds for all the LULCs; VV\_As for AuFor and Euc) and almost all related severity categories, and all the relative categories of severity in the months of January-February 2020. Observing the plots of the climatic variables (Figure 8.5), this can be correlated to an exceptional decrease in rainfall (3.11 mm in February 2020) that occurred in conjunction with exceptionally mild temperature levels (14.35 °C in February 2020: +1.75 °C compared to February 2019; + 7.85 °C compared to February 2018). However,

the co-polarised signal seems to have been perceptibly driven by the rainfall in all the possible path-severity-LULC combinations, and more than the other profiles, with parallelism between curve fluctuations and a general increasing trend after the fire event. Ban et al. (2020) explained that the rain events after the fire and intercept bare soil, encountering little or no interception by the destroyed vegetation, influence the co-polarized signal inducing its increase. Furthermore, the same authors observed that the VV backscatter values were generally higher than VH, an aspect also found in the profiles of the current study. Minchella et al. (2009) also observed increasing VV backscatter using C-band in Mediterranean forest ecosystems affected by the fire. The VV dynamic patterns of burned vegetation were driven by soil moisture fluctuations during the monitored five years after the fire event, especially at high fire severity. Periods at a lower soil dielectric constant, such as summer, resulted in lower VV backscatter values. Indeed, rapid re-growth of forest cover increases the similarity to herbaceous vegetation patterns (Minchella et al., 2009). These observations could explain the presence of high amplitudes (high fluctuations) during the different seasons of VV profiles, in some cases proportional to the fire severity category. However, given the relatively short observation period (three years), the attenuation effects given by the increasing vegetation recovery were not observed.

### **8.3.3. SAR polarization dependency**

The abovementioned aspects concern the more general topic of differences between cross- and co-polarization in interacting with the surfaces covered by forest. Immediately after a severe fire event and for the first post-fire year, oppositely to the perceptible increase already described for VV backscatter, a noticeable decrease in the VH backscatter is observable (Figure 8.4). This opposite behaviour of the two polarizations accords with other studies (De Luca, Silva, & Modica, 2021a; Imperatore et al., 2017; Mari et al., 2017). The burn of stems and large branches reduces the volumetric backscattering contribution of these structural vegetation components (i.e., scatterers), to which the cross-polarized signal is sensitive. Consequently, as microwave penetration through the damaged canopy increases, the effect of surface and double bounce dispersion on total backscatter is more prominent, induced by the greater proportion of exposed soil moisture components and the underlying soil (to which the co-polarized signal is sensitive) (Chen et al., 2018; Martins et al., 2016; Tanase et al., 2011; Tanase, Santoro, De La Riva, et al., 2010). In unburned forested areas, the high reflection pattern of VV co-polarized signal is instead associated with backscattering returned from vertical stand largest trees and trunks (Martins et al., 2016).

As expected, except for the VV\_Ds profile for Euc class, no ability to distinguish between different severity categories was observed in all co-polarized combinations. When the severity of the fire that affected the forest vegetation was moderate, the decrease in VH is more gradual as the trees most affected are those of the intermediate vertical layer, which contribute less to the total AGB than the specimens of the dominant layer. Regarding the VH profile for the Pas/Shr class, it is more difficult to interpret its patterns, especially for the higher severity categories. Due to their biases, a clear conclusion cannot be obtained when only using single-polarization temporal backscattering, despite the higher overcome of cross-polarized already observed in other studies (Martins et al., 2016; Tanase et al., 2011). Agree with Chen et al. (2018). Instead, dual-polarized VIs improved the delineation of the proportionality between fire severity and time profiles, demonstrating their attitude to decrease the cross- and co-polarized biases.,

### **8.3.4. SAR orbit path dependency**

The separate analysis of the orbit paths made it possible to delineate the divergences arising from the sensor geometry on the temporal profiles. This was due to the look direction of the SAR, which causes the signal to interact geometrically differently with the local structural orientation of the regrowing forest (M. Tanase et al., 2011). A fundamental role is played by the effects of the terrain, which determines the local angle of incidence of the microwave beam (Gimeno & San-Miguel-Ayanz, 2004; Kurum, 2015; Tanase, Santoro, De La Riva, et al., 2010). The presence of reliefs can cause radar shadow effects, for which some areas facing the side opposite the radar beam are not detected by one of the two paths (Richards, 2009a), as well as directly influencing the local soil water balance (Christopoulou et al., 2019; Röder et al., 2008; Viana-Soto et al., 2017). This confirms the need to use both orbit paths to construct complete information about what is observed. Some authors have highlighted the role of both orbits in increasing the detection capabilities of burned areas (De Luca, Silva, & Modica, 2021a; Donezar et al., 2019) or the LULC classification (Sayedain et al., 2020). A further observation is that the differences between orbit paths are noticeable when the single polarizations are compared. Integrating these two in the dual-polarized indexes seems to attenuate the look direction effects.

### **8.3.5. *Spatial distribution of vegetation recovery rate, the BRR***

The spatial distribution of the vegetation recovery categories, represented by the optical BRR (Figures 8.9-8.11), complies with what emerges from the analysis of the temporal profiles. The BRR results (Figure 8.11) demonstrated that the surface occupied by native forest reaching the highest recovery level was more than Euc vegetation at the end of the observed period (2021). Even observing the map of Figure 8.9, it is clear that the west-east development track, spatially and temporally traced by the vegetation regrowth, follows the disposition of the areas occupied by AuFor vegetation when compared to the LULC map. When optical VIs based on NIR ( $BRR_{NDVI}$ ) and RedEdge ( $BRR_{NDRE}$ , in supplementary material) are used, most pixels fell into the higher recovery categories since the first year after the fire event than when using the index NBR. Furthermore, the SWIR-based index includes most of the pixels within the lowest recovery classes (Very low and Low) in the first two post-fire years. The other optical indices did not detect pixels in the very low category, while less than 1% of the pixels fell in the low category. The season of occurrence of the fire also influences the characteristics with which it affects the vegetable fuel. A higher humidity of the fuel could increase the variability of the fire and, equivalently, of the VIs responses (Lacouture et al., 2020), especially of SWIR-based ones. Although, in the present study, having the fire occurred during the dry season (August 2018), it was characterized by homogeneous severity and intensity over large and contiguous areas (De Luca, Silva, Oom, et al., 2021).

The relative increase of  $BRR_{RVI}$  recovery in the subsequent year was noticeable compared to the respective optical indices. The BRR relative to the RVI index showed that most of the pixels already fell into higher recovery categories in the first year after the fire. However, the spatial distributional track of the recovery adheres to that of optical BRRs. Anyway, if the relative change over time is analyzed and compared to the  $BRR_{NDVI}$ , a more gradual recovery is detectable for the  $BRR_{RVI_{As}}$ , as already found in the temporal profile. However, the more complex interpretation of the SAR makes it more challenging to characterise specific spatial patterns. Factors such as the different influence exerted by the remaining charcoal on the fire-affected surfaces, the high sensitivity to humidity, and the wavelength used suggest that a further examination is needed concerning the efficiency of using the SAR-based BRR.

### **8.3.6. *SAR wavelength dependency***

The behaviour of SAR is obviously determined by the wavelength used. The use of dual-polarized allowed to capture the different recovery dynamics between the severity category and the vegetation type. The penetration capacity of SAR allows a more gradual and realistic regrowth of the vegetation structure, unlike the earlier saturation that occurred in the optical profiles, which implies a limitation for long-term monitoring, as pointed out by other scholars. Tanase et al. (2011) observed that NDVI reached unburned reference values 30 years earlier than cross-polarized backscatter in post-fire Mediterranean forest regrowth. For the same purpose, Polychronaki et al. (2014) revealed that while the sensitivity of the NDVI to short vegetation recovery led to earlier saturation, C-band VV backscatter differentiated regrowth stages in dense pine forests for the first 18 years after the event. In Zhou et al. (2019), complete recovery of tundra vegetation was detected in three years, two years less than those estimated from C-band SAR data. In the present study, the SAR profiles did not reach the total recovery values dictated by the unburned profiles, highlighting the usefulness of this supplementary information for ambient monitoring. After three years, the regenerated vegetation could not reach pre-fire density levels. In any case, an easier achievement of unburned values resulted when C-band interacted with native complex vegetation. A high degree of recovery is also observed in Pas/Shr profiles. This accords with what other studies noted, such as the abovementioned Zhou et al. (2019) in which, monitoring short vegetation post-fire dynamics in a tundra environment, the C-band reached a saturation level in the first five years after the fire, failing after a certain threshold to detect the occurring changes. Also, Tanase et al. (2011) demonstrated that although a strong sensitivity to the different recovery stages is present when C-band was used in the first decade after the event, the highest discrimination was observed at L-band. Quegan et al. (2000) determined that the backscatter coefficient in C-band became stable for areas occupied by forest vegetation with more than 30-40 tons·ha<sup>-1</sup> of biomass. For the same reason, any green surface covers not consumed by fire or even partially damaged might contribute intrusively to the optical reflectance values, making it challenging to discriminate patterns related to the underlying vegetation only by this type of sensor (Lacouture et al., 2020). SAR short bands are also more susceptible to signal decorrelation factors, such as noise caused by tree crowns that move with the wind (Brisco et al., 2017).

This high sensitivity of the C-band to vegetation smaller scattering elements might allow greater efficacy in detecting the effects of fire on non-complex structures and the regrowth phases of short vegetation (herbaceous, shrubs, etc.) (Martins et al., 2016; Minchella et al., 2009; Tanase et al., 2011; Zhou et al., 2019) or, parallelly, when forest vegetation structure which had been affected by lower fire severity was not sufficiently damaged. In the latter case, insignificant changes could be observed in longer wavelengths (L and P band) (Menges et al., 2010). For example, Martins et al. (2016) criticized the L-band based indices (including dual-polarized indices) because they failed to differentiate between fire-related tropical forest degradation classes. However, this wavelength has been found to be sensitive to forest structures. Moreover, it was demonstrated that, during the first period after the fire event, the lower penetration capacity of the C-band allows it to be less affected by soil influence than the L-band when vegetation structure had been semi-destroyed by the fire (Zhou et al., 2019). The remnant of the burned trees on site might further influence the cross-polarized backscatter response in C-band. Tanase et al. (2011) observed an increase in the values. A lower backscatter was instead observed where artificial post-fire managing processes were carried out, removing the burned standing trees after a fire. This could lead to confusion with forest regrowth the first year after the fire event.

### **8.3.7. Additional observation about recovery rates and optical profiles**



In Mediterranean ecosystems, the recovery process is very complex, as it can vary based on environmental (soil, microclimate, etc.) and landscape (geomorphology, aspect, etc.) variables, vegetation (type and quantity of vegetation present before and after the fire), as well as specific factors of the fire event (e.g., severity, occurrence, etc.) (Christopoulou et al., 2019; Emilio Chuvieco, 2009; De Luis et al., 2006; Mitchell et al., 2009; Montès et al., 2004). Generally, the first stage of post-fire dynamic auto-succession is usually characterized by prompt and massive colonization of pioneer Mediterranean annual grasses and perennial woody shrubs (Fabaceae, Cistaceae, Lamiaceae, Pteridofite, etc.) or pioneer trees (Capitanio & Carcaillet, 2008; De Luis et al., 2006; Mitchell et al., 2009; Montès et al., 2004). Most of the taxa recognizable in a post-fire environment play a fundamental ecological role in the general recovery of degraded or abandoned areas (e.g., ex agriculture) in Mediterranean territories (Xofis et al., 2022). The tracing of the spectral profiles related to the rapid post-fire recovery is thus generally highly related to the sensitivity of the VIs towards the dynamics of herbaceous vegetation rather than the regrowth of the tree canopy (Morresi et al., 2019). This is typical also in other environments biomes: in the sub-tropical climate, with perennial understory plants resprouting from belowground buds immediately after the fire and reaching pre-fire condition after a few months (Lacouture et al., 2020); Zhou et al., (2019), analyzing the first 3 years of post-fire recovery of a Tundra ecosystem, observed that graminoid herbaceous vegetation actuate the most significant colonization (35-50% cover), followed by deciduous and ericaceous shrubs (33-42% cover). This leads to an increase in spectral optical profile values and, thus, according to some authors (Frazier et al., 2015; Morresi et al., 2019), biased estimates of the real trend of tree canopies' spectral recovery.

The second stage, generally observable in the medium and long term, in the areas previously occupied by the forest or surrounded by it, involves filling the gaps by the forest seedlings (Frazier et al., 2015; Montès et al., 2004). The renewal that occurs in the medium and long term inside the gaps left by fires causes an increase in reflectance in specific wavelengths and in any case, a general rise in optical brightness. The gaps caused by parts of dead and/or destroyed foliage expose the underlying layers, which are rapidly colonized by flourishing herbaceous pioneer vegetation already from the first post-fire vegetative seasons. This translates into an increase in reflectance in the infrared wavelengths at the optical spectral level, especially in the Red-Edge and NIR (Meng et al., 2015, 2018). Consequently, the spectral trajectories of forest recovery do not necessarily match directly to changes in the succession of one of the two forest layers (Frazier et al., 2015). This step can be anticipated where the woody species are characterized by a high capacity for asexual (es. *Eucalyptus*, *Quercus*, etc.) or sexual (Mediterranean pines) regeneration (Capitanio & Carcaillet, 2008; Filipe X Catry, Moreira, et al., 2013; Montès et al., 2004). In the case of tree species, the recovery rate and patterns are related to their adaptations to fire (Filipe X Catry, Pausas, et al., 2013; Chompuchan & Lin, 2017).

Moreover, the thermo-Mediterranean cork oak has also adopted mechanical defense related to the bark, especially the cork oak, making it difficult to damage the internal tissues from fires of moderate severity (Filipe X Catry et al., 2012; Filipe X Catry, Pausas, et al., 2013). The simultaneous initial growth of both short and woody vegetation causes increases in optical reflectance and SAR backscatter. The competition phase that follows determines the closure of the foliage of the new individuals, causing an impenetrable barrier between the optical sensor and the undercover vegetation (Meng et al., 2018). The latter, however, continues to develop below the canopy, as well as the shade-tolerant tree seedlings and the height and DBH of dominant tree seedlings (Capitanio & Carcaillet, 2008; Frazier et al., 2015). In this case, the SAR has higher detection potential thanks to its ability to penetrate inside the canopy coverage as a function of the wavelength. Some authors (Meng et al., 2018) assume it is unrealistic to

consider that the rapid recovery of optical spectral profiles is caused by the contributions of all the different forest vertical layers (stratum). Optical spectral vegetation indices, in fact, cannot separate the vegetation recovery of the upper layers from that of the lower layers. The same authors (Meng et al., 2018) advise associating well the relationship between recovery rate (and burn severity gradient) with the time passed since the event, that is to distinguish the various temporal passages in which the different types of spectral signatures originating from the succession of different layers of regrowing vegetation can overlap and lead to errors, especially for the higher categories of burn severity. For example, in the short term, the spectral patterns of the still destroyed tree's foliage can be influenced by the regrowth of the underlayer vegetation, while in the long term, the regrown tree crowns cover the underlying layers of grass and shrubs. To overcome these limitations, Meng et al. (2018) used the combination of structural data from active sensors (LiDAR) so that the real structural nature of the regrown vegetation could be better isolated from the purely spectral response.

This is true only when the post-fire recovery process is considered as the pre-fire structural and species-specific conditions return. This approach contrasts with the natural dynamics, sometimes causal or typical, determined by numerous factors. Furthermore, plants and ecosystems could change their environment in the short or long term during the succession stages, achieving new levels of equilibrium that are more convenient, although different from the initial states (De Luis et al., 2006; Montès et al., 2004).

#### **8.3.8. *Additional observation about site topography and geomorphology influence on recovery dynamics***

Local water availability is determined by the topographical and geomorphological factors of the site. Aspect, for example, is related to solar radiation and, thus, moisture accumulation (and evapotranspiration), besides photosynthetic activity. Generally, warmer sides receiving higher solar radiation are slightly less favorable for the affirmation of humidity-demanding vegetation due to the accelerated transpiration, leading to more severe drought stress, especially in the earliest stage of recovery (Christopoulou et al., 2019; José Vidal-Macua et al., 2017; Röder et al., 2008; Viana-Soto et al., 2017). Also, considering the variable photosensitivity of plants, how these factors act both indirectly and directly on the selectivity of the species during post-fire recovery is easily deductible (José Vidal-Macua et al., 2017; Röder et al., 2008).

Lithological features also affect hydrological factors such as absorption, retention, and water drainage. Rock basement nature plays a fundamental role in either soil production (quantitatively and qualitatively) and loss (erosion), as well as in planting succession and competition by their root penetration capability (fundamental for stability and nutrients accessing) (Christopoulou et al., 2019; José Vidal-Macua et al., 2017). On the other hand, fire directly affects the rock basement and soil structure by removing roots and destroying the litter layer. This causes changes in the chemical-physical properties of the substrate and induces indirect and direct effects e.g., reduced water interception, storage, and infiltration capacity and an increase in overland erosive flow erosion (Diakakis et al., 2017).

#### **8.3.9. *Final considerations***

Considering the findings of the present study, as well as the consulted literature, we found that the optical S2 and SAR S1 VIs appeared to have a higher aptitude for monitoring vegetation regrowth, which can be used effectively as complementary information to assess and monitor the short-term response of ecosystems to fire. Some limitations persist, such as the predisposition of optical data to reach saturation, partially compensated by the weak SAR C-band penetration capacity through the forest canopy. Further literature examination and considerations

concerning the SAR wavelength dependency are reported in the supplementary material. Integrating multi-frequency SAR (L-band and/or P-band), VHR data, or LiDAR information can optimize the capture of the spectral and structural properties of the regrowth vegetation and quantify the understory seedling recovery rate more precisely (Meng et al., 2018).

Besides those already argued, many factors influence the SAR results or help their interpretation. The behaviour of the SAR depends very much on the environmental conditions, and further investigations will have to be carried out. In this study, two climatic variables are taken into consideration. However, we would like to suggest other parameters that should be investigated and compared, including pedological and lithological characteristics, soil moisture, topography, and territory geomorphology. Besides the heterogeneity of LULCs analyzed (especially AuFor and Pas/Shr), the topographical variability of the Mediterranean ecosystem strongly influences the microwave signal (Tanase et al., 2011; Tanase, Santoro, De La Riva, et al., 2010; Tanase, Santoro, Wegmüller, et al., 2010), as highlighted by the differences resulted from the dependent analysis of the orbital path. The use of averaged ROIs value for both the optical and SAR dataset, added to the speckle noise filter applied to SAR, attenuated the variability of each curve (Frazier et al., 2015; Martins et al., 2016; Minchella et al., 2009; Tanase et al., 2011). Several studies investigated how topographical and geomorphological variables positively or negatively influence local vegetation recovery dynamics and population post-fire biodiversity and how they are affected in turn (Christopoulou et al., 2019; Diakakis et al., 2017; José Vidal-Macua et al., 2017; Röder et al., 2008; Viana-Soto et al., 2017). Slope and aspect, for example, determine solar wave incidence radiation, which largely influences both water/moisture balance, evapotranspiration, and photosynthetic activity (Röder et al., 2008). On the other hand, slope and lithology affect erodibility, water drainage/accumulation, as well as root penetration capacity (Christopoulou et al., 2019). More considerations based on current literature are reported in the supplementary material.

#### **8.4. Conclusions**

The results reported in this study show that Mediterranean ecosystems respond rapidly to disturbances, initiating effective restoration processes. However, earlier recovery of unburned values is attributable to a premature saturation affecting both NIR-based indices and SAR C-band wavelength. Regrowth trends are observable from the first months after the fire event reaching an apparent almost complete recovery occurring by the three years of analysis in optical and SAR VIs. The vegetation type influences the time and the magnitude of recovery temporal activity in terms of spectral response, with a noticeable difference between native and non-native forest vegetation. However, the proportionality between recovery pattern and fire severity categories was kept. The higher degree of recovery occurred for the autochthonous forest class (AuFor), followed by Pas/Shr, reflected the higher adaptability of these ecosystems to stress regimes and efficiency in restoring the ecological equilibrium, directly proportional to their more differentiated structure and biodiversity compared to the area occupied by eucalyptus plantations. These observations were corroborated by the BRR, representing the spatial distribution of recovery rate, whose outcomes demonstrated that the surface occupied by highly and very highly recovered AuFor vegetation was more than that occupied by Euc vegetation during the three years of observation; even more evident when optical indices were used ( $BRR_{NBR}$ ,  $BRR_{NDVI}$  and  $BRR_{NDRE}$ ). In order to account for the natural phenological temporal effects, the BRR calculation was optimized using the RF machine learning regressor with which the hypothetical unburned conditions of the fire-affected area for each time of estimation of the index were predicted

and reconstructed. However, although optical BRR has been demonstrated to be effective, the SAR-based needs further studies for its interpretation.

A high proportionality was found between the fire severity and the recovery profiles during the first two post-fire years, following an equally proportionated sharp decrease in optical and SAR values. Some exceptions persisted, such as for the SAR co-polarized (VV) profiles, due to their high moisture and exposed soil dependency. In fact, from the comparison and correlation of climate variables and temporal profiles, it has been clear that the precipitation events directly affected the C-band SAR profiles, especially in the categories of higher severity, where the interception of the vegetation cover guarantees the precipitation attenuation had been lacking. This denotes the menace of fire events toward the hydrological balance of the soil.

Considering these aspects, the management of SAR images required greater attention due to the higher presence of outliers and speckle noise caused by the intrinsic nature of the data. Using long time-series, the biases are more evident; however, several pre-processing processes were used to optimize the workflow and mitigate these issues, such as the speckle filter and the time average. Optical-related biases were also finely addressed, such as eliminating the clouds through the new product provided by Sentinel Team (s2cloudless) and subsequent linear interpolation to reconstruct the fill gaps.

Generally, this study demonstrated that the combined use of different sensors is essential to correctly delineate the dynamics that occur in Mediterranean fire-frequented habitats, compensating for the limitations of the single sensor, especially when a small temporal scale is needed. Moreover, the integration of free and open-source analysis software with equally free-available high temporal and spatial resolution data enables the accessibility by a wider audience involved in the forest risks monitoring framework.

However, the dynamics of post-fire Mediterranean vegetation must be further examined in long-term monitoring protocols in this and other study areas to assess the complete response even to delayed effects. Moreover, additional indicators and sensors may be necessary to determine which combination of temporal patterns best reflects the real post-fire dynamics in the Mediterranean ecosystems and their chemical, physiological and structural features. Focusing on SAR data, medium-long term monitoring may require the integration of multifrequency techniques with longer wavelengths (L-, P-band), able to penetrate further into the regenerated canopy, thus enabling in better understanding of forest recovery processes. The imminent availability of new data types (e.g., ESA BIOMAASS mission, Le Toan et al., 2011) and the development of cloud platforms (e.g., multi-mission algorithm and analysis platform, MAAP, 2022) will optimize the performance and the already high inter-compatibility of these resources. Further investigation could also involve the machine learning regression models to predict temporal and spatial recovery patterns, basing the regression on the values of the recovery metrics calculated. In this regard, we believe our results will efficiently provide helpful information.

## 9. General conclusions and future perspectives

In the Mediterranean Basin, although wildland fires are a natural element playing a key role in ecological processes and bringing benefits when severity and frequency are low, considering the intrinsic fire-adaptation of several habitats, human-induced changes in both climate and landscapes have been worsening fire regimes (increased severity, frequency, and distribution of wildland fires), making them socially, economically, and ecologically unmanageable. Accurate and tempestive information about the impacts of the fire on the environment, how its effects are distributed over time and space, and what is the response of the environment during the subsequent years after the event, are therefore of primary importance to predict and manage post-fire processes, in order to mitigate the degradation of forests and, landscapes, and the loss of ecosystem services.

In the present Ph.D. thesis, these purposes have been fulfilled by proposing several case studies constituting a complete open-source workflow for post-fire assessment, based on remote sensing data and geo-informatic techniques. It involved: i) the knowledge of the pre-fire conditions of the study site; ii) the precise semi-automatic identification, mapping and quantification of burned areas and perimeters; iii) the estimation, quantification, and classification, as well as spectral analysis, of the damages induced on vegetation cover; iv) the use of multitemporal observations of spectral-physiological response of vegetation and post-fire recovery. In particular, the potential of the integrated use of SAR (Sentinel-1) and optical (Sentinel-2) free-available satellite data was explored. Each single case study represents an innovative/optimized approach which contributed to cover some gaps in the present state of the art and that could be applied operationally in a general post-fire context, namely in Mediterranean forest and woodland ecosystems. The research was conducted in several Mediterranean areas, with similar environmental characteristics, located at around the 38° parallel of two different Countries (Portugal and Italy), to test the operability of the methodological workflow and its various components. In our opinion, the approaches proposed in this Ph.D. thesis could be extended to other European ecosystems. Future studies might test and validate the provided methodologies on different and more extended study areas to assess their versatility.

Within the overall objective of the research activity, several milestones have been fulfilled:

- ✓ In-depth practical investigation of the interaction between multispectral and SAR information with different land cover types, namely burned and unburned vegetation.
- ✓ Development of optimized approaches for the pre-processing of raw SAR data, to reduce the geometric and radiometric effects dependent on the local conditions of the surface (e.g., topography, roughness, humidity, local angle of incidence) that typically affect the backscatter signal.
- ✓ Multitemporal analysis for the characterization of spectral proprieties of post-fire recovery vegetation, by highlighting the difference between optical and SAR observations. Moreover, differentiating the analysis by type of vegetation and fire severity.
- ✓ Employment of advanced algorithms to find the most suitable hyperparameters values machine learning models, to maximize their performance.
- ✓ Finding that, although optical information alone achieves sufficient results, optical and SAR imagery synergy can improve the accuracy in all cases.

Emphasis was placed on the implementation of open-source image processing algorithms, Python-based libraries and machine learning models to develop semi-automatic procedures for extracting, processing, modelling and interpreting the information, and obtain quantitative-qualitative maps of the estimated aspects. A considerable milestone has been achieved with the use of deep learning (Chapter 6): these advanced artificial

intelligence (AI) algorithms have not been investigated in the literature as much as the classic machine learning models (e.g., random forest, support vector machine) for the study of fire events. Investing in deep learning-based workflows development might return minimise the presence of commission and omission errors in outcomes.

The results obtained demonstrate the efficiency of the interoperability of the various platforms, software, and libraries. They enable both to build an almost complete processing and analysis workflow, with a high degree of interchangeability and flexibility in the choice of components, and guarantee a high degree of shareability and full repeatability. Further developments could involve the use of open-source cloud computing platforms, where a large database of satellite imagery and computing power is accessible to all users (scientists, researchers, developers and amateurs).

The availability of innovative programming technologies with user-friendly interfaces enabled the exploitation of sophisticated calculation operations for information processing and data mining to a wide audience of researchers and scientists, bringing the full support of AI in various applications to be customary. However, paradoxically, the biggest obstacle remains the scarcity of sample field data which are necessary for the calibration of remote sensing methods: e.g., widely distributed and georeferenced measurements about severity assessment, dendrometric-structural forest values, land cover, habitats classification. Our hope is that greater effort (shared by both the researchers themselves and the administrators) will be spent in order to homogenize and make available the data already present, and to organize (finance) relevant campaigns aimed at covering the entire European territory. An effort on par with what has been done for the distribution of the same processing algorithms. So as, in an autonomous and efficient way, remote sensing researchers can develop and validate more and more models, inevitably leading to greater reliability of the same. Doing so would increase the autonomy of remote sensing scientists, allowing the validation of a greater number of models which, inevitably, would transform into a greater number of more effective and versatile results.



## 10. Acknowledgements

This thesis was co-financed with the support of the European Commission, the European Social Fund (ESF) and the *Regione Calabria* using the fund: *POR Calabria FESR/FSE 2014-2020 Asse 12 Azione 10.5.6 “Mobilità internazionale di dottorandi”*. The author, the Tutor and the Co-tutor are solely responsible for this thesis. The European Commission and the *Regione Calabria* decline any responsibility for the use that may be made of the information contained therein.



## 11. References

- Addison, P., & Oommen, T. (2018). Utilizing satellite radar remote sensing for burn severity estimation. *International Journal of Applied Earth Observation and Geoinformation*.  
<https://doi.org/10.1016/j.jag.2018.07.002>
- Alcañiz, M., Outeiro, L., Francos, M., & Úbeda, X. (2018). Effects of prescribed fires on soil properties: A review. *Science of The Total Environment*, 613–614, 944–957.  
<https://doi.org/https://doi.org/10.1016/j.scitotenv.2017.09.144>
- Alcaras, E., Costantino, D., Guastaferro, F., Parente, C., & Pepe, M. (2022). Normalized Burn Ratio Plus (NBR+): A New Index for Sentinel-2 Imagery. In *Remote Sensing* (Vol. 14, Issue 7).  
<https://doi.org/10.3390/rs14071727>
- Alves, A. M., Pereira, J. S., & Silva, J. M. N. (2007). *O Eucaliptal em Portugal: Impactes Ambientais e Investigação Científica* (ISAPress (ed.)). ISAPress.
- Amos, C., Petropoulos, G. P., & Ferentinos, K. P. (2019). Determining the use of Sentinel-2A MSI for wildfire burning & severity detection. *International Journal of Remote Sensing*, 40(3), 905–930.  
<https://doi.org/10.1080/01431161.2018.1519284>
- Aragones, D., Rodriguez-Galiano, V. F., Caparros-Santiago, J. A., & Navarro-Cerrillo, R. M. (2019). Could land surface phenology be used to discriminate Mediterranean pine species? *International Journal of Applied Earth Observation and Geoinformation*, 78(February), 281–294. <https://doi.org/10.1016/j.jag.2018.11.003>
- Arevalo-Ramirez, T., Villacrés, J., Fuentes, A., Reszka, P., & Auat Cheein, F. A. (2020). Moisture content estimation of Pinus radiata and Eucalyptus globulus from reconstructed leaf reflectance in the SWIR region. *Biosystems Engineering*, 193, 187–205.  
<https://doi.org/https://doi.org/10.1016/j.biosystemseng.2020.03.004>
- Aspromonte Park. (2022). *Aspromonte Park*. <http://www.parconazionaleaspromonte.it/pagina.php?id=41>
- Aubard, V., Paulo, J. A., & Silva, J. M. N. (2019). Long-term monitoring of cork and holm oak stands productivity in Portugal with Landsat imagery. *Remote Sensing*, 11(5). <https://doi.org/10.3390/rs11050525>
- Axel, A. C. (2018). Burned Area Mapping of an Escaped Fire into Tropical Dry Forest in Western Madagascar Using Multi-Season Landsat OLI Data. In *Remote Sensing* (Vol. 10, Issue 3).  
<https://doi.org/10.3390/rs10030371>
- Baldrige, A. M., Hook, S. J., Grove, C. I., & Rivera, G. (2009). The ASTER spectral library version 2.0. *Remote Sensing of Environment*, 113(4), 711–715. <https://doi.org/https://doi.org/10.1016/j.rse.2008.11.007>
- Ban, Y., Zhang, P., Nascetti, A., Bevington, A. R., & Wulder, M. A. (2020). Near Real-Time Wildfire Progression Monitoring with Sentinel-1 SAR Time Series and Deep Learning. *Scientific Reports*, 10(1), 1–15. <https://doi.org/10.1038/s41598-019-56967-x>
- Barbosa, P. M., Pereira, J. M. C., & Grégoire, J.-M. (1998). Compositing Criteria for Burned Area Assessment Using Multitemporal Low Resolution Satellite Data. *Remote Sensing of Environment*, 65(1), 38–49.  
[https://doi.org/https://doi.org/10.1016/S0034-4257\(98\)00016-9](https://doi.org/https://doi.org/10.1016/S0034-4257(98)00016-9)
- Barbosa, P. M., Stroppiana, D., Grégoire, J. M., & Pereira, J. M. C. (1999). An assessment of vegetation fire in Africa (1981-1991): Burned areas, burned biomass, and atmospheric emissions. *Global Biogeochemical Cycles*, 13(4), 933–950. <https://doi.org/10.1029/1999GB900042>
- Belenguer-Plomer, M. A., Chuvieco, E., & Tanase, M. A. (2019). Temporal Decorrelation of C-Band

- Backscatter Coefficient in Mediterranean Burned Areas. In *Remote Sensing* (Vol. 11, Issue 22).  
<https://doi.org/10.3390/rs11222661>
- Belenguer-Plomer, M. A., Tanase, M. A., Fernandez-Carrillo, A., & Chuvieco, E. (2019). Burned area detection and mapping using Sentinel-1 backscatter coefficient and thermal anomalies. *Remote Sensing of Environment*, 233(July 2018), 111345. <https://doi.org/10.1016/j.rse.2019.111345>
- Boardman, J. W., Kruse, F. A., & Green, R. O. (1995). Mapping target signatures via partial unmixing of AVIRIS data. *Proc. Summaries JPL Airborne Earth Sci. Workshop*. <http://hdl.handle.net/2014/33635>
- Boschetti, L., Roy, D. P., Giglio, L., Huang, H., Zubkova, M., & Humber, M. L. (2019). Global validation of the collection 6 MODIS burned area product. *Remote Sensing of Environment*, 235, 111490.  
<https://doi.org/https://doi.org/10.1016/j.rse.2019.111490>
- Boschetti, L., Roy, D. P., Justice, C. O., & Humber, M. L. (2015). MODIS–Landsat fusion for large area 30m burned area mapping. *Remote Sensing of Environment*, 161, 27–42.  
<https://doi.org/https://doi.org/10.1016/j.rse.2015.01.022>
- Bot, K., & Borges, J. G. (2022). A Systematic Review of Applications of Machine Learning Techniques for Wildfire Management Decision Support. In *Inventions* (Vol. 7, Issue 1).  
<https://doi.org/10.3390/inventions7010015>
- Breiman, L. (2001). Random forests. *Machine Learning*, 45(1), 5–32. <https://doi.org/10.1023/A:1010933404324>
- Brisco, B., Ahern, F., Murnaghan, K., White, L., Canisus, F., & Lancaster, P. (2017). Seasonal change in wetland coherence as an aid to wetland monitoring. *Remote Sensing*, 9(2), 1–19.  
<https://doi.org/10.3390/rs9020158>
- Cabral, A., De Vasconcelos, M. J. P., Pereira, J. M. C., Bartholomé, É., & Mayaux, P. (2003). Multi-temporal compositing approaches for SPOT-4 vegetation. *International Journal of Remote Sensing*, 24(16), 3343–3350. <https://doi.org/10.1080/0143116031000075936>
- Campos-Taberner, M., García-Haro, F. J., Camps-Valls, G., Grau-Muedra, G., Nutini, F., Busetto, L., Katsantonis, D., Stavrakoudis, D., Minakou, C., Gatti, L., Barbieri, M., Holecz, F., Stroppiana, D., & Boschetti, M. (2017). Exploitation of SAR and optical sentinel data to detect rice crop and estimate seasonal dynamics of leaf area index. *Remote Sensing*, 9(3), 1–17. <https://doi.org/10.3390/rs9030248>
- Cansler, C. A., & McKenzie, D. (2012). How robust are burn severity indices when applied in a new region? Evaluation of alternate field-based and remote-sensing methods. *Remote Sensing*, 4(2), 456–483.  
<https://doi.org/10.3390/rs4020456>
- Capitanio, R., & Carcaillet, C. (2008). Post-fire Mediterranean vegetation dynamics and diversity: A discussion of succession models. *Forest Ecology and Management*, 255(3), 431–439.  
<https://doi.org/https://doi.org/10.1016/j.foreco.2007.09.010>
- Carreiras, J. M. B., Quegan, S., Tansey, K., & Page, S. (2020). Sentinel-1 observation frequency significantly increases burnt area detectability in tropical SE Asia. *Environmental Research Letters*, 15(5).  
<https://doi.org/10.1088/1748-9326/ab7765>
- Cascio, W. E. (2018). Wildland fire smoke and human health. *Science of The Total Environment*, 624, 586–595.  
<https://doi.org/https://doi.org/10.1016/j.scitotenv.2017.12.086>
- Catry, F X, Moreira, F., Deus, E., Silva, J. S., & Águas, A. (2015). Assessing the extent and the environmental drivers of Eucalyptus globulus wildling establishment in Portugal: results from a countrywide survey.

- Biological Invasions*, 17(11), 3163–3181. <https://doi.org/10.1007/s10530-015-0943-y>
- Catry, Filipe X, Moreira, F., Cardillo, E., & Pausas, J. G. (2012). *Post-Fire Management of Cork Oak Forests BT - Post-Fire Management and Restoration of Southern European Forests* (F. Moreira, M. Arianoutsou, P. Corona, & J. De las Heras (eds.); pp. 195–222). Springer Netherlands. [https://doi.org/10.1007/978-94-007-2208-8\\_9](https://doi.org/10.1007/978-94-007-2208-8_9)
- Catry, Filipe X, Moreira, F., Tujeira, R., & Silva, J. S. (2013). Post-fire survival and regeneration of *Eucalyptus globulus* in forest plantations in Portugal. *Forest Ecology and Management*, 310, 194–203. <https://doi.org/https://doi.org/10.1016/j.foreco.2013.08.036>
- Catry, Filipe X, Pausas, J. G., Moreira, F., Fernandes, P. M., & Rego, F. (2013). Post-fire response variability in Mediterranean Basin tree species in Portugal. *International Journal of Wildland Fire*, 22(7), 919–932. <https://doi.org/10.1071/WF12215>
- Celik, T. (2009). Unsupervised Change Detection in Satellite Images Using Principal Component Analysis and  $k$ -Means Clustering. *IEEE Geoscience and Remote Sensing Letters*, 6(4), 772–776. <https://doi.org/10.1109/LGRS.2009.2025059>
- Chang, C., Wu, C., Member, S., & Chen, H. (2010). Random Pixel Purity Index. *IEEE Geoscience and Remote Sensing Letters*, 7(2), 324–328. <https://doi.org/10.1109/LGRS.2009.2034610>
- Chang, C.-I., & Wu, C.-C. (2015). Design and Development of Iterative Pixel Purity Index. *IEEE Journal of Selected Topics in Applied Earth Observations and Remote Sensing*, 8(6), 2676–2695. <https://doi.org/10.1109/JSTARS.2015.2403259>
- Chang, Chein-I, & Plaza, A. (2006). A fast iterative algorithm for implementation of pixel purity index. *IEEE Geoscience and Remote Sensing Letters*, 3(1), 63–67. <https://doi.org/10.1109/LGRS.2005.856701>
- Chatziantoniou, A., Petropoulos, G. P., & Psomiadis, E. (2017). Co-Orbital Sentinel 1 and 2 for LULC mapping with emphasis on wetlands in a mediterranean setting based on machine learning. *Remote Sensing*, 9(12). <https://doi.org/10.3390/rs9121259>
- Chen, L., Wang, Y., Ren, C., Zhang, B., & Wang, Z. (2019). Assessment of multi-wavelength SAR and multispectral instrument data for forest aboveground biomass mapping using random forest kriging. *Forest Ecology and Management*. <https://doi.org/10.1016/j.foreco.2019.05.057>
- Chen, W., Jiang, H., & Moriya, K. (2018). Monitoring of post-fire forest regeneration under different restoration treatments based on ALOS / PALSAR data. *New Forests*, 49(1), 105–121. <https://doi.org/10.1007/s11056-017-9608-2>
- Chen, X., Vogelmann, J. E., Rollins, M., Ohlen, D., Key, C. H., Yang, L., Huang, C., & Shi, H. (2011). Detecting post-fire burn severity and vegetation recovery using multitemporal remote sensing spectral indices and field-collected composite burn index data in a ponderosa pine forest. *International Journal of Remote Sensing*, 32(23), 7905–7927. <https://doi.org/10.1080/01431161.2010.524678>
- Chompuchan, C., & Lin, C. Y. (2017). Assessment of forest recovery at Wu-Ling fire scars in Taiwan using multi-temporal Landsat imagery. *Ecological Indicators*, 79(April), 196–206. <https://doi.org/10.1016/j.ecolind.2017.04.038>
- Chou, W.-C., Lin, W.-T., & Lin, C.-Y. (2008). Vegetation recovery patterns assessment at landslides caused by catastrophic earthquake: A case study in central Taiwan. *Environmental Monitoring and Assessment*, 152(1), 245. <https://doi.org/10.1007/s10661-008-0312-8>

- Choudhury, A. M., Marcheggiani, E., Galli, A., Modica, G., & Somers, B. (2021). *Mapping the Urban Atmospheric Carbon Stock by LiDAR and WorldView-3 Data*.
- Christopoulou, A., Fyllas, N. M., Andriopoulos, P., Koutsias, N., Dimitrakopoulos, P. G., & Arianoutsou, M. (2014). Post-fire regeneration patterns of *Pinus nigra* in a recently burned area in Mount Taygetos, Southern Greece: The role of unburned forest patches. *Forest Ecology and Management*, 327, 148–156. <https://doi.org/https://doi.org/10.1016/j.foreco.2014.05.006>
- Christopoulou, A., Mallinis, G., Vassilakis, E., Farangitakis, G.-P., Fyllas, N. M., Kokkoris, G. D., & Arianoutsou, M. (2019). Assessing the impact of different landscape features on post-fire forest recovery with multitemporal remote sensing data: the case of Mount Taygetos (southern Greece). *International Journal of Wildland Fire*, 28(7), 521–532. <https://doi.org/10.1071/WF18153>
- Chu, T., & Guo, X. (2013). Remote sensing techniques in monitoring post-fire effects and patterns of forest recovery in boreal forest regions: A review. *Remote Sensing*, 6(1), 470–520. <https://doi.org/10.3390/rs6010470>
- Chust, G., Ducrot, D., & Pretus, J. L. L. (2004). Land cover discrimination potential of radar multitemporal series and optical multispectral images in a Mediterranean cultural landscape. *International Journal of Remote Sensing*, 25(17), 3513–3528. <https://doi.org/10.1080/0143116032000160480>
- Chuvieco, E., & Martin, M. P. (1994). Global fire mapping and fire danger estimation using AVHRR images. *Photogrammetric Engineering and Remote Sensing*, 60(5), 563–570. <https://www.scopus.com/inward/record.uri?eid=2-s2.0-0028431013&partnerID=40&md5=99923433d7d5b3b054772f36d617981f>
- Chuvieco, Emilio. (2009). Earth observation of wildland fires in mediterranean ecosystems. In *Earth Observation of Wildland Fires in Mediterranean Ecosystems*. Springer Berlin Heidelberg. <https://doi.org/10.1007/978-3-642-01754-4>
- Chuvieco, Emilio. (2020). *Fundamentals of Satellite Remote Sensing* (4th ed.). CRC Press Taylor & Francis Group. <https://doi.org/https://doi.org/10.1201/9780429506482>
- Chuvieco, Emilio, Martínez, S., Román, M. V., Hantson, S., & Pettinari, M. L. (2014). Integration of ecological and socio-economic factors to assess global vulnerability to wildfire. *Global Ecology and Biogeography*, 23(2), 245–258. <https://doi.org/10.1111/geb.12095>
- Chuvieco, Emilio, Mouillot, F., van der Werf, G. R., San Miguel, J., Tanasse, M., Koutsias, N., García, M., Yebra, M., Padilla, M., Gitas, I., Heil, A., Hawbaker, T. J., & Giglio, L. (2019). Historical background and current developments for mapping burned area from satellite Earth observation. *Remote Sensing of Environment*, 225(November 2018), 45–64. <https://doi.org/10.1016/j.rse.2019.02.013>
- Chuvieco, Emilio, Ventura, G., Martín, M. P., & Gómez, I. (2005). Assessment of multitemporal compositing techniques of MODIS and AVHRR images for burned land mapping. *Remote Sensing of Environment*, 94(4), 450–462. <https://doi.org/10.1016/j.rse.2004.11.006>
- Chuvieco, Emilio, Yue, C., Heil, A., Mouillot, F., Alonso-Canas, I., Padilla, M., Pereira, J. M., Oom, D., & Tansey, K. (2016). A new global burned area product for climate assessment of fire impacts. *Global Ecology and Biogeography*, 25(5), 619–629. <https://doi.org/10.1111/geb.12440>
- Congalton, R. G., & Green, K. (2019). Assessing the Accuracy of Remotely Sensed Data. Principles and Practices. In *CRC Press*.

- Copernicus Access Hub. (2022). *Copernicus Access Hub*. <https://scihub.copernicus.eu/>
- Corona, P., Lamonaca, A., & Chirici, G. (2008). Remote sensing support for post fire forest management. *IForest - Biogeosciences and Forestry*, 1(1), 6–12. <https://doi.org/https://doi.org/10.3832/ifor0305-0010006>
- Crowley, M. A., Cardille, J. A., White, J. C., & Wulder, M. A. (2019). Generating intra-year metrics of wildfire progression using multiple open-access satellite data streams. *Remote Sensing of Environment*, 232(July), 111295. <https://doi.org/10.1016/j.rse.2019.111295>
- Cutler, D. R., Edwards, T. C., Beard, K. H., Cutler, A., Hess, K. T., Gibson, J., & Lawler, J. J. (2007). Random forests for classification in ecology. *Ecology*, 88(11), 2783–2792. <https://doi.org/10.1890/07-0539.1>
- Daldegan, G. A., Roberts, D. A., & Ribeiro, F. D. F. (2019). Remote Sensing of Environment Spectral mixture analysis in Google Earth Engine to model and delineate fire scars over a large extent and a long time-series in a rainforest-savanna transition zone. *Remote Sensing of Environment*, 232(November 2018), 111340. <https://doi.org/10.1016/j.rse.2019.111340>
- De Luca, G., Modica, G., Fattore, C., & Lasaponara, R. (2020). Unsupervised Burned Area Mapping in a Protected Natural Site. An Approach Using SAR Sentinel-1 Data and K-mean Algorithm. In *Computational Science and Its Applications – ICCSA 2020. Lecture Notes in Computer Science, vol 12253* (Vol. 1). Springer International Publishing. [https://doi.org/10.1007/978-3-030-58814-4\\_5](https://doi.org/10.1007/978-3-030-58814-4_5)
- De Luca, G., N. Silva, J. M., Cerasoli, S., Araújo, J., Campos, J., Di Fazio, S., & Modica, G. (2019a). Object-Based Land Cover Classification of Cork Oak Woodlands using UAV Imagery and Orfeo ToolBox. *Remote Sensing*, 11(10), 1238. <https://doi.org/10.3390/rs11101238>
- De Luca, G., N. Silva, J. M., Cerasoli, S., Araújo, J., Campos, J., Di Fazio, S., & Modica, G. (2019b). Object-Based Land Cover Classification of Cork Oak Woodlands using UAV Imagery and Orfeo ToolBox. *Remote Sensing*, 11(10), 1238. <https://doi.org/10.3390/rs11101238>
- De Luca, G., Silva, J. M. N., Di Fazio, S., & Modica, G. (2022). Integrated use of Sentinel-1 and Sentinel-2 data and open-source machine learning algorithms for land cover mapping in a Mediterranean region. *European Journal of Remote Sensing*, 55(1), 52–70. <https://doi.org/10.1080/22797254.2021.2018667>
- De Luca, G., Silva, J. M. N., & Modica, G. (2021a). A workflow based on Sentinel-1 SAR data and open-source algorithms for unsupervised burned area detection in Mediterranean ecosystems. *GIScience and Remote Sensing*, 58(4), 516–541. <https://doi.org/10.1080/15481603.2021.1907896>
- De Luca, G., Silva, J. M. N., & Modica, G. (2021b). A workflow based on Sentinel-1 SAR data and open-source algorithms for unsupervised burned area detection in Mediterranean ecosystems. *GIScience & Remote Sensing*, 00(00), 1–26. <https://doi.org/10.1080/15481603.2021.1907896>
- De Luca, G., Silva, J. M. N., & Modica, G. (2022). Short-term temporal and spatial analysis for post-fire vegetation regrowth characterization and mapping in a Mediterranean ecosystem using optical and SAR image time-series. *Geocarto International*, 1–35. <https://doi.org/10.1080/10106049.2022.2097482>
- De Luca, G., Silva, J. M. N., Oom, D., & Modica, G. (2021). Combined Use of Sentinel-1 and Sentinel-2 for Burn Severity Mapping in a Mediterranean Region. In *Computational Science and Its Applications – ICCSA 2021. Lecture Notes in Computer Science* (pp. 139–154). [https://doi.org/10.1007/978-3-030-87007-2\\_11](https://doi.org/10.1007/978-3-030-87007-2_11)
- De Luis, M., Raventós, J., & González-Hidalgo, J. C. (2006). Post-fire vegetation succession in Mediterranean



- gorse shrublands. *Acta Oecologica*, 30(1), 54–61.  
<https://doi.org/https://doi.org/10.1016/j.actao.2006.01.005>
- De Santis, A., & Chuvieco, E. (2007). Burn severity estimation from remotely sensed data: Performance of simulation versus empirical models. *Remote Sensing of Environment*, 108(4), 422–435.  
<https://doi.org/10.1016/j.rse.2006.11.022>
- De Santis, A., & Chuvieco, E. (2009). GeoCBI: A modified version of the Composite Burn Index for the initial assessment of the short-term burn severity from remotely sensed data. *Remote Sensing of Environment*, 113(3), 554–562. <https://doi.org/10.1016/j.rse.2008.10.011>
- De Santis, A., Chuvieco, E., & Vaughan, P. J. (2009). Short-term assessment of burn severity using the inversion of PROSPECT and GeoSail models. *Remote Sensing of Environment*, 113(1), 126–136.  
<https://doi.org/10.1016/j.rse.2008.08.008>
- Delegido, J., Verrelst, J., Alonso, L., & Moreno, J. (2011). Evaluation of sentinel-2 red-edge bands for empirical estimation of green LAI and chlorophyll content. *Sensors*, 11(7), 7063–7081.  
<https://doi.org/10.3390/s110707063>
- Dempster, A. P., Laird, N. M., & Rubin, D. B. (1977). Maximum Likelihood from Incomplete Data Via the EM Algorithm . *Journal of the Royal Statistical Society: Series B (Methodological)*.  
<https://doi.org/10.1111/j.2517-6161.1977.tb01600.x>
- Dennison, P. E., Halligan, K. Q., & Roberts, D. A. (2004). A comparison of error metrics and constraints for multiple endmember spectral mixture analysis and spectral angle mapper. *Remote Sensing of Environment*, 93(3), 359–367. <https://doi.org/https://doi.org/10.1016/j.rse.2004.07.013>
- Dennison, P. E., & Roberts, D. A. (2003). Endmember selection for multiple endmember spectral mixture analysis using endmember average RMSE. *Remote Sensing of Environment*, 87(2), 123–135.  
[https://doi.org/https://doi.org/10.1016/S0034-4257\(03\)00135-4](https://doi.org/https://doi.org/10.1016/S0034-4257(03)00135-4)
- Deutscher, J., Perko, R., Gutjahr, K., Hirschmugl, M., & Schardt, M. (2013). Mapping tropical rainforest canopy disturbances in 3D by COSMO-SkyMed spotlight inSAR-stereo data to detect areas of forest degradation. *Remote Sensing*, 5(2), 648–663. <https://doi.org/10.3390/rs5020648>
- Dhanachandra, N., Manglem, K., & Chanu, Y. J. (2015). Image Segmentation Using K -means Clustering Algorithm and Subtractive Clustering Algorithm. *Procedia Computer Science*, 54, 764–771.  
<https://doi.org/https://doi.org/10.1016/j.procs.2015.06.090>
- Di Fazio, S., Modica, G., & Zoccali, P. (2011). *Evolution Trends of Land Use / Land Cover in a Mediterranean Forest*. June. <https://doi.org/10.1007/978-3-642-21928-3>
- Diakakis, M., Nikolopoulos, E. I., Mavroulis, S., Vassilakis, E., & Korakaki, E. (2017). Observational evidence on the effects of mega-fires on the frequency of hydrogeomorphic hazards. The case of the Peloponnese fires of 2007 in Greece. *Science of The Total Environment*, 592, 262–276.  
<https://doi.org/https://doi.org/10.1016/j.scitotenv.2017.03.070>
- Dijk, D. Van, Shoaie, S., Leeuwen, T. Van, & Veraverbeke, S. (2021). Spectral signature analysis of false positive burned area detection from agricultural harvests using Sentinel-2 data. *International Journal of Applied Earth Observations and Geoinformation*, 97(September 2020), 102296.  
<https://doi.org/10.1016/j.jag.2021.102296>
- Donchyts, G., Schellekens, J., Winsemius, H., Eisemann, E., & van de Giesen, N. (2016). A 30 m resolution

- surfacewater mask including estimation of positional and thematic differences using landsat 8, SRTM and OPenStreetMap: A case study in the Murray-Darling basin, Australia. *Remote Sensing*, 8(5).  
<https://doi.org/10.3390/rs8050386>
- Donezar, U., De Blas, T., Larrañaga, A., Ros, F., Albizua, L., Steel, A., & Broglia, M. (2019). Applicability of the multitemporal coherence approach to sentinel-1 for the detection and delineation of burnt areas in the context of the copernicus emergency management service. *Remote Sensing*, 11(22).  
<https://doi.org/10.3390/rs11222607>
- Drake, N. A., Mackin, S., & Settle, J. J. (1999). Mapping Vegetation, Soils, and Geology in Semiarid Shrublands Using Spectral Matching and Mixture Modeling of SWIR AVIRIS Imagery. *Remote Sensing of Environment*, 68(1), 12–25. [https://doi.org/10.1016/S0034-4257\(98\)00097-2](https://doi.org/10.1016/S0034-4257(98)00097-2)
- Drusch, M., Del Bello, U., Carlier, S., Colin, O., Fernandez, V., Gascon, F., Hoersch, B., Isola, C., Laberinti, P., Martimort, P., Meygret, A., Spoto, F., Sy, O., Marchese, F., & Bargellini, P. (2012). Sentinel-2: ESA's Optical High-Resolution Mission for GMES Operational Services. *Remote Sensing of Environment*, 120, 25–36. <https://doi.org/10.1016/j.rse.2011.11.026>
- Eitel, J. U. H., Vierling, L. A., Litvak, M. E., Long, D. S., Schulthess, U., Ager, A. A., Krofcheck, D. J., & Stoscheck, L. (2011). Broadband, red-edge information from satellites improves early stress detection in a New Mexico conifer woodland. *Remote Sensing of Environment*, 115(12), 3640–3646.  
<https://doi.org/10.1016/j.rse.2011.09.002>
- Epting, J., Verbyla, D., & Sorbel, B. (2005). Evaluation of remotely sensed indices for assessing burn severity in interior Alaska using Landsat TM and ETM+. *Remote Sensing of Environment*.  
<https://doi.org/10.1016/j.rse.2005.03.002>
- ESA. (2021). *ESA Sentinel Homepage*.
- ESA. (2022). *ESA Sentinel-2 Homepage*. <https://sentinels.copernicus.eu/web/sentinel/missions/sentinel-2>
- Eva, H., & Lambin, E. F. (1998). Burnt area mapping in Central Africa using ATSR data. *International Journal of Remote Sensing*, 19(18), 3473–3497. <https://doi.org/10.1080/014311698213768>
- Evangelides, C., & Nobajas, A. (2020). Red-Edge Normalised Difference Vegetation Index (NDVI705) from Sentinel-2 imagery to assess post-fire regeneration. *Remote Sensing Applications: Society and Environment*, 17, 100283. <https://doi.org/10.1016/j.rsase.2019.100283>
- FAO. (2020). *Global Forest Resources Assessment 2020. Main Report*. (FAO (ed.)). FAO.  
<https://doi.org/10.4060/ca9825en>
- Farasin, A., Colomba, L., & Garza, P. (2020). Double-Step U-Net: A Deep Learning-Based Approach for the Estimation of Wildfire Damage Severity through Sentinel-2 Satellite Data. In *Applied Sciences* (Vol. 10, Issue 12). <https://doi.org/10.3390/app10124332>
- Farr, T. G., Rosen, P. A., Caro, E., Crippen, R., Duren, R., Hensley, S., Kobrick, M., Paller, M., Rodriguez, E., Roth, L., Seal, D., Shaffer, S., Shimada, J., Umland, J., Werner, M., Oskin, M., Burbank, D., & Alsdorf, D. (2007). The Shuttle Radar Topography Mission. *Reviews of Geophysics*, 45(2), 1–33.  
<https://doi.org/10.1029/2005RG000183>
- Fernández-García, V., Marcos, E., Fernández-Guisuraga, J. M., Fernández-Manso, A., Quintano, C., Suárez-Seoane, S., & Calvo, L. (2021). Multiple endmember spectral mixture analysis (Mesma) applied to the study of habitat diversity in the fine-grained landscapes of the cantabrian mountains. *Remote Sensing*,

- 13(5), 1–19. <https://doi.org/10.3390/rs13050979>
- Fernández-García, V., Santamarta, M., Fernández-Manso, A., Quintano, C., Marcos, E., & Calvo, L. (2018). Burn severity metrics in fire-prone pine ecosystems along a climatic gradient using Landsat imagery. *Remote Sensing of Environment*, 206(February 2017), 205–217. <https://doi.org/10.1016/j.rse.2017.12.029>
- Fernández-Manso, A., Fernández-Manso, O., & Quintano, C. (2016). SENTINEL-2A red-edge spectral indices suitability for discriminating burn severity. *International Journal of Applied Earth Observation and Geoinformation*. <https://doi.org/10.1016/j.jag.2016.03.005>
- Fernandez-Manso, A., Quintano, C., & Roberts, D. A. (2016). Burn severity influence on post-fire vegetation cover resilience from Landsat MESMA fraction images time series in Mediterranean forest ecosystems. *Remote Sensing of Environment*, 184, 112–123. <https://doi.org/https://doi.org/10.1016/j.rse.2016.06.015>
- Fernández-Manso, A., Quintano, C., Suarez-Seoane, S., Marcos, E., & Calvo, L. (2021). *Remote Sensing Techniques for Monitoring Fire Damage and Recovery of Mediterranean Pine Forests: Pinus pinaster and Pinus halepensis as Case Studies BT - Pines and Their Mixed Forest Ecosystems in the Mediterranean Basin* (G. Ne'eman & Y. Osem (eds.); pp. 585–599). Springer International Publishing. [https://doi.org/10.1007/978-3-030-63625-8\\_27](https://doi.org/10.1007/978-3-030-63625-8_27)
- Fernández-Manso, Ó., Quintano, C., & Fernández-Manso, A. (2009). Combining spectral mixture analysis and object-based classification for fire severity mapping. *Investigación Agraria: Sistemas y Recursos Forestales*, 18(3), 296–313.
- Fernández, A., Illera, P., & Casanova, J. L. (1997). Automatic mapping of surfaces affected by forest fires in Spain using AVHRR NDVI composite image data. *Remote Sensing of Environment*, 60(2), 153–162. [https://doi.org/https://doi.org/10.1016/S0034-4257\(96\)00178-2](https://doi.org/https://doi.org/10.1016/S0034-4257(96)00178-2)
- Ferretti, A., Monti-Guarnieri, A., Prati, C., & Rocca, F. (2007). *InSAR Principles: Guidelines for SAR Interferometry Processing and Interpretation* (K. Fletcher (ed.)). ESA Publications.
- Filippini, F. (2018). BAIS2: Burned Area Index for Sentinel-2. *Proceedings*, 5177. <https://doi.org/10.3390/ecrs-2-05177>
- Filippini, F. (2019). Exploitation of sentinel-2 time series to map burned areas at the national level: A case study on the 2017 Italy wildfires. *Remote Sensing*, 11(6). <https://doi.org/10.3390/rs11060622>
- Fornacca, D., Ren, G., & Xiao, W. (2018). Evaluating the best spectral indices for the detection of burn scars at several post-fire dates in a Mountainous Region of Northwest Yunnan, China. *Remote Sensing*, 10(8). <https://doi.org/10.3390/rs10081196>
- Franke, J., Barradas, A. C. S., Borges, M. A., Menezes Costa, M., Dias, P. A., Hoffmann, A. A., Orozco Filho, J. C., Melchiori, A. E., & Siegert, F. (2018). Fuel load mapping in the Brazilian Cerrado in support of integrated fire management. *Remote Sensing of Environment*, 217, 221–232. <https://doi.org/https://doi.org/10.1016/j.rse.2018.08.018>
- Fraser, R. H., Li, Z., & Cihlar, J. (2000). Hotspot and NDVI Differencing Synergy (HANDS): A New Technique for Burned Area Mapping over Boreal Forest. *Remote Sensing of Environment*, 74(3), 362–376. [https://doi.org/https://doi.org/10.1016/S0034-4257\(00\)00078-X](https://doi.org/https://doi.org/10.1016/S0034-4257(00)00078-X)
- Frazier, R. J., Coops, N. C., & Wulder, M. A. (2015). Boreal Shield forest disturbance and recovery trends using Landsat time series. *Remote Sensing of Environment*, 170, 317–327. <https://doi.org/10.1016/j.rse.2015.09.015>

- Frison, P. L., Fruneau, B., Kmiha, S., Soudani, K., Dufrêne, E., Le Toan, T., Koleček, T., Villard, L., Mougin, E., & Rudant, J. P. (2018). Potential of Sentinel-1 data for monitoring temperate mixed forest phenology. *Remote Sensing*, 10(12). <https://doi.org/10.3390/rs10122049>
- Frolking, S., Palace, M. W., Clark, D. B., Chambers, J. Q., Shugart, H. H., & Hurtt, G. C. (2009). Forest disturbance and recovery: A general review in the context of spaceborne remote sensing of impacts on aboveground biomass and canopy structure. *Journal of Geophysical Research: Biogeosciences*, 114(3). <https://doi.org/10.1029/2008JG000911>
- Fukunaga, K., & Hostetler, L. D. (1975). The Estimation of the Gradient of a Density Function, with Applications in Pattern Recognition. *IEEE Transactions on Information Theory*. <https://doi.org/10.1109/TIT.1975.1055330>
- Gallagher, M. R., Skowronski, N. S., Lathrop, R. G., Green, E. J., Gallagher, M. R., Skowronski, N. S., & Lathrop, R. G. (2020). An Improved Approach for Selecting and Validating Burn Severity Indices in Forested Landscapes An Improved Approach for Selecting and Validating Burn Severity Indices in feux dans des milieux forestiers. *Canadian Journal of Remote Sensing*, 46(1), 100–111. <https://doi.org/10.1080/07038992.2020.1735931>
- Gao, B. (1996). NDWI—A normalized difference water index for remote sensing of vegetation liquid water from space. *Remote Sensing of Environment*, 58(3), 257–266. [https://doi.org/https://doi.org/10.1016/S0034-4257\(96\)00067-3](https://doi.org/https://doi.org/10.1016/S0034-4257(96)00067-3)
- García-Llamas, P., Suárez-Seoane, S., Fernández-Guisuraga, J. M., Fernández-García, V., Fernández-Manso, A., Quintano, C., Taboada, A., Marcos, E., & Calvo, L. (2019). Evaluation and comparison of Landsat 8, Sentinel-2 and Deimos-1 remote sensing indices for assessing burn severity in Mediterranean fire-prone ecosystems. *International Journal of Applied Earth Observation and Geoinformation*, 80, 137–144. <https://doi.org/https://doi.org/10.1016/j.jag.2019.04.006>
- Garcia, M., Saatchi, S., Casas, A., Koltunov, A., Ustin, S., Ramirez, C., Garcia-Gutierrez, J., & Balzter, H. (2017). Quantifying biomass consumption and carbon release from the California Rim fire by integrating airborne LiDAR and Landsat OLI data. *Journal of Geophysical Research: Biogeosciences*, 122(2), 340–353. <https://doi.org/https://doi.org/10.1002/2015JG003315>
- Georgopoulos, N., Stavrakoudis, D., & Gitas, I. Z. (2019). Object-Based Burned Area Mapping Using Sentinel-2 Imagery and Supervised Learning Guided by Empirical Rules. *IGARSS 2019 - 2019 IEEE International Geoscience and Remote Sensing Symposium*, 9980–9983. <https://doi.org/10.1109/IGARSS.2019.8900134>
- Ghosh, S. M., Behera, M. D., & Paramanik, S. (2020). Canopy height estimation using sentinel series images through machine learning models in a Mangrove Forest. *Remote Sensing*, 12(9). <https://doi.org/10.3390/RS12091519>
- Giannetti, F., Pecchi, M., Travaglini, D., Francini, S., Amico, G. D., Vangi, E., Coccozza, C., & Chirici, G. (2021). Estimating VAIA Windstorm Damaged Forest Area in Italy Using Time Series Sentinel-2 Imagery and Continuous Change Detection Algorithms. 1–16.
- Giglio, L., Boschetti, L., Roy, D. P., Humber, M. L., & Justice, C. O. (2018). The Collection 6 MODIS burned area mapping algorithm and product. *Remote Sensing of Environment*, 217(July), 72–85. <https://doi.org/10.1016/j.rse.2018.08.005>
- Gimeno, M., San-Miguel-Ayanz, J., & Schmuck, G. (2004). Identification of burnt areas in Mediterranean forest

- environments from ERS-2 SAR time series. *International Journal of Remote Sensing*, 25(22), 4873–4888.  
<https://doi.org/10.1080/01431160412331269715>
- Gimeno, Meritxell, & San-Miguel-Ayanz, J. (2004). Evaluation of RADARSAT-1 data for identification of burnt areas in Southern Europe. *Remote Sensing of Environment*, 92(3), 370–375.  
<https://doi.org/10.1016/j.rse.2004.03.018>
- Gitas, I., Mitri, G., Veraverbeke, S., & Polychronaki, A. (2012a). Advances in Remote Sensing of Post-Fire Vegetation Recovery Monitoring - A Review. In L. Fatoyinbo (Ed.), *Remote Sensing of Biomass - Principles and Applications* (pp. 143–176). InTech. <https://doi.org/10.5772/20571>
- Gitas, I., Mitri, G., Veraverbeke, S., & Polychronaki, A. (2012b). Advances in Remote Sensing of Post-Fire Vegetation Recovery Monitoring - A Review. *Remote Sensing of Biomass - Principles and Applications, March*. <https://doi.org/10.5772/20571>
- Gitas, I. Z., Mitri, G. H., & Ventura, G. (2004). Object-based image classification for burned area mapping of Creus Cape, Spain, using NOAA-AVHRR imagery. *Remote Sensing of Environment*, 92(3), 409–413.  
<https://doi.org/https://doi.org/10.1016/j.rse.2004.06.006>
- Goetz, S. J., Bunn, A. G., Fiske, G. J., & Houghton, R. A. (2005). *Satellite-observed photosynthetic trends across boreal North America associated with climate and fire disturbance SCIENCES*.
- Goodwin, N. R., & Collett, L. J. (2014). Development of an automated method for mapping fire history captured in Landsat TM and ETM+ time series across Queensland, Australia. *Remote Sensing of Environment*, 148, 206–221. <https://doi.org/https://doi.org/10.1016/j.rse.2014.03.021>
- Google Earth. (2022). *Google Earth*. <https://earth.google.com/web/>
- Goutte, C., & Gaussier, E. (2005). A Probabilistic Interpretation of Precision, Recall and F-Score, with Implication for Evaluation. *Lecture Notes in Computer Science*, 3408, 345–359.  
[https://doi.org/10.1007/978-3-540-31865-1\\_25](https://doi.org/10.1007/978-3-540-31865-1_25)
- Gouveia, C., Dacamara, C. C., Trigo, R. M., Lisboa, U. De, & Tecnologia, S. De. (2010). Post-fire vegetation recovery in Portugal based on spot / vegetation data. *Natural Hazards and Earth System Sciences*, 10(4), 673–684. <https://doi.org/https://doi.org/10.5194/nhess-10-673-2010>, 2010.
- Grabska, E., Hawryło, P., & Socha, J. (2020). Continuous Detection of Small-Scale Changes in Scots Pine Dominated Stands Using Dense Sentinel-2 Time Series. *Remote Sensing*, 12(8), 1298.  
<https://doi.org/10.3390/RS12081298>
- Grabska, E., Hostert, P., Pflugmacher, D., & Ostapowicz, K. (2019). Forest stand species mapping using the sentinel-2 time series. *Remote Sensing*, 11(10). <https://doi.org/10.3390/rs11101197>
- Hachani, A., Ouessar, M., Paloscia, S., Santi, E., & Pettinato, S. (2019). Soil moisture retrieval from Sentinel-1 acquisitions in an arid environment in Tunisia: application of Artificial Neural Networks techniques. *International Journal of Remote Sensing*, 40(24), 9159–9180.  
<https://doi.org/10.1080/01431161.2019.1629503>
- Hamdi, Z. M., Brandmeier, M., & Straub, C. (2019). Forest damage assessment using deep learning on high resolution remote sensing data. *Remote Sensing*, 11(17), 1–14. <https://doi.org/10.3390/rs11171976>
- Han, A., Qing, S., Bao, Y., Na, L., Bao, Y., Liu, X., Zhang, J., & Wang, C. (2021). Short-term effects of fire severity on vegetation based on sentinel-2 satellite data. *Sustainability (Switzerland)*, 13(1), 1–22.  
<https://doi.org/10.3390/su13010432>

- Hardy, C. C. (2005). Wildland fire hazard and risk: Problems, definitions, and context. *Forest Ecology and Management*, 211(1–2), 73–82. <https://doi.org/10.1016/j.foreco.2005.01.029>
- Häusler, M., Nunes, J. P., Soares, P., Sánchez, J. M., Silva, J. M. N., Warneke, T., Keizer, J. J., & Pereira, J. M. C. (2018). Assessment of the indirect impact of wildfire (severity) on actual evapotranspiration in eucalyptus forest based on the surface energy balance estimated from remote-sensing techniques. *International Journal of Remote Sensing*, 39(20), 6499–6524. <https://doi.org/https://doi.org/10.1080/01431161.2018.1460508>
- Hawbaker, T. J., Vanderhoof, M. K., Beal, Y.-J., Takacs, J. D., Schmidt, G. L., Falgout, J. T., Williams, B., Fairaux, N. M., Caldwell, M. K., Picotte, J. J., Howard, S. M., Stitt, S., & Dwyer, J. L. (2017). Mapping burned areas using dense time-series of Landsat data. *Remote Sensing of Environment*, 198, 504–522. <https://doi.org/https://doi.org/10.1016/j.rse.2017.06.027>
- Heylen, R., & Scheunders, P. (2013). Multidimensional Pixel Purity Index for Convex Hull Estimation and Endmember Extraction. *IEEE Transactions on Geoscience and Remote Sensing*, 51(7), 4059–4069. <https://doi.org/10.1109/TGRS.2012.2226734>
- Hill, J., Stellmes, M., Udelhoven, T., Röder, A., & Sommer, S. (2008). Mediterranean desertification and land degradation. Mapping related land use change syndromes based on satellite observations. *Global and Planetary Change*, 64(3–4), 146–157. <https://doi.org/10.1016/j.gloplacha.2008.10.005>
- Holben, B. N. (1986). Characteristics of maximum-value composite images from temporal AVHRR data. *International Journal of Remote Sensing*, 7(11), 1417–1434. <https://doi.org/10.1080/01431168608948945>
- Hosseini, M., & McNairn, H. (2017). Using multi-polarization C- and L-band synthetic aperture radar to estimate biomass and soil moisture of wheat fields. *International Journal of Applied Earth Observation and Geoinformation*, 58, 50–64. <https://doi.org/10.1016/j.jag.2017.01.006>
- Hu, X., Ban, Y., & Nascetti, A. (2021). Uni-Temporal Multispectral Imagery for Burned Area Mapping with Deep Learning. In *Remote Sensing* (Vol. 13, Issue 8). <https://doi.org/10.3390/rs13081509>
- Huang, Z., Cao, C., Chen, W., Xu, M., Dang, Y., Singh, R. P., Bashir, B., Xie, B., & Lin, X. (2020). Remote Sensing Monitoring of Vegetation Dynamic Changes after Fire in the Greater Hinggan Mountain Area: The Algorithm and Application for Eliminating Phenological Impacts. *Remote Sensing*, 12(1), 156. <https://doi.org/10.3390/rs12010156>
- Hudak, A. T., Morgan, P., Bobbitt, M. J., Smith, A. M. S., Lewis, S. A., Lentile, L. B., Robichaud, P. R., Clark, J. T., & McKinley, R. A. (2007). The Relationship of Multispectral Satellite Imagery to Immediate Fire Effects. *Fire Ecology*, 3(1), 64–90. <https://doi.org/10.4996/fireecology.0301064>
- ICNF. (2017). *10º Relatório Provisório de Incêndios Florestais - 2017*.
- Ienco, D., Interdonato, R., Gaetano, R., & Ho Tong Minh, D. (2019). Combining Sentinel-1 and Sentinel-2 Satellite Image Time Series for land cover mapping via a multi-source deep learning architecture. *ISPRS Journal of Photogrammetry and Remote Sensing*, 158(September), 11–22. <https://doi.org/10.1016/j.isprsjprs.2019.09.016>
- Immitzer, M., Vuolo, F., & Atzberger, C. (2016). First experience with Sentinel-2 data for crop and tree species classifications in central Europe. *Remote Sensing*, 8(3). <https://doi.org/10.3390/rs8030166>
- Imperatore, P., Azar, R., Calo, F., Stroppiana, D., Brivio, P. A., Lanari, R., & Pepe, A. (2017). Effect of the Vegetation Fire on Backscattering: An Investigation Based on Sentinel-1 Observations. *IEEE Journal of*



- Selected Topics in Applied Earth Observations and Remote Sensing*, 10(10), 4478–4492.  
<https://doi.org/10.1109/JSTARS.2017.2717039>
- Inglada, J., Vincent, A., Arias, M., Tardy, B., Morin, D., & Rodes, I. (2017). Operational High Resolution Land Cover Map Production at the Country Scale Using Satellite Image Time Series. *Remote Sensing*, 9(1), 95.  
<https://doi.org/10.3390/rs9010095>
- Inoue, Y., Qi, J., Olioso, A., Kiyono, Y., Horie, T., Asai, H., Saito, K., Ochiai, Y., Douangsavanh, L., Qi, J., Olioso, A., Kiyono, Y., Horie, T., Asai, H., Saito, K., & Ochiai, Y. (2019). *Reflectance characteristics of major land surfaces in slash - and - burn ecosystems in Laos*. 1161.  
<https://doi.org/10.1080/01431160701442039>
- José Vidal-Macua, J., Ninyerola, M., Zabala, A., Domingo-Marimon, C., & Pons, X. (2017). Factors affecting forest dynamics in the Iberian Peninsula from 1987 to 2012. The role of topography and drought. *Forest Ecology and Management*, 406, 290–306. <https://doi.org/https://doi.org/10.1016/j.foreco.2017.10.011>
- Kasischke, E. S., French, N. H. F., Harrell, P., Christensen, N. L., Ustin, S. L., & Barry, D. (1993). Monitoring of wildfires in Boreal Forests using large area AVHRR NDVI composite image data. *Remote Sensing of Environment*, 45(1), 61–71. [https://doi.org/https://doi.org/10.1016/0034-4257\(93\)90082-9](https://doi.org/https://doi.org/10.1016/0034-4257(93)90082-9)
- Kasischke, E. S., Tanase, M. A., Bourgeau-Chavez, L. L., & Borr, M. (2011). Soil moisture limitations on monitoring boreal forest regrowth using spaceborne L-band SAR data. *Remote Sensing of Environment*, 115(1), 227–232. <https://doi.org/10.1016/j.rse.2010.08.022>
- Kattenborn, T., Lopatin, J., Förster, M., Braun, A. C., & Fassnacht, F. E. (2019). UAV data as alternative to field sampling to map woody invasive species based on combined Sentinel-1 and Sentinel-2 data. *Remote Sensing of Environment*, 227(January), 61–73. <https://doi.org/10.1016/j.rse.2019.03.025>
- Kaufman, Y. J., & Remer, L. A. (1994). Detection of Forests Using Mid-IR Reflectance: An Application for Aerosol Studies. *IEEE Transactions on Geoscience and Remote Sensing*, 32(3), 672–683.  
<https://doi.org/10.1109/36.297984>
- Keeley, J. E. (2009). Fire intensity, fire severity and burn severity: A brief review and suggested usage. *International Journal of Wildland Fire*, 18(1), 116–126. <https://doi.org/10.1071/WF07049>
- Kennedy, R. E., Yang, Z., Cohen, W. B., Pfaff, E., Braaten, J., & Nelson, P. (2012). Spatial and temporal patterns of forest disturbance and regrowth within the area of the Northwest Forest Plan. *Remote Sensing of Environment*, 122, 117–133. <https://doi.org/10.1016/j.rse.2011.09.024>
- Keras Homepage. (2022). *Keras Homepage*. <https://keras.io/>
- Key, C. H. (2006). Ecological and Sampling Constraints on Defining Landscape Fire Severity. *Fire Ecology*, 2(2), 34–59. <https://doi.org/10.4996/fireecology.0202034>
- Key, C. H., & Benson, N. C. (2006). Landscape Assessment ( LA ) Sampling and Analysis Methods. In *FIREMON: Fire effects monitoring and inventory system*.
- Kim, Y., Jackson, T., Bindlish, R., Hong, S., Jung, G., & Lee, K. (2014). Retrieval of Wheat Growth Parameters With Radar Vegetation Indices. *IEEE Geoscience and Remote Sensing Letters*, 11(4), 808–812.  
<https://doi.org/10.1109/LGRS.2013.2279255>
- Kim, Y., Jackson, T., Bindlish, R., Lee, H., & Hong, S. (2012). Radar Vegetation Index for Estimating the Vegetation Water Content of Rice and Soybean. *IEEE Geoscience and Remote Sensing Letters*, 9(4), 564–568. <https://doi.org/10.1109/LGRS.2011.2174772>

- Kim, Yunjin, & Van Zyl, J. J. (2009). A time-series approach to estimate soil moisture using polarimetric radar data. *IEEE Transactions on Geoscience and Remote Sensing*. <https://doi.org/10.1109/TGRS.2009.2014944>
- Knipling, E. B. (1970). Physical and physiological basis for the reflectance of visible and near-infrared radiation from vegetation. *Remote Sensing of Environment*, 1(3), 155–159.  
[https://doi.org/https://doi.org/10.1016/S0034-4257\(70\)80021-9](https://doi.org/https://doi.org/10.1016/S0034-4257(70)80021-9)
- Knopp, L., Wieland, M., Rättich, M., & Martinis, S. (2020). A deep learning approach for burned area segmentation with Sentinel-2 data. *Remote Sensing*, 12(15). <https://doi.org/10.3390/RS12152422>
- Kokaly, R. F., Rockwell, B. W., Haire, S. L., & King, T. V. V. (2007). Characterization of post-fire surface cover, soils, and burn severity at the Cerro Grande Fire, New Mexico, using hyperspectral and multispectral remote sensing. *Remote Sensing of Environment*, 106(3), 305–325.  
<https://doi.org/https://doi.org/10.1016/j.rse.2006.08.006>
- Kurum, M. (2015). *C-Band SAR Backscatter Evaluation of 2008 Gallipoli Forest Fire*. 12(5), 1091–1095.
- Lacouture, D. L., Broadbent, E. N., & Crandall, R. M. (2020). Detecting Vegetation Recovery after Fire in A Fire-Frequented Habitat Using Normalized Difference Vegetation Index (NDVI). *Forests*, 11(7), 749.  
<https://doi.org/10.3390/f11070749>
- Lanorte, A., Danese, M., Lasaponara, R., & Murgante, B. (2013). Multiscale mapping of burn area and severity using multisensor satellite data and spatial autocorrelation analysis. *International Journal of Applied Earth Observation and Geoinformation*, 20(1), 42–51. <https://doi.org/10.1016/j.jag.2011.09.005>
- Lapini, Pettinato, Santi, Paloscia, Fontanelli, & Garzelli. (2020). Comparison of Machine Learning Methods Applied to SAR Images for Forest Classification in Mediterranean Areas. *Remote Sensing*, 12(3), 369.  
<https://doi.org/10.3390/rs12030369>
- Lary, D. J., Alavi, A. H., Gandomi, A. H., & Walker, A. L. (2016). Machine learning in geosciences and remote sensing. *Geoscience Frontiers*, 7(1), 3–10. <https://doi.org/10.1016/j.gsf.2015.07.003>
- Lasaponara, R., & Tucci, B. (2019). Identification of Burned Areas and Severity Using SAR Sentinel-1. *IEEE Geoscience and Remote Sensing Letters*, 16(6), 917–921. <https://doi.org/10.1109/LGRS.2018.2888641>
- Lasko, K. (2019). Incorporating Sentinel-1 SAR imagery with the MODIS MCD64A1 burned area product to improve burn date estimates and reduce burn date uncertainty in wildland fire mapping Incorporating Sentinel-1 SAR imagery with the MODIS MCD64A1 burned area product to imp. *Geocarto International*, 0(0), 1–21. <https://doi.org/10.1080/10106049.2019.1608592>
- Le Toan, T., Quegan, S., Davidson, M. W. J., Balzter, H., Paillou, P., Papathanassiou, K., Plummer, S., Rocca, F., Saatchi, S., Shugart, H., & Ulander, L. (2011). The BIOMASS mission: Mapping global forest biomass to better understand the terrestrial carbon cycle. *Remote Sensing of Environment*, 115(11), 2850–2860.  
<https://doi.org/https://doi.org/10.1016/j.rse.2011.03.020>
- Lee, J.-S., & Pottier, E. (2009). Filtering of Single Polarization SAR Data. In CRC Press. (Ed.), *Polarimetric Radar Imaging. From Basics to Applications* (1th ed.). CRC Press.  
<https://doi.org/https://doi.org/10.1201/9781420054989>
- Lehmann, E. A., Caccetta, P., Lowell, K., Mitchell, A., Zhou, Z. S., Held, A., Milne, T., & Tapley, I. (2015). SAR and optical remote sensing: Assessment of complementarity and interoperability in the context of a large-scale operational forest monitoring system. *Remote Sensing of Environment*, 156, 335–348.  
<https://doi.org/10.1016/j.rse.2014.09.034>

- Lentile, L.B., Holden, Z. A., Smith, A. M. S., Falkowski, M. J., Hudak, A. T., Morgan, P., Lewis, S. A., Gessler, P. E., & Benson, N. C. (2006). Remote sensing techniques to assess active fire characteristics and post-fire effects. *International Journal of Wildland Fire*, 15(3), 319–345.  
<https://doi.org/https://doi.org/10.1071/WF05097>
- Lentile, Leigh B, Smith, A. M. S., Hudak, A. T., Morgan, P., Bobbitt, M. J., Lewis, S. A., & Robichaud, P. R. (2009). Remote sensing for prediction of 1-year post-fire ecosystem condition. *International Journal of Wildland Fire*, 18(5), 594–608. <https://doi.org/https://doi.org/10.1071/WF07091>
- Li, M., Zang, S., Zhang, B., Li, S., & Wu, C. (2014). A Review of Remote Sensing Image Classification Techniques: the Role of Spatio-contextual Information. *European Journal of Remote Sensing*, 47(1), 389–411. <https://doi.org/10.5721/EuJRS20144723>
- Li, W., Niu, Z., Shang, R., Qin, Y., Wang, L., & Chen, H. (2020). High-resolution mapping of forest canopy height using machine learning by coupling ICESat-2 LiDAR with Sentinel-1, Sentinel-2 and Landsat-8 data. *International Journal of Applied Earth Observation and Geoinformation*, 92, 102163.  
<https://doi.org/https://doi.org/10.1016/j.jag.2020.102163>
- Lin, C.-Y., Lo, H.-M., Chou, W.-C., & Lin, W.-T. (2004). Vegetation recovery assessment at the Jou-Jou Mountain landslide area caused by the 921 Earthquake in Central Taiwan. *Ecological Modelling*, 176(1), 75–81. <https://doi.org/https://doi.org/10.1016/j.ecolmodel.2003.12.037>
- Llorens, R., Sobrino, J. A., Fernández, C., Fernández-Alonso, J. M., & Vega, J. A. (2021). A methodology to estimate forest fires burned areas and burn severity degrees using Sentinel-2 data. Application to the October 2017 fires in the Iberian Peninsula. *International Journal of Applied Earth Observation and Geoinformation*, 95, 102243. <https://doi.org/https://doi.org/10.1016/j.jag.2020.102243>
- Lobo, A., Chic, O., & Casterad, A. (1996). Classification of Mediterranean crops with multisensor data: per-pixel versus per-object statistics and image segmentation. *International Journal of Remote Sensing*, 17(12), 2385–2400. <https://doi.org/10.1080/01431169608948779>
- MacQueen, J. (1967). Some methods for classification and analysis of multivariate observations. *Proceedings of the Fifth Berkeley Symposium on Mathematical Statistics and Probability*.
- Mallinis, G., Mitsopoulos, I., & Chrysafi, I. (2018). Evaluating and comparing sentinel 2A and landsat-8 operational land imager (OLI) spectral indices for estimating fire severity in a mediterranean pine ecosystem of Greece. *GIScience and Remote Sensing*. <https://doi.org/10.1080/15481603.2017.1354803>
- Mandal, D., Kumar, V., Ratha, D., Dey, S., Bhattacharya, A., Lopez-sanchez, J. M., McNairn, H., & Rao, Y. S. (2020). Remote Sensing of Environment Dual polarimetric radar vegetation index for crop growth monitoring using sentinel-1 SAR data. *Remote Sensing of Environment*, 247(January), 111954.  
<https://doi.org/10.1016/j.rse.2020.111954>
- Mari, N., Laneve, G., Cadau, E., & Porcasi, X. (2017). *Fire Damage Assessment in Sardinia : the use of ALOS / PALSAR data for post fire effects management* *Fire Damage Assessment in Sardinia : the use of ALOS / PALSAR data for post fire effects management*. 7254. <https://doi.org/10.5721/EuJRS20124521>
- Martinis, S., Caspard, M., Plank, S., Clandillon, S., & Haouet, S. (2017). Mapping burn scars, fire severity and soil erosion susceptibility in Southern France using multisensoral satellite data. *International Geoscience and Remote Sensing Symposium (IGARSS), 2017-July*, 1099–1102.  
<https://doi.org/10.1109/IGARSS.2017.8127148>

- Martins, F. S. R. V., dos Santos, J. R., Galvao, L. S., & Xaud, H. A. M. (2016). Sensitivity of ALOS / PALSAR imagery to forest degradation by fire in northern Amazon. *International Journal of Applied Earth Observations and Geoinformation*, 49, 163–174. <https://doi.org/10.1016/j.jag.2016.02.009>
- Martins, M. J., Cerdeira, J. O., Silva, P., Arsénio, P., Silva, Á., Bellu, A., & Costa, J. C. (2015). *Bioclimatological mapping tackling uncertainty propagation : application to mainland Portugal*. <https://doi.org/10.1002/joc.4357>
- Marzialetti, F., Giulio, S., Malavasi, M., Sperandii, M. G., Acosta, A. T. R., & Carranza, M. L. (2019). Capturing coastal dune natural vegetation types using a phenology-based mapping approach: The potential of Sentinel-2. *Remote Sensing*, 11(12). <https://doi.org/10.3390/rs11121506>
- Mayaux, P., Gond, V., & Bartholome, E. (2000). A near-real time forest-cover map of Madagascar derived from SPOT-4 VEGETATION data. *International Journal of Remote Sensing*, 21(16), 3139–3144. <https://doi.org/10.1080/01431160050145018>
- Meddens, A. J. H., Kolden, C. A., & Lutz, J. A. (2016). Detecting unburned areas within wildfire perimeters using Landsat and ancillary data across the northwestern United States. *Remote Sensing of Environment*, 186, 275–285. <https://doi.org/https://doi.org/10.1016/j.rse.2016.08.023>
- Mendes, F. de S., Baron, D., Gerold, G., Liesenberg, V., & Erasmi, S. (2019). Optical and SAR remote sensing synergism for mapping vegetation types in the endangered Cerrado/Amazon ecotone of Nova Mutum-Mato Grosso. *Remote Sensing*, 11(10). <https://doi.org/10.3390/rs11101161>
- Meng, R., Dennison, P. E., Huang, C., Moritz, M. A., & D’Antonio, C. (2015). Effects of fire severity and post-fire climate on short-term vegetation recovery of mixed-conifer and red fir forests in the Sierra Nevada Mountains of California. *Remote Sensing of Environment*, 171, 311–325. <https://doi.org/https://doi.org/10.1016/j.rse.2015.10.024>
- Meng, R., Wu, J., Zhao, F., Cook, B. D., Hanavan, R. P., & Serbin, S. P. (2018). Measuring short-term post-fire forest recovery across a burn severity gradient in a mixed pine-oak forest using multi-sensor remote sensing techniques. *Remote Sensing of Environment*, 210(September 2017), 282–296. <https://doi.org/10.1016/j.rse.2018.03.019>
- Menges, C. H., Bartolo, R. E., Bell, D., Hill, G. J. E., Bartolo, R. E., Bell, D., & The, G. J. E. H. (2010). *The effect of savanna fires on SAR backscatter in northern Australia*. 1161. <https://doi.org/10.1080/01431160410001712945>
- Meyer, F. (2019). Spaceborne Synthetic Aperture Radar: Principles, Data Access, and Basic Processing Techniques. In *The SAR Handbook. Comprehensive Methodologies for Forest Monitoring and Biomass Estimation* (pp. 21–43). <https://doi.org/10.25966/nr2c-s697>
- Michel, J., Youssefi, D., & Grizonnet, M. (2015). Stable Mean-Shift Algorithm and Its Application to the Segmentation of Arbitrarily Large Remote Sensing Images. *IEEE Transactions on Geoscience and Remote Sensing*, 53(2), 952–964. <https://doi.org/10.1109/TGRS.2014.2330857>
- Miettinen, J., & Liew, S. C. (2008). Comparison of multitemporal compositing methods for burnt area detection in Southeast Asian conditions. *International Journal of Remote Sensing*, 29(4), 1075–1092. <https://doi.org/10.1080/01431160701281031>
- Miettinen, Jukka, Hyer, E., Chia, A. S., Kwok, L. K., & Liew, S. C. (2013). Detection of vegetation fires and burnt areas by remote sensing in insular Southeast Asian conditions: current status of knowledge and

- future challenges. *International Journal of Remote Sensing*, 34(12), 4344–4366.  
<https://doi.org/10.1080/01431161.2013.777489>
- Miller, J. D., Knapp, E. E., Key, C. H., Skinner, C. N., Isbell, C. J., Creasy, R. M., & Sherlock, J. W. (2009). Calibration and validation of the relative differenced Normalized Burn Ratio (RdNBR) to three measures of fire severity in the Sierra Nevada and Klamath Mountains, California, USA. *Remote Sensing of Environment*, 113(3), 645–656. <https://doi.org/10.1016/j.rse.2008.11.009>
- Miller, J. D., & Thode, A. E. (2007). Quantifying burn severity in a heterogeneous landscape with a relative version of the delta Normalized Burn Ratio (dNBR). *Remote Sensing of Environment*, 109(1), 66–80. <https://doi.org/10.1016/j.rse.2006.12.006>
- Minchella, A., Del Frate, F., Capogna, F., Anselmi, S., & Manes, F. (2009). Use of multitemporal SAR data for monitoring vegetation recovery of Mediterranean burned areas. *Remote Sensing of Environment*, 113(3), 588–597. <https://doi.org/10.1016/j.rse.2008.11.004>
- Mitchell, R. J., Simonson, W., Flegg, L. A., Santos, P., & Hall, J. (2009). A comparison of the resilience of four habitats to fire, and the implications of changes in community composition for conservation: A case study from the serra de monchique, portugal. *Plant Ecology and Diversity*, 2(1), 45–56. <https://doi.org/10.1080/17550870902752421>
- Mitri, G. H., & Gitas, I. Z. (2004). A semi-automated object-oriented model for burned area mapping in the Mediterranean region using Landsat-TM imagery. *International Journal of Wildland Fire*, 13(3), 367–376. <https://doi.org/10.1071/WF03079>
- Mitri, George H., & Gitas, I. Z. (2012). Mapping post-fire forest regeneration and vegetation recovery using a combination of very high spatial resolution and hyperspectral satellite imagery. *International Journal of Applied Earth Observation and Geoinformation*, 20(1), 60–66. <https://doi.org/10.1016/j.jag.2011.09.001>
- Modica, G., De Luca, G., Messina, G., & Praticò, S. (2021a). Comparison and assessment of different object-based classifications using machine learning algorithms and UAVs multispectral imagery in the framework of precision agriculture. *European Journal of Remote Sensing*, 54(1), 431–460. <https://doi.org/10.1080/22797254.2021.1951623>
- Modica, G., De Luca, G., Messina, G., & Praticò, S. (2021b). Comparison and assessment of different object-based classifications using machine learning algorithms and UAVs multispectral imagery in the framework of precision agriculture. *European Journal of Remote Sensing*, 54(1), 431–460. <https://doi.org/in press>
- Modica, Giuseppe, Merlino, A., Solano, F., & Mercurio, R. (2015). An index for the assessment of degraded mediterranean forest ecosystems. *Forest Systems*. <https://doi.org/10.5424/fs/2015243-07855>
- Modica, Giuseppe, Messina, G., De Luca, G., Fiozzo, V., & Praticò, S. (2020). Monitoring the vegetation vigor in heterogeneous citrus and olive orchards. A multiscale object-based approach to extract trees' crowns from UAV multispectral imagery. *Computers and Electronics in Agriculture*, 175(May), 105500. <https://doi.org/105500>
- Modica, Giuseppe, Solano, F., Merlino, A., Di Fazio, S., Barreca, F., Laudari, L., & Fichera, C. R. (2016). Using Landsat 8 imagery in detecting cork oak (*Quercus suber* L.) woodlands: a case study in Calabria (Italy). *Journal of Agricultural Engineering*, 47(4), 205–215. <https://doi.org/10.4081/jae.2016.571>
- Monaco, S., Pasini, A., Apiletti, D., Colomba, L., Garza, P., & Baralis, E. (2020). Improving Wildfire Severity Classification of Deep Learning U-Nets from Satellite Images. *2020 IEEE International Conference on*

- Big Data (Big Data)*, 5786–5788. <https://doi.org/10.1109/BigData50022.2020.9377867>
- Monroe, A. P., Aldridge, C. L., O'Donnell, M. S., Manier, D. J., Homer, C. G., & Anderson, P. J. (2020). Using remote sensing products to predict recovery of vegetation across space and time following energy development. *Ecological Indicators*, 110(November 2019), 105872. <https://doi.org/10.1016/j.ecolind.2019.105872>
- Montès, N., Ballini, C., Bonin, G., & Faures, J. (2004). A comparative study of aboveground biomass of three Mediterranean species in a post-fire succession. *Acta Oecologica*, 25(1), 1–6. <https://doi.org/https://doi.org/10.1016/j.actao.2003.10.002>
- Montorio, R., Pérez-Cabello, F., Borini Alves, D., & García-Martín, A. (2020). Unitemporal approach to fire severity mapping using multispectral synthetic databases and Random Forests. *Remote Sensing of Environment*, 249, 112025. <https://doi.org/https://doi.org/10.1016/j.rse.2020.112025>
- Moreira, F., Ascoli, D., Safford, H., Adams, M. A., Moreno, J. M., Pereira, J. M. C., Catry, F. X., Armesto, J., Bond, W., González, M. E., Curt, T., Koutsias, N., McCaw, L., Price, O., Pausas, J. G., Rigolot, E., Stephens, S., Tavsanoglu, C., Vallejo, V. R., ... Fernandes, P. M. (2020). Wildfire management in Mediterranean-type regions: paradigm change needed. *Environmental Research Letters*, 15(1), 11001. <https://doi.org/10.1088/1748-9326/ab541e>
- Moreno, J. M., Morales-Molino, C., Torres, I., & Arianoutsou, M. (2021). *Fire in Mediterranean Pine Forests: Past, Present and Future BT - Pines and Their Mixed Forest Ecosystems in the Mediterranean Basin* (G. Ne'eman & Y. Osem (eds.); pp. 421–456). Springer International Publishing. [https://doi.org/10.1007/978-3-030-63625-8\\_21](https://doi.org/10.1007/978-3-030-63625-8_21)
- Morin, D., Planells, M., Guyon, D., Villard, L., Mermoz, S., Bouvet, A., Thevenon, H., Dejoux, J. F., Le Toan, T., & Dedieu, G. (2019). Estimation and mapping of forest structure parameters from open access satellite images: Development of a generic method with a study case on coniferous plantation. *Remote Sensing*, 11(11). <https://doi.org/10.3390/rs11111275>
- Morresi, D., Marzano, R., Lingua, E., Motta, R., & Garbarino, M. (2022). Mapping burn severity in the western Italian Alps through phenologically coherent reflectance composites derived from Sentinel-2 imagery. *Remote Sensing of Environment*, 269, 112800. <https://doi.org/https://doi.org/10.1016/j.rse.2021.112800>
- Morresi, D., Vitali, A., Urbinati, C., & Garbarino, M. (2019). Forest spectral recovery and regeneration dynamics in stand-replacing wildfires of central Apennines derived from Landsat time series. *Remote Sensing*, 11(3). <https://doi.org/10.3390/rs11030308>
- Mpakairi, K. S., Ndaimani, H., & Kavhu, B. (2020). Exploring the utility of Sentinel-2 MSI derived spectral indices in mapping burned areas in different land-cover types. *Scientific African*, 10, e00565. <https://doi.org/10.1016/j.sciaf.2020.e00565>
- Nagpal, A., Jatain, A., & Gaur, D. (2013). Review based on data clustering algorithms. *2013 IEEE Conference on Information & Communication Technologies*, 298–303. <https://doi.org/10.1109/CICT.2013.6558109>
- Nascimento, J. M. P., & Dias, J. M. B. (2005). Vertex component analysis: A fast algorithm to unmix hyperspectral data. *IEEE Transactions on Geoscience and Remote Sensing*, 43(4), 898–910. <https://doi.org/10.1109/TGRS.2005.844293>
- Nasirzadehdizaji, R., Sanli, F. B., Abdikan, S., Cakir, Z., Sekertekin, A., & Ustuner, M. (2019). Sensitivity analysis of multi-temporal Sentinel-1 SAR parameters to crop height and canopy coverage. *Applied*

- Sciences (Switzerland)*. <https://doi.org/10.3390/app9040655>
- Navarro, G., Caballero, I., Silva, G., Parra, P.-C., Vázquez, Á., & Caldeira, R. (2017). Evaluation of forest fire on Madeira Island using Sentinel-2A MSI imagery. *International Journal of Applied Earth Observation and Geoinformation*, 58, 97–106. <https://doi.org/10.1016/j.jag.2017.02.003>
- Nicolau, A. P., Flores-Anderson, A., Griffin, R., Herndon, K., & Meyer, F. J. (2021). Assessing SAR C-band data to effectively distinguish modified land uses in a heavily disturbed Amazon forest. *International Journal of Applied Earth Observation and Geoinformation*, 94(March 2020), 102214. <https://doi.org/10.1016/j.jag.2020.102214>
- Numbisi, F. N., Van Coillie, F. M. B., & De Wulf, R. (2019). Delineation of cocoa agroforests using multiseason sentinel-1 SAR images: A low grey level range reduces uncertainties in GLCM texture-based mapping. *ISPRS International Journal of Geo-Information*, 8(4). <https://doi.org/10.3390/ijgi8040179>
- Ok, A. O., Senaras, C., & Yuksel, B. (2013). Automated Detection of Arbitrarily Shaped Buildings in Complex Environments From Monocular VHR Optical Satellite Imagery. *IEEE Transactions on Geoscience and Remote Sensing*, 51(3), 1701–1717. <https://doi.org/10.1109/TGRS.2012.2207123>
- Ostroukhov, A., Klimina, E., Kuptsova, V., & Naito, D. (2022). Estimating Long-Term Average Carbon Emissions from Fires in Non-Forest Ecosystems in the Temperate Belt. In *Remote Sensing* (Vol. 14, Issue 5). <https://doi.org/10.3390/rs14051197>
- Otón, G., Ramo, R., Lizundia-Loiola, J., & Chuvieco, E. (2019). Global detection of long-term (1982-2017) burned area with AVHRR-LTDR data. *Remote Sensing*, 11(18). <https://doi.org/10.3390/rs11182079>
- Paloscia, S., Macelloni, G., Pampaloni, P., & Sigismondi, S. (1999). The potential of c- and l-band sar in estimating vegetation biomass: the ers-1 and jers-1 experiments. *IEEE Transactions on Geoscience and Remote Sensing*. <https://doi.org/10.1109/36.774723>
- Parks, S. A., Dillon, G. K., & Miller, C. (2014). A new metric for quantifying burn severity: The relativized burn ratio. *Remote Sensing*, 6(3), 1827–1844. <https://doi.org/10.3390/rs6031827>
- Pedregosa, F., Varoquaux, G., Gramfort, A., Michel, V., Thirion, B., Grisel, O., Blondel, M., Prettenhofer, P., Weiss, R., Dubourg, V., Vanderplas, J., Passos, A., Cournapeau, D., Brucher, M., Perrot, M., & Duchesnay, É. (2011). Scikit-learn: Machine learning in Python. *Journal of Machine Learning Research*, 12, 2825–2830. <https://www.scopus.com/inward/record.uri?eid=2-s2.0-80555140075&partnerID=40&md5=63e53cee7a9711760872d4d103e5453a>
- Pepe, A., Stroppiana, D., Calo, F., Imperatore, P., Boschetti, L., Bignami, C., & Brivio, P. A. (2018a). *Exploitation of Copernicus Sentinels data for sensing fire-disturbed vegetated areas. Institute for the Electromagnetic Sensing of the Environment ( IREA ). 7593–7596.*
- Pepe, A., Stroppiana, D., Calo, F., Imperatore, P., Boschetti, L., Bignami, C., & Brivio, P. A. (2018b). *Exploitation of Copernicus Sentinels data for sensing fire-disturbed vegetated areas. Institute for the Electromagnetic Sensing of the Environment ( IREA ). 7593–7596.*
- Pereira-Pires, J. E., Aubard, V., Ribeiro, R. A., Fonseca, J. M., Silva, J. M. N., & Mora, A. (2020). Semi-Automatic Methodology for Fire Break Maintenance Operations Detection with Sentinel-2 Imagery and Artificial Neural Network. In *Remote Sensing* (Vol. 12, Issue 6). <https://doi.org/10.3390/rs12060909>
- Pereira, A. A., Libonati, R., Oom, D., Tavares, L. M. C., & Pereira, J. M. (2017). Avaliação de técnicas de compósitos multitemporais em imagens PROBA-V para o mapeamento de áreas queimadas. *Anais Do*



- Pereira, Allan Arantes, Pereira, J. M. C., Libonati, R., Oom, D., & Carvalho, L. M. T. (2016). Multitemporal image compositing evaluation algorithms for PROBA-V burned area analysis. *Proba-V Symposium, January*, 2015–2016.
- Pereira, J. M. C., Sousa, A. M. O., Sá, A. C. L., Martin, M. P., & Chuvieco, E. (1999). Regional scale burnt area mapping in Southern Europe using NOAA-AVHRR 1km data. In *Remote Sensing of Large Wildfires in the European Mediterranean basin*. Springer, Berlin, Heidelberg. [https://doi.org/10.1007/978-3-642-60164-4\\_8](https://doi.org/10.1007/978-3-642-60164-4_8)
- Pereira, José M. C., Sá, A. C. L., Sousa, A. M. O., Silva, J. M. N., Santos, T. N., & Carreiras, J. M. B. (1999). Spectral characterisation and discrimination of burnt areas. In *Remote Sensing of Large Wildfires*. [https://doi.org/10.1007/978-3-642-60164-4\\_7](https://doi.org/10.1007/978-3-642-60164-4_7)
- Pereira, José M.C. (1999). A comparative evaluation of NOAA/AVHRR vegetation indexes for burned surface detection and mapping. *IEEE Transactions on Geoscience and Remote Sensing*. <https://doi.org/10.1109/36.739156>
- Pereira, P., Francos, M., Brevik, E. C., Ubeda, X., & Bogunovic, I. (2018). Post-fire soil management. *Current Opinion in Environmental Science & Health*, 5, 26–32. <https://doi.org/10.1016/j.coesh.2018.04.002>
- Periasamy, S. (2018). Significance of dual polarimetric synthetic aperture radar in biomass retrieval: An attempt on Sentinel-1. *Remote Sensing of Environment*. <https://doi.org/10.1016/j.rse.2018.09.003>
- Perko, R., Raggam, H., Deutscher, J., Gutjahr, K., & Schardt, M. (2011). Forest assessment using high resolution SAR data in X-Band. *Remote Sensing*, 3(4), 792–815. <https://doi.org/10.3390/rs3040792>
- Phiri, D., & Morgenroth, J. (2017). Developments in Landsat Land Cover Classification Methods: A Review. *Remote Sensing*, 9(9), 967. <https://doi.org/10.3390/rs9090967>
- Picotte, J. J., & Robertson, K. M. (2011). Validation of remote sensing of burn severity in south-eastern US ecosystems. *International Journal of Wildland Fire*. <https://doi.org/10.1071/WF10013>
- Pipia, L., Muñoz-Marí, J., Amin, E., Belda, S., Camps-Valls, G., & Verrelst, J. (2019). Fusing optical and SAR time series for LAI gap filling with multioutput Gaussian processes. *Remote Sensing of Environment*, 235(September), 111452. <https://doi.org/10.1016/j.rse.2019.111452>
- Plaza, A., & Chang, C.-I. (2005). Fast implementation of pixel purity index algorithm. *Proc.SPIE*, 5806. <https://doi.org/10.1117/12.602374>
- Pollino, M., & Modica, G. (2013). Free Web Mapping Tools to Characterise Landscape Dynamics and to Favour e-Participation. In Springer (Ed.), Murgante B. et al. (eds) *Computational Science and Its Applications – ICCSA 2013. Lecture Notes in Computer Science*, vol 7973. Springer, Berlin, Heidelberg. [https://doi.org/10.1007/978-3-642-39646-5\\_41](https://doi.org/10.1007/978-3-642-39646-5_41)
- Polychronaki, A., Gitas, I. Z., & Minchella, A. (2014). Monitoring post-fire vegetation recovery in the Mediterranean using SPOT and ERS imagery. *International Journal of Wildland Fire*, 23(5), 631–642. <https://doi.org/10.1071/WF12058>
- Polychronaki, Anastasia, & Gitas, I. Z. (2010). The development of an operational procedure for burned-area mapping using object-based classification and ASTER imagery. *International Journal of Remote Sensing*, 31(4), 1113–1120. <https://doi.org/10.1080/01431160903334497>

- Polychronaki, Anastasia, & Gitas, I. Z. (2012). Burned area mapping in greece using SPOT-4 HRVIR images and object-based image analysis. *Remote Sensing*, 4(2), 424–438. <https://doi.org/10.3390/rs4020424>
- Polychronaki, Anastasia, Gitas, I. Z., Veraverbeke, S., & Debieu, A. (2013). Evaluation of ALOS PALSAR imagery for burned area mapping in greece using object-based classification. *Remote Sensing*, 5(11), 5680–5701. <https://doi.org/10.3390/rs5115680>
- Poon, P. K., & Kinoshita, A. M. (2018). Estimating evapotranspiration in a post-fire environment using remote sensing and machine learning. *Remote Sensing*, 10(11). <https://doi.org/10.3390/rs10111728>
- Praticò, S., Solano, F., Di Fazio, S., & Modica, G. (2021). Machine learning classification of mediterranean forest habitats in google earth engine based on seasonal sentinel-2 time-series and input image composition optimisation. *Remote Sensing*, 13(4), 1–28. <https://doi.org/10.3390/rs13040586>
- Pulvirenti, L., Squicciarino, G., Fiori, E., Fiorucci, P., Ferraris, L., Negro, D., Gollini, A., Severino, M., & Puca, S. (2020). An automatic processing chain for near real-time mapping of burned forest areas using sentinel-2 data. *Remote Sensing*, 12(4). <https://doi.org/10.3390/rs12040674>
- Qi, J., & Kerr, Y. (1997). On current compositing algorithms. *Remote Sensing Reviews*, 15(1–4), 235–256. <https://doi.org/10.1080/02757259709532340>
- Quegan, S., Toan, T. Le, Yu, J. J., Ribbes, F., & Floury, N. (2000). Multitemporal ERS SAR analysis applied to forest mapping. *IEEE Transactions on Geoscience and Remote Sensing*. <https://doi.org/10.1109/36.842003>
- Quintano, C, Fernández-Manso, A., Fernández-Manso, O., & Shimabukuro, Y. E. (2006). Mapping burned areas in Mediterranean countries using spectral mixture analysis from a uni-temporal perspective. *International Journal of Remote Sensing*, 27(4), 645–662. <https://doi.org/10.1080/01431160500212195>
- Quintano, Carmen, Fernández-Manso, A., Calvo, L., & Roberts, D. A. (2019a). Vegetation and soil fire damage analysis based on species distribution modeling trained with multispectral satellite data. *Remote Sensing*, 11(15). <https://doi.org/10.3390/rs11151832>
- Quintano, Carmen, Fernández-Manso, A., Calvo, L., & Roberts, D. A. (2019b). Vegetation and Soil Fire Damage Analysis Based on Species Distribution Modeling Trained with Multispectral Satellite Data. In *Remote Sensing* (Vol. 11, Issue 15). <https://doi.org/10.3390/rs11151832>
- Quintano, Carmen, Fernandez-Manso, A., & Roberts, D. A. (2017). Burn severity mapping from Landsat MESMA fraction images and Land Surface Temperature. *Remote Sensing of Environment*, 190(March), 83–95. <https://doi.org/10.1016/j.rse.2016.12.009>
- Quintano, Carmen, Fernández-Manso, A., & Roberts, D. A. (2013). Multiple Endmember Spectral Mixture Analysis (MESMA) to map burn severity levels from Landsat images in Mediterranean countries. *Remote Sensing of Environment*, 136, 76–88. <https://doi.org/10.1016/j.rse.2013.04.017>
- Quintano, Carmen, Fernández-Manso, A., & Roberts, D. A. (2020). Enhanced burn severity estimation using fine resolution ET and MESMA fraction images with machine learning algorithm. *Remote Sensing of Environment*, 244, 111815. <https://doi.org/https://doi.org/10.1016/j.rse.2020.111815>
- Quintano, Carmen, Fernández-Manso, A., Shimabukuro, Y. E., & Pereira, G. (2012). Spectral unmixing. *International Journal of Remote Sensing*, 33(17), 5307–5340. <https://doi.org/10.1080/01431161.2012.661095>
- Radoux, J., & Defourny, P. (2008). Quality assessment of segmentation results devoted to object-based classification. In *Object-Based Image Analysis. Spatial Concepts for Knowledge-Driven Remote Sensing*

- Applications* (pp. 257–271). Springer-Verlag Berlin Heidelberg.
- Ramezan, C. A., Warner, T. A., & Maxwell, A. E. (2019). Evaluation of sampling and cross-validation tuning strategies for regional-scale machine learning classification. *Remote Sensing*, *11*(2).  
<https://doi.org/10.3390/rs11020185>
- Rehman, T. U., Mahmud, M. S., Chang, Y. K., Jin, J., & Shin, J. (2019). Current and future applications of statistical machine learning algorithms for agricultural machine vision systems. *Computers and Electronics in Agriculture*, *156*, 585–605. <https://doi.org/https://doi.org/10.1016/j.compag.2018.12.006>
- Reid, C. E., Brauer, M., Johnston, F. H., Jerrett, M., Balmes, J. R., & Elliott, C. T. (2016). Critical Review of Health Impacts of Wildfire Smoke Exposure. *Environmental Health Perspectives*, *124*(9), 1334–1343.  
<https://doi.org/http://dx.doi.org/10.1289/ehp.1409277>
- Riaño, D., Chuvieco, E., Ustin, S., Zomer, R., Dennison, P., Roberts, D., & Salas, J. (2002). Assessment of vegetation regeneration after fire through multitemporal analysis of AVIRIS images in the Santa Monica Mountains. *Remote Sensing of Environment*, *79*(1), 60–71. [https://doi.org/https://doi.org/10.1016/S0034-4257\(01\)00239-5](https://doi.org/https://doi.org/10.1016/S0034-4257(01)00239-5)
- Richards, J. A. (2009a). Corretting and Calibrating Radar Imagery. In Springer-Verlag Berlin Heidelberg (Ed.), *Remote Sensing with Imaging Radar* (1th ed.). Springer-Verlag Berlin Heidelberg.  
<https://doi.org/10.1007/978-3-642-02020-9>
- Richards, J. A. (2009b). Scattering from Earth Surface Features. In S.-V. B. Heidelberg (Ed.), *Remote Sensing with Imaging Radar* (1th ed.). Springer-Verlag Berlin Heidelberg. <https://doi.org/10.1007/978-3-642-02020-9>
- Richards, J. A. (2009c). The Radiation Framework. In Springer-Verlag Berlin Heidelberg (Ed.), *Remote Sensing with Imaging Radar* (1th ed.). Springer-Verlag Berlin Heidelberg. <https://doi.org/10.1007/978-3-642-02020-9>
- Roberts, D. A., Dennison, P. E., Gardner, M. E., Hetzel, Y., Ustin, S. L., & Lee, C. T. (2003). Evaluation of the potential of Hyperion for fire danger assessment by comparison to the Airborne Visible/Infrared Imaging Spectrometer. *IEEE Transactions on Geoscience and Remote Sensing*, *41*(6), 1297–1310.  
<https://doi.org/10.1109/TGRS.2003.812904>
- Roberts, D. A., Smith, M. O., & Adams, J. B. (1993). Green vegetation, nonphotosynthetic vegetation, and soils in AVIRIS data. *Remote Sensing of Environment*, *44*(2), 255–269.  
[https://doi.org/https://doi.org/10.1016/0034-4257\(93\)90020-X](https://doi.org/https://doi.org/10.1016/0034-4257(93)90020-X)
- Robichaud, P. R., Lewis, S. A., Laes, D. Y. M., Hudak, A. T., Kokaly, R. F., & Zamudio, J. A. (2007). Postfire soil burn severity mapping with hyperspectral image unmixing. *Remote Sensing of Environment*, *108*(4), 467–480. <https://doi.org/https://doi.org/10.1016/j.rse.2006.11.027>
- Röder, A., Hill, J., Duguy, B., Alloza, J. A., & Vallejo, R. (2008). Using long time series of Landsat data to monitor fire events and post-fire dynamics and identify driving factors. A case study in the Ayora region (eastern Spain). *Remote Sensing of Environment*, *112*(1), 259–273.  
<https://doi.org/https://doi.org/10.1016/j.rse.2007.05.001>
- Rodman, K. C., Andrus, R. A., Veblen, T. T., & Hart, S. J. (2021). Remote Sensing of Environment Disturbance detection in landsat time series is influenced by tree mortality agent and severity , not by prior disturbance. *Remote Sensing of Environment*, *254*(December 2020), 112244. <https://doi.org/10.1016/j.rse.2020.112244>

- Rogan, J., & Franklin, J. (2001). Mapping Wildfire Burn Severity in Southern California Forests and Shrublands Using Enhanced Thematic Mapper Imagery. *Geocarto International*, 16(4), 91–106.  
<https://doi.org/10.1080/10106040108542218>
- Romeo, F., Marziliano, P. A., Turrión, M. B., & Muscolo, A. (2020). Short-term effects of different fire severities on soil properties and *Pinus halepensis* regeneration. *Journal of Forestry Research*, 31(4), 1271–1282. <https://doi.org/10.1007/s11676-019-00884-2>
- Rosa, I. M. D., Pereira, J. M. C., & Tarantola, S. (2011). Atmospheric emissions from vegetation fires in Portugal (1990–2008): Estimates, uncertainty analysis, and sensitivity analysis. *Atmospheric Chemistry and Physics*, 11(6), 2625–2640. <https://doi.org/10.5194/acp-11-2625-2011>
- Roteta, E., Bastarrika, A., Padilla, M., Storm, T., & Chuvieco, E. (2019). Development of a Sentinel-2 burned area algorithm: Generation of a small fire database for sub-Saharan Africa. *Remote Sensing of Environment*, 222(November 2018), 1–17. <https://doi.org/10.1016/j.rse.2018.12.011>
- Roth, K. L., Dennison, P. E., & Roberts, D. A. (2012). Comparing endmember selection techniques for accurate mapping of plant species and land cover using imaging spectrometer data. *Remote Sensing of Environment*, 127, 139–152. <https://doi.org/https://doi.org/10.1016/j.rse.2012.08.030>
- Rousseeuw, P. J. (1987). Silhouettes: A graphical aid to the interpretation and validation of cluster analysis. *Journal of Computational and Applied Mathematics*, 20(C), 53–65. [https://doi.org/10.1016/0377-0427\(87\)90125-7](https://doi.org/10.1016/0377-0427(87)90125-7)
- Ruiz-Ramos, J., Marino, A., & Boardman, C. P. (2018). Using sentinel 1-SAR for monitoring long term variation in burnt forest areas. *International Geoscience and Remote Sensing Symposium (IGARSS)*, 2018-July(July 2017), 4901–4904. <https://doi.org/10.1109/IGARSS.2018.8518960>
- Ryu, J. H., Han, K. S., Hong, S., Park, N. W., Lee, Y. W., & Cho, J. (2018). Satellite-Based Evaluation of the Post-Fire Recovery Process from the Worst Forest Fire Case in South Korea. *Remote Sensing*, 10(6). <https://doi.org/10.3390/rs10060918>
- Saatchi, S. (2019a). SAR Methods for Mapping and Monitoring Forest Biomass. In *The SAR Handbook. Comprehensive Methodologies for Forest Monitoring and Biomass Estimation*. NASA.  
<https://doi.org/10.25966/nr2c-s697>
- Saatchi, S. (2019b). SAR Methods for Mapping and Monitoring Forest Biomass. In *The SAR Handbook. Comprehensive Methodologies for Forest Monitoring and Biomass Estimation*. NASA.  
<https://doi.org/10.25966/nr2c-s697>
- Saatchi, S., Ulander, L., Williams, M., Quegan, S., Letoan, T., Shugart, H., & Chave, J. (2012). Forest biomass and the science of inventory from space. *Nature Climate Change*, 2(12), 826–827.  
<https://doi.org/10.1038/nclimate1759>
- Sali, M., Piaser, E., Boschetti, M., Brivio, P. A., Sona, G., Bordogna, G., & Stroppiana, D. (2021). A burned area mapping algorithm for sentinel-2 data based on approximate reasoning and region growing. *Remote Sensing*, 13(11). <https://doi.org/10.3390/rs13112214>
- San-Miguel-Ayanz, J., de Rigo, D., Caudullo, G., Houston Durrant, T., & Mauri, A. (2016). *European Forest Tree Species* (P. O. of the E. Union (ed.)). Publication Office of the European Union.  
<https://doi.org/10.2788/4251>
- San-Miguel-Ayanz, Jesús, Durrant, T., Boca, R., Libertà, G., Branco, A., de Rigo, D., Ferrari, D., Maianti, P.,

- Vivancons, A., Costa, H., Lana, F., Löffler, P., Nuijten, D., Ahlgren, A. C., & Leray, T. (2018). *Forest Fires in Europe, Middle East and North Africa 2017* (E. Commission (ed.)). Publications Office of the European Union. <https://doi.org/10.2760/27815>
- San-Miguel-Ayanza, J., Durrant, T., Boca, R., Libertà, G., Branco, A., de Rigo, D., Ferrari, D., Maianti, P., Vivancons, T. A., Oom, D., & Pfeiffer, H. (2019). *Forest Fires in Europe, Middle East and North Africa 2018. JRC Technical Report* (Publications Office of the European Union (ed.)). Publications Office of the European Union. <https://doi.org/10.2760/1128>
- Sankey, T. T., Moffet, C., & Weber, K. (2008). Postfire Recovery of Sagebrush Communities: Assessment Using Spot-5 and Very Large-Scale Aerial Imagery. *Rangeland Ecology & Management*, 61(6), 598–604. <https://doi.org/https://doi.org/10.2111/08-079.1>
- Santi, E., Paloscia, S., Pettinato, S., Fontanelli, G., Mura, M., Zolli, C., Maselli, F., Chiesi, M., Bottai, L., & Chirici, G. (2017). The potential of multifrequency SAR images for estimating forest biomass in Mediterranean areas. *Remote Sensing of Environment*, 200(May 2018), 63–73. <https://doi.org/10.1016/j.rse.2017.07.038>
- Santos, F. L. M., Libonati, R., Peres, L. F., Pereira, A. A., Narcizo, L. C., Rodrigues, J. A., Oom, D., Pereira, J. M. C., Schroeder, W., & Setzer, A. W. (2020). Assessing VIIRS capabilities to improve burned area mapping over the Brazilian Cerrado. *International Journal of Remote Sensing*, 41(21), 8300–8327. <https://doi.org/10.1080/01431161.2020.1771791>
- Santoso, A. W., Pebrianti, D., Bayuaji, L., & Zain, J. M. (2015). Performance of various speckle reduction filters on Synthetic Aperture Radar image. *2015 4th International Conference on Software Engineering and Computer Systems, ICSECS 2015: Virtuous Software Solutions for Big Data, August*, 11–14. <https://doi.org/10.1109/ICSECS.2015.7333103>
- Saulino, L., Rita, A., Migliozi, A., Maffei, C., Allevato, E., Garonna, A. Pietro, & Saracino, A. (2020). Detecting Burn Severity across Mediterranean Forest Types by Coupling Medium-Spatial Resolution Satellite Imagery and Field Data. *Remote Sensing*, 12(4), 1–21. <https://doi.org/10.3390/rs12040741>
- Sayedain, S. A., Maghsoudi, Y., & Eini-Zinab, S. (2020). Assessing the use of cross-orbit Sentinel-1 images in land cover classification. *International Journal of Remote Sensing*, 41(20), 7801–7819. <https://doi.org/10.1080/01431161.2020.1763512>
- Schepers, L., Haest, B., Veraverbeke, S., Spanhove, T., Borre, J. Vanden, & Goossens, R. (2014). Burned area detection and burn severity assessment of a heathland fire in Belgium using airborne imaging spectroscopy (APEX). *Remote Sensing*, 6(3), 1803–1826. <https://doi.org/10.3390/rs6031803>
- Schwatke, C., Scherer, D., & Dettmering, D. (2019). Automated extraction of consistent time-variable water surfaces of lakes and reservoirs based on Landsat and Sentinel-2. In *Remote Sensing* (Vol. 11, Issue 9). <https://doi.org/10.3390/rs11091010>
- Semeraro, T., Vacchiano, G., Aretano, R., & Ascoli, D. (2019). Application of vegetation index time series to value fire effect on primary production in a Southern European rare wetland. *Ecological Engineering*, 134(March), 9–17. <https://doi.org/10.1016/j.ecoleng.2019.04.004>
- Senthilnath, J., Kandukuri, M., Dokania, A., & Ramesh, K. N. (2017). Application of UAV imaging platform for vegetation analysis based on spectral-spatial methods. *Computers and Electronics in Agriculture*, 140, 8–24. <https://doi.org/https://doi.org/10.1016/j.compag.2017.05.027>

- Sertel, E., & Alganci, U. (2016). Comparison of pixel and object-based classification for burned area mapping using SPOT-6 images. *Geomatics, Natural Hazards and Risk*, 7(4), 1198–1206.  
<https://doi.org/10.1080/19475705.2015.1050608>
- Settle, J. J., & Drake, N. A. (1993). Linear mixing and the estimation of ground cover proportions. *International Journal of Remote Sensing*, 14(6), 1159–1177. <https://doi.org/10.1080/01431169308904402>
- Setzer, A. W., & Pereira, M. C. (1991). Amazonia biomass burnings in 1987 and an estimate of their tropospheric emissions. In *Ambio* (Vol. 20, Issue 1, pp. 19–22). <https://doi.org/10.2307/4313765>
- SHAP. (2022). *SHAP KernelExplainer Doc*. <https://shap-lrjball.readthedocs.io/en/latest/generated/shap.KernelExplainer.html>
- Shaun, K., Ndaïmani, H., & Kavhu, B. (2020). Exploring the utility of Sentinel-2 MSI derived spectral indices in mapping burned areas in different land-cover types. *Scientific African*, 10, e00565.  
<https://doi.org/10.1016/j.sciaf.2020.e00565>
- Shimabukuro, Y. E., & Ponzoni, F. J. (2019). *Spectral Mixture for Remote Sensing. Linear Model and Applications* (C. Springer (ed.); 1th ed.). Springer, Cham. <https://doi.org/10.1007/978-3-030-02017-0>
- Shimabukuro, Y. E., & Smith, J. A. (1991). The least-squares mixing models to generate fraction images derived from remote sensing multispectral data. *IEEE Transactions on Geoscience and Remote Sensing*, 29(1), 16–20. <https://doi.org/10.1109/36.103288>
- Shimabukuro, Yosio Edemir, Miettinen, J., Beuchle, R., Grecchi, R. C., Simonetti, D., & Achard, F. (2015). Estimating Burned Area in Mato Grosso, Brazil, Using an Object-Based Classification Method on a Systematic Sample of Medium Resolution Satellite Images. *IEEE Journal of Selected Topics in Applied Earth Observations and Remote Sensing*, 8(9), 4502–4508. <https://doi.org/10.1109/JSTARS.2015.2464097>
- Shufelt, J. A. (1999). Performance evaluation and analysis of monocular building extraction from aerial imagery. *IEEE Transactions on Pattern Analysis and Machine Intelligence*, 21(4), 311–326.  
<https://doi.org/10.1109/34.761262>
- Silva, J. M.N., Cadima, J. F. C. L., Pereira, J. M. C., & Grégoire, J. M. (2004). Assessing the feasibility of a global model for multi-temporal burned area mapping using SPOT-VEGETATION data. *International Journal of Remote Sensing*. <https://doi.org/10.1080/01431160412331291251>
- Silva, João M.N., Moreno, M. V., Le Page, Y., Oom, D., Bistinas, I., & Pereira, J. M. C. (2019). Spatiotemporal trends of area burnt in the Iberian Peninsula, 1975–2013. *Regional Environmental Change*, 19(2), 515–527. <https://doi.org/10.1007/s10113-018-1415-6>
- Siqueira, P. (2019). Forest Stand Height Estimation. In *The SAR Handbook. Comprehensive Methodologies for Forest Monitoring and Biomass Estimation*. NASA. <https://doi.org/10.25966/nr2c-s697>
- Sistema Nacional de Informação Geográfica (SNIG). (2021).
- Small, D. (2011). Flattening gamma: Radiometric terrain correction for SAR imagery. *IEEE Transactions on Geoscience and Remote Sensing*, 49(8), 3081–3093. <https://doi.org/10.1109/TGRS.2011.2120616>
- Smiraglia, D., Filipponi, F., Mandrone, S., Tornato, A., & Taramelli, A. (2020). Agreement index for burned area mapping: Integration of multiple spectral indices using Sentinel-2 satellite images. *Remote Sensing*, 12(11). <https://doi.org/10.3390/rs12111862>
- Smith, A M S, Lentile, L. B., Hudak, A. T., & Morgan, P. (2007). Evaluation of linear spectral unmixing and

- $\Delta$ NBR for predicting post-fire recovery in a North American ponderosa pine forest. *International Journal of Remote Sensing*, 28(22), 5159–5166. <https://doi.org/10.1080/01431160701395161>
- Smith, Alistair M S, Wooster, M. J., Drake, N. A., Dipotso, F. M., Falkowski, M. J., & Hudak, A. T. (2005). Testing the potential of multi-spectral remote sensing for retrospectively estimating fire severity in African Savannahs. *Remote Sensing of Environment*, 97(1), 92–115. <https://doi.org/https://doi.org/10.1016/j.rse.2005.04.014>
- snap. (n.d.).
- snap cookbook. (n.d.).
- Soares, C., Silva, J. M. N., Boavida-Portugal, J., & Cerasoli, S. (2022). Spectral-Based Monitoring of Climate Effects on the Inter-Annual Variability of Different Plant Functional Types in Mediterranean Cork Oak Woodlands. In *Remote Sensing* (Vol. 14, Issue 3). <https://doi.org/10.3390/rs14030711>
- Sokolova, M., Japkowicz, N., & Szpakowicz, S. (2006). *Beyond Accuracy, F-Score and ROC: A Family of Discriminant Measures for Performance Evaluation* (Issue c, pp. 1015–1021). [https://doi.org/10.1007/11941439\\_114](https://doi.org/10.1007/11941439_114)
- Sokolova, M., & Lapalme, G. (2009). A systematic analysis of performance measures for classification tasks. *Information Processing and Management*, 45(4), 427–437. <https://doi.org/10.1016/j.ipm.2009.03.002>
- Solano, F., Colonna, N., Marani, M., & Pollino, M. (2019). *Geospatial Analysis to Assess Natural Park Biomass Resources for Energy Uses in the Context of the Rome Metropolitan Area BT - New Metropolitan Perspectives* (F. Calabrò, L. Della Spina, & C. Bevilacqua (Eds.); pp. 173–181). Springer International Publishing.
- Solans Vila, J. P., & Barbosa, P. (2010). Post-fire vegetation regrowth detection in the Deiva Marina region (Liguria-Italy) using Landsat TM and ETM+ data. *Ecological Modelling*, 221(1), 75–84. <https://doi.org/https://doi.org/10.1016/j.ecolmodel.2009.03.011>
- Somers, B., Asner, G. P., Tits, L., & Coppin, P. (2011). Endmember variability in Spectral Mixture Analysis: A review. *Remote Sensing of Environment*, 115(7), 1603–1616. <https://doi.org/https://doi.org/10.1016/j.rse.2011.03.003>
- Song, C., & Woodcock, C. E. (2003). Monitoring forest succession with multitemporal Landsat images: factors of uncertainty. *IEEE Transactions on Geoscience and Remote Sensing*, 41(11), 2557–2567. <https://doi.org/10.1109/TGRS.2003.818367>
- Sousa, A. M. O., Pereira, J. M. C., & Silva, J. M. N. (2003). Evaluating the performance of multitemporal image compositing algorithms for burned area analysis. *International Journal of Remote Sensing*, 24(6), 1219–1236. <https://doi.org/10.1080/01431160110114466>
- Souza, C., Firestone, L., Silva, L. M., & Roberts, D. (2003). Mapping forest degradation in the Eastern Amazon from SPOT 4 through spectral mixture models. *Remote Sensing of Environment*, 87(4), 494–506. <https://doi.org/https://doi.org/10.1016/j.rse.2002.08.002>
- Spadoni, G. L., Cavalli, A., Congedo, L., & Munafò, M. (2020). Analysis of Normalized Difference Vegetation Index (NDVI) multi-temporal series for the production of forest cartography. *Remote Sensing Applications: Society and Environment*, 20, 100419. <https://doi.org/https://doi.org/10.1016/j.rsase.2020.100419>
- Spampinato, G. (2014). *Guida alla flora dell'Aspromonte* (Laruffa Editore (Ed.)). Laruffa Editore.



- <http://www.parconazionaleaspromonte.it/emporio-dettaglio.php?id=584>
- Spampinato, G., Cameriere, P., Caridi, D., & Crisafulli, A. (2002). *Carta della vegetazione reale del Parco Nazionale dell'Aspromonte*.
- Spracklen, B., & Spracklen, D. V. (2021). Synergistic use of sentinel-1 and sentinel-2 to map natural forest and acacia plantation and stand ages in north-central vietnam. *Remote Sensing*, 13(2), 1–19.  
<https://doi.org/10.3390/rs13020185>
- Storey, E. A., Lee West, K. R., & Stow, D. A. (2021). Utility and optimization of LANDSAT-derived burned area maps for southern California. *International Journal of Remote Sensing*, 42(2), 486–505.  
<https://doi.org/10.1080/01431161.2020.1809741>
- Stroppiana, D., Azar, R., Calò, F., Pepe, A., Imperatore, P., Boschetti, M., Silva, J. M. N., Brivio, P. A., & Lanari, R. (2015). Integration of optical and SAR data for burned area mapping in Mediterranean regions. *Remote Sensing*, 7(2), 1320–1345. <https://doi.org/10.3390/rs70201320>
- Stroppiana, D., Pinnock, S., Pereira, J. M. C., & Grégoire, J.-M. (2002). Radiometric analysis of SPOT-VEGETATION images for burnt area detection in Northern Australia. *Remote Sensing of Environment*, 82(1), 21–37. [https://doi.org/https://doi.org/10.1016/S0034-4257\(02\)00021-4](https://doi.org/https://doi.org/10.1016/S0034-4257(02)00021-4)
- Subasi, A. (2020). Chapter 2 - Data preprocessing. In *Practical Machine Learning for Data Analysis Using Python* (pp. 27–89). <https://doi.org/10.1016/B978-0-12-821379-7.00002-3>
- Sunderman, S. O., & Weisberg, P. J. (2011). Remote sensing approaches for reconstructing fire perimeters and burn severity mosaics in desert spring ecosystems. *Remote Sensing of Environment*, 115(9), 2384–2389.  
<https://doi.org/https://doi.org/10.1016/j.rse.2011.05.001>
- Suryoprayogo, H., Ramdani, F., & Utaminigrum, F. (2018). Mapping Paddy Growth Stage Based-on Hyperspectral EO-1 Hyperion Using Pixel Purity Index Endmember Extraction Algorithm. *Journal of Telecommunication, Electronic and Computer Engineering (JTEC)*, 10(1-6 SE-Articles), 47–54.  
<https://jtec.utem.edu.my/jtec/article/view/3666>
- Szigarski, C., Jagdhuber, T., Baur, M., Thiel, C., Parrens, M., Wigneron, J., Piles, M., & Entekhabi, D. (2018). Analysis of the Radar Vegetation Index and Potential Improvements. *Remote Sensing*, 10, 1776, 1–15.  
<https://doi.org/doi:10.3390/rs10111776>
- Tanase, M. A., Kennedy, R., & Aponte, C. (2015a). Fire severity estimation from space: A comparison of active and passive sensors and their synergy for different forest types. *International Journal of Wildland Fire*, 24(8), 1062–1075. <https://doi.org/10.1071/WF15059>
- Tanase, M. A., Kennedy, R., & Aponte, C. (2015b). Radar Burn Ratio for fire severity estimation at canopy level: An example for temperate forests. *Remote Sensing of Environment*, 170, 14–31.  
<https://doi.org/10.1016/j.rse.2015.08.025>
- Tanase, M., de la Riva, J., Santoro, M., Pérez-Cabello, F., & Kasischke, E. (2011). Sensitivity of SAR data to post-fire forest regrowth in Mediterranean and boreal forests. *Remote Sensing of Environment*, 115(8), 2075–2085. <https://doi.org/10.1016/j.rse.2011.04.009>
- Tanase, Mihai A., Belenguer-Plomer, M. A., Roteta, E., Bastarrika, A., Wheeler, J., Fernández-Carrillo, Á., Tansey, K., Wiedemann, W., Navratil, P., Lohberger, S., Siegert, F., & Chuvieco, E. (2020). Burned Area Detection and Mapping: Intercomparison of Sentinel-1 and Sentinel-2 Based Algorithms over Tropical Africa. *Remote Sensing*, 12(2), 334. <https://doi.org/10.3390/rs12020334>

- Tanase, Mihai A., Santoro, M., Aponte, C., & De La Riva, J. (2014). Polarimetric properties of burned forest areas at C- and L-band. *IEEE Journal of Selected Topics in Applied Earth Observations and Remote Sensing*. <https://doi.org/10.1109/JSTARS.2013.2261053>
- Tanase, Mihai A., Santoro, M., De La Riva, J., Pérez-Cabello, F., & Le Toan, T. (2010). Sensitivity of X-, C-, and L-band SAR backscatter to burn severity in Mediterranean pine forests. *IEEE Transactions on Geoscience and Remote Sensing*, 48(10), 3663–3675. <https://doi.org/10.1109/TGRS.2010.2049653>
- Tanase, Mihai A., Santoro, M., Wegmüller, U., de la Riva, J., & Pérez-Cabello, F. (2010). Properties of X-, C- and L-band repeat-pass interferometric SAR coherence in Mediterranean pine forests affected by fires. *Remote Sensing of Environment*. <https://doi.org/10.1016/j.rse.2010.04.021>
- Tane, Z., Roberts, D., Veraverbeke, S., Casas, Á., Ramirez, C., & Ustin, S. (2018). Evaluating Endmember and Band Selection Techniques for Multiple Endmember Spectral Mixture Analysis using Post-Fire Imaging Spectroscopy. In *Remote Sensing* (Vol. 10, Issue 3). <https://doi.org/10.3390/rs10030389>
- Tansey, K., Gre, J., Stroppiana, D., Pereira, M. C., Boschetti, L., Maggi, M., Brivio, P. A., & Fraser, R. (2004). *Vegetation burning in the year 2000 : Global burned area estimates from SPOT VEGETATION data*. 109, 1–22. <https://doi.org/10.1029/2003JD003598>
- Tansey, K., Grégoire, J.-M., Binaghi, E., Boschetti, L., Brivio, P. A., Ershov, D., Flasse, S., Fraser, R., Graetz, D., Maggi, M., Peduzzi, P., Pereira, Jo., Silva, J., Sousa, A., & Stroppiana, D. (2004). A Global Inventory of Burned Areas at 1 Km Resolution for the Year 2000 Derived from Spot Vegetation Data. *Climatic Change*, 67(2), 345–377. <https://doi.org/10.1007/s10584-004-2800-3>
- The Python Language Reference*. (2021).
- Tompkins, S., Mustard, J. F., Pieters, C. M., & Forsyth, D. W. (1997). Optimization of endmembers for spectral mixture analysis. *Remote Sensing of Environment*, 59(3), 472–489. [https://doi.org/https://doi.org/10.1016/S0034-4257\(96\)00122-8](https://doi.org/https://doi.org/10.1016/S0034-4257(96)00122-8)
- Trudel, M., Charbonneau, F., & Leconte, R. (2012). Using RADARSAT-2 polarimetric and ENVISAT-ASAR dual-polarization data for estimating soil moisture over agricultural fields. *Canadian Journal of Remote Sensing*, 38(4), 514–527. <https://doi.org/10.5589/m12-043>
- Valkó, O., & Deák, B. (2021). Increasing the potential of prescribed burning for the biodiversity conservation of European grasslands. *Current Opinion in Environmental Science & Health*, 22, 100268. <https://doi.org/https://doi.org/10.1016/j.coesh.2021.100268>
- Vanderhoof, M. K., Hawbaker, T. J., Teske, C., Ku, A., Noble, J., & Picotte, J. (2021). *Mapping Wetland Burned Area from Sentinel-2 across the Southeastern United States and Its Contributions Relative to Landsat-8 ( 2016 – 2019 )*. 8.
- Veraverbeke, S, Somers, B., Gitas, I., Katagis, T., Polychronaki, A., & Goossens, R. (2012). Spectral mixture analysis to assess post-fire vegetation regeneration using Landsat Thematic Mapper imagery: Accounting for soil brightness variation. *International Journal of Applied Earth Observation and Geoinformation*, 14(1), 1–11. <https://doi.org/https://doi.org/10.1016/j.jag.2011.08.004>
- Veraverbeke, Sander, & Hook, S. J. (2013). Evaluating spectral indices and spectral mixture analysis for assessing fire severity, combustion completeness and carbon emissions. *International Journal of Wildland Fire*, 22(5), 707–720. <https://doi.org/10.1071/WF12168>
- Verbyla, D. L. V., Kasischke, E. S. K., & Hoy, E. E. H. (2008). *Seasonal and topographic effects on estimating*

- fire severity from Landsat TM / ETM + data*. 2006, 527–534.
- Verhegghen, A., Eva, H., Ceccherini, G., Achard, F., Gond, V., Gourlet-Fleury, S., & Cerutti, P. O. (2016). The potential of sentinel satellites for burnt area mapping and monitoring in the Congo Basin forests. *Remote Sensing*, 8(12), 1–22. <https://doi.org/10.3390/rs8120986>
- Viana-Soto, A., Aguado, I., & Martínez, S. (2017). Assessment of Post-Fire Vegetation Recovery Using Fire Severity and Geographical Data in the Mediterranean Region (Spain). In *Environments* (Vol. 4, Issue 4). <https://doi.org/10.3390/environments4040090>
- Villa, P., Stroppiana, D., Fontanelli, G., Azar, R., & Brivio, P. A. (2015). In-season mapping of crop type with optical and X-band SAR data: A classification tree approach using synoptic seasonal features. *Remote Sensing*, 7(10), 12859–12886. <https://doi.org/10.3390/rs71012859>
- Wang, L., Yan, J., & Ma, Y. (2019). *Cloud Computing in Remote Sensing* (C. and Hall/CRC (Ed.); 1st ed.). CRC Press Taylor & Francis Group.
- Wang, Q., Adiku, S., Tenhunen, J., & Granier, A. (2005). On the relationship of NDVI with leaf area index in a deciduous forest site. *Remote Sensing of Environment*, 94(2), 244–255. <https://doi.org/https://doi.org/10.1016/j.rse.2004.10.006>
- Waske, B., & Braun, M. (2009). Classifier ensembles for land cover mapping using multitemporal SAR imagery. *ISPRS Journal of Photogrammetry and Remote Sensing*, 64(5), 450–457. <https://doi.org/10.1016/j.isprsjprs.2009.01.003>
- Winter, M. E. (1999). N-FINDR: an algorithm for fast autonomous spectral end-member determination in hyperspectral data. *Proc.SPIE*, 3753. <https://doi.org/10.1117/12.366289>
- Xie, Y., Sha, Z., & Yu, M. (2008). Remote sensing imagery in vegetation mapping: a review. *Journal of Plant Ecology*. <https://doi.org/10.1093/jpe/rtn005>
- Xofis, P., Spiliotis, J. A., Chatzigiovanakis, S., & Chrysomalidou, A. S. (2022). Long-Term Monitoring of Vegetation Dynamics in the Rhodopi Mountain Range National Park-Greece. In *Forests* (Vol. 13, Issue 3). <https://doi.org/10.3390/f13030377>
- Yang, J., Gong, P., Fu, R., Zhang, M., Chen, J., Liang, S., Xu, B., Shi, J., & Dickinson, R. (2013). The role of satellite remote sensing in climate change studies. *Nature Climate Change*, 3(10), 875–883. <https://doi.org/10.1038/nclimate1908>
- Yu, Y., & Saatchi, S. (2016). Sensitivity of L-band SAR backscatter to aboveground biomass of global forests. *Remote Sensing*, 8(6). <https://doi.org/10.3390/rs8060522>
- Zhang, P., Nascetti, A., Ban, Y., & Gong, M. (2019). An implicit radar convolutional burn index for burnt area mapping with Sentinel-1 C-band SAR data. *ISPRS Journal of Photogrammetry and Remote Sensing*, 158(April), 50–62. <https://doi.org/10.1016/j.isprsjprs.2019.09.013>
- Zhang, W., Brandt, M., Wang, Q., Prishchepov, A. V., Tucker, C. J., Li, Y., Lyu, H., & Fensholt, R. (2019). From woody cover to woody canopies: How Sentinel-1 and Sentinel-2 data advance the mapping of woody plants in savannas. *Remote Sensing of Environment*, 234(August), 111465. <https://doi.org/10.1016/j.rse.2019.111465>
- Zhang, Y., Ling, F., Wang, X., Foody, G. M., Boyd, D. S., Li, X., Du, Y., & Atkinson, P. M. (2021). Tracking small-scale tropical forest disturbances: Fusing the Landsat and Sentinel-2 data record. *Remote Sensing of Environment*, 261, 112470. <https://doi.org/https://doi.org/10.1016/j.rse.2021.112470>

- Zhao, P., Lu, D., Wang, G., Wu, C., Huang, Y., & Yu, S. (2016). Examining spectral reflectance saturation in landsat imagery and corresponding solutions to improve forest aboveground biomass estimation. *Remote Sensing*. <https://doi.org/10.3390/rs8060469>
- Zheng, Z., Zeng, Y., Li, S., & Huang, W. (2016). A new burn severity index based on land surface temperature and enhanced vegetation index. *International Journal of Applied Earth Observation and Geoinformation*. <https://doi.org/10.1016/j.jag.2015.11.002>
- Zhong, Y., Ma, A., Ong, Y. soon, Zhu, Z., & Zhang, L. (2018). Computational intelligence in optical remote sensing image processing. In *Applied Soft Computing Journal*. <https://doi.org/10.1016/j.asoc.2017.11.045>
- Zhou, Z., Liu, L., Jiang, L., Feng, W., & Samsonov, S. V. (2019). Using long-term SAR backscatter data to monitor post-fire vegetation recovery in tundra environment. *Remote Sensing*, 11(19). <https://doi.org/10.3390/rs11192230>

## 12. Websites

- aria2 download utility Homepage. 2020. Accessed 05 October 2020. <https://aria2.github.io/>
- ASF. 2022. Accessed 04 October 2022. <https://asf.alaska.edu/>.
- Copernicus Open Access Hub. 2022. Accessed 04 October 2022. <https://scihub.copernicus.eu/>. Last access 04/01/2022.
- Copernicus Long Term Archive Access. 2021. Accessed 5 January 2021. <https://scihub.copernicus.eu/userguide/LongTermArchive>.
- COS. 2018. Accessed 21 July 2022. <https://www.dgterritorio.gov.pt/Carta-de-Uso-e-Ocupacao-do-Solo-para-2018>.
- EFFIS Annual Fire Reports. 2022. Accessed October 04, 2022. <https://effis.jrc.ec.europa.eu/reports-and-publications/annual-fire-reports>.
- EFFIS Rapid Damage Assessment. 2022. Accessed 26 September 2022. <https://effis.jrc.ec.europa.eu/about-effis/technicavl-back-ground/rapid-damage-assessment>.
- ESA sen2cor Homepage. (2022). Accessed 04 October 2022. <https://step.esa.int/main/snap-supported-plugins/sen2cor/>.
- ESA Sentinel Homepage. 2022. Accessed 04 October 2022. <https://sentinel.esa.int/web/sentinel/home>.
- ESA SNAP Homepage 2022. Accessed 04 October 2022. <http://step.esa.int/main/toolboxes/snap/>.
- ESA SNAP Cookbook 2022. Accessed 04 October 2022. <https://senbox.atlassian.net/wiki/spaces/SNAP/pages/24051769/Cookbook>.
- ESA Sentinel-1 User Guide. 2016. Accessed 02 January 2021. <https://sentinel.esa.int/web/sentinel/user-guides/sentinel-1-sar/resolutions/level-1-ground-range-detected>.
- Esri ArcGIS World Imagery. 2021. Accessed 19 March 2021. <https://www.arcgis.com/home/item.html?id=10df2279f9684e4a9f6a7f08febac2a9>.
- European Environment Agency. 2022. Accessed 21 September 2022. [https://www.eea.europa.eu/data-and-maps/daviz/burnt-for-est-area-in-five-3/#tab-chart\\_5](https://www.eea.europa.eu/data-and-maps/daviz/burnt-for-est-area-in-five-3/#tab-chart_5).
- FIREMON Project. 2006. Accessed 02 October 2022. <https://www.firelab.org/project/firemon>.
- Google Earth Engine Guides. 2022. Accessed 04 October 2022. <https://developers.google.com/earth-engine/guides>.
- Google Earth Homepage. 2022. Accessed 04 October 2022. <https://www.google.it/intl/it/earth/>.
- ICNF. 2017. Accessed 18 May 2022. <https://www.icnf.pt/api/file/doc/2c45facee8d3e4f8>.
- LightGBM documentation. 2022. Accessed 08 January 2022. <https://lightgbm.readthedocs.io/en/latest/index.html>.
- MAAP. 2022. Accessed 04 October 2022. <https://earth-data.nasa.gov/esds/map>.
- OTB Homepage. 2021. Accessed 19 March 2021. <https://www.orfeo-toolbox.org/>.
- Scikit-learn Homepage. 2022. Accessed 04 October 2022. <https://scikit-learn.org/stable/#>.
- Sentinel2-cloud-detector repository. 2022. Accessed 04 October 2022. <https://github.com/sentinel-hub/sentinel2-cloud-detector>.
- Sentinel Hub Homepage. 2022. Accessed 04 October 2022. <https://www.sentinel-hub.com/>.
- SHAP. 2022. Accessed 04 October 2022. <https://shap.readthedocs.io/en/latest/index.html#>.
- SIG-ICNF. 2021. Accessed 20 January 2021. <https://sig.icnf.pt/portal/home/item.html?id=983c4e6c4d5b4666b258a3ad5f3ea5af>.
- SNIG. 2021. Accessed 20 January 2021. <https://sig.icnf.pt/portal/home/item.html?id=983c4e6c4d5b4666b258a3ad5f3ea5af>.
- SNIRH. 2022. Accessed 04 October 2022. <https://snirh.apambiente.pt/>.

- The Python Language Reference. 2022. Accessed 04 October 2022. <https://docs.python.org/3/reference/>.